GFZ
Helmholtz Centre
POTSDAM

INSTITUTE OF GEOSCIENCES

Universität
Potsdam

Modeling Stress and Dike Pathways in Calderas: Towards a Physics-based Forecast of Eruptive Vent Locations

Lorenzo Mantiloni, BSc, MSc
October, 2023

Cumulative dissertation
to obtain the academic degree
"Doctor Rerum Naturalium" (Dr. rer. nat.)
in the scientific discipline Geophysics

Submitted to the
Faculty of Mathematics and Natural Sciences
at the University of Potsdam, Germany

Primary advisor: Prof. Dr. Torsten Dahm
Co-advisor: Prof. Dr. Eleonora Rivalta

Reviewers: Prof. Dr. Eleonora Rivalta
Dr. Elisa Trasatti
Prof. Dr. Andy Hooper

Examining committee: Prof. Dr. Eva Eibl
Prof. Dr. Torsten Dahm
Prof. Dr. Frank Krüger

Statement of originality

I hereby declare that this thesis is, to the best of my knowledge, original, and the product of my own work. All the assistance received in preparing this thesis and the sources used have been acknowledged.

Lorenzo Mantiloni

Potsdam, October 2023

Abstract

Volcanic hazard assessment relies on physics-based models of hazards, such as lava flows and pyroclastic density currents, whose outcomes are very sensitive to the location where future eruptions will occur. On the contrary, forecast of vent opening locations in volcanic areas typically relies on purely data-driven approaches, where the spatial density of past eruptive vents informs the probability maps of future vent opening. Such techniques may be sub-optimal in volcanic systems with missing or scarce data, and where the controls on magma pathways may change over time. An alternative approach was recently proposed, relying on a model of stress-driven pathways of magmatic dikes. In that approach, the crustal stress was optimized so that dike trajectories linked consistently the location of the magma chamber to that of past vents. The retrieved information on the stress state was then used to forecast future dike trajectories. The validation of such an approach requires extensive application to nature. Before doing so, however, several important limitations need to be removed, most importantly the two-dimensional (2D) character of the models and theoretical concepts.

In this thesis, I develop methods and tools so that a physics-based strategy of stress inversion and eruptive vent forecast in volcanoes can be applied to three dimensional (3D) problems.
In the first part, I test the stress inversion and vent forecast strategy on analog models, still within a 2D framework, but improving on the efficiency of the stress optimization.
In the second part, I discuss how to correctly account for gravitational loading/unloading due to complex 3D topography with a Boundary-Element numerical model. Then, I develop a new, simplified but fast model of dike pathways in 3D, designed for running large numbers of simulations at minimal computational cost, and able to backtrack dike trajectories from vents on the surface. Finally, I combine the stress and dike models to simulate dike pathways in synthetic calderas.
In the third part, I describe a framework of stress inversion and vent forecast strategy in 3D for calderas. The stress inversion relies on, first, describing the magma storage below a caldera in terms of a probability density function. Next, dike trajectories are backtracked from the known locations of past vents down through the crust, and the optimization algorithm seeks for the stress models which lead trajectories through the regions of highest probability. I apply the new strategy to the synthetic scenarios presented in the second part, and I exploit the results from the stress inversions to produce probability maps of future vent locations for some of those scenarios.
In the fourth part, I present the inversion of different deformation source models applied to the ongoing ground deformation observed across the Rhenish Massif in Central Europe. The region includes the Eifel Volcanic Fields in Germany, a potential application case for the vent forecast strategy. The results show how the observed deformation may be due to melt accumulation in sub-horizontal structures in the lower crust or upper mantle.

The thesis concludes with a discussion of the stress inversion and vent forecast strategy, its limitations and applicability to real volcanoes. Potential developments of the modeling tools and concepts presented here are also discussed, as well as possible applications to other geophysical problems.

Zusammenfassung

Die Analyse vulkanischer Gefahren basiert auf physikalischen Gefahrenmodellen wie Lavaströmen und pyroklastischen Dichteströmen, deren Ergebnisse von den Lokationen der Eruptionen abhängt. Die Vorhersage der Lokationen von Spaltenöffnungen (eruptive vent opening) in Vulkangebieten basiert typischerweise auf rein datengesteuerten Ansätzen, bei denen die räumliche Verteilung vergangener Eruptionsspalten die Wahrscheinlichkeitskarten zukünftiger Spaltöffnungen beeinflusst. Solche Techniken sind in Vulkansystemen mit fehlenden oder knappen Daten suboptimal, ebenso wie dort, wo sich physikalische Bedingungen der Magmapfade im Laufe der Zeit verändern können. Kürzlich wurde ein alternativer Ansatz vorgeschlagen, der auf einem Modell spannungsbedingter Magmagänge basiert. Bei diesem Ansatz wurde die Krustenspannung so optimiert, dass die Verläufe der Magmagänge- sowohl mit der Lage der Magmakammer als auch mit der Lage früherer Spaltenöffnungen konsistent sind Die erlangten Informationen über den Spannungszustand werden dann zur Vorhersage zukünftiger Magmagänge verwendet. Die Validierung eines solchen Ansatzes erfordert eine umfassende Anwendung auf natürliche Vulkansysteme. Zuvor müssen jedoch einige wichtige Einschränkungen beseitigt werden, insbesondere der zweidimensionale (2D) Charakter der Modelle und theoretischen Konzepte.

In dieser Arbeit entwickle ich Methoden und Software, um physikbasierte Strategien der Spannungsinversion und der Vorhersage von Lokationen von Magmagängen in Vulkanen auf dreidimensionale (3D) Probleme anwenden zu können.

Im ersten Teil teste ich die Spannungsinversion und die Vorhersage von eruptiven Magmagängen an analogen Modellen, immer noch innerhalb eines 2D-Rahmens, aber mit verbesserter Effizienz der Spannungsoptimierung.

Im zweiten Teil diskutiere ich, wie die gravitative Belastung/Entlastung aufgrund einer komplexen 3D-Topographie mit einem numerischen Grenzelementmodell berücksichtigt werden kann. Anschließend entwickle ich ein neues, vereinfachtes, aber effizientes Modell der Magmagang-Ausbreitung in 3D Dieses ist für die Durchführung einer großen Anzahl von Simulationen mit minimalem Rechenaufwand konzipiert und dabei in der Lage, Magmagang-Ausbreitungen an der Oberfläche zurückzuverfolgen. Schließlich kombiniere ich die Spannungs- und Magma-Ausbreitungsmodelle, um Magmagänge in synthetischen Calderas zu simulieren.

Im dritten Teil erarbeite ich ein Rahmenmodell für Spannungsinversion und dreidimensionale Magmagang-Vorhersagen für Calderas. Die Spannungsinversion beruht auf der Annahme einer Magmaspeicherung unterhalb einer Caldera, deren Geometrie durch eine Wahrscheinlichkeitsdichtefunktion beschrieben wird. Vergangene Eruptionsstandorte werden durch die Erdkruste zurück propagiert, dabei werden die Spannungsmodelle so optimiert, dass die Endpunkte der Optimierung (Starpunkte der Magmagänge) mit der angenommenen Magmakammer übereinstimmen. Ich verwende die synthetischen Szenarien aus dem zweiten Teil, um die Spannungsinversion in kontrollieren Szenarien zu testen.

Im vierten Teil analysieren wir die Bodenverformung im Rheinischen Massiv, Mitteleuropa. Die Region umfasst die Eifel-Vulkanfelder in Deutschland, die einen potenziellen Anwendungsfall für die Strategie zur Vorhersage von Spalteneruptionen darstellen. Dabei nutze ich in den Inversionen unterschiedliche Deformations-Quellmodelle, um jährliche Magmavolumenänderungen aufzulösen, unter der Annahme, das Magma in die Lithosphäre injiziert wird. Die Ergebnisse zeigen, dass die beobachtete Verformung auf die Ansammlung von Schmelze in subhorizontalen Strukturen in der unteren Kruste oder im oberen Mantel zurückzuführen sein könnte.

Abschließend diskutiere ich die Limitationen der erarbeiteten Konzepte und die Möglichkeiten für Anwendungen sowohl in verschiedenen Hochrisko-Vulkanen, als auch in anderen Kontexten, wie besispielsweise in tektonischen und geothermischen Modellierungen.

Acknowledgments

This thesis is the realization of a long journey that has profoundly changed me, professionally and, most of all, personally. None of it would have been possible without my mentors, companions and friends, to whom I extend my gratitude here.

Eleonora Rivalta:
There is really no way to express my gratitude to Eleonora. She has been a fantastic mentor, and I owe to her competence, passion and patience most of my growth from naive student to (hopefully less) naive researcher. Eleonora is equally talented in being a leader in her field, making sure her students give and get the best, and taking care of the countless challenges and commitments of a hectic life. She has guided me throughout my PhD and offered me invaluable opportunities. She has set an example of dedication to work, passion for nature and good practice in science that I will always strive to match. Most importantly, she is a wonderful human being. She has fully motivated me to pursue a life in research.

Torsten Dahm:
Torsten has been a great supervisor, providing key insights and suggestions to this work and helping me better communicating its results. He has motivated me to broaden my interests in research, exchange ideas and share my skills with my colleagues. The section he leads is a truly friendly and supportive environment where research can thrive, and it has been my great privilege to be part of it.

Susanne Köster:
Nothing in Section 2.1 could work without Susanne. There is no easy way to thank her for the countless times she has helped me with administrative tasks and bureaucratic issues, both work-related and personal, during my years in Germany. Her relentless dedication to helping me out in any situation, as she does for everyone in the section, deserves nothing but praise.

Tim Davis:
Tim's skills, passion and resourcefulness have been an inspiration to me. His PhD's and earlier work has offered me the numerical model included in this thesis. He has introduced me to the fascinating world of Boundary Elements, contributed substantially to many concepts, and helped me spot many a mistake along the way.

Mehdi Nikkhoo:
Mehdi is a gentleman and an extremely talented scientist. His competence, rigor and dedication to science are something I can hardly match, but have a lot to learn from. His work has laid the foundation of most of the modeling tools employed here. His support throughout my PhD

has been so important, especially in challenging me to always question and improve my results, and pushing me to take initiative and responsibility for my own path.

Francesco Maccaferri and Luigi Passarelli:
Francesco and Luigi left Section 2.1 shortly after I joined it. Nonetheless, they have always been present throughout my PhD, helping shaping the scientific questions and bringing in key concepts in my work, Francesco on the dike modeling side, and Luigi on the statistical side. Thank you for all the insights, suggestions and coffees.

Valentina Armeni, Ayleen Gaete and Francesca Silverii:
Valentina, Ayleen and Francesca have been fantastic colleagues and friends, who helped me grow as a researcher and enjoy my time while doing so. Ayleen introduced me to the secrets of gelatin analog models and shared countless, pleasant hours with me in the lab. Valentina helped me grounding my models into the real-life world, and has infected me somehow with her love for geology. Francesca has set yet another, invaluable example of competence and passion for science, taught me more than one thing on ground deformation modeling and inversion techniques, and guided me through many wonders of Berlin.

Virginie Pinel:
Virginie is the french partner of the project that funded this work. I had the pleasure of being hosted by her at the Institut des Sciences de la Terre in Le-Bourget-du-Lac in 2022. I have benefited immensely from her expertise and motivation, and she has always offered me a great support. A good portion of this work has been shaped by her experience and suggestions. I am also grateful to her research group, with special thanks to Séverine Furst for her support during the writing of this thesis.

Kyle Anderson:
Kyle hosted me in the United States Geological Survey Moffett Field campus during my research visit to California in 2022. He is a passionate and talented scientist, who contributed to the late stage of this work with key concepts and feedback, and has offered me the opportunity to meet a vast and stimulating research environment.

Gert Zöller:
Gert was my first employer at the University of Potsdam, when this work started. He has provided helpful guidance in the early stages of the project, helped me with some complicated bureaucracy, and motivated me to develop the statistical concepts included in this thesis.

Valérie Cayol:
Valérie has welcomed me on a visit to her research group at the Laoratoire Magmas et Volcans in Clermont-Ferrand, and has offered me her support in more than one occasion ever since. The exchange of ideas and perspectives between our groups has been very instructive.

Section 2.1:
I am deeply grateful to all members of Section 2.1. Each one of you has taught me something, and I have nothing but nice memories of my years with you. A special mention to the technicians Ralf Bauz, Sylvio Mielitz, Stefan Mikulla and Peter Neuendorf for their support with countless gelatin experiments. Another special mention to Gesa Petersen for her precious help with an intimidating Zusammenfassung.

Berlin & Potsdam friends:
Well, they are also my colleagues, some from Section 2.1. As corny as it will sound, you have made my life special. Here I go for names only, and yes, I'm going to mention all of you - brace

for it. Thanks to Ajay, Alea, Angela, Asim, Behnam, Camilo, Carla, Cristina, Daniel, Dilara, Elif, Henning, Jamal, Karina, Malte, Marius, Ming-Hsuan, Nima, Pablo, Pınar, Pouria, Reza, Shubham, Simone, Stefan, Ugur and Vivien for all the coffee breaks, the endless discussions on religion, politics and nonsense, the well-deserved weekends and the adventures we shared. Thanks also to Robin, a longtime friend who helped me find my way in Germany, and to Linda and Christina, dearest friends who have never forgotten to check on me during these years.

Family:

Last but not least, I am grateful to my parents, Laura and Roberto, and my sister, Beatrice, for supporting me throughout my studies and helping me get where I am. You have offered me the opportunity to pursue my dreams, even if it means living far away from you. Neither this work, nor anything else before it would have been possible without you.

Contents

List of Figures

List of Tables

Abbreviations and Symbols

Abbreviations	
LEFM	Linear Elastic Fracture Mechanics
PDE	Partial Differential Equations
BE(s)	Boundary Element(s)
FE(s)	Finite Element(s)
DDM	Displacement Discontinuity Method
PDF	Probability Density Function
PPD	Posterior Probability Distribution
SAM	Simplified Analytical Model (of dike trajectories)
TIM	Three-dimensional Intrusion Model
MDT	Minimum Distance (from BEs) Threshold

Symbols	Physical meaning	Unit (and value, if fixed)
σ	Stress	Pa
$\vec{v}_1, \vec{v}_2, \vec{v}_3$	Principal stress axes, from most to least compressive	
$\sigma_1, \sigma_2, \sigma_3$	Magnitudes of principal stresses	Pa
ν	Poisson's ratio	
E	Young's modulus	Pa
ρ	Density	kg/m^3
g	Acceleration due to gravity	9.81 m/s^2
K	Stress intensity factor	Pa$\sqrt{\text{m}}$
K_C	Fracture toughness	Pa$\sqrt{\text{m}}$

Chapter 1

Introduction

1.1 Motivation

Volcanic eruptions have been the cause of major natural disasters throughout history. They may involve a wide range of both primary hazards, such as tephra falls, pyroclastic and lava flows, and secondary hazards, such as lahars, debris avalanches, tsunamis, and have the potential to induce global climate change. Primary hazards alone have been responsible of massive life and property loss during historical volcanic eruptions (Auker et al., 2013). They currently pose a threat to many densely-populated areas all over the world, with more than 800 million people living within 100 km of active volcanoes (Brown et al., 2015). Developing and improving plans for disaster and risk management is, thus, extremely important to mitigate the impact of future events. Volcanic hazard assessment is essential for this purpose, and it relies on effective forecasting of volcanic eruptions and their associated phenomena.

Forecast of volcanic activity is a primary goal in volcanology (Sparks, 2003; Poland and Anderson, 2020), yet a dauntingly complex one to achieve. Short-term forecast aims at predicting the behavior and outcomes of a specific episode of volcanic activity, such as whether unrest in a volcano will lead to an eruption, or if, where and when a magmatic intrusion propagating at depth will eventually reach the surface. In contrast, long-term forecast deals with estimating the spatial and temporal susceptibility of a region to different hazards: for instance, the expected time interval between major eruptions, or what areas are more likely to be invaded by lava flows, if a future eruption occurs at a given location. Both short and long-term forecast involve probabilistic approaches to the knowledge and uncertainty on a given volcanic system, and, most importantly, the understanding of the physical processes underlying volcanic hazards. Scientific research has often tackled these processes individually, but a comprehensive approach to describe the state of volcanic systems and forecast their future behavior is currently lacking, and riddled with challenges.

Modeling of specific volcanic hazards have attained a remarkable degree of sophistication in recent decades, resulting, for instance, in reliable probability maps of pyroclastic density current (Neri et al., 2015; Reyes et al., 2018) or lava flow invasion (Connor et al., 2015; Richter et al., 2016; Gallant et al., 2018; Musacchio et al., 2021). In the context of long-term forecast, however, all such models rely on one critical input: the knowledge of where next eruptions are more likely to occur, as even small variations in the starting location and orientation of an eruptive vent may drastically change the outcomes of subsequent hazards (Connor et al., 2015). In this regard, several eruptions in recent years (Kilauea, Hawaii, 2018 Patrick et al. 2020; Sierra Negra, Galápagos, 2018 Davis et al. 2021; Fagradasfjall, Iceland, 2021 Pedersen et al. 2022; Nyiragongo, Democratic Republic of the Congo, 2021 Smittarello et al. 2022; Cumbre Vieja volcano, La Palma, 2021 De Luca et al. 2022) have shown that magma can propagate along counterintuitive paths and breach the surface in areas that had experienced no eruptive

events in decades or centuries. This is a major scientific problem which remains, to this day, surprisingly poorly addressed.

The end product of a forecast of locations of future eruptions is a probability map of opening of eruptive vents. Many methods in this regard are available in literature. Most of them, however, are entirely based on statistical, data-driven approaches, and rely mainly on the spatial distribution of past eruptive vents. This is in contrast with the assessment of other volcanic hazards, which, as mentioned earlier, typically relies on advanced physics-based models. The ability of data-driven approaches to forecast future eruptive vents is strictly correlated to the amount and quality of the data on the eruptive history of a given region. Probability maps produced with separate data sets may differ considerably from one another, depending on which past vents have been included. This implies that missing or unreliable data may undermine the accuracy of such methods. Some of these approaches also neglect any knowledge of the age of past vents, thus discarding any information on the volcano behavior coming from changes in their pattern over time. This is a critical issue, since vent migration, changes in eruptive style or vent orientation over time are observed in many volcanic regions, and are evidence that the factors controlling magma propagation in the subsurface may also have changed. Including such factors is the key to predicting future magma pathways and vents. Physics-based models of magma propagation (e.g Dahm, 2000a; Kühn and Dahm, 2008; Maccaferri et al., 2010; Davis et al., 2020) provide the theoretical framework to address the challenge.

In principle, a predictive model of magma pathways links unambiguously a magma storage volume to a vent on the surface, once a set of parameters describing the physics and geometry of magma propagation is known. If we are to apply such a model to a volcano, we need to constrain those parameters, e.g. by means of statistical techniques, so that the model predictions are compatible with the available data. We may then employ the same model to forecast the locations of future eruptions. Such a model may not be as sensitive to outliers or missing data as fully data-driven approaches are, since data uncertainty is included in the statistically-constrained information on the model parameters.

Applying magma propagation models to forecast future vents in real volcanic regions entails a number of challenges. Models need to be validated against observations and, at the same time, to be simple: that is, they should rely on few, physically meaningful parameters that may be constrained with scarce data. As such, they always involve some assumptions. Rivalta et al. (2019) made the first step in this direction, combining physics-based models of magma propagation with a statistical method to forecast the locations of future vents. They applied that strategy to one case study only: the Campi Flegrei caldera in Italy. They focused on dike propagation modeling, and aimed at constraining the state of stress of the volcano so that magma was brought from the known location of a magma chamber to the known locations of past vents. They relied, however, on a two-dimensional (2D) approach both in the dike and the stress modeling, and assumed an axisymmetric topography for the Campi Flegrei area. Consequently, their strategy is still in its infancy, and needs to be equipped with concepts and tools for an upgrade to three dimensions (3D) and further applications to nature.

The problem of dike propagation involves modeling both the trajectory and the velocity of a dike (Rivalta et al., 2015). Calculating the dike velocity requires the knowledge of the dike trajectory, as some of the driving forces of a dike (e.g. magma buoyancy force, external stresses) depend on the dike location, size and shape. For decades, dike trajectories have been addressed mainly with 2D models (e.g. Dahm, 2000a; Maccaferri et al., 2011). In the most elementary approach, dike pathways are traced as streamlines perpendicular to the least-compressive principal stress direction (Anderson, 1937; Muller and Pollard, 1977; Roman and Jaupart, 2014). Such a model, despite its simplicity, has proven effective for statistical purposes (Rivalta et al., 2019). In recent years, modeling of dike trajectories has advanced significantly.

Davis et al. (2020, 2021) introduced a fully 3D numerical model which can reproduce both dike pathways and the changes in the dike shape along them. That model however, requires relatively long computational times, and is not suited for statistical applications with large numbers of simulations. Other works have focused on the velocity (Pinel et al., 2017; Davis et al., 2023) or growth of 3D planar dikes Heimisson et al. (2015); Zia and Lecampion (2020); Pansino et al. (2022). However, 3D equivalents of the simplified, yet computationally efficient streamline approach are still missing. Moreover, the crustal stress state in volcanic regions, which is a required input for dike models, is still poorly understood, despite the numerous analytical and numerical models which can be used to represent specific stress-generating mechanisms.

The present dissertation is motivated by the need for new, effective methods that may improve our capability of forecasting the location of volcanic activity in high-risk areas around the world. It develops and tests new tools for 3D modeling of the stress state in volcanoes and dike pathways, then integrates them with established statistical procedures and newly-defined concepts to produce probability maps of future vent opening in volcanic areas with easily-available computational resources.

The following sections of this chapter provide an overview on the state of the art of dike propagation and crustal stress models, as well as on the relevant branches of solid mechanics and statistics this dissertation relies on. The chapter concludes with the outline of the objectives and achievements of the present work.

1.2 Forecasting the locations of future eruptions

Volcanic hazard assessment requires to answer three key questions: where, when, and how the next eruption will occur (Selva et al., 2012). Addressing each of such questions comes with different challenges. The style and impact of eruptions at specific volcanoes have been represented through eruptive scenarios, which are an essential tool to educate the population and inform the decision makers on the threats posed by volcanic activity, leading to better risk prevention and management. They rely on the application of models to simulate the inception, evolution and impacts of one or multiple volcanic hazards, identifying what areas are more prone to experiencing them. The last decades have seen a wide range of numerical techniques being developed to model individual volcanic hazards, producing, for instance, susceptibility maps of lava flow (Connor et al., 2012; Cappello et al., 2015; Gallant et al., 2018) and pyroclastic density current invasion (Todesco et al., 2006; Neri et al., 2015; Esposti Ongaro et al., 2020). In order to produce meaningful results, eruptive scenarios need to be informed by accurate data on the eruptive history, including the style, mass eruption rate, magma composition and fluid content, precursors, duration and impacts of past eruptions. The reliability of any eruptive scenario depends on answering the first question: where is the next eruption more likely to occur? The answer might seem relatively straightforward in the case of single volcanic edifices, where most eruptions may be expected to occur through the main crater. Flank eruptions, however, are commonly observed at significant distances from the main crater at most volcanoes (e.g. Etna, Italy, Acocella and Neri 2003, see Figure 1.1b; Piton de la Fournaise, Réunion Islands, Michon et al. 2015; Kilauea, Hawaii, Patrick et al. 2019a), and in some cases are not associated to any eruption from the summit conduit (e.g. Fernandina, Galápagos, 1995, Jónsson et al. 1999; Bárðarbunga, Iceland, 2014 Sigmundsson et al. 2015; Nyiragongo, Democratic Republic of the Congo, 2022, Smittarello et al. 2022). Identifying areas that are most susceptible to future eruptions in volcanic systems with no main edifice, such as calderas and monogenetic volcanic fields, is much more complex, since past vents are usually sparse and relatively scarce, as the examples in Figure 1.1 show.
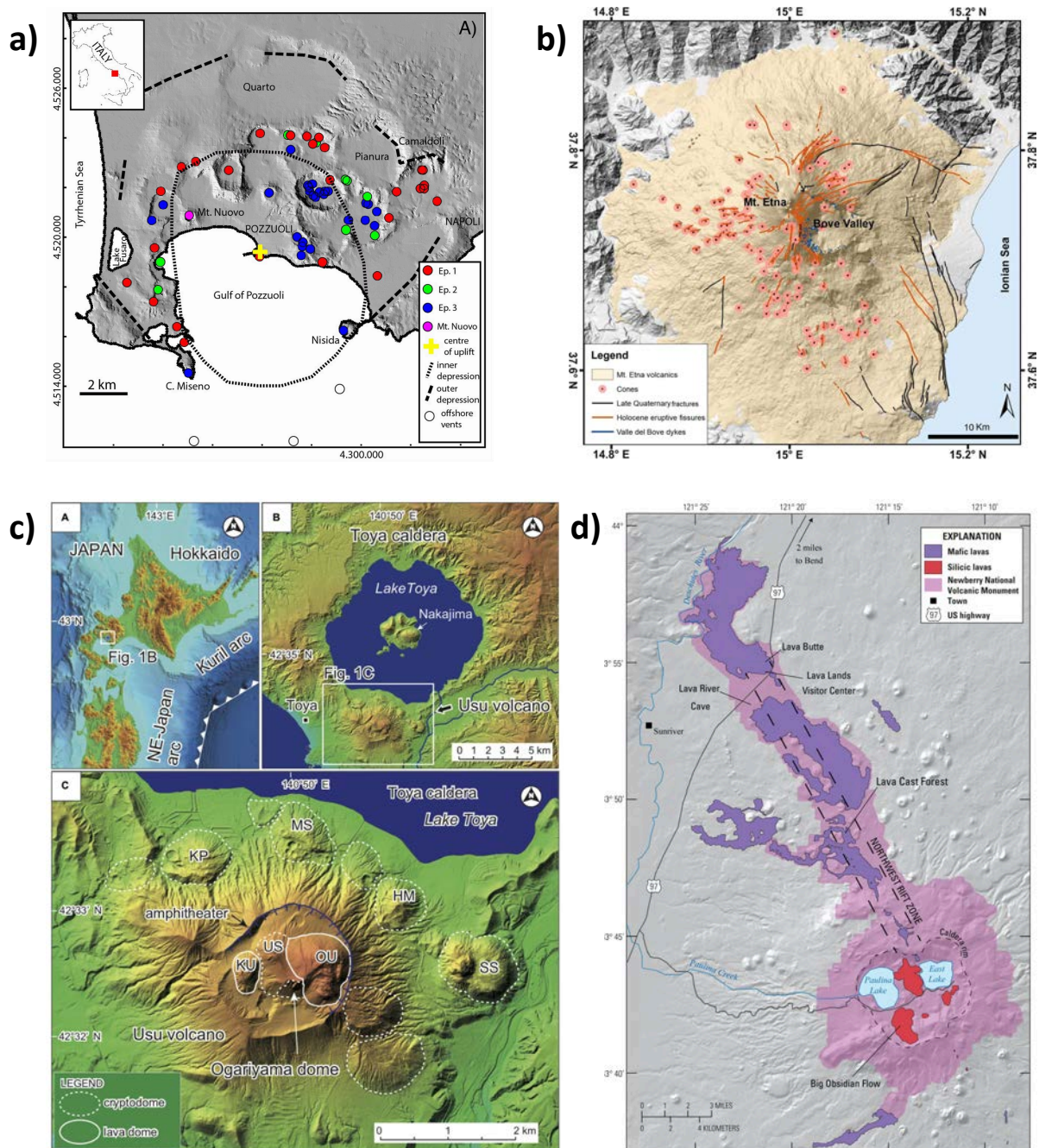
Figure 1.1: Examples of vent distributions in volcanic regions. a): locations of past vents in Campi Flegrei caldera, Italy. Different colors mark different epochs of eruptive activity. Reproduced from Rivalta et al. (2019), Figure 2a. b): distribution of cones and eruptive fissures over Etna, Italy. Reproduced from Scudero et al. (2019), Figure 1. c): distribution of cryptodomes and lava domes over Usu volcano, part of the Toya caldera volcanic system, Hokkaido, Japan. Reproduced from Goto and Tomiya (2019), Figure 1. d): most recently-erupted lavas in Newberry Volcano, Oregon. Reproduced from Jensen and Donnelly-Nolan (2017), Figure 5.

While models of volcanic hazards address the physics of the processes that cause them, the spatial probability of future eruptions is usually determined by techniques which rely entirely on statistics, where some a priori information on the current state of the system, based on a set of data, is translated through Bayesian inference into a posterior probability distribution for the spatial recurrence of volcanic activity. The underlying assumption is that future vents are expected to open close to previous ones, or, to quote Martin et al. (2004), '... *the apple does not fall far from the tree*'. A common procedure consists in retrieving the distribution of
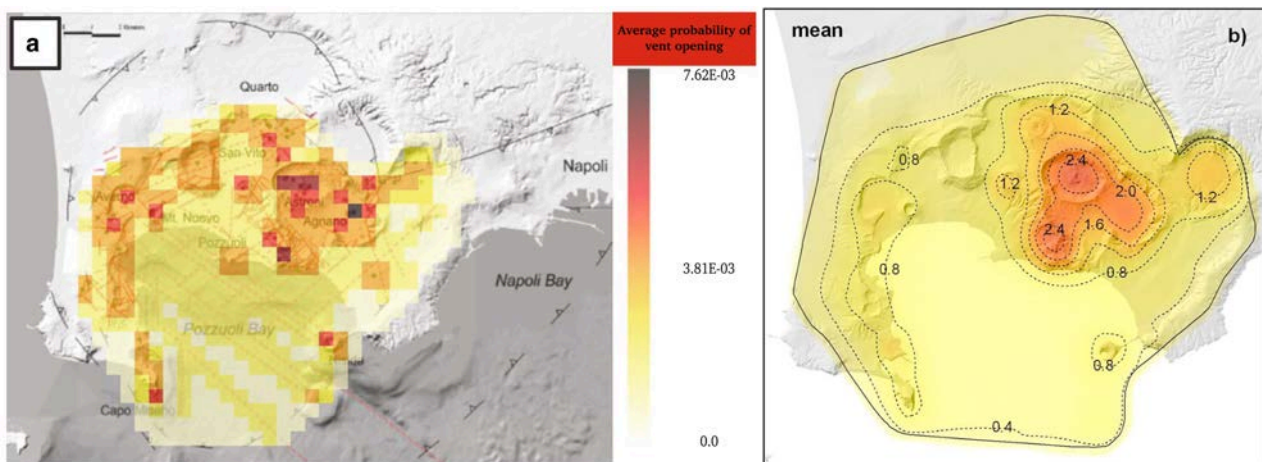
Figure 1.2: Two examples of probability maps, conditional on the occurrence of an eruption and computed through different methods, of vent opening in Campi Flegrei caldera, Italy. a): average value of posterior probability over a grid of 500 m × 500 m cells. Reproduced from Selva et al. (2012), Figure 3a. b): average of posterior probability per square km. Reproduced from Bevilacqua et al. (2015), Figure 8b.

past eruptive vents and then transforming it into a probability density function (PDF). Thus, the probability of vent opening, given that an eruption will occur, can be calculated over any finite area in the region. Such PDFs are usually computed through kernel density estimation (Silverman, 1986), where the probability of a new eruption is a function of the distance from the nearest vent and a smoothing constant (Lutz and Gutmann, 1995; Connor and Hill, 1995). Similar methods have been applied to produce probability or 'susceptibility' maps for many volcanic regions at different scales: from single volcanoes (Etna, Wadge et al., 1994; Cappello et al., 2012; Tenerife, Canary Islands, Marti and Felpeto, 2010) and calderas (Campi Flegrei, Bartolini et al., 2013) to monogenetic volcanic fields (Yucca Mountain region, Nevada, Connor and Hill, 1995; Chichinautzin volcanic field, Mexico, Nieto-Torres and Del Pozzo, 2019) and whole volcanic arcs (Tohoku, Japan, Martin et al., 2004). Another method is to divide a volcanic region into a regular grid of cells and assign each a weight based on a set of features associated with high or low eruption susceptibility. Such features may include geological, geophysical and geochemical data: the presence of past vents, faults and surface fracture density (Selva et al., 2012; Bevilacqua et al., 2015), ground deformation, seismicity, gravity anomalies, active fumaroles and rock alteration (Alberico et al., 2002). The assumption is that all such features contribute, to different degrees, to the weakness of the local crust, which is implied to favor eruptions.

A common assumption is that the opening of a vent is an intrinsically stochastic process, while the deterministic nature of magma trajectories is not acknowledged, in spite of decade-long understanding on the patterns of magmatic intrusions, e.g. dike orientations, in the field (e.g. Muller and Pollard, 1977; Nakamura, 1977; Gudmundsson, 2002). Consequently, records of past vents that are scarce and with large uncertainties inevitably lead to coarse probability maps in the forecast of future eruptions. As an example, the last eruption in Campi Flegrei (Monte Nuovo, 1538 CE, Di Vito et al., 1987) hit an area distant from previous vents, and would have been difficult to anticipate. The same area was, in fact, assigned different probabilities of vent opening in Selva et al. (2012) and Bevilacqua et al. (2015) (compare Figure 1.2a and Figure 1.2b). The assumption that new vents tend to occur close to the old ones is especially inadequate in monogenetic volcanic fields, where vents are usually scattered over a vast area, form at irregular time intervals and rarely experience more than one eruption (Le Corvec et al., 2013b).

A further drawback of data-driven approaches to eruptive vent forecasting is that they are difficult to validate. A retrospective validation may be carried out by partitioning the data into calibration and validation sets (e.g. earlier and recent eruptions, respectively), computing the maps on the basis of the first set and assessing the performance on the second. This would, however, lower the number of data used to inform the map, leading to more uncertainty.

Another consideration by Selva et al. (2012) is that volcanic systems may evolve over time through distinct 'reference states', each characterized by a consistent behavior (e.g. recurrent vent patterns Smith et al., 2011 or fissure orientations Chadwick and Dieterich, 1995). It is, then, important to establish a current reference state for a volcano in order to forecast its future behavior. That consideration implies that the observed vent distribution is the result of a hitherto unknown physical mechanism, and hints at a possible alternative approach. Bartolini et al. (2013) and Marti and Felpeto (2010) also acknowledge that vent locations are determined by the conditions in the crust, namely the stress state, which, however, cannot be observed directly and are thus not constrained. In particular, Marti and Felpeto (2010) mention physical models of the stress state in the subsurface as a potential complement to directly-observable data when informing a probability map. The first attempt in this regard, however, was marked by Rivalta et al. (2019), who integrated Bayesian inference with a physics-based model of magma propagation to produce probability maps of future vent opening. The strategy of Rivalta et al. (2019) relies on a parsimonious model with a small set of parameters, which are constrained so that the model simulations are consistent with the observed vent locations. Contrary to previous approaches, the PDF of future vents is not computed directly from observed data, but rather inferred by large numbers of simulations where the parameters are randomly drawn from the constrained PDFs of the model parameters. Such PDFs can also be updated to account for changes in the state of the volcano, with no need for new calibrations. Rivalta et al. (2019) applied their method to the Campi Flegrei caldera, providing a mechanical explanation to the inward vent migration and the concentration of vents over an onshore ring. They also showed that the strategy is effective in assigning a high probability to the location of the Monte Nuovo eruption, while explaining both the inward vent migration and the onshore vent concentration as the consequence of changes in the mechanical state of the caldera. The small amount of parameters to constrain also makes the approach much less sensitive to scarce data. The strategy, however, was formulated in a 2D framework, and relied on some drastic assumptions on magma origin and propagation, as well as on the caldera morphology. Nonetheless, it paves the way to a new class of eruptive vent forecast techniques that may significantly improve volcanic hazard assessment.

In order to explain the details of the model in Rivalta et al. (2019) and how the strategy can be further developed, we first need to outline the state of the art of magma propagation modeling, to which the following sections are devoted.

1.3 Theoretical framework

1.3.1 General linear elasticity

The models discussed in this dissertation rely on the theory of linear elasticity: a branch of continuum mechanics describing the response of solid objects to an applied force per unit area, or traction. The theory requires the assumption of infinitesimal strain. In a homogeneous, isotropic solid, we can define infinitesimal elements whose volume is much smaller than the one of the solid, but large enough such that the medium properties within it can still be assumed homogeneous. The infinitesimal strain assumption prescribes that the displacement of such elements is much smaller than the dimensions of the solid. Here and in the following of this

dissertation, we employ a Cartesian coordinate system to describe physical quantities, unless specified otherwise. In such a system, described by the coordinates $x_1 = x$, $x_2 = y$, $x_3 = z$, the infinitesimal strain tensor ϵ_{ij} in 3D can be written as

$$\epsilon_{ij} = \frac{1}{2}\left(\frac{\partial u_i}{\partial x_j} + \frac{\partial u_j}{\partial x_i}\right) \tag{1.1}$$

(e.g. Pollard et al., 2005, chap. 8), where u_i, $i = 1, 2, 3$ are the components of displacement, and the partial derivatives $\frac{\partial u_i}{\partial x_j}$ are the extension of an element along the direction of the i-th coordinate over its original length along the j-th coordinate.

In a homogeneous, isotropic, linearly-elastic medium, the stress tensor σ_{ij} is then related to ϵ_{ij} by the constitutive equation

$$\sigma_{ij} = \lambda\delta_{ij}\epsilon_{ij} + 2\mu\epsilon_{ij} \tag{1.2}$$

(e.g Jaeger et al., 2007, chap. 5), where δ_{ij} is the Kronecker delta and λ and μ are the Lamé parameters, related to the Poisson's ratio ν and the Young's modulus E as

$$\lambda = \frac{E\nu}{(1+\nu)(1-2\nu)}; \quad \mu = \frac{E}{2(1+\nu)} \tag{1.3}$$

E is the ratio between the change in stress and the longitudinal shortening/extension, that is, the change in length of the element along the direction the traction is applied, while ν is the ratio between the transverse and longitudinal shortening/extension (Jaeger et al., 2007, chap. 5). In Equation 1.2, the ij-th component of σ_{ij} denotes the i-th component of the traction acting on the plane perpendicular to the j-th coordinate.

The stress tensor σ_{ij} has three eigenvectors, known as principal stress axes. They define a coordinate system where the shear stress components ($\sigma_{ij}, i \neq j$) are zero. In this dissertation, we refer to the eigenvectors of σ_{ij} as $\vec{v}_1$, $\vec{v}_2$, $\vec{v}_3$, and to their magnitudes as σ_1, σ_2, σ_3, where σ_1 and σ_3 correspond to the most and least-compressive principal stress, respectively. Note that we adopt the positive sign convention, where a traction component is positive if it points in the positive coordinate direction. Consequently, tensional and compressive stress are respectively associated to positive and negative values.

1.3.2 Fracture mechanics

The formation and propagation of fractures in rocks is the key mechanism of a wide range of processes in the solid Earth. A fracture, or crack, is a displacement discontinuity in a solid, resulting from the action of stress. The dynamics and characteristics of fractures within linearly-elastic solids are described by the principles of Linear Elastic Fracture Mechanics (LEFM).

Fractures are distinguished into shear and tensile, according to whether the displacement is tangent or perpendicular to their surface, respectively. Tensile cracks, in particular, can be created by fluids and allow them to flow through solid media. As such, they are especially relevant in the context of magma transport through the Earth's crust.

Cracks are created when the applied stresses exceed the tensile or shear strength of the rock. In a similar fashion, the growth and propagation of a crack is controlled by the stress intensity along its tip-line, which in turn is determined by the loading applied on the faces of the crack (e.g. an internal pressure or a far-field stress). This problem was first addressed by the works of Inglis (1913); Griffith (1921) and Griffith (1924), who found that stress intensity at the tip of a fracture scales with the square root of the fracture length. In particular, Griffith (1921, 1924) approached the growth of a crack in terms of energy equilibrium: the energy required to
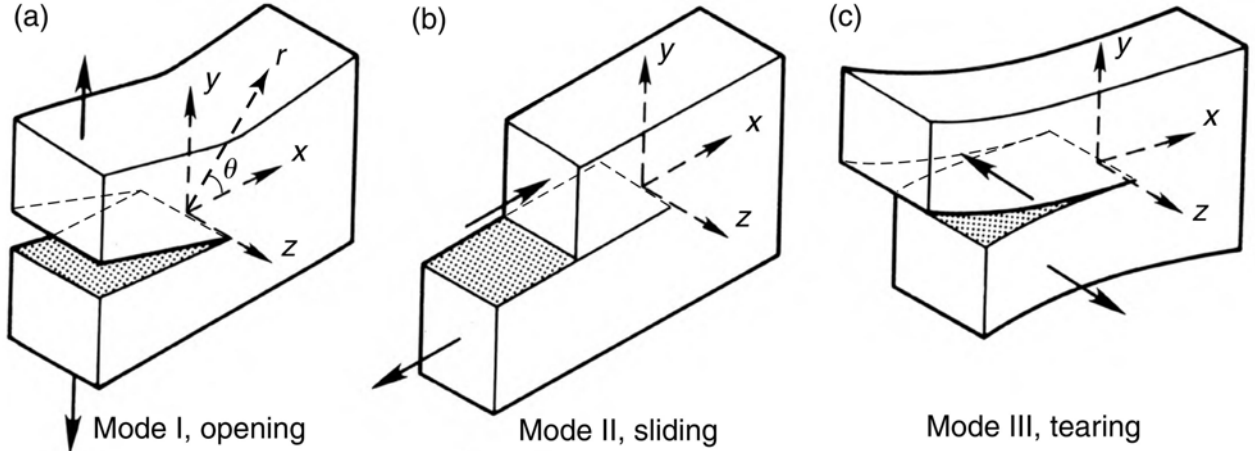
Figure 1.3: Three modes of fracture. a): Mode-I, opening fracture. b): Mode-II, shear fracture with displacement perpendicular to the crack's tip-line. c): Mode-III, shear fracture with displacement parallel to the crack's tip-line. Reproduced from Pollard et al. (2005), p. 372, Figure 9.30.

increase the crack surface by a unit area equals the release of an amount G of elastic potential energy, or strain energy, in the solid. G is known as the strain energy release rate. Later, Irwin (1957) formalized the relation between the stresses around the tip of a line crack, under plane strain or plane stress condition, as:

$$\sigma_{ij}(r,\theta) = \frac{K}{\sqrt{2\pi r}} f_{ij}(\theta) + O(r^{\frac{1}{2}}), \quad K \propto \sqrt{EG} \tag{1.4}$$

(Tada et al., 2000; Paris, 2014), where r and θ are polar coordinates with the origin at the crack's tip (see Figure 1.3a), $f_{ij}(\theta)$ is a dimensionless function depending on the crack's geometry and load, and K is the stress intensity factor, with units of Pa$\sqrt{\text{m}}$. Irwin (1958) introduced three modes of K (K_I, K_{II} and K_{III}), each associated to three modes of deformation around cracks. Mode-I cracks are tensile, or opening, fractures, while Mode-II and Mode-III are shear fractures, where the faces slide over one another perpendicular or parallel to the leading edge of the crack, respectively. Irwin (1957) and Irwin (1958) derived expressions for σ_{ij} and K in Equation 1.4 for the three modes in plane strain or plane stress configuration (see e.g. Tada et al. (2000)). Plane strain/stress approximation is adequate for 3D geometries as long as the distance from the crack's tip, measured along the x-axis in Figure 1.3a, is small compared to the crack length on the plane of its leading edge, coinciding with the z-axis in Figure 1.3a (Pollard et al., 2005, p. 372). Moreover, thanks to linear elasticity, the superposition of the three modes can describe any problem of local deformation and stress field around crack tips.

Mode-I tensile cracks are central to this dissertation, due to their relevance in magma transport modeling. It is worth noticing how, in Equation 1.4, the stress components are singular for vanishing r, that is, at the crack's tip, and the term f_{ij} depends exclusively on θ. Consequently, K accounts for all information on the geometry of the crack and the stress load. Expressions of K_I for different crack shape, size and loading conditions are available (e.g. Murakami et al., 1987; Tada et al., 2000). For instance, K_I for a line crack of length a under a constant remote stress σ is:

$$K_I = \sigma\sqrt{\pi a} \tag{1.5}$$

(Tada et al., 2000, p. 125), while K_I for the same crack under a linear stress gradient which vanishes at the crack's center and has magnitude $\pm p$ at the crack's left and right tip, respectively, is:

$$K_I^{\pm} = \pm\frac{1}{2}p\sqrt{\pi a} \tag{1.6}$$

(Tada et al., 2000, p. 154).

An opening crack can grow when K_I at its tip exceeds the fracture toughness K_C of the host medium (Secor Jr and Pollard, 1975). Determining K_I for specific crack geometries and loading conditions is therefore critical to study the propagation of fluid-filled fractures.

1.3.3 Boundary Element methods

Boundary Element (BE) methods are a numerical technique for solving boundary value problems widely used in science and engineering (Crouch et al., 1983). In boundary value problems, partial differential equations express the physics governing a region of space, R, enclosed by a boundary, C, where a set of constraints (boundary conditions) is prescribed. The partial differential equations must then be solved in R so that they satisfy the boundary conditions on C. A boundary value problem is well posed (e.g Sizikov et al., 2011) when its solution is unique and its behavior depends continuously on the boundary conditions.

Analytical solutions to boundary value problems are usually available only under specific assumptions, when R is homogeneous and the geometry of C is simple. More complex problems can be solved by numerical techniques. BE methods rely on the fact that it is easier to find an analytical solution to a problem in an infinite homogeneous region including R, rather than within R itself. The general idea is to find an analytical solution for a point disturbance (e.g. a point force) applied at a point P in the infinite region. Such a solution is singular in P, and is thus referred to as a 'singular solution'. In principle, if the singular solution produced exactly the boundary conditions prescribed on C, it would have solved the boundary value problem within R. This is unlikely to happen with one singular solution, but, if the partial differential equations (PDE) governing the problem are linear, multiple singular solutions in the infinite space can be added together so that the boundary conditions on C are, at least approximately, satisfied.

Each singular solution is applied at a point in space and associated with an intensity. In a BE method, the contour C is divided into a set of N Boundary Elements, and N singular solutions are chosen and scaled so that their superposition satisfies the boundary conditions at the midpoint of each element. This is done by, first, applying each singular solution at the midpoint of each BE and, then, solving a system of N linear equations for the singular solution intensities. Once this system has been solved, we can find the solution to the original problem at any point in R.

Another widely-used numerical technique, alternative to BE methods, is represented by Finite Element methods (e.g. Dieterich and Decker, 1975; Clough, 1980; Reddy, 2019). They rely on discretizing the whole region R into a network of finite elements, and evaluating the solution to the partial differential equations at the nodes of such a network. This also leads to a system of linear equations, where the solutions on the nodes within R are related to the boundary conditions on the nodes lying on C. Depending on the problem, BE methods have clear advantages over FE methods. The equation systems in FE methods are much larger, and thus more computationally expensive, than those in BE methods. Moreover, BE methods are especially efficient if the region of interest where we want to calculate our solutions lies outside the boundary C. Such is the case, for instance, of a pressurized crack in an infinite medium. Then, a BE method requires only the discretization of C. On the contrary, a FE method need a discretization of an infinite space with a finite network of elements, whose outer boundary should be placed as far as possible from C, so that the conditions imposed there do not have a significant effect on the solutions close to C (Crouch et al., 1983).

The Displacement Discontinuity method (DDM), introduced by Crouch (1976); Crouch et al. (1983), is a special class of BE methods, where the singular solutions consist of the analytical

solution to the problem of a finite dislocation in space. Such dislocations have usually a uniform slip across their surface ('Volterra dislocations' Volterra, 1907). According to this method, the boundary C can be discretized into a mesh of dislocations, each being allowed a constant discontinuity in displacement. Then, the computational nodes are the dislocation centroids, where both displacement and traction boundary conditions B_i, $i = 1,...,N$ can be assigned. The resulting system of linear equations can be expressed through a matrix A of boundary influence coefficients (Crouch et al., 1983), such that the effect (induced displacement or stress) of a unit displacement of the i-*th* BE on a point j in space is described by the coefficient A_{ij}. Once A is computed, we can solve for the displacements X_j of each dislocation that satisfy the boundary conditions B_i (Crouch, 1976; Martel and Muller, 2000):

$$A_{ij}X_j = B_i. \tag{1.7}$$

Consequently, the displacement and stress field at arbitrary points in space can be calculated as the cumulative effect of all the X_j at such points.

The DDM has been applied to a variety of geomechanical problems, such as the deformation induced by pressurized cracks or cavities in an elastic full or half-space (e.g. Cayol and Cornet, 1997; Dahm, 2000a; Maerten, 2010; Salzer et al., 2014; Bathke et al., 2015). Triangular dislocations (Comninou and Dundurs, 1975; Jeyakumaran et al., 1992) are often employed, as they can be used to represent complex geometries without any discontinuity in the final mesh (Maerten, 2010). In the last decade, the analytical solutions for triangular dislocations by Nikkhoo and Walter (2015) removed the numerical instabilities and artifact singularities present in previous solutions. Their solutions were then employed in the BE toolbox '*Cut&Displace*' (Davis et al., 2017, 2019), which I employ in this dissertation to model the effect of topographic loads on the Earth's crust according to the method by Martel and Muller (2000). The numerical model of fluid-filled crack propagation in 3D by Davis et al. (2020, 2021), described later and used in some instances, is also based on *Cut&Displace*.

1.4 Modeling magma propagation

Magma often intrudes the host rock in the form of dikes: tabular intrusions whose thickness is much smaller than their length and breadth. Field observations have shown that dikes are the most common form of magma transport in the Earth's crust, especially in the case of basaltic eruptions, or in mid-oceanic ridges and continental rift zones (Lister and Kerr, 1991; Rubin, 1995). Although the opposite can sometimes be observed (Gudmundsson, 1983; Delaney et al., 1986; Valentine and Krogh, 2006), field observations suggest that, in most cases, dikes open their own pathway through the crust, rather than following pre-existing fractures (Gudmundsson, 1995; Clifton and Kattenhorn, 2006; Seymour et al., 2020). Exposed dike outcrops have also revealed how dikes tend to align perpendicularly to the least-compressive principal stress direction, $\vec{v}_3$, according to the regional tectonic stress regime (Muller and Pollard, 1977; Nakamura, 1977; Pollard et al., 2005, chap. 6; Ziv et al., 2000; Gudmundsson, 2002). As a consequence, pre-existing faults do not favor dike emplacement, since they are optimally oriented to accommodate shear stress.

1.4.1 Dike propagation models

Dike propagation in the Earth's crust has been addressed within the broader problem of hydraulic fractures propagating through an elastic medium (Hubbert and Willis, 1957; Secor Jr and Pollard, 1975; Pollard and Holzhausen, 1979, e.g.). Hydraulic fractures are tensile cracks
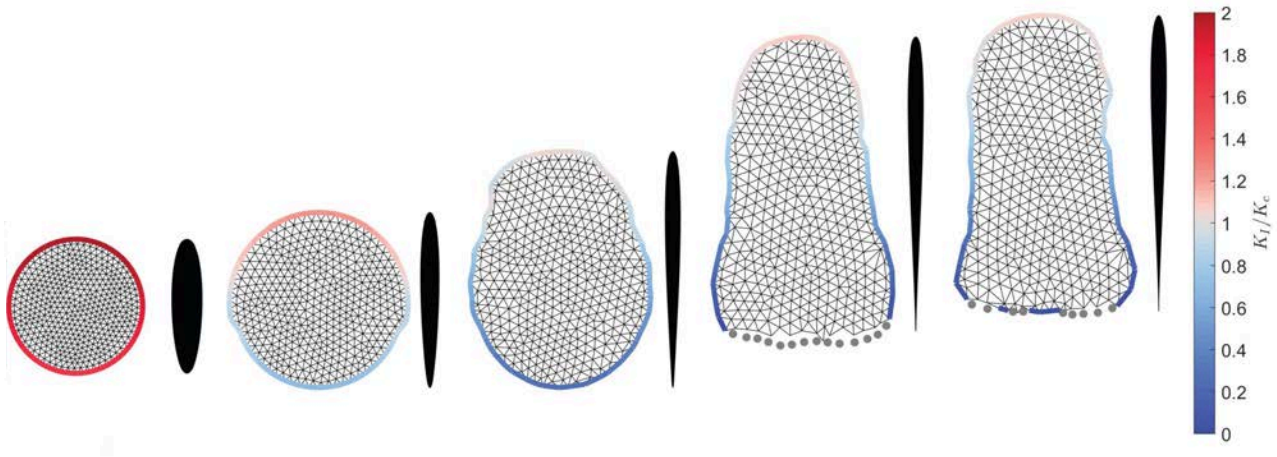
Figure 1.4: Illustration of the numerical dike propagation model in 3D ('Three-dimensional Intrusion Model', or 'TIM') by Davis et al. (2020, 2021). From left to right, front view of a circular tensile crack with an assigned fixed volume in a homogeneous elastic medium. The crack is modeled as a mesh of triangular dislocations. It first expands and then ascends under the effect of the combined external stress and fluid buoyancy force gradient, progressively changing shape. Colors represent the ratio between the stress intensity factor K and the fracture toughness of the medium K_C along the tip-line. Grey points are the dislocations removed in the previous step of the simulations. The black profiles at the right of the crack are cross-section views. Reproduced from Davis et al. (2020), Geophys. Res. Lett., Figure 2.

filled with a fluid and kept open by their internal pressure. The fluid density may be less, larger or equal to that of the host rock. In the first case, if certain conditions are met, the crack will ascend thanks to the buoyancy force of the fluid, and its trajectory will be determined by the balance between it and the external stress field of the host rock (Weertman, 1971; Dahm, 2000a). The propagation velocity, in turn, is controlled by the viscous flow of the fluid within the crack (Lister, 1990; Lister and Kerr, 1991; Nakashima, 1993; Nunn, 1996; Dahm, 2000b). To this day, no model can comprehensively address all such factors and predict both pathways and velocities of cracks in 3D, although some works have made significant progress in this respect (e.g. Zia and Lecampion, 2020; Pinel et al., 2022; Furst et al., 2023). Notwithstanding the complexity of the physical problem, many tailored approaches have been successfully applied to a variety of phenomena. They include propagation of crevasses in glaciers, industrial processes, fracking and, most importantly for our purposes, propagation of magmatic dikes.

Most models of dike trajectories have been limited for decades to 2D. The simplest 2D approaches (Anderson, 1937; Muller and Pollard, 1977; Pollard, 1987; Roman and Jaupart, 2014) represent dikes as streamlines perpendicular to $\vec{v}_3$. More sophisticated 2D models of dike propagation take into account the maximum circumferential stress criterion (Muller et al., 2001; Ito and Martel, 2002), or maximize the rate of strain energy release (Dahm, 2000a; Maccaferri et al., 2010). These models may include some properties of the fluid within the dikes, such as density and compressibility, and inhomogeneities in the host rock, such as density and rigidity layering (Maccaferri et al., 2011). A recent model by (Pinel et al., 2017, 2022) also accounts for the viscosity of the fluid filling the dike, integrating velocity-oriented and pathways-focused approaches towards a comprehensive model of dike propagation. However, similar to other 2D approaches, such a model works under plane strain assumption.

Realistic models of dike pathways require describing propagation in 3D. As a first step to

addressing such challenge, Sigmundsson et al. (2015) and Heimisson et al. (2015) developed models for the lateral propagation of dikes, applying them to the dike observed at Bárðarbunga, Iceland, in 2014. Dikes were represented in terms of rectangular dislocations (Okada, 1992). The pathways were not yet fully 3D, since the dikes were vertical and propagating at either a fixed depth (Sigmundsson et al., 2015) or the level of neutral buoyancy (Heimisson et al., 2015). More recently, a BE numerical model of dike propagation in 3D was developed by Davis et al. (2020, 2021). It relies on computing the ratio between the mode-I stress intensity factor, K_I, and the fracture toughness K_C (see e.g. Pollard et al., 2005, chap. 9) of the host rock along the tip-line of the dike to determine its advance. In order to compute K_I, the model assumes a fixed volume for the dike, and resolves for the uniform internal fluid pressure necessary to open the dike against the external stress. Then, K_I is calculated at the midpoint of the BEs lying on the dike's tip-line, depending on the components of displacement discontinuity on such BEs. Such calculations were made possible by the work of Davis et al. (2019), who, building on the 2D approach by Olson (1991), derived the following expressions for the three-modes stress intensity factors when approximating a 3D crack with BEs:

$$\left\{ \begin{array}{c} K_I \\ K_{II} \\ K_{III} \end{array} \right\} = \left\{ \begin{array}{c} D_n \\ D_{II} \\ D_{III} \end{array} \right\} \frac{\sqrt{\pi}\mu}{2\sqrt{h}(1-\nu)} c \qquad (1.8)$$

(Davis et al., 2019, Equation 25), where D_n, D_{II}, D_{III} are, respectively, the normal displacement of the BE, and the displacement perpendicular and parallel to the crack's edge. h is the distance between the tip-line and the midpoint of the BE, and $c = \frac{1}{1.834}$ is a correction factor accounting for the errors due to the numerical approximation. Davis et al. (2019) calibrated c comparing the predictions from analytical solutions for K and displacement of a crack of radius a to those of a BE model simulating the same crack.

Furthermore, the model relies on the maximum circumferential stress criterion (Erdogan and Sih, 1963; Pollard et al., 2005, chap. 9) to determine the bending or twisting of the tip-line outside of the plane of the dike.

Consequently, the dike can advance along complex pathways and change its shape in the process. The model, which was only tested by Davis et al. (2021) on the 2018 dike at Sierra Negra, Galápagos (Figure 1.5b), is described in detail in Chapter 2, and referred to as 'Three-dimensional Intrusion Model (TIM)' in this dissertation.

No 3D equivalent of the simple $\vec{v}_3$-perpendicular streamline approach in 2D was available at the beginning of this work. Simply extending the 2D approach to 3D is of no avail, since $\vec{v}_3$ identifies a surface, rather than a direction, perpendicular to itself, and the dike pathway will remain undetermined.
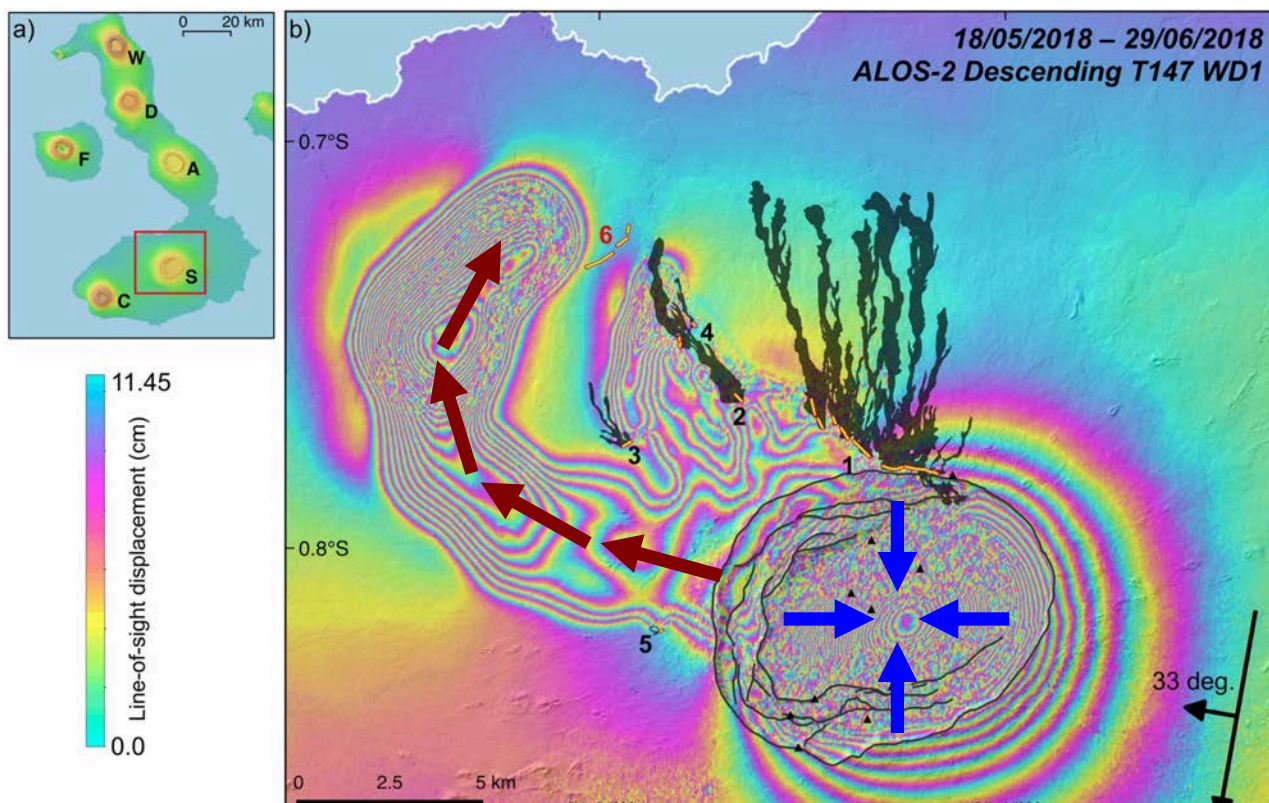
Figure 1.5: Propagation of a sill during the 2018 eruption of Sierra Negra volcano, Galápagos. a): Location of Sierra Negra volcano. Volcanoes labeled as Wolf (W), Darwin (D), Fernandina (F), Alcedo (A), Sierra Negra (S) and Cerro Azul (C). b): Interferogram of SAR data from the ALOS-2 satellite, spanning the sill propagation phase. Each color cycle represents 11.45 cm displacement, positive towards the satellite and negative away from it. Lava flows produced during the time period spanned by the interferogram are marked in dark gray, while eruptive fissures are marked by yellow lines. Black triangles mark the location of Global Navigation Satellite System stations, and black arrows show the satellite orbit direction (N–S), look direction (E–W), and the incidence angle in degrees. The path followed by the sill as it propagated is marked with dark red arrows. Blue arrows represent the subsidence within the summit caldera following the onset of eruptive activity. Modified from Davis et al. (2021), Geophys. Res. Lett., Figure 1.

1.5 Stress state in volcanic regions

Models of dike pathways rely on the knowledge of the stress state in the host rock. Stresses in the Earth's crust, however, are not directly observable, and can only be inferred through *in situ* measurements (see e.g. Jaeger et al., 2007, chap. 13.6, 13.7), such as hydraulic fracturing of boreholes (Zoback and Healy, 1992; Amadei and Stephansson, 1997) or flat-jack methods, where a slot is cut into the rock surface and the subsequent rock deformation is first recorded and then compensated by a hydraulic jack inserted into the slot (Amadei et al., 1997). Earthquakes are also an important source of information on the stress state at depth, as retrieved focal mechanisms are related to the orientation of the principal stresses (Zoback et al., 1989).

Indirect stress measurements can only account for the local stress field, and are often spatially sparse. Hence, inferring regional stresses from such measurements is inadequate when large stress heterogeneities are expected over short spatial scales, as is the case for volcanic regions. The problem can be addressed by mathematical models, where the effects of distinct stress sources are superimposed to produce the total stress field σ_{ij}. Nevertheless, stress modeling poses numerous challenges.

The stress state in the Earth's crust can be expressed as a competition between stress-generating and stress-homogenizing processes (e.g. McGarr and Gay, 1978; Stephansson, 1988; Savage et al., 1992). In the case of active volcanic areas, deposition of eruptive products, pres-
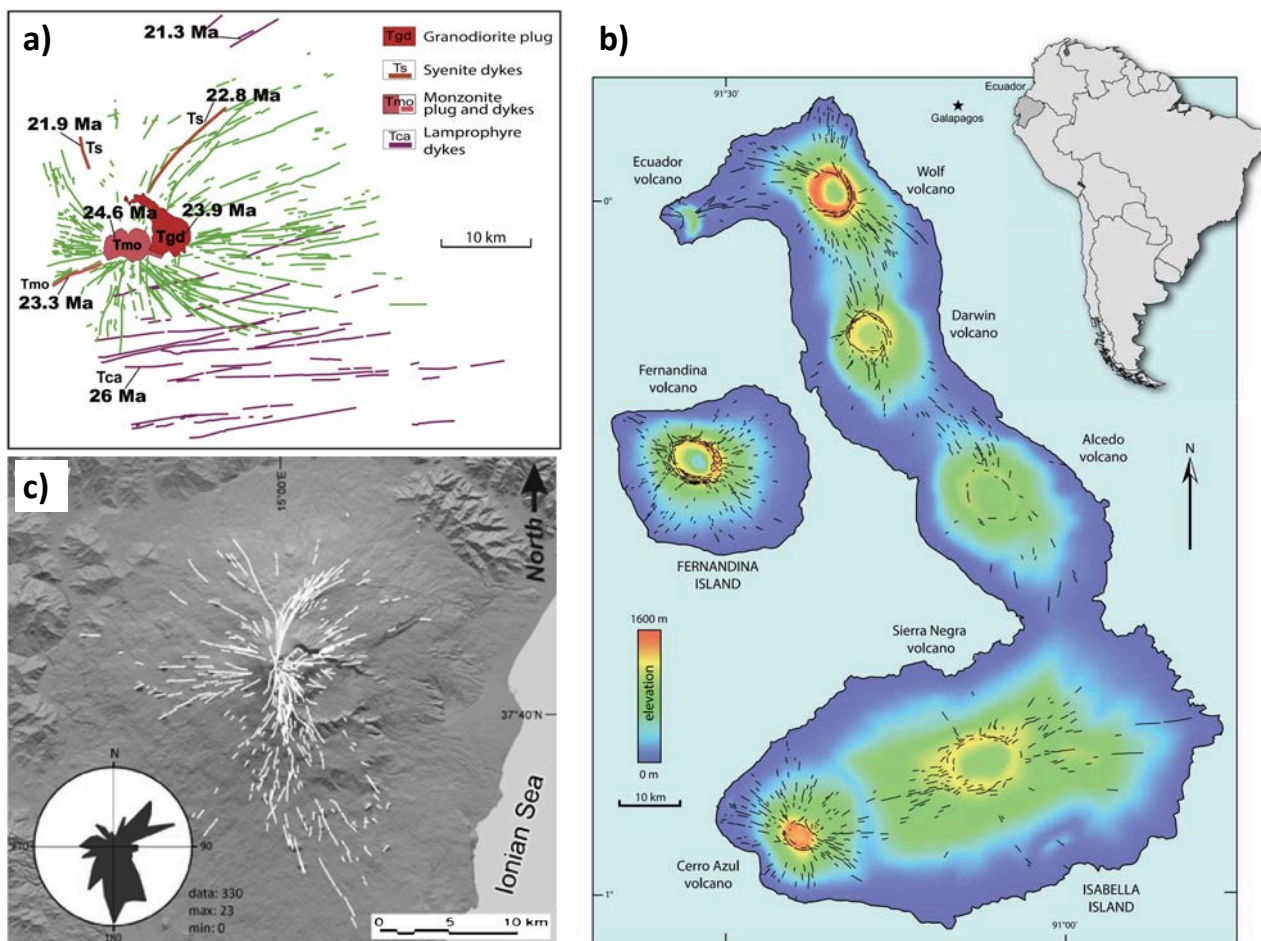
Figure 1.6: Examples of dike patterns in volcanoes. a): dikes and intrusions in Spanish Peaks, Colorado, divided into four categories of magma composition. The most ancient dikes are shown in purple; the most recent dikes are shown in green and orange. Reproduced from Roman and Jaupart (2014), Figure 1. b): map of eruptive fissures (solid black lines) over Fernandina and Isabela Islands, Galápagos. Topographic elevation is represented by a color scale. Reproduced from Maerten et al. (2022), Figure 7. c): historical eruptive fissures over Etna, Italy. The rose diagram represents the distribution of fissure orientation. Reproduced from Cappello et al. (2012), Figure 2e.

surization of magma reservoirs and topography-altering events, such as caldera formation and flank collapses, lead to stress buildup and heterogeneity (e.g. Dieterich, 1988; McGuire and Pullen, 1989; Ventura et al., 1999; Walter et al., 2005). On the other hand, repeating magmatic intrusions, seismicity and other anelastic processes, such as hydrothermal alteration and viscoelasticity, tend to bring the stress state to isotropic (McGarr and Gay, 1978; Stephansson, 1988; Savage et al., 1992). For instance, dike emplacement is favored across surfaces perpendicular to $\vec{v_3}$, but leads to compression of the surrounding rocks along the same direction, thus bringing σ_3 closer to σ_1 (Chadwick and Dieterich, 1995; Kühn and Dahm, 2008; Bagnardi et al., 2013; Corbi et al., 2016). At the same time, faulting and earthquakes dissipate shear stress.

The first step in modeling the overall stress state of a volcanic region is to identify the mechanism of stress generation and relief, many of which are unknown or not directly observable. I now provide a summary of the stress sources that are most commonly considered to explain ground deformation and dike patterns in volcanic regions.

- Tectonic stress: a far-field stress resulting from tectonic processes on a continental to regional scale. A common choice in literature is to assume uniform tectonic stress for the whole crust or even lithosphere (McKenzie, 1978; Müller et al., 1992) and for horizontal distances up to hundreds of km. This assumption is justified by field measures of

subsurface stress over regional to continental scales (Zoback, 1992; Heidbach et al., 2007; Pierdominici and Heidbach, 2012; Yang et al., 2014; Heidbach et al., 2016), and can hold true as long as the scale of the region of interest is small enough.

- Gravitational loading/unloading due to topography: the effect of surface load distribution on the crust. Topographic highs, such as volcanic edifices, depress the underlying rocks, while topographic excavations, such as calderas, are associated with decompression and uplift of the crust. Topography in volcanic regions is often characterized by both small and large wavelength features, leading to pronounced stress heterogeneity. The stress contribution of topography has been modeled through a variety of analytical and numerical techniques (Savage et al., 1985; McTigue and Mei, 1987; Martel and Muller, 2000).

- Magma chambers: they can either pressurize or decompress due to the influx or removal of magma, respectively. Both processes stress the surrounding rocks. Many analytical models of the stress generated by pressurized cavities of different shapes are available in literature, considering both elastic (Kiyoo, 1958; Yang et al., 1988) and anelastic (Dragoni and Magnanensi, 1989) rheology. Numerical models can account for complex host rock rheologies and magma chamber shapes (e.g. Gudmundsson, 2006; Currenti and Williams, 2014), as well as mechanical layering in the host rock (Gudmundsson and Brenner, 2004).

- Pre-existing faults and magmatic intrusions: the stess generated by faults as they slip has been modelled analytically (e.g. Steketee, 1958; Okada, 1992) and numerically (e.g. Bonafede and Neri, 2000). Similarly, the stress induced by dikes or other intrusions as they are emplaced in the crust has been computed by both analytical (Rubin and Gillard, 1998) and numerical models (Ito and Martel, 2002).

Eruptive fissures in active volcanoes and exposed dike swarms in eroded volcanic systems are often oriented according to specific patterns. Figure 1.6 provides three examples. In particular, the orientation of exposed dikes in Spanish Peaks, Colorado (Figure 1.6a), shows a noticeable difference between older and more recent intrusions: early dikes tend to be parallel to each other, aligning with the regional tectonic stress, while recent dikes are curved and arranged in a radial pattern centered on a later volcanic edifice. Such a change in dike pattern has been explained in terms of a pressurized magma chamber (Muller and Pollard, 1977). Magma reservoirs, in fact, have been often regarded as the driving factor in determining local stress and dike pathways (Grosfils and Head, 1994; Gudmundsson, 1998; Chestler and Grosfils, 2013; Pansino and Taisne, 2019). Roman and Jaupart (2014), however, proposed a different explanation. They compared the stresses due to a volcanic edifice to those due to a pressurized magma reservoir, and showed that the second contribution decays away from its source much faster than the first. The implication is that stresses due to pressurized reservoirs are important in the proximity of the source and thus in determining the location of dike nucleation (Gudmundsson, 2006; Grosfils et al., 2015), but not as much in controlling dike trajectories. A similar argument applies to the stress induced by pre-existing faults and intrusions, although the cumulative effect of repeating dike emplacement, as discussed earlier, can have a strong influence on the stress state within volcanic edifices (Cayol and Cornet, 1998; Dumont et al., 2022).

Different works have shown how patterns of exposed dikes and distribution of volcanism can be explained by a combination of tectonic stress and gravitational loading/unloading: examples in this regard are the vent pattern in Fernandina, Galápagos (Corbi et al., 2015), included in Figure 1.6b, and the offset of Etnean volcanism from its mantle melt source (Neri et al., 2018). The role of gravitational loading/unloading in controlling dike pathways has been also highlighted by works on mechanical (McGuire and Pullen, 1989; Pinel and Jaupart, 2004) and analog (Acocella et al., 2009; Corbi et al., 2016) models.

Regardless of what the dominant stress sources are, models of stress state in volcanoes need to be constrained by observations. Dike pathways and, consequently, the locations of eruptive vents fed by dikes are controlled by stress. Hence, the key to constrain the stress state of a volcanic area is matching the distribution of past vents with the results of a stress-driven model of dike trajectories. Such was the strategy proposed for the Campi Flegrei caldera by Rivalta et al. (2019), who considered tectonic stress and gravitational unloading due to the caldera excavation as the dominant factors controlling magma pathways in the subsurface, and aimed at constraining posterior PDFs of their magnitude.

1.6 Objectives

The goal of this dissertation is to develop a physics-based forecast strategy of future vent locations that is ready to be applied to real volcanoes. Bringing the strategy by Rivalta et al. (2019) to 3D so that it can be applied to real volcanoes is very challenging, as several gaps need to be filled, both in the models and in the statistical approach. In particular:

- The 3D dike propagation model by Davis et al. (2020, 2021) requires too long computation times to be used in an optimization procedure (for instance, simulating a 10-km-long dike pathway takes around 3-5 minutes on commonly-available personal computers, while a stress optimization requires at least tens of thousands of simulations for each dike trajectory).

- The method by Martel and Muller (2000) to calculate topographic loading stresses with BE models relies on assumptions on the unperturbed stress state in the crust. Therefore, it cannot be applied to dynamic topographies such as volcanoes without first clarifying those assumptions.

- Including numerical models of gravitational loading in a stress optimization procedure requires an efficient method to treat topographic loads of unknown intensity in 3D.

- Simulating dike trajectories from depth to surface requires assumptions on the dike starting points and the magma storage volumes the dikes depart from. Such assumptions need to be justified.

The research objectives of the dissertation are, then, as follows:

1. Develop a fast and flexible model of dike pathways in 3D, suited for statistical applications.

2. Define a comprehensive 3D framework for constraining the stress state and forecast future vent locations in volcanic regions. More specifically:
   - Combine physics-based, deterministic models of magma transport with statistics to optimize the parameters of a stress model so that simulations of magma pathways match the observed vent distribution.
   - Define a cost function informing the optimization process, weighing the results of the simulations against prior knowledge on vent distribution and magma storage.

3. Test comprehensively the models, the stress inversion and the vent forecast strategy on synthetic data in order to calibrate model parameters, explore uncertainties and assess performance under different assumptions, so that the procedure is finally mature for applications to real scenarios.

1.7 Thesis outline

This dissertation is divided into six chapters, including the present one. Chapters from 2 to 5 address the research objectives in the following order:

- Chapter 2: Applies the stress inversion and vent forecast strategy of Rivalta et al. (2019) to a set of analog models, where air-filled cracks propagate within stressed gelatin blocks, and adopts a more computationally-efficient Markov Chain Monte Carlo algorithm to optimize a 2D stress model for the gelatin blocks.

- Chapter 3: Introduces a new, simplified but fast model of dike pathways in 3D, named 'SAM', where dikes are represented by penny-shaped cracks of fixed radius and advance along trajectories perpendicular to $\vec{v}_3$, while the gradient of external stress and magma buoyancy force controls the direction of propagation. The model can also backtrack dike trajectories from known vents, and is compared to the numerical dike propagation model of Davis et al. (2020, 2021), developed after the start of this work. The chapter also illustrates a BE numerical model of gravitational loading/unloading associated with complex 3D topographies, and combines the stress and dike models to simulate dike trajectories in synthetic calderas.

- Chapter 4: Describes a stress inversion and vent forecast strategy in 3D for calderas, building on the previously-developed models and statistical method, and re-defining the inverse problem of stress optimization in terms of backtracking dike trajectories from the known locations of past vents down to the estimated location of a magma storage volume. The strategy is applied to the synthetic scenarios presented in Chapter 3, discussing the results for different a priori knowledge and assumptions on fixed model parameters.

- Chapter 5: Models the ongoing ground deformation across the Rhenish Massif testing deformation sources of varying shape, size and depth, and tests the hypothesis that the observed deformation may be due to melt accumulation in sub-horizontal, sill-like structures in the lower crust or upper mantle. The Rhenish Massif includes the Eifel Volcanic Fields in Germany, a region that has the potential to witness new eruptions and, as such, is a potential candidate for the application of the vent forecast strategy. Constraining the structure of the Eifel magmatic system would be the first step towards such an application, and the chapter highlights the challenges and uncertainties involved in doing so, as well as the data needed to validate or disprove the current results.

The dissertation concludes with Chapter 6, which provides a summary of the achievements and results, as well as pointing out the scientific questions and modeling challenges still unresolved, and suggesting future applications and developments.

1.8 Publications and author's contribution

1.8.1 Published articles

- **Not included as a chapter in this thesis: Mantiloni, L.**, Nespoli, M, Belardinelli, M. E., Bonafede, M. (2020). Deformation and stress in hydrothermal regions: The case of a disk-shaped inclusion in a half-space. Journal of Volcanology and Geothermal Research, 403, 107011. doi:10.1016/j.jvolgeores.2020.107011.

  L. Mantiloni developed the semi-analytical solutions for displacement and stress field presented in the work, performed the inversion of ground deformation data and wrote the first draft.

- Chapter 2: **Mantiloni, L.**, Davis, T., Gaete Rojas, A. B., Rivalta, E. (2021). Stress Inversion in a Gelatin Box: Testing Eruptive Vent Location Forecasts With Analog Models. Geophysical Research Letters, 48(6), e2020GL090407. doi:10.1029/2020GL090407.

  L. Mantiloni designed and performed the analog models, set up the numerical model of the gelatin box, developed and run the stress inversion algorithm, created the figures and wrote the first draft.

- Chapter 3: **Mantiloni, L.**, Rivalta, E., Davis, T. (2023). Mechanical modeling of pre-eruptive magma propagation scenarios at calderas. Journal of Geophysical Research: Solid Earth, 128 (3). doi:10.1029/2022JB025956.

  L. Mantiloni developed the 3D dike propagation model, implemented the numerical stress model, performed synthetic scenarios and figure creation, and wrote the first draft.

1.8.2 Submitted / under revision articles

- Chapter 4: **Mantiloni, L.**, Rivalta, E., Davis, T., Passarelli, L., Anderson, K. (in preparation).

  L. Mantiloni defined the stress inversion framework, developed the 'compound-stress' model, performed stress inversions and vent forecasts on synthetic scenarios, created the figures, and wrote the first draft.

- Chapter 5: Silverii, F., **Mantiloni, L.**, Rivalta, E., Dahm, T. (**submitted** to Geophysical Research Letters: 27/01/2023). Lithospheric sill intrusions and present-day ground deformation at Rhenish Massif, Central Europe.

  L. Mantiloni helped defining concepts, analyzing data and performing inversions of ground deformation, as well as writing the final draft.

1.8.3 Published code

- TPE-Source: MATLAB code implementing the displacement and stress field solutions for the disk-shaped, thermo-poro-elastic deformation source described in Mantiloni et al. (2020). **Not relevant for the purpose of this thesis.** Available at https://github.com/LorenzoMantiloni/TPE-Source.

- **SAM: Simplified Analytical Model of Dyke Pathways in Three Dimensions.** MATLAB software implementing the dike propagation model described in Chapter 3. Available at https://doi.org/10.5880/GFZ.2.1.2023.001 and https://github.com/LorenzoMantiloni/SAM-Simplified-Analytical-Model-of-Dyke-Propagation-in-Three-Dimensions. The software includes a Manual.

Chapter 2

Stress inversion in a gelatin box: testing eruptive vent location forecasts with analog models

Abstract

Assessing volcanic hazard in regions of distributed volcanism is challenging because of the uncertain location of future vents. A statistical-mechanical strategy to forecast such locations was recently proposed: here we further develop and test it with analog models. We stress a gelatin block laterally and with surface excavations, and observe air-filled crack trajectories. We use the observed surface arrivals to sample the distributions of parameters describing the stress state of the gelatin block, combining deterministic crack trajectory simulations with a Monte Carlo approach. While the individual stress parameters remain unconstrained, we effectively retrieve their ratio and successfully forecast the arrival points of subsequent cracks.[1]

Plain Language Summary

In regions of distributed volcanism, eruption locations (vents) are scattered over a large area. Forecasting the new eruption locations over such regions is critically important, as many are densely populated. One of the main difficulties is dealing with few known past eruptions, that is, the data available to constrain forecast models are scarce. Thus, we develop a forecast strategy by applying extension or compression to blocks of gelatin with surface excavations and observing the propagation of air-filled cracks. Such models, if properly scaled, are an analog for magma propagation in the Earth's crust. We use the surface arrival points of some observed cracks to retrieve the statistical distributions of a few parameters controlling the stress field. Next, we use such distributions to forecast the arrival points of other observed cracks. Although we could not retrieve all the stress parameters accurately, the forecasts we perform are reliable. Our strategy may help retrieving the state of stress in volcanic regions and forecast the location of future vents.

2.1 Introduction

In many volcanic regions, eruptive vents may be spatially scattered: they sometimes cluster along rift zones or are distributed over areas that may exceed 10,000 km^2. Some of these

---

regions are densely populated. In order to better protect human life and infrastructure, it is important to better understand the factors determining vent distributions and improve vent location forecasts.

The most common approaches to probabilistic forecasts of future vent opening locations rely on the spatial density of past eruptive events, sometimes complemented with the surface distribution of structural features, such as faults and fractures (Connor and Hill, 1995; Martin et al., 2004; Selva et al., 2012; Bevilacqua et al., 2015). Such models, however, often remain poorly constrained due to scarce or spatially sparse data, and cannot be easily validated in volcanic systems where eruptions are infrequent.

Recently, Rivalta et al. (2019) proposed a mechanical-statistical approach to inversely constrain the state of stress, and thus magma pathways, of a volcanic region on the basis of the known location of magma reservoirs and past eruptive vents. Dike trajectories are assumed to follow a 'least resistance to opening' path calculated from the elastic stress field, which is optimized so that any magma batch released from the magma reservoir reaches one of the past eruptive vents. Once the stress field is constrained, the trajectories of future dikes can be forecast. Rivalta et al. (2019) applied the concept only to Campi Flegrei caldera in Italy, performing inversions on two stress parameters: namely, the tectonic and the unloading stress. As independent estimates of such parameters in nature are affected by large uncertainties, it remains unclear how accurately the model can capture them, how much other factors, such as medium layering, were biasing the results, and how this would affect the forecast.

Here, we delve deeper into the stress inversion concept, investigating these issues in a controlled setting: air-filled cracks propagating in a gelatin box. Such analog experimental setups have proven useful in validating dike propagation models (Watanabe et al., 2002; Maccaferri et al., 2019), for example, assessing the influence of surface loads (Muller et al., 2001; Gaete et al., 2019), rigidity layering (Maccaferri et al., 2010) and external stress fields (Acocella and Tibaldi, 2005). We stress the gelatin with extension/compression and surface excavations, shown in previous works to be the dominant stressing mechanisms in volcanic regions (Roman and Jaupart, 2014; Maccaferri et al., 2014; Corbi et al., 2016). Here we do not intend to reproduce a specific geologic setting, but rather to test the ability of our strategy to retrieve the state of stress and the relative importance of surface excavations and regional stresses. We chose a valley-shaped surface geometry so that the stresses within the gelatin block can be approximated by plane strain, but our setup may provide insights on the same stress-generating mechanisms also in caldera-like settings. First, we run a series of experiments where we track the propagation of air-filled cracks. Second, we use a boundary element (BE) model to calculate expected crack trajectories with a realistic topography, combined with a Markov Chain Monte Carlo (MCMC) algorithm to sample two parameters describing the state of stress within the gelatin. This improves on Rivalta et al. (2019) both in terms of numerical modeling and sampling algorithm used. Third, we validate our strategy by running forecasts for additional cracks, which we compare to further injections.

2.2 Methods

2.2.1 Experimental Setup

We use a perspex container of size $A \times B \times C = 40 \times 20 \times 20$ cm (Figure 2.1a). We let a 2.0 $wt\%$ or 2.5 $wt\%$ aqueous solution of 220 Bloom pig gelatin powder solidify in the box at $T = 8°$ C for 20 h. These concentration values are well characterized in previous works (e.g. Di Giuseppe et al., 2009; Kavanagh et al., 2013; Gaete et al., 2019; Smittarello, 2019). Along the y-direction,

the gelatin block surface is molded to include a rectangular excavation of width $w = 6 - 7$ cm and varying depth h (Figure 2.1a), causing surface unloading (Gaete et al., 2019). The height of the gelatin block, H, varied throughout the experiments (see Figure 2.1a). Compression or extension were imposed on the set gelatin by inserting or removing two plastic plates of thickness $d = 2.5 \pm 0.1$ mm at the box sides, separated from the medium by a transparent plastic film (Figure 2.1a). We chose $d = \pm 2.5$ mm both to work with a small strain, $e = 2d/A$, and to obtain ratios between stresses due to extension/compression and unloading comparable with estimates in nature (see section 2.2.2).

Air is injected into the gelatin from the bottom of the box, resulting in ascending air-filled cracks. Different injections are made through different holes at 1 cm intervals, both to avoid the reopening of previous cracks and to observe trajectories over as wide a section of the gelatin block as possible. Air has often been used as a magma analog in gelatin-based models (Menand et al., 2010; Corbi et al., 2016). Air is nearly inviscid, so that trajectories are not influenced by viscous effects, which are investigated in other works (e.g. Smittarello, 2019; Pinel et al., 2019). All experiments were carried out at room temperature, with timescales short enough (≤ 1 h) to maintain the experiments in an elastic regime (Kavanagh et al., 2013). The Young's modulus E of the gelatin was determined case by case by applying a small cylindrical load on the surface and measuring the resultant subsidence under the assumption of a half space (Kavanagh et al., 2013). E was mostly within the $2000 - 3500$ Pa range (supporting information, Table S2). We assumed the Poisson's ratio is $\nu = 0.49$ (van Otterloo and Cruden, 2016) and take $\rho_{gel} = 1020 \, \mathrm{kg \cdot m^{-3}}$ for the gelatin density (Smittarello, 2019). We attached polarized sheets on the box front and back walls (Figure 2.1c) to observe stress inhomogeneities during the experiments. The resulting sequences of colored fringes (Table 2.1) visualize the differential stress $(\sigma_1 - \sigma_3)$ perpendicular to the light direction (Gaete et al., 2019).

We present seven experiments (2DLA-i, i= 1,...,7), involving extension (2DLA-1,3,4,5,6,7), compression (2DLA-2) and layering (2DLA-3,4). Three more experiments with compression were discarded as most of the cracks hit the box walls (see Figure S2.3). We measure the surface arrival points of the cracks (x_i^{obs}). In 2DLA-5,6,7, we changed the state of stress midway in the experiments: we performed N^I injections, then removed the side plates (2DLA-5) or partially refilled the surface excavation with water (2DLA-6,7), and finally injected N^F more cracks (see Table 2.1 and Figure S2.2). The data from 2DLA-6 and 2DLA-7 were also pooled to test the method with a larger data set. All the respective data sets are collected in the supporting information and published as a separate data publication (Mantiloni et al., 2021a).

Inhomogeneities of various nature affect the outcome of the experiments. Some of them are unplanned, such as temperature differences up to $\sim 3°$ C between the gelatin surface and the bottom (see Table S2.2), leading to differences in the Young's modulus (≤ 600 Pa) that are of the same order of, or may exceed, the uncertainties on our measures (van Otterloo and Cruden, 2016), and localised strain concentrations induced when removing and, especially, inserting the side plates. Conversely, rigidity layering is intentionally introduced in experiments 2DLA-3 & 2DLA-4 (Table 2.1): elastic interfaces were welded by pouring a $\sim 25°$ C second layer (Kavanagh et al., 2017). In 2DLA-3, the bottom layer had a higher gelatin concentration, and thus rigidity, than the top one, and reverse in 2DLA-4. The Young's modulus E of the bottom and top layers was measured and estimated from other measurements for the same concentration, respectively (Table S2.2). For these two experiments, we assume a homogeneous medium in the numerical model and an 'effective' Young's modulus obtained by carrying out the measurement on the whole block. The aim here was to test the performance of the strategy when ignoring an existing layered structure in the simulations.
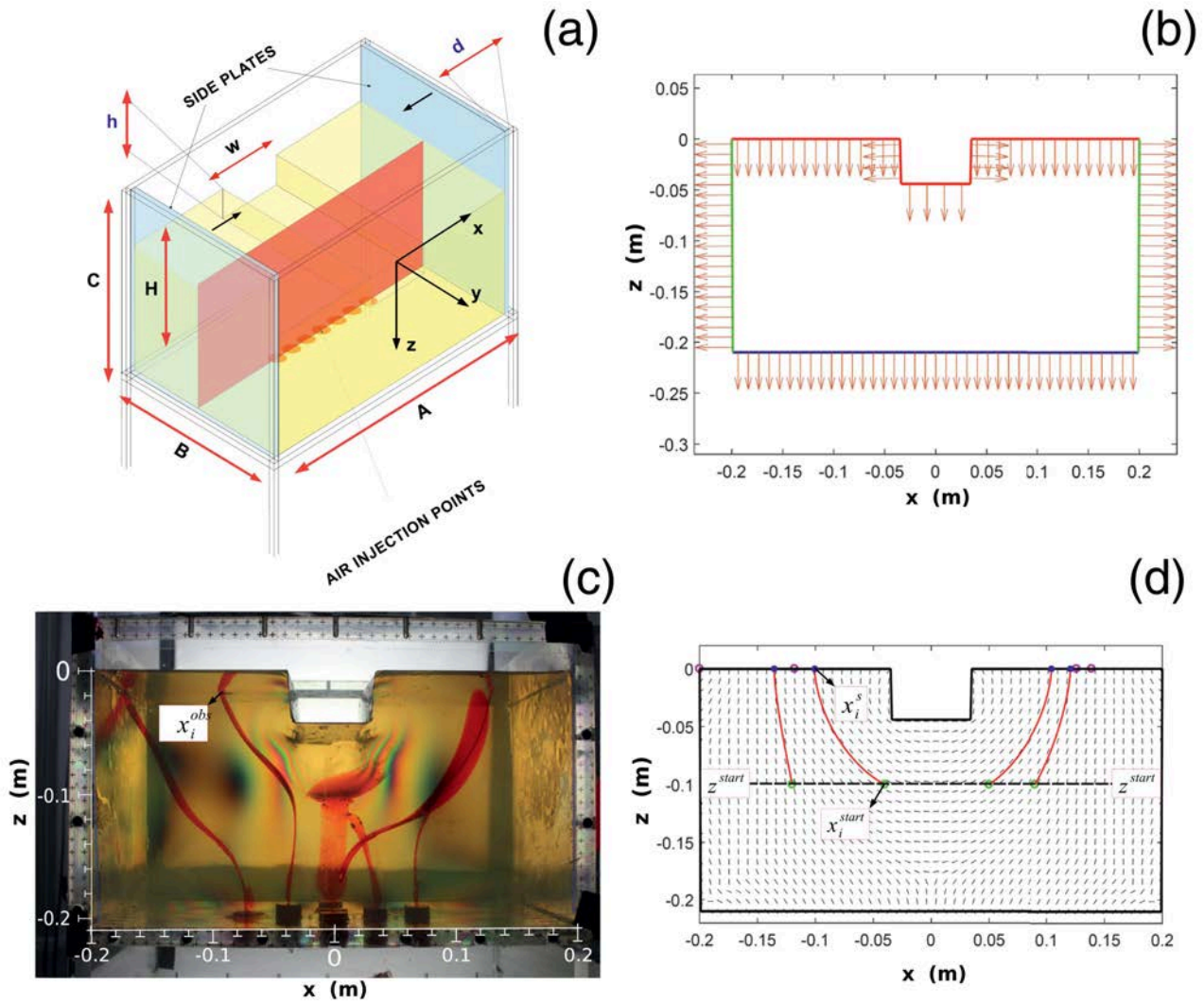
Figure 2.1: a): Schematic view of the gelatin box: the side plates are highlighted in blue, the median plane of the block in red. The quantities are defined in section 2.2.3. b): Discretization of the box and its surface over the median plane. Arrows: normals to BEs. The length of the illustrated BEs is larger than the one we employed. c): Front view of the gelatin box at the conclusion of experiment 2DLA-2 (compression): crack trajectories are marked post-intrusion with red ink. d): Numerical simulation of 2DLA-2 (c) from random parameters: x_i^s are marked with blue dots, x_i^{obs} with magenta circles. Simulated trajectories are highlighted in red and σ_1 directions are drawn in black. z^{start} is marked by a black dashed line. BE, boundary element.

2.2.2 Scaling

The length scaling factor between our experiments and nature is given by the buoyancy length Secor Jr and Pollard (1975):

$$L = \left(\frac{K_C}{\pi^{\frac{1}{2}} \Delta \rho g} \right)^{\frac{2}{3}} \tag{2.1}$$

where K_C is the medium fracture toughness and $\Delta \rho$ is the density contrast between the host medium and the injected fluid. Taking $\Delta \rho_r = 100$ kg·m^{-3}, $\Delta \rho_{gel} = 1000$ kg·m^{-3} as the rock-magma and gelatin-air density contrasts, respectively, $K_C^r = 0.2 - 1 \cdot 10^9$ Pa·m$^{\frac{1}{2}}$ as the rock fracture toughness and $K_C^{gel} = 60 - 80$ Pa·m$^{\frac{1}{2}}$ for a gelatin with Young's modulus in the range of $E = 2000 - 3000$ Pa (Kavanagh et al., 2013; Smittarello, 2019), we obtain $L^* = 3.3 \cdot 10^{-6}$ – $1.2 \cdot 10^{-5}$, where the asterisk refers to the ratio between analog and natural values. Thus, the excavation width range $w = 6 - 7$ cm we measured (Table S2.2) corresponds to $6 - 20$ km in nature, compatible with the broad range of lateral scales (100 m – 100 km) displayed by unloading mechanisms on Earth, such as the development of rifts or calderas or icecap melting. Likewise, a typical starting depth of $100 - 150$ mm (Table 2.1) corresponds to $10 - 50$ km in nature. Such a starting depth for dikes is deep, but not unreasonable. The stress scaling factor is calculated by dividing the unload stress $\sigma_U = \rho_{gel} g h$ for the excavation in the gelatin by the one for the natural case. Taking $h = 2 - 5$ cm (Table 2.1) and excavations $0.1 - 1$ km deep, assuming $\rho_r = 2500$ kg·m^{-3}, we obtain $\sigma^* = 8 \cdot 10^{-6} - 1 \cdot 10^{-4}$. We also require the ratio between the stresses arising from lateral strain and the unloading to be comparable to natural cases. In our experiments, such ratio $Ee / \rho_{gel} g h$, where $e = 2d/A = 1.25 \cdot 10^{-2}$, is in the range $0.04 -$ 0.31. The same ratio in nature, for rifts or calderas $100 - 1000$ m deep, assuming $\rho_r = 2500$ kg·m^{-3} and a typical range for absolute values of tectonic stresses of $1 - 10$ MPa (Heidbach et al., 2016), is $0.04 - 4.00$, which comprises our experimental range, even if the latter lies close to its lower limit. An overview of our scaling factors is reported in the supporting information (Table S2.1).

2.2.3 Numerical Modeling

We assume an elastic rheology in the numerical model. This is commonplace in previous works (Anderson, 1937; Muller and Pollard, 1977; Roman and Jaupart, 2014) and supported by field observations on dikes (Lister and Kerr, 1991; Gudmundsson, 2002). There is, however, evidence of non-elastic dike propagation in nature (Spacapan et al., 2017; Poppe et al., 2020), which is reproduced in different analog models (e.g. Poppe et al., 2019).

To calculate the elastic stresses within the gelatin, we use the two-dimensional (2D) BE code '*Cut&Displace*' (Crouch et al., 1983; Davis et al., 2017, 2019). We approximate the experiment's geometry as plane strain, as we observed no strain in the analog model's y-direction (Figure 2.1a). The box bottom, top and walls are discretized into BEs of length $l_{BE} = 2$ mm (Figure 2.1b). Displacement is set to zero on the bottom elements, while we impose fixed displacement on the side walls, equal to d or $-d$ for extension or compression, respectively. The free surface is shaped to model the excavation; stress boundary conditions are imposed on them to reproduce the gravitational stress due to the unload (Martel and Muller, 2000, Equation 1). We assume that w and the position of the excavation are known exactly, and we employ the measured values of E for each experiment. In the data pooling of 2DLA-6&7 (see section 2.2.1), we assumed for E and h the arithmetic mean of the respective values from the two experiments, as these were similar but not identical (Table 2.1).

We calculate the principal stress directions on a dense grid of observation points within the box. We simulate the crack trajectories assuming that the cracks open against, and propagate

perpendicular to, the least compressive stress axis, σ_3 (Anderson, 1951). This assumption makes a good approximation of real trajectories provided the size and volume of the cracks are not too large (Watanabe et al., 2002; Maccaferri et al., 2019) and the effects of viscosity can be neglected, as well as those of external stress gradients (Dahm, 2000a). The more these assumptions are far from reality, the larger the mismatch between real and σ_3-perpendicular trajectories. More complex dike trajectory models exist for simulations in 2D (Dahm, 2000a; Maccaferri et al., 2011) and recently also in three dimensions (3D) (Davis et al., 2020). However, the predictive power of models increases if their complexity is reduced with regard to accurate explanatory dike trajectory models (see e.g. Forster and Sober, 1994). Thus, we opt for the simpler option of σ_3-perpendicular trajectories, which also necessitate much shorter computation time and better serve the stochastic part of our strategy.

If the cracks are misaligned with the stress field at injection, they will require some distance to realign (Menand et al., 2010; Maccaferri et al., 2019). The starting depth in the simulations is shallower than the injection depth so that this readjustment occurs at least partly.

2.2.4 MCMC Scheme

Our sampling procedure relies on the Delayed Rejection and Adaptive Metropolis MCMC algorithm (Haario et al., 2006; Laine, 2013). The set of N observed arrivals (x_i^{obs}, $i = 1,...,N$) is first divided into two subsets N^I and N^F ('I' and 'F' stand respectively for 'inversion' and 'forecast'). The N^I set is used to sample the two parameters d and h. The size of our data sets varies from a minimum $N^I = 2$ in 2DLA-2 to a maximum of $N^I = 5$ in 2DLA-6&7 (see the supporting information, Tables S2.3 and S2.4).

At start, ranges and guesses for the parameters d and h are fixed together with a common starting depth for the cracks, z^{start}. Starting locations, x_i^{start}, are assigned as the horizontal coordinate of the upper tips of the observed cracks at z^{start}. At each iteration, we simulate N^I crack trajectories and sample d and h in order to minimize the objective function

$$S = \sum_{i=1}^{N^I} (x_i^s - x_i^{obs})^2 \tag{2.2}$$

where x_i^s are the simulated arrivals.
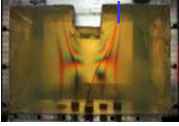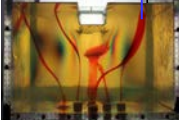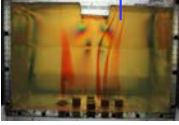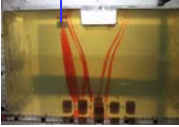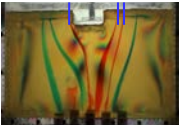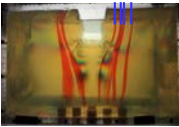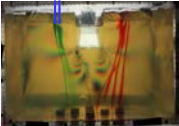
The squares of the uncertainties on the two parameters ($\Delta d = \pm 0.1$ mm; $\Delta h = \pm 1$ mm) populate the diagonal of the covariance matrix. $M = 10^4$ iterations were made for every chain. Our runs highlight a correlation between d and h, as expected from Rivalta et al. (2019), so we consider a further parameter: $R = d/h$, which partly removes the trade-off, and use the posterior probability distributions (PPDs) of d and R to perform the forecasts.

2.2.5 Forecasting Approach

After performing the inversions, we run $M^F = 10^3$ iterations of N^F simulations for the forecasts, where we sample the parameters (d, R) from their PPDs. Starting points are drawn from Gaussian distributions centered on $x_i^{start,F}$, $z_i^{start,F}$, with standard deviation $\sigma = 1$ mm. The combined distribution of simulated arrivals is compared to the observed arrivals set aside for the forecast $x_i^{obs,F}$. We measure the success of a forecast from how far the median $x_i^{med,F}$ of the simulated arrivals lies from $x_i^{obs,F}$. Thus, for each individual i-th forecast, we define $\Delta x_i^F = |x_i^{obs,F} - x_i^{med,F}|$ and compare it to the standard deviation δx_i^F of the distribution (see Table 2.1).

A different approach is adopted in experiments 2DLA-5 and 2DLA-6&7 to account for the modified state of stress between the N^I and N^F cracks. In 2DLA-5, we fit the PPDs of d and

Table 2.1: Experiments, Measured Parameters, and Results.

# Exp.	Picture	h ± 1 mm	d ± 0.1 mm	R $(\times 10^{-3})$	h^{med} mm	d^{med} mm	R^{med} $(\times 10^{-3})$	$x_i^{med,F}$ mm	δx_i^F mm	Δx_i^F mm
	Experiments		**Measured Parameters**				**Results**		**Forecasts**	
2DLA-1 Extension		50	2.5	63 ± 4	51	4.9	100	67	7	2
2DLA-2 Compression		44	-2.5	-57 ± 4	73	-3.5	-55	115	39	11
2DLA-3 Extension Layered		21	2.5	120 ± 10	63	3.9	69	75	9	1
2DLA-4 Extension Layered		24	2.5	104 ± 8	59	5.8	102	-85	6	1
2DLA-5 Updated Extension		24	0 **2.5**	0 ± 10^{-2} **104 ± 8**	64	0.4	8×10^{-3}	-54 66 77	43 36 34	1 6 10
2DLA-6 Extension Refilled		58 (65) **28 (35)**	2.5 (2.5)	(39 ± 2) **(71 ± 7)**	64	2.5	39	63 76 84 102	10 7 6 4	3 1 2 1
2DLA-7 Extension Refilled		72 (65) **32 (35)**	2.5 (2.5)	(39 ± 2) **(71 ± 7)**				-84 -73	8 6	4 0

Note: blue markers in the pictures indicate the arrivals used for the forecast (see Figure 2.2b): in 2DLA-5, 2DLA-6 and 2DLA-7 these coincide with the injections following the stress update (differently colored trajectories in pictures of 2DLA-5 and 2DLA-7 stand for preupdate and postupdate). Arithmetic means assumed for h and R in 2DLA-6&7 are indicated in parentheses (section 2.2.3). Updated d and h (section 2.2.5) are in boldface. h^{med}, d^{med}, R^{med}: medians of the respective PPDs (section 2.3.2). $x_i^{med,F}$, δx_i^F and Δx_i^F are defined in section 2.2.5 and refer to forecasts for individual $x_i^{obs,F}$. For further information, see the supporting information, Tables S2.3 - S2.4 (measured quantities) and S2.5 (inversion results).
Abbreviation: PPD, posterior probability distribution.

R with Beta functions and then update them by shifting the mean value and their upper and lower limits to account for the added extension (from $d = 0$ mm to $d = 2.5$ mm). In 2DLA-6&7, we use the same strategy, except that we update h (subtracting the height of the water filling the surface excavation) and R.

2.3 Results

2.3.1 Experimental Results and Numerical Modeling

Experiments with extension and compression resulted in markedly different observations. Surface unloading deflects vertical crack trajectories, as seen in both natural (Tibaldi, 2004; Corbi et al., 2015) and experimental (Corbi et al., 2016; Gaete et al., 2019) settings. Regional extension competes against the former, leading to more vertical trajectories (Maccaferri et al., 2014). Compression, instead, tends to rotate σ_1 to horizontal Menand et al. (2010), thus amplifying the effect of the unloading. The effect of extension is observed in 2DLA-5, where extension was applied after N^I cracks had propagated, by comparing green (early) to red (late) trajectories (Table 2.1). The partial refilling in experiments 2DLA-6 and 2DLA-7 (Table 2.1) reduced the influence of the unloading and led to less deflected trajectories. Trajectory simulations for the experiments with extension are not identical to, but closely match the observations, if the measured d and h are employed.

Trajectories in compressional settings (2DLA-2 and discarded experiments, see Figure S2.3) tend to diverge significantly from each other and spread the uncertainty of the initial location into scattered arrival locations. Simulations with the imposed parameters fail to reproduce these data sets. This is reflected in the outcome of the inversions and forecasts, as we explain later on.

Dike trajectories are deflected towards the vertical direction when passing from a high-rigidity layer to a low-rigidity one and viceversa, as theoretically predicted by Maccaferri et al. (2010) (see experiments 2DLA-3 and 2DLA-4, Table 2.1).

2.3.2 Parameters sampling

We find that in most cases the retrieved PPDs fail to constrain d and h individually, though they generally succeed in constraining their ratio R. This can be seen in the joint distributions for R and h (Figure 2.2a). In the homogeneous extensional cases, the PPDs for d and especially h are generally spread. In spite of this, the imposed value of d is well recovered in 2DLA-5 and 2DLA-6 & 7 (see Table S2.5). The distributions of h tend to be uniform. In contrast, the PPD for R is always peaked around or close to the imposed value (Figure 2.2a). The PPDs, including those of h, are more peaked when more data are available (2DLA-6&7). In the layered cases, the medians of all the PPDs are rather far from the respective imposed values, except for R in 2DLA-4. This was expected, since we purposely neglected the medium layering in the modeling (see section 2.2.1).

In the only compressional case (2DLA-2), the PPDs are extremely spread and fail to constrain the parameters, though the median of R is close to the imposed value (Figure 2.2a).

2.3.3 Forecasts

In spite of the PPDs for d and h being often spread or even uniform, the forecast distribution generally shows N^F sharp peaks (Figure 2.2b, Table 2.1). Moreover, in spite of the PPDs for d and h failing to accurately recover the imposed values, the peaks of the forecast distribution
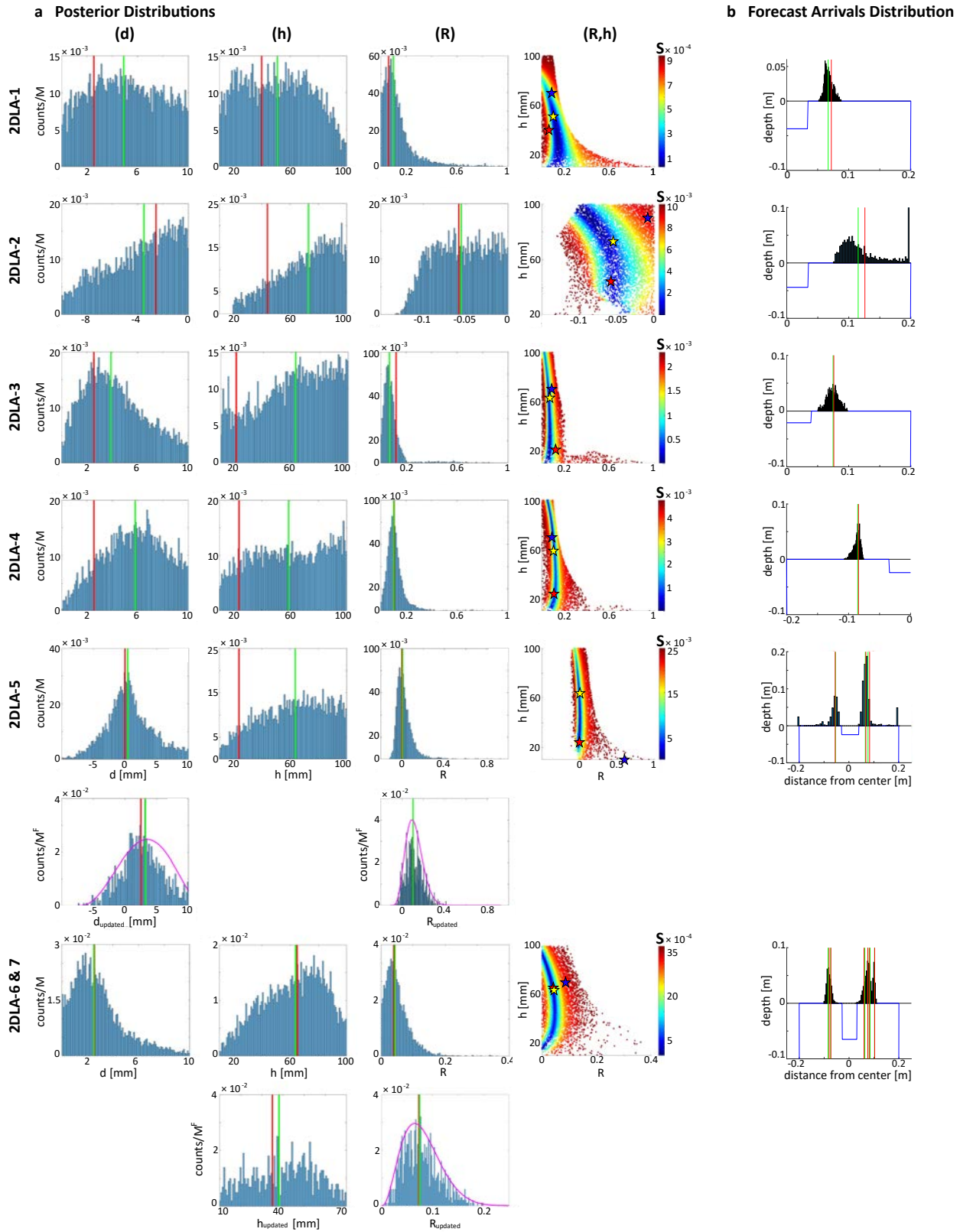
Figure 2.2: Summary of inversion and forecast results. a): PPDs for parameters d, h and R and joint PPD for (R,h). Red lines show the measured values; green lines the medians (Table 2.1). The Beta functions used to fit and update the distributions in 2DLA-5 and 2DLA-6&7 are plotted in magenta. Last column from left: the starting guess, measured and median values are represented, respectively, by a blue, red and yellow star. The color palette shows the value of S (Equation 2.2) for every sampled point in the parameters' space, from dark red (higher S) to blue (lower S). b): countings of forecast arrivals displayed on a scheme of the box (the surface topography shown is before the refilling in 2DLA-6&7). Red lines: positions of $x_i^{obs,F}$; green lines: medians of the forecasts for individual $x_i^{obs,F}$ (see also Tables 2.1 and S2.3). PPD, posterior probability distribution.

generally coincide or are very close to the observed arrivals (Figure 2.2b, Table 2.1). This includes the layered cases. Again, the compressional case 2DLA-2 marks an exception: the forecast is rather spread (see δx_i^F values in Table 2.1) and shows two maxima, one closer to the box center and a sharp one at the box margin (Figure 2.2b); this is due to the fact that many simulated cracks hit the right side of the box. Neither of the maxima coincides with the observed arrival, and the median falls ~ 1 cm away (Figure 2.2b, Table 2.1).

Two secondary peaks are also obtained in the combined forecast distribution for 2DLA-5 ($N^F = 3$), as the sampling range for d allowed for both positive (extension) and negative (compression) values. This is reflected also in the spread of the individual distributions (Table 2.1). The two main maxima are here close to the box center and show good agreement with $x_i^{obs,F}$. Considering the three individual distributions separately, the distances Δx_i^F between the three $x_i^{obs,F}$ and the medians $x_i^{med,F}$ are well within δx_i^F of the respective distributions. In 2DLA-6&7 ($N^F = 6$), three clear maxima are observed in the combined forecast distribution, showing again good agreement with the $x_i^{obs,F}$, which are ≤ 4 mm away from the medians of the respective individual distributions (Table 2.1).

In all extensional experiments with $N^F = 1$, the observed arrivals $x_i^{obs,F}$ are always within 2 mm from the medians (Table 2.1).

2.4 Discussion

While the inversion algorithm generally failed to retrieve the imposed values of the parameters d and h (Figure 2.2a), the forecast strategy proved very effective in identifying high-probability regions for crack arrivals on the surface (Table 2.1 and Figure 2.2). This apparent contradiction arises from the fact that the inversions effectively recover the imposed value of $R = d/h$. Physically, this is because the curvature of the trajectories is controlled by R, rather than d or h individually, as also found by Roman and Jaupart (2014).

Forecasts are successful in spite of scarce data sets and when layering of the medium is neglected. If data sets are larger (5 data points for 2 parameters), the state of stress is recovered more accurately. In principle, our procedure could be used also to constrain the elastic parameters, but information on the stress state would be necessary as they trade off. To test this possibility, we ran an inversion for E on the N^F data set of 2DLA-5, and we found the sampled E distribution peaks very close to the measured value (results are shown in Figure S2.4b).

The forecast strategy applied in experiments 2DLA-5 and 2DLA-6&7 also proved effective in accounting for the modification of the stress field over time, validating the evolving-stress forecast method by Rivalta et al. (2019).

Several factors may contribute to the failure of the approach in compressional settings, even though there is inherently no difference in the σ_3-perpendicular propagation of cracks under remote compression rather than extension. Both unloading and compression lead to more horizontal σ_1 directions within the medium. Thus, the mismatch between the crack orientation and σ_1 right after the injection is larger and they need more space to align. Moreover, a horizontal σ_1 may encourage cracks to propagate towards the back or the front walls of the box, whose effect on the gelatin may undermine the plane strain assumption (in compressional cases, these walls prevent the gelatin to expand along the y-axis, thus inducing compression also in this direction). Furthermore, side plate insertion and the non-frictionless contact between gelatin and box walls induced local stress concentrations at the box corners, affecting nearby trajectories (Figure S2.3). Such effects may arise from the size of our box and could be reduced by employing a larger tank. However, as σ_3-perpendicular trajectories tend to diverge in compres-

sional settings (including nature), simulations are more sensitive to any variability of initial and boundary conditions or model parameters, and forecasts are therefore more challenging.

A further limitation arises from the limited number of experiments we carried out. In spite of this, we did observe clear common patterns in experiments with similar settings (section 2.3.1). Our experimental setup allowed for several factors, including variable starting crack length and orientation, elastic heterogeneities and possible interactions between successive injections, to play a role. This is reflected in the fact that observed and modeled trajectories do not coincide in general (section 2.3.1), though the forecasts are fairly good. This is not contradictory, as our forecast strategy includes a stochastic model to treat such variability.

Another remarkable issue is the nearly-uniform trend observed in the PPDs for h (Figure 2.2a), which appears to be systematic even when larger data sets are available (as opposed to the PPDs of d, cfr 2DLA-1 and 2DLA-5). This arises from the fact that very shallow or very deep surface unloads, for the same d and starting points, lead to similar arrivals. We surmise that this effect, observed both in the numerical simulations and in a separate experiment (Figure S2.4a), is due to the relaxation of the surface excavation's walls under gravity.

2.5 Conclusive Remarks

We conclude that a mixed deterministic-stochastic strategy is effective in constraining the ratio of different stress-generating mechanisms and forecasting the arrival points of air-filled cracks in gelatin blocks. The strategy performs well on small data sets and may be, therefore, suitable for applications to volcanic regions where few vent locations are available. Future developments may focus on relaxing some of the limitations in our current numerical simulations, such as upgrading to 3D, including the viscous flow in the cracks, or addressing rheologies different from elastic. This will facilitate direct application to producing probabilistic maps of vent location for volcanic systems in nature.

Acknowledgments

Data Availability Statement

All data employed in this work are available at the GFZ Data Services repository: https://doi.org/10.5880/GFZ.2.1.2021.001 (Mantiloni et al., 2021a).

Chapter 3

Mechanical modeling of pre-eruptive magma propagation scenarios at calderas

Abstract

Simulating magma propagation pathways requires both a well-calibrated model for the stress state of the volcano and models for dike advance within such a stress field. Here, we establish a framework for calculating computationally efficient and flexible magma propagation scenarios in the presence of caldera structures. We first develop a three-dimensional (3D) numerical model for the stress state at volcanoes with mild topography, including the stress induced by surface loads and unloading due to the formation of caldera depressions. Then, we introduce a new, simplified 3D model of dike propagation. Such a model captures the complexity of 3D magma trajectories with low running time, and can backtrack dikes from a vent to the magma storage region. We compare the new dike propagation model to a previously published 3D model. Finally, we employ the simplified model to produce shallow dike propagation scenarios for a set of synthetic caldera settings with increasingly complex topographies. The resulting synthetic magma pathways and eruptive vent locations broadly reproduce the variability observed in natural calderas.[1]

Plain Language Summary

Understanding the pathways that bring magma from an underground chamber to the surface helps to prepare for future eruptions in volcanic areas. Dikes are fractures filled with magma and represent the most common mechanism of magma transport in the Earth's crust. Their trajectories may be curved if the Earth's crust is deformed by the load of topography or by tectonic forces. Here we first discuss a model of such deformation processes in volcanic regions with complex but mild topography. Then, we develop a simplified dike propagation model that we compare to a more sophisticated one. Next, we combine our models and simulate magma pathways in artificially-generated scenarios.

3.1 Introduction

Geophysical observations of ground deformation and seismicity in volcanic areas have highlighted how some eruptions are preceded by a long phase of magma propagation in the form of magma-filled dikes (Einarsson et al., 1980; Ebinger et al., 2010; Nakada et al., 2005; Uhira

---

[1] Originally published as: Mantiloni, L., Rivalta, E., Davis, T. (2023). Mechanical modeling of pre-eruptive magma propagation scenarios at calderas. Journal of Geophysical Research: Solid Earth, 128(3), e2022JB025956. doi:10.1029/2022JB025956

et al., 2005; Wright et al., 2012; Sigmundsson et al., 2015; Patrick et al., 2020; Cesca et al., 2020; Davis et al., 2021; Smittarello et al., 2022). Some recent dikes have propagated for over 70 km, reaching locations that had not experienced any fissure opening in decades or centuries; in some cases the ensuing lava flows have resulted in massive property damage (Patrick et al., 2020; Martí et al., 2022) or loss of life (Smittarello et al., 2022). The associated dike trajectories have also displayed a variety of geometries, from horizontal to oblique to vertical, and shapes, from planar to segmented, curved or twisted (Branca et al., 2003; Bagnardi et al., 2013; Xu and Jónsson, 2014; Sigmundsson et al., 2015; Patrick et al., 2020; Davis et al., 2021; Dumont et al., 2022; Smittarello et al., 2022; Martí et al., 2022). In spite of the importance of this process, there are still no models to forecast, in three dimensions, the trajectory taken by magma during propagation in the shallow crust.

Our physical understanding of dike trajectories have progressed significantly in the last decades. Both early (Anderson, 1937) and more recent works (Dahm, 2000a) have established that dike pathways are largely determined by the balance between the elastic stresses in the host rock and the buoyancy force resulting from the density contrast between magma and rock. As a rule of thumb, dikes open against the direction of the least-compressive principal stress axis (Ziv et al., 2000; Gudmundsson, 2002; Pollard et al., 2005), while the combined effect of the external stress and the magma buoyancy force determines their direction of propagation (Weertman, 1971; Pollard, 1987; Rubin, 1995; Taisne et al., 2011; Rivalta et al., 2015; Townsend et al., 2017). The simplest two-dimensional (2D) trajectory models are streamlines perpendicular to the least-compressive stress axis (Anderson, 1937; Pollard, 1987), while the most sophisticated approaches model dikes as cracks steered in the direction of maximum strain energy release rate (Dahm, 2000a; Maccaferri et al., 2010, 2011). Dike trajectory models have recently evolved from two dimensional (Anderson, 1937; Muller and Pollard, 1977; Pollard, 1987; Dahm, 2000a) to partially (Sigmundsson et al., 2015; Heimisson et al., 2015; Pansino et al., 2022) or fully three-dimensional (3D) by Davis et al. (2020, 2021). The latter model extends to 3D the maximum strain energy release rate trajectory calculation approach introduced by Dahm (2000a); a 3D equivalent of the simple 2D streamline approaches is still missing.

The 3D model by Davis et al. (2020, 2021) has been applied to explain the counterintuitive trajectory of the 2018 dike at Sierra Negra, Galápagos. Importantly, Davis et al. (2021) confirmed the pivotal importance of a well-calibrated stress field in modeling dike trajectories: contributions from different stress-generating mechanisms, such as topographic gravitational loading and regional stress field, needed to be carefully adjusted in order to steer the dike on the observed trajectory. If we want to simulate 3D dike propagation at arbitrary volcanoes, we also need to determine their state of stress. This problem was addressed by Rivalta et al. (2019), who suggested a stress inversion strategy which involves, first, establishing the relevant sources of stress for the specific volcano, and then, tuning their relative intensity so that simulated dikes starting from the known location of magma storage reach the known locations of past eruptive vents. This strategy was tested on Campi Flegrei caldera in Italy, using only 2D (plane strain) stress models and 2D streamlines for dike propagation.

Extending the stress calibration strategy by Rivalta et al. (2019) to 3D would pave the way to forecast dike pathways in 3D at any arbitrary volcano. A preliminary step is to set up 3D stress and dike trajectory models that are computationally efficient for the large number of simulations needed by the stress calibration procedure. In this study, we first develop computationally efficient 3D stress field calculations for scenarios with topographic reliefs. Then, we develop a fast, semi-analytical 3D dike propagation model that approximates the sophisticated model by Davis et al. (2020, 2021) but retains the simplicity of 2D streamlines and can also backtrack a dike trajectory from eruptive vent to magma chamber. Finally, we show how to integrate all these models to produce realistic pre-eruptive magma propagation scenarios. We focus on

calderas, setting up synthetic topographies inspired by natural systems.

3.2 Method formulation

We assume a homogeneous, isotropic and linearly elastic medium as the host rock, described by rock density ρ_r, Young's modulus E and Poisson's ratio ν. g is the acceleration due to gravity. Symbols and parameters are defined in Table 3.1.

3.2.1 A modular approach to understanding stress states

We describe the state of stress within the host rock by a stress tensor σ_{ij}. Tensional stresses are positive. σ_{ij} is diagonalized to retrieve magnitudes, σ_1, σ_2, σ_3, from most compressive to least compressive, respectively, and eigenvectors, $\vec{v_1}$, $\vec{v_2}$, $\vec{v_3}$, which identify the orientations of the principal stress axes.

We build our 3D stress model following the first-order linear approach by Rivalta et al. (2019), who expressed the elastic stress field σ_{ij} of a volcanic region as the superposition of perturbations from a background stress state σ_{ij}^0, each stemming from a different stress-generating mechanism. The approach neglects coupling between the stress sources. We limit our analysis to tectonic stresses and gravitational loading/unloading because dike patterns can often be explained by a combination of the two mechanisms (Roman and Jaupart, 2014; Corbi et al., 2015; Heimisson et al., 2015; Maccaferri et al., 2017; Neri et al., 2018). Not including other mechanisms, such as pressurized magma reservoirs or faults, has the advantage of limiting the number of parameters in the model, while retaining the stress mechanisms with the largest influence. More contributions can be easily added, if needed in specific cases.

We write the stress tensor at any point in the crust as:

$$\sigma_{ij}(x,y,z) - \sigma_{ij}^0(z) = \sigma_{ij}^T + \sigma_{ij}^G(x,y,z) \tag{3.1}$$

where the terms on the right side arise, respectively, from the regional tectonic stress (T) and the gravitational loading/unloading (G).

The first step is to define the unperturbed state of stress, σ_{ij}^0, before any of the sources on the right hand side of Equation 3.1 became active. There are two main assumptions in literature: a laterally-confined medium, that is, no lateral strain can be produced after gravity is turned on (e.g. Martel and Muller, 2000; Savage et al., 1985), resulting in a vertical $\vec{v_1}$:

$$\sigma_{xx}^0 = \frac{\nu}{(1-\nu)}\rho_r g z, \quad \sigma_{yy}^0 = \frac{\nu}{(1-\nu)}\rho_r g z, \quad \sigma_{zz}^0 = \rho_r g z. \tag{3.2}$$

or a lithostatic stress state:

$$\sigma_{xx}^0 = \sigma_{yy}^0 = \sigma_{zz}^0 = \rho_r g z. \tag{3.3}$$

Field measurements of subsurface stress (Jaeger et al., 2007) lie somewhat in between those two assumptions. Therefore, σ_{ij}^0 can be written as:

$$\sigma_{xx}^0 = \sigma_{yy}^0 = k\rho_r g z, \quad \sigma_{zz}^0 = \rho_r g z, \tag{3.4}$$

where $k \in [\frac{\nu}{(1-\nu)}, 1]$ (Jaeger et al., 2007; Muller et al., 2001; Slim et al., 2015). In this study, we set $k = 1$ and assume a lithostatic unperturbed stress.

The second step is to superimpose the tectonic stress, expressed in terms of three independent components σ_{xx}^T, σ_{yy}^T, σ_{xy}^T, here assumed uniform (e.g. McKenzie, 1978; Müller et al., 1992).

The third step is to consider gravitational stresses associated to surface loading or unloading. This has often been modeled by distributions of normal forces onto a half-space (Dahm, 2000b; Maccaferri et al., 2014; Neri et al., 2018), which, however, neglect the shear stresses imposed by the topography and provide no information on the stress within the topography itself (McTigue and Mei, 1981). More sophisticated analytical solutions exist, but are either 2D (Savage et al., 1985; McTigue and Mei, 1981) or only for simple topographies (McTigue and Mei, 1987). Stress due to surface loading/unloading decays over a vertical distance that scales with the radius of the topographic feature (e.g. Jaeger et al., 2007; Pollard et al., 2005; Roman and Jaupart, 2014). Consequently, principal stresses can change in both intensity and orientation over short distances. This has several implications discussed later (Section 3.2.2.1).

Martel and Muller (2000) and Slim et al. (2015) described how to implement topographic loads within Boundary Element (BE) models, where the topography is discretized into a mesh of dislocations. They considered the effect of topographic loading as akin to cutting an infinite body subject to gravity in two halves along a surface defined by the topography. The gravitational stress imposed by the upper half onto the lower one is then subtracted from the background stress of the body (Martel and Muller, 2000, Figure 3). In practice, this is achieved through imposing boundary conditions on the BEs, depending on the coordinate z of their midpoints and the rock density, which control the overburden or excavation pressure imposed by the topography.

One important point in models such as Martel and Muller (2000) is that the boundary conditions at the BEs representing the topography are univocally fixed only once the datum level, that is the unperturbed surface before any topography is created, is set. This was rarely clarified in past applications (e.g. Chadwick and Dieterich, 1995; Urbani et al., 2017; Neri et al., 2018). Identifying such surface is not always trivial but critical, as different choices lead to different outcomes for the displacement and stress field. We show this in Figure 3.1a, where we compare $\vec{v}_1$ from the analytical solution by McTigue and Mei (1981) for a valley adjacent to a ridge under plane strain assumption to 2D numerical models where the datum level is set to, successively, the flat extremes of the profile, the ridge summit and the valley bottom. The first model shares the same assumption on the datum level with the analytical solution, hence the good agreement for that case. Such assumption is straightforward to adopt when the topography becomes uniformly flat away from the loaded/unloaded region. However, this is not always the case, and the optimal choice of datum level may depend on the situation. Take e.g. a caldera lying on a coastline, which divides two regions, the mainland and the sea floor, at different elevations. We consider a similar case in our synthetic scenarios, and we solve the ambiguity in the datum level by setting it to the ground elevation before the caldera was formed: this coincides with the sea level in that case. If, for instance, we were to study the formation of an edifice and, later, of a caldera at its summit, we would first set the edifice datum level at its base, and then set the caldera datum level at the edifice summit. Consequently, the topography preceding the reference event (in our scenarios, the caldera formation) informs the datum level.

A further issue regarding the calculation of surface loading/unloading stresses is that they are not immutable. Volcanic regions host a variety of stress-generating and stress-relieving mechanisms acting on different time scales. For example, the build-up of a volcanic edifice consists of progressive accumulation of eruptive material that loads and stresses the underlying crust (McGuire and Pullen, 1989), while, at the same time, magmatic intrusions, earthquakes and inelastic processes tend to relax shear stresses and homogenize principal stresses (Chadwick and Dieterich, 1995). Quantifying stresses within large topographic loads at a particular point in time is thus non-trivial. Here we avoid this issue by focusing on calderas that we assume have formed relatively recently in the history of the volcano, and consider otherwise only mild
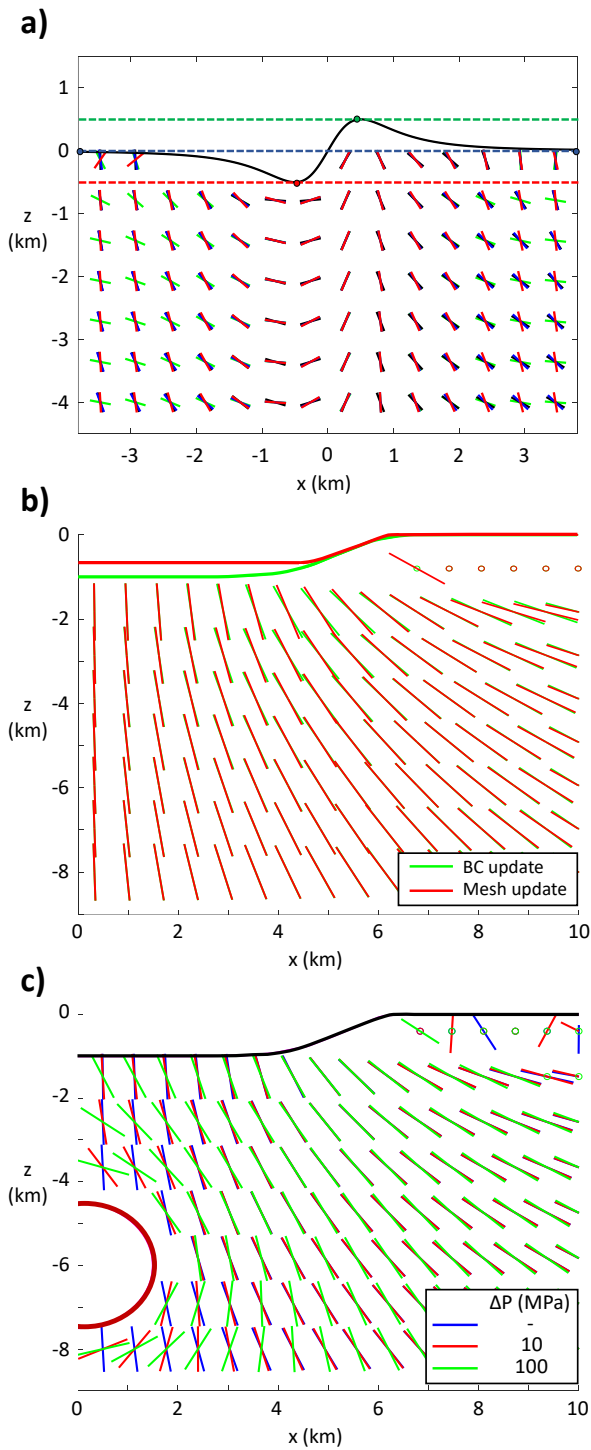
Figure 3.1: a): Datum level choice: $\vec{v}_1$ orientation due to gravitational loading/unloading of a valley adjacent to a ridge (profile is drawn in black) under plane strain condition. The analytical solution by McTigue and Mei (1981) (black) is compared to our numerical solution with datum level fixed at the flat extremes of the topography (blue), the ridge summit (green) and the valley bottom (red). b): Evolving topography: a 1-km-deep axisymmetric caldera is refilled by 1/3 of its original depth. $\vec{v}_3$ orientation and topographic profiles for two mechanically-equivalent models of caldera unloading with different reference topographic relief and boundary conditions. c): Importance of reservoir: $\vec{v}_3$ orientation for three models involving a 1-km-deep axisymmetric caldera and vanishing tectonic stress. Two models include a 6-km-deep spherical magma reservoir of 1.5 km radius with overpressures ΔP=10 MPa (red) and 100 MPa (green) respectively; one has no reservoir (blue).

topographies, so that modeling dike propagation within edifices is not necessary. We elaborate further on this point in Section 3.4. We note that when we use the term 'caldera', we are referring to the general surface depression that is associated with all calderas. Differences in the origin, structure and setting of calderas (e.g. Cole et al., 2005; Acocella, 2007) are neglected.

We compute $\sigma_{ij}^G(x, y, z)$ in Equation 3.1 following Martel and Muller (2000); Slim et al. (2015). We employ the 3D BE tool *Cut&Displace* (Davis et al., 2017, 2019), based on the displacement discontinuity method by Crouch et al. (1983). We use *DistMesh* by Persson and Strang (2004) to discretize the topography into a mesh of triangular dislocations (Nikkhoo and Walter, 2015), acting as BEs. The 3D mesh needs to be larger than the region of interest, so that its edges are distant enough from the volume where we compute the stress. We find that a mesh with a diameter three times the lateral extent of the studied region is enough for that purpose, and we adopt this choice in all our models. If a coastline is present, the outer mesh tapers to two horizontal surfaces at different height, representing the far-field mainland and the far-field sea floor. Once the datum level is fixed, stress boundary conditions are imposed on each BE as previously described. The load imposed by the water column on the bathymetry is also included.

Calderas are usually filled with eruptive material or sediments over time (e.g. Orsi et al., 1996; Hildreth et al., 2017). Our model can account for this in several ways: the original buried caldera floor may be meshed as the reference topographic relief, and the corresponding BEs may be loaded accounting for the pressure deficit due to the density contrast between the deeper host rock and the layers above. Alternatively, the current caldera topography may be meshed as the reference topographic relief, and the unloading pressure resulting from the missing mass due to lower density infill is factored in the boundary conditions. Calculations for these options for a synthetic caldera (Figure 3.1c) show good agreement except in the proximity of the caldera rim. Here we follow the former approach in one scenario, as illustrated later.

We remark that some of the stress sources we neglect, such as magma reservoirs, are in principle straightforward to include in our BE model. In order to show the minor relative influence of such sources, we compare in Figure 3.1b the orientation of $\vec{v}_3$ for three different models: one without and two with a pressurized, spherical magma chamber, with overpressure of 10 MPa and 100 MPa, all involving the same surface unloading and tectonic stress. Only with extremely large overpressures the effects of the pressurization are felt at a distance of up to one source diameter. This validates in 3D a similar argument by Rivalta et al. (2019) (see their Figure 1).

3.2.2 Three-dimensional dike propagation model

3.2.2.1 Simplified Analytical Model (SAM)

Next, we develop a computationally-efficient 3D dike propagation model that provides a 3D equivalent to 2D $\vec{v}_3$-perpendicular streamlines. There is no straightforward method to compute streamlines in 3D, as the direction of $\vec{v}_3$ alone identifies a surface, while the direction of propagation on that surface remains undetermined. Davis et al. (2020, 2021) developed a point-wise, analytical dike trajectory calculator, similar to Sigmundsson et al. (2015) but fully 3D and more comprehensive in terms of factors considered. Its purpose was to justify why an observed dike took a specific direction depending on the magma buoyancy and the external state of stress, and falls short of being a propagation model. Here we turn that approach into a simplified 3D propagation model that can also backtrack dike trajectories downward from a vent to the magma storage region. We henceforth refer to our model as the 'Simplified Analytical Model' (SAM).

Table 3.1: Parameters and abbreviations of the dike propagation model.

Parameters		
Description	Symbol	Units
Host rock density	ρ_r	kg/m^3
Magma density	ρ_m	kg/m^3
Mode I stress intensity factor	K	Pa$\sqrt{\text{m}}$
Host rock fracture toughness	K_C	Pa$\sqrt{\text{m}}$
Young's modulus	E	Pa
Poisson's ratio	ν	
Dike radius	c	m
Number of observation points along the dike tip-line	n	
Backtracked dike radius	c_B	m
Description	Abbreviation	
Forward dike trajectory	FT	
Dike starting point	F_0	
Dike surface	Σ	
Observation points	O_i, $i = 1,...,n$	
Dike arrival point	F_A	
Points defining dike trajectory	F_i, $i = 1,...,A\text{-}1$	
Projected dike arrival point	F_A^P	
Backtracked dike trajectory	BT	
Points defining backtracked trajectory	B_i	
Backtracked dike starting point	BSP	

In the analytical model by Davis et al. (2020, 2021), propagation of the tip-line of a dike occurs when the local mode I stress intensity factor, K, is larger than the fracture toughness, K_C, of the host rock (e.g. Secor Jr and Pollard, 1975). The dike is represented as a tensile penny-shaped crack with a fixed volume, V, and radius, c. It is assumed that external stress varies linearly in every direction over the crack surface, and that internal pressure varies linearly with z proportional to $\rho_m g \sin \beta$, where β is the crack dip. In such case, K can be written as:

$$K = \frac{3\mu V}{4(1-\nu)c^2\sqrt{\pi c}} + \frac{4}{3\pi}\Delta\gamma^{max}c\sqrt{\pi c}\cos\alpha, \tag{3.5}$$

(Tada et al., 2000), where $\Delta\gamma^{max}$ is the maximum value over all orientations across the crack plane of the 'pressure gradient', $\Delta\gamma$, calculated as the difference of the external stress and internal magma pressure over the crack diameter, and α is the angle spanning the circumference of the crack away from the direction of $\Delta\gamma^{max}$ (see Figure 3.2b). The second contribution in Equation 3.5, which is largest for $\alpha = 0$, determines the maximum of K and, thus, the direction of propagation of the crack. If $R_K = K/K_C > 1$, the crack propagates (see Figure 1 in Davis et al., 2020).

In SAM, we simplify such approach by forcing the dike to open against the local $\vec{v_3}$, and calculating K simply as

$$K = \frac{4}{3\pi}\Delta\gamma c\sqrt{\pi c}. \tag{3.6}$$

This is equivalent to neglecting the role played by the dike volume and K_C in determining whether the dike will advance. On the other hand, the buoyancy force contributes to $\Delta\gamma$, and plays a role in determining the direction of propagation on the $\vec{v_3}$-perpendicular surface.

In a Cartesian reference frame, where the z-axis is positive upward (Figure 3.2a), we calculate forward dike trajectories (FTs) as 'paths of local steepest ascent', corresponding to the steepest increase of $\Delta\gamma$, as follows:

1. We produce a stress model for the hosting medium (section 3.2.1).

2. We choose a starting point F_0 for the dike (for instance, at the edge of a magma reservoir).

3. We compute σ_3 and $\vec{v_3}$ at F_0 and identify the local surface Σ perpendicular to $\vec{v_3}$. The dike is then defined as a penny-shaped crack of radius c lying on Σ (Figure 3.2a).

4. We generate a ring of n regularly-spaced observation points O_i, $i = 1...n$ along the dike tip-line (Figure 3.2b).

5. We calculate σ_3^i at each O_i and use it to calculate $\Delta\gamma$ for every point on the dike tip-line as:

$$\Delta\gamma_i = \frac{(\sigma_3^i - \sigma_3^j)}{2c} - \rho_m g \frac{(z_O^i - z_O^j)}{2c}, \tag{3.7}$$

where z_O^i, z_O^j are the vertical coordinates of points O_i, O_j, with O_j antipodal to O_i.

6. We calculate K^i at each O_i according to Equation 3.6 and determine the point F_1 where $K^i = K^{max}$. This will identify the direction of propagation of the dike (Figure 3.2b). Such direction coincides with that of the maximum pressure gradient across the plane of the crack. Note that negative K are always predicted at some O_i and imply unrealistic interpenetration of the crack faces. This poses no issue, however, since we are only interested in finding K^{max}.

We reiterate the previous steps taking F_1 as the current F_0 and produce a chain of points identifying the trajectory of the dike. The dike stops once at least one of the observation points generated in step 3 reaches a minimum distance threshold (MDT) between the observation points and the mesh, in order to prevent artifacts singularities in the stress calculations. This is a characteristic issue of BE models, and can be mitigated with finer meshing (Slim et al., 2015). Here we fix the MDT to 800 m away from the nearest BE, as this is the average size of the dislocations of the mesh we employ. Dikes may be propagated past their F_A until they hit the surface at a 'projected' arrival point, F_A^P, assuming that they maintain the dip and strike calculated at F_A (Figure 3.2b). This is akin to assuming that dikes do not have the space to adjust to the local stress field in the last $\sim$1 km before reaching the free surface. Moreover, a SAM dike is forced to stop if the trajectory becomes horizontal, or if the difference in the strike and dip angles between the current direction of propagation and the one at the previous step is larger than a given threshold. This prevents abrupt turning of the dike pathways.

SAM trajectories depend on two parameters, c and n. We found that values of n equal or greater than 12 lead to nearly identical dike pathways; we set n to 12 in all scenarios calculated later. In contrast, different c lead to different trajectories and arrival points for the same starting points and stress field. Large c (e.g. > 2 km if the dike starting point is 10 km deep) sample the stress field in too few points and approximate $\Delta\gamma$ too coarsely to produce accurate trajectories, while very small c (e.g. < 50 m for the starting depth mentioned above) follow principal stress directions nearly point-wise, but are more computationally expensive. We show later how c may be calibrated to better match a more sophisticated dike propagation model.

SAM also allows for the propagation of anti-buoyant dikes, that is, dikes filled with $\rho_m > \rho_r$ propagating downward through the crust. Dike trajectories, however, cannot be backtracked by simply inverting the density contrast between magma and rocks: an anti-buoyant dike starting from the arrival point of a buoyant one and propagating downward with the same c and n
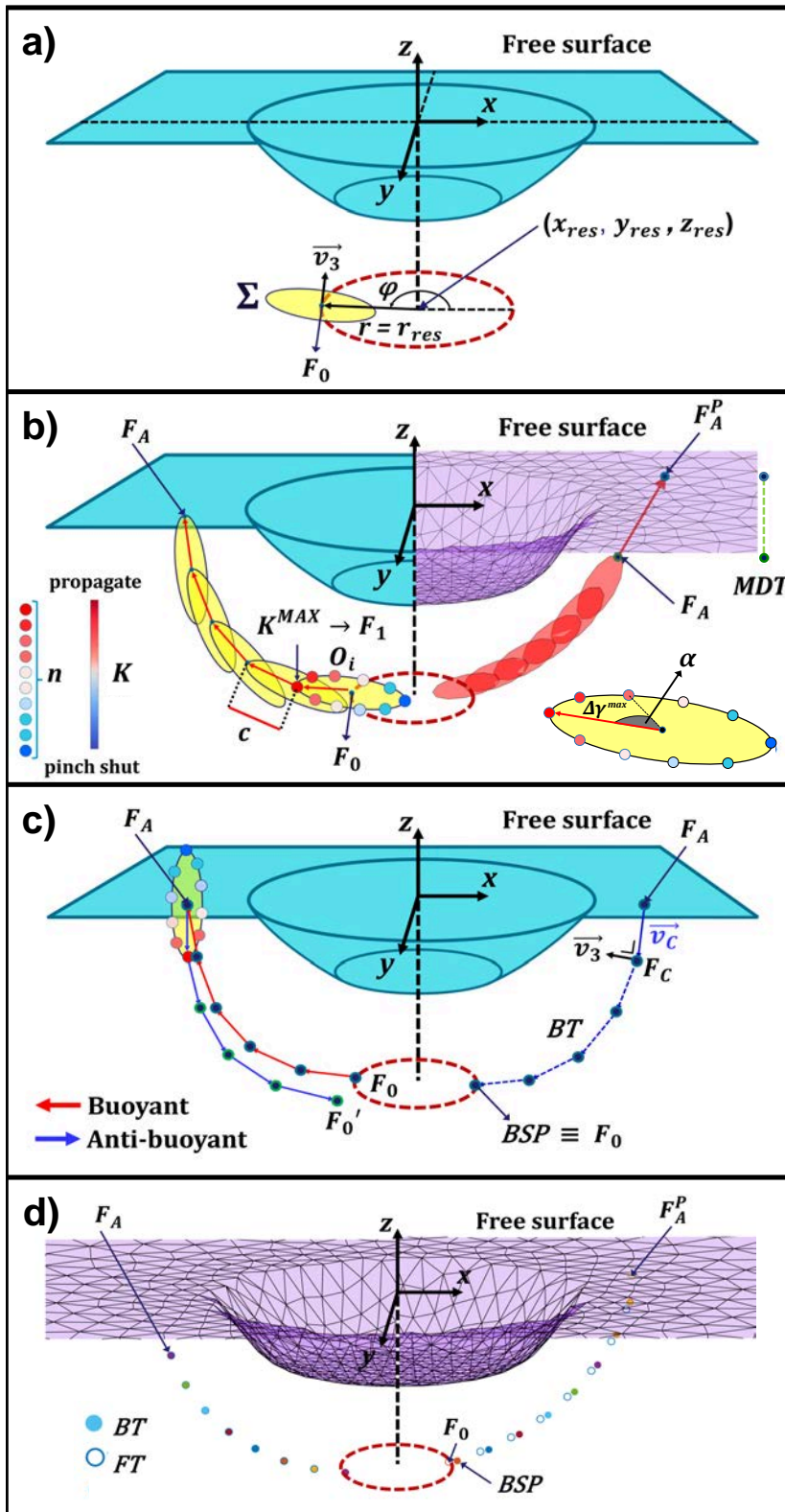
Figure 3.2: Simplified Analytical Model (SAM) framework. a): reference systems employed throughout the work. Blue surface: simplified topography with a circular caldera. Red dotted line: edge of a magma storage region where the dike departs. Yellow surface: dike's initial surface (Σ). b): Left: full SAM trajectory. Colored dots: observation points O_i; the colors are associated to K according to the colorbar. Right: Boundary Element mesh of the topography (vertically exaggerated) and actual forward trajectory (FT) from scenario 'Circular-Caldera' (Section 3.2.3), extended until the free surface. Green dashed line on the right: minimum distance threshold. Bottom-right corner: O_i, direction of $\Delta\gamma^{max}$ (red arrow) and angle α away from $\Delta\gamma^{max}$ as defined in Equation 3.5. c): Backtracking of SAM trajectories. Left: comparison between buoyant (red) and anti-buoyant (blue) trajectories. Right: representation of the backtracking algorithm outlined in Section 3.2.2.1. d): Backtracked trajectories (BTs) of the FT shown in (b). Left: BT starts from the actual arrival point. Right: BT starts from the projected arrival point. Colored dots on both sides represent the BTs; empty blue dots the original FT.

will not pass through the same points (see Figure 3.2c), even if the difference between forward trajectories (FTs) and backtracked trajectories (BTs) decreases for smaller values of c.

We backtrack FTs, from known arrival points F_A and with assumed parameters c_B and n_B, as follows:

1. Starting from F_A, we find a candidate point B_C at a distance c_B such that the scalar product between $\vec{v}_3$ at B_C and the vector $\vec{v}_C$ pointing from B_C to F_A is minimal (Figure 3.2d).

2. We run one step of the forward model from B_C and calculate the vector between the predicted and actual F_A; we then shift B_C by that same vector and iterate this procedure until the desired precision is attained. B_C is taken as the first point B_1 of the BT.

3. The algorithm stops as soon as a specific requirement is satisfied: for instance, the current B_j falls within the known magma storage region. The lastly-recovered point of the BT becomes then the "backtracked starting point" (BSP) (Figure 3.2d).

The first step of the algorithm is modified when starting from a point F_A^P lying on the free surface, as we no longer fix the distance between B_C and F_A^P to a specific c_B, but let it vary over a specific range (for a FT with given c, we find a 0-3c range enough for our purpose).

We tested the method against known FTs, and found that it is able to retrieve each F_0 within a range of a few tens of meters ($\sim$0.2-0.5% of a 6-km caldera radius) if starting from F_A, and a few hundreds ($\sim$2-5% of the same caldera radius) if starting from F_A^P, provided the same radius c of the forward model is employed ($c_B = c$). If that is not the case, the distance between actual and backtracked starting point ($\Delta_{BSP} = |F_0 - BSP|$) increases with the difference between the backtrack radius c_B and c.

3.2.2.2 Three-dimensional Intrusion Model (TIM)

We later validate SAM against the full-3D numerical dike propagation model by Davis et al. (2020) and Davis et al. (2021). The model needs the dike volume (V), assumed constant during the propagation. Here, the dike starts as a penny-shaped crack centered at a specific starting point and arranged according to a starting dip and strike; these can be either arbitrary or coincide with the local $\vec{v}_3$. The dike starting radius is taken as $c_0 = \sqrt{V/1.6\pi}$. The dike is meshed, and R_K is computed at every tip-line BE (Davis et al., 2019); the tip-line is advanced or retreated by an amount proportional to the local R_K, depending on its sign, and the crack is remeshed. The crack can also bend out of its plane according to the maximum circumferential stress criterion (Pollard et al., 2005; Davis et al., 2021). The dike can thus advance along complex trajectories and change its shape in the process. We refer to this model as 'Three-dimensional Intrusion Model' (TIM).

TIM relies on finer discretization (at the scale of individual BEs) when calculating K. Comparing the two models is therefore critical to verify the validity of the approximations in SAM, especially at shallow depths, where even minor topographic features have a non-negligible influence and lead to more heterogeneous stress gradients (see Section 3.2.1).

Before comparing TIM and SAM trajectories, we illustrate how to combine the stress and dike models introduced so far into synthetic scenarios of dike propagation.

3.2.3 Configuration of the dike propagation scenarios

We produce a total of nine synthetic scenarios (Tables 3.2 and 3.3). We first generate a stress model, evaluating which stress mechanisms are most relevant. Here, as discussed in Section 3.2.1, we limit our analysis to tectonic stresses and gravitational loading/unloading.

We consider increasingly complex topographies with a caldera located at the origin of the Cartesian reference frame (see Figure 3.2a). We employ four main topographic settings, each used in one or more scenarios:

- Setting 1: a flat topography with a circular caldera of radius $R_C = 6$ km and maximum depth $d = 500$ m. The depth of the caldera, which has steep slopes and a flat floor, varies with r according to:

$$z = -d \exp\left(-r^6\right) \tag{3.8}$$

- Setting 2: we add a coastline, modeled as a steep elevation step along the y-axis. In this way, we break the axial symmetry of the previous setting. The bathymetry lies 100 m below the datum level. The caldera has $R_C = 6$ km, $d = 450$ m, and depth varying with r as in (1).

- Setting 3: we maintain the bathymetry of (2), but we include two hills (heights 791 m and 355 m, base diameter $\sim$15 km). The caldera has $R_C = 6$ km and $d = 424$ m. The caldera shape is made irregular by adding Gaussian noise to Equation 3.8. In one scenario we model a topography evolving from (3) to (3b), where the caldera is partially refilled, its maximum depth changing to $d = 221$ m. This setting is inspired by the morphology of Campi Flegrei caldera.

- Setting 4: an elliptic caldera with $d = 150$ m, semi-major and semi-minor axes $a_C = 8$ km and $b_C = 4$ km, respectively. A circular resurgent dome with $h = 150$ m and 4.8 km diameter is located 3 km offset from the caldera center. The external topography has some gently-sloping hills (the maximum height is 157 m), but no bathymetry. This setting is inspired by the morphology of Long Valley caldera.

We calculate the gravitational loading/unloading as described in Section 3.2.1, using $E = 15$ GPa, $\nu = 0.25$ and setting ρ_r as in Table 3.3. Then, we superimpose to the resulting stress field the tectonic stress components σ_{ij}^T, different for each scenario.

Next, we choose a model of dike propagation and define the needed input. TIM needs dike volumes (V^k), magma densities (ρ_m^k), K_C of the host rock and a starting geometry for the k-th dike. We use $K_C = 70$ MPa·m$^{1/2}$. Starting dike radii (c_0^k) are determined by V^k (see Section 3.2.2.2 and Davis et al., 2021). SAM needs c and ρ_m.

We use the first three scenarios, 'Vertical-TIM', 'Lateral-Dike', and 'Complex-Coastline', to compare the performance and features of TIM and SAM. In the additional six scenarios, we produce only SAM dike pathways with fixed $c = 1.2$ km and $\rho_m = 2300$ kg/m^3. We start with the most simplified topography ('Circular-Caldera'). Then, we progressively add new elements, such as a coastline ('Simplified-Coastline', 'Tectonic-Shear'), hills and caldera refilling ('Refilling-Caldera', 'Two-Reservoirs') and a resurgent dome ('Elliptic-Caldera'), studying their impact on dike trajectories. In three scenarios, the arrival points of SAM dikes are projected past the MDT to the free surface (see Section 3.2.2.1). All scenarios involve tensional stresses, whose principal axes coincide with the coordinate axes except for Tectonic-Shear (Table 3.2).

We fix the location, depth (z^{res}) and radius (r^{res}) of the magma reservoirs, which constitute the rock volumes where dikes depart from. We remark that here the reservoirs have no contribution to the stress field. All magma reservoirs are circular, sill-like and centered at the origin of the reference frame. In Elliptic-Caldera, however, we consider a vertically-elongated reservoir centered below the summit of the resurgent dome.

The number of simulated dikes (N) varies among the scenarios (Table 3.2). Dike starting points are described by depth z_0^k, radius $r_0^k = r^{\text{res}}$ and angle ϕ_0^k, $k = 1,...,N$, according to the

Table 3.2: Modeled scenarios. Columns are: chosen setting, number of SAM dikes (in parentheses, number of those reaching the MDT), caldera depth, resurgent dome height, tectonic stress components, host rock and reservoir parameters for each scenario. SAM, Simplified Analytical Model; MDT, minimum distance threshold.

Scenario	Setting	N		d	h	σ_{xx}^T	σ_{yy}^T	σ_{xy}^T	ρ_r	r^{res}	z^{res}
				m	m	MPa	MPa	MPa	kg/m^3	km	km
Vertical-TIM	1	2	(2)	500	-	1	0	0	2500	6	-6
Lateral-Dike	3	1	(0)	424	-	1	0.4	0	2800	10.2	-6
Complex-Coastline	3	9	(9)	424	-	1	0.4	0	2800	3	-6
Circular-Caldera	1	12	(12)	500	-	1	0.5	0	2500	2	-6
Simplified-Coastline	2	24	(20)	450	-	1	1	0	2500	2	-6
Tectonic-Shear	2	20	(10)	450	-	0.8	0.8	-1	2500	2	-6
Refilling-Caldera	3-3b	20	(15)	424	-	1	0.4	0	2800	3	-4
		20	(19)	221							
Two-Reservoirs	3	50	(39)	424	-	1	0.4	0	2800	3	-4
										6	-8
Elliptic-Caldera	4	30	(26)	150	150	1	0.6	0	2500	1	-6

cylindrical reference frame in Figure 3.2a. In the most simplified scenarios, we assume equally-spaced starting points for dikes. In the most complex scenarios, we randomize the starting points by drawing ϕ_0^k from an uniform distribution. Starting depths coincide with the depth of the magma reservoir ($z_0^k = z^{res}$), with two exceptions. In Two-Reservoirs, we consider two different starting depths, with the aim of representing two separate magma storage volumes. In Elliptic-Caldera, we draw z_0^k from a Beta distribution (e.g. Johnson et al., 1994) skewed towards the top of the reservoir (see Figure 3.5f). This is to simulate a case where dike nucleation probability may change with depth.

3.2.4 SAM and TIM comparison

We now proceed to validate SAM against TIM to assess under which conditions the two models produce matching dike pathways. We use Vertical-TIM, which offers the simplest topography, and Lateral-Dike, which offers the most complex one, to compare TIM and SAM pathways under different starting conditions and settings. Then, we use Complex-Coastline to calibrate c in SAM.

If TIM dikes start misoriented with respect to the external stress field, they can progressively adjust to it as they advance, while SAM dikes start and remain perpendicular to $\vec{v_3}$. This can lead to discrepancies between SAM and TIM dike pathways. We show this in Vertical-TIM (Figure 3.3a), where three vertically-oriented TIM dikes with different volumes (V^k) and starting radii (c_0^k) and two SAM dikes with different c propagate from the same starting point and with the same ρ_m (Table 3.3). In Figure 3.3a, TIM and SAM dikes first diverge, and later become roughly parallel, as TIM dikes adjust to the stress directions. Dikes with larger volumes require larger distances to do so, as already captured by 2D models (Dahm, 2000a; Maccaferri et al., 2010, 2019). We also notice how the SAM dike with the smallest c follow the stress field more closely.

In Lateral-Dike we show a situation where SAM captures 3D propagation as well as TIM. We run a TIM dike starting beneath a topographic high, and compare it to a SAM dike with radius $c = 1.2$ km starting from the same point. In this model, we set both dikes to be weakly buoyant ($\rho_r - \rho_m = 100$ kg/m³) and start aligned to the local stress directions. In these conditions (Tables 3.2, 3.3), they both propagate laterally along similar trajectories, as dictated
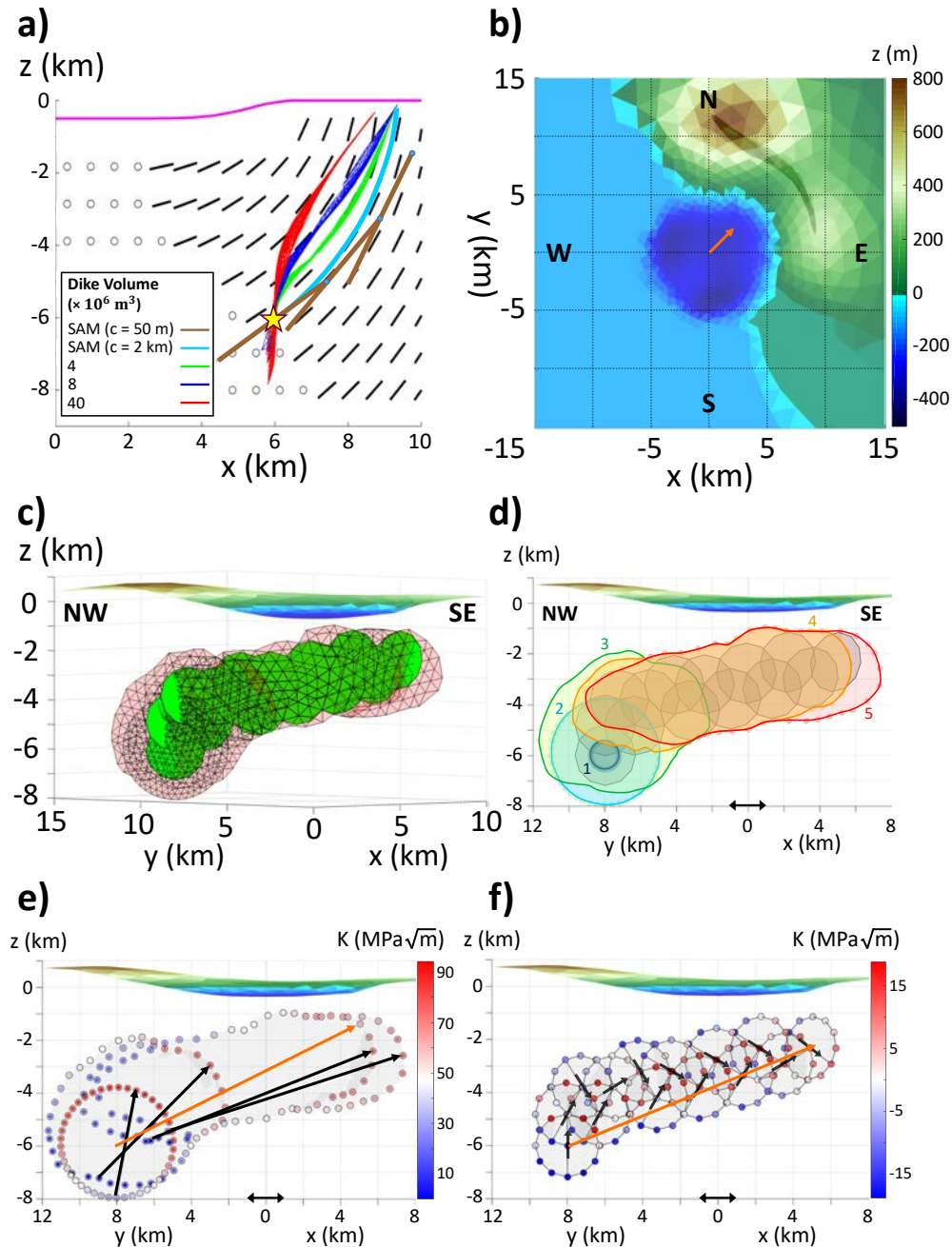
Figure 3.3: TIM and SAM comparison. a): Vertical-TIM scenario: two SAM dikes with different c are compared to three TIM dikes with the same magma density and increasingly larger volumes. All dikes start from $x = 6$ km, $y = 0$ km, $z = -6$ km; TIM dikes are vertically-oriented at the starting point. TIM pathways are shown as meshes representing steps in dike propagation, including starting and final configuration of dike. Black segments show $\vec{v}_1$ projected over the x-z plane; black circles represent out-of-plane $\vec{v}_1$. Topography is represented as a magenta line. Blue dots mark the actual trajectory of SAM dike with largest c. b): Lateral-Dike scenario: top view of topography of Setting 3, with TIM and SAM dikes propagating laterally beneath a topographic high. Both dikes start from $x = 2$ km, $y = 10$ km, $z = -6$ km, aligned to local $\vec{v}_3$. Color scale of topography is common throughout the Figure. c): NW-SE view of (b) looking from the direction shown in (b) as an orange arrow. TIM dike represented as superposition of red meshes from five steps in the dike simulation, from start to end. Each step of SAM pathway is a green circle. d): Outlines of the five steps of TIM pathway shown in (c). SAM cracks are superposed in gray. e): Values of K computed along tip-line of TIM meshes, as well as K gradient directions for each step (black) and K gradient direction averaged over whole pathway (orange). Step 1. in (d) not shown here. f): Values of K computed at observation points along tip-line of SAM cracks, as well as K gradient directions for each step (black) and K gradient direction averaged over whole pathway except for last step where dike stops (orange). For host rock and magma properties see Table 3.3.
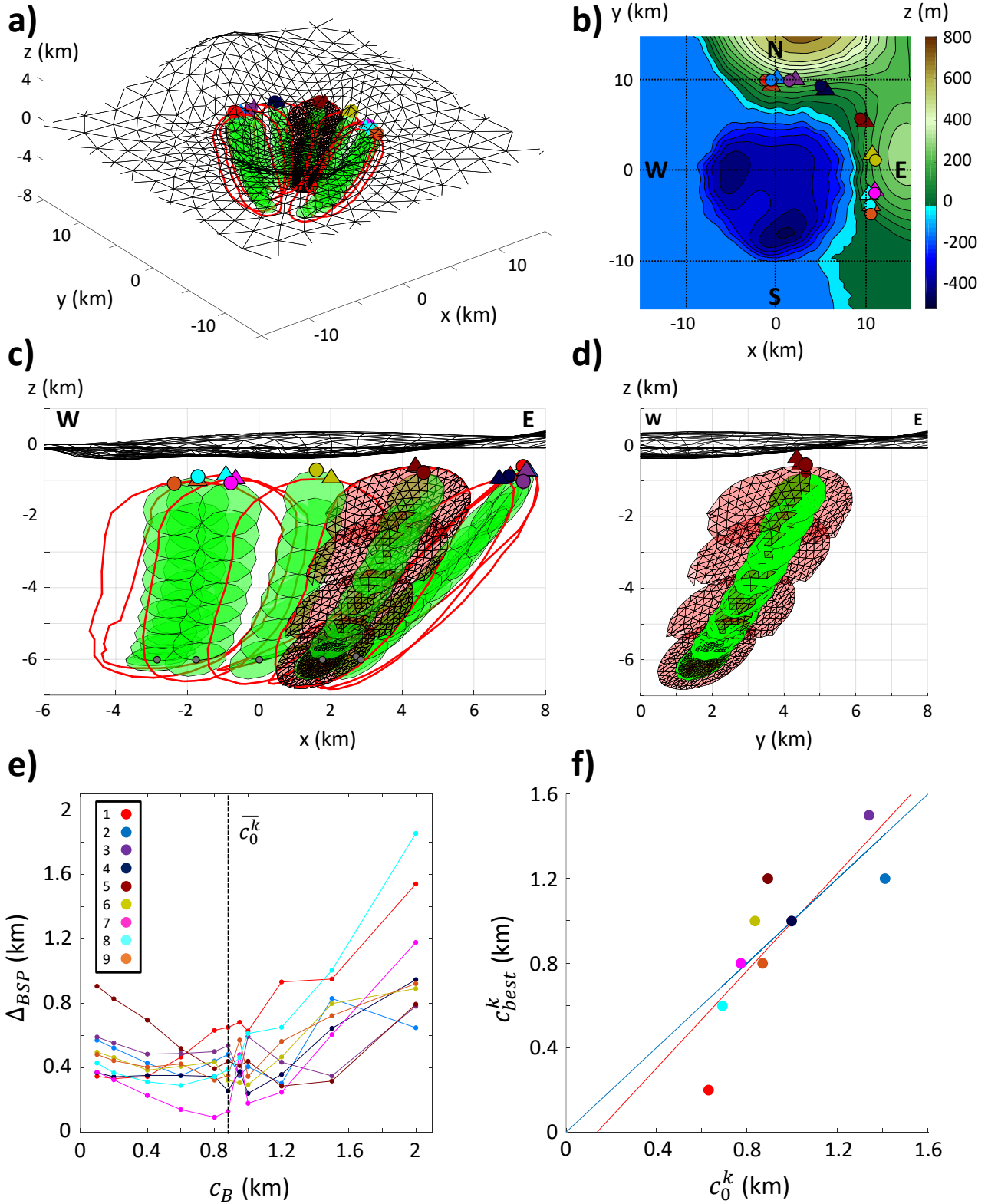
Figure 3.4: Complex-Coastline scenario. a): synthetic topography with a vertical exaggeration factor of 5, dike pathways (green for Simplified Analytical Model (SAM), red outlines for Three-dimensional Intrusion Model (TIM)) and and arrival points of TIM (triangles) and SAM (dots) dikes. b): elevation map and arrival points. c): W-E view of TIM and SAM pathways, dike starting (gray dots) and arrival points. d): detail of TIM and SAM pathways for the fifth dike. e): SAM backtracking method applied to TIM pathways; distance between the actual and backtracked starting point Δ_{BSP} versus c_B (see Table 3.1). Black dotted line marks the average of c_0^k of TIM dikes. Colors are the same of TIM and SAM arrival points in (b) and (c), and numbers in the inset follow the order of Table 3.3. f): c_{best}^k: c_B yielding the smallest Δ_{BSP} versus starting dike radius for each dike. The red line fitting the data is compared to the bisector (blue line).

Table 3.3: Parameters of Three-dimensional Intrusion Model dikes.

Dike	V_k $\cdot 10^6$ m^3	c_0^k km	ρ_m^k kg/m^3
Vertical-TIM			
1	4	0.89	2300
2	8	1.26	2300
3	40	2.82	2300
Lateral-Dike			
1	4	0.89	2700
Complex-Coastline			
1	2	0.63	2300
2	10	1.41	2250
3	9	1.34	2100
4	5	0.99	2280
5	4	0.89	2350
6	3.5	0.83	2300
7	3	0.77	2270
8	3.8	0.87	2390
9	2.4	0.69	2300

by the external stress and the low magma buoyancy: such behavior may not be captured by 2D dike models. In Figure 3.3e,f we observe that K values in SAM can be very different from the ones in TIM, and the SAM dike follows a longer, zigzagging pathway. This is due to the large c employed, which makes the dike advance too far to capture at each step the heterogeneity of the pressure gradient. Notwithstanding these differences, the overall directions of the pressure gradient (orange arrows in Figure 3.3e,f) are consistent, and the dikes follow each other closely even at shallow depths. In a test not reported here, we run the same scenario with a larger magma buoyancy ($\rho_m = 2300$ kg/m^3), and both TIM and SAM dikes ascended towards the free surface instead of propagating laterally. This shows how accounting for the magma buoyancy force in SAM makes it different from a simple '3D streamline' approach, as SAM dikes do not necessarily follow $\vec{v}_1$.

In Complex-Coastline (Figure 3.4a,b,c,d), we study a case where TIM dikes start optimally-oriented (i.e. perpendicular to $\vec{v}_3$). We run nine TIM dikes with different V^k, c_0^k and ρ_m (Table 3.3), and compare them to forward SAM trajectories. Despite the V^k, c_0^k and ρ_m^k being different from one dike to another, the arrival points and final orientations of the SAM dikes are consistent with the outcomes of the TIM dikes, and SAM trajectories follow closely TIM ones. Such match is closest when we take $c = \bar{c}_0^k$, that is, the average of the c_0^k (Figure 3.4c).

In order to refine our calibration of c, we perform a comparison between TIM dikes and backtracked SAM dikes, evaluating how accurately their starting points are recovered with different values of backtrack radius c_B (Figure 3.4e,f). We find that the performance of our backtracking method in recovering the SP of the TIM dikes depends on the c_B we employ (see Table 3.1 for abbreviations). Both large (> 1.2 km) and small (< 0.6 km) c_B perform poorly. On the other hand, the distance between SP and BSP of each dike, Δ_{BSP}, is smallest for c_B equal or close to $\bar{c}_0^k = 880$ m (black vertical line in Figure 3.4e). The minimum of Δ_{BSP} for all dikes except for the one with the smallest V^k (Table 3.3) is found in the range 600 m $\leq c_B \leq 1$ km. A plot of c_0^k versus c_{best}^k, that is, the c_B leading to the most accurate BSP for the k-th dike, shows that the best-fit line comes close to the bisector of the quadrant and, thus, $c_B = c_0^k = \sqrt{V^k/1.6\pi}$ provides a good estimate for the optimal radius c in SAM

(Figure 3.4f).

In summary, SAM provides trajectories close to TIM dike trajectories only when the latter are well-oriented within the external stress field. In that case, the two models compare well even if the predicted values of K are very different. The optimal c for SAM may be chosen on the basis of the volumes of TIM dikes. The implication is that, in a real scenario, knowledge on the volume of actual dikes could inform the choice of c for both forward and backward SAM. We add that, in Lateral-Dike, the running time of one step of SAM is ~ 100 times faster than that of one step of TIM.
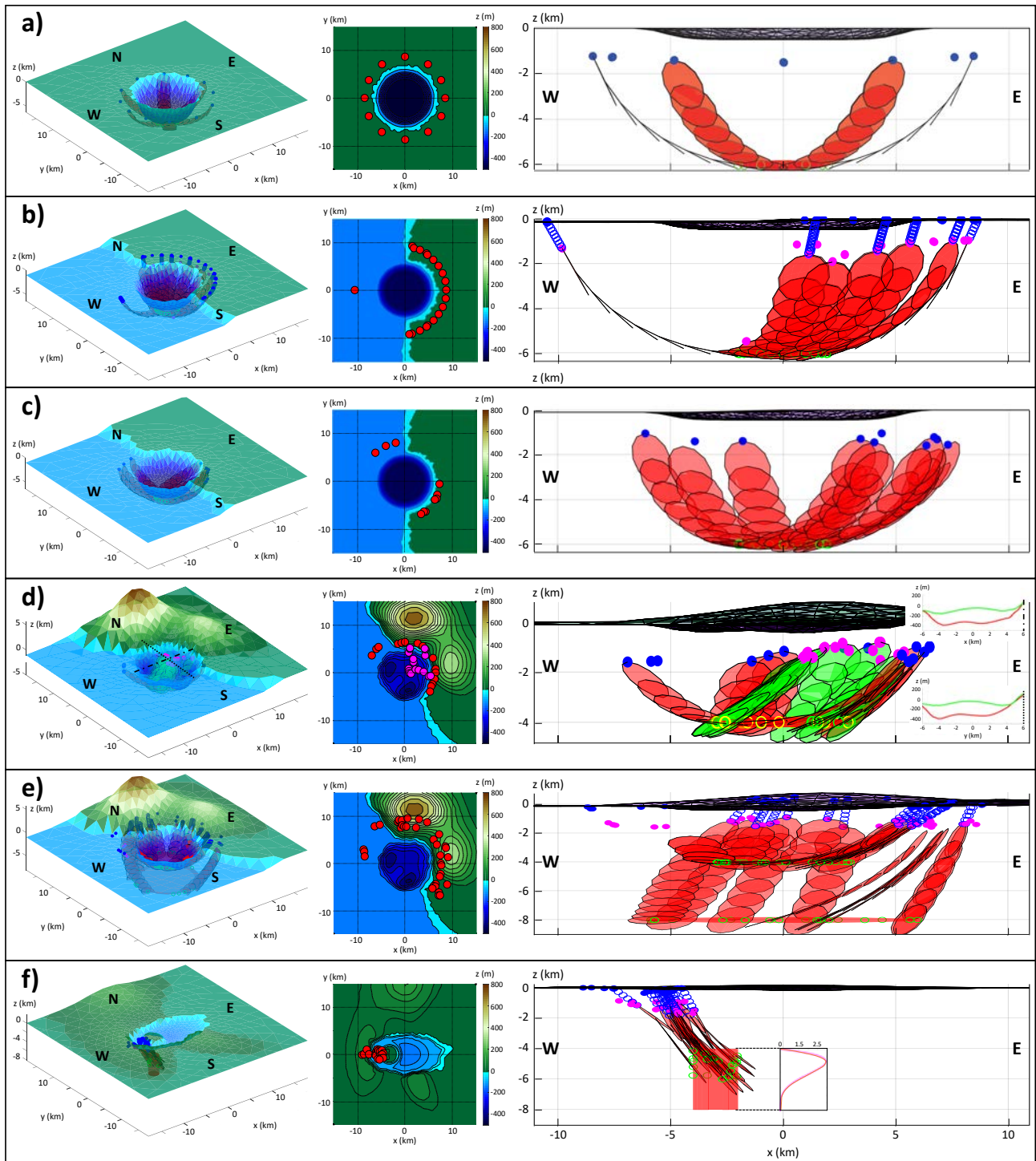
Figure 3.5: Topography and selected Simplified Analytical Model dike trajectories for Circular-Caldera to Elliptic-Caldera scenarios. Left panels: synthetic topography and dike trajectories; central panels: elevation map and dike arrival points; right panels: W-E view of topography and dike trajectories. One out of two trajectories is shown for all scenarios, but all arrival points are displayed. a): Circular-Caldera. b): Simplified-Coastline. c): Tectonic-Shear. d): Refilling-Caldera: in left panel, both original and updated synthetic topographies are shown, with two cross-sections along x (dots and dashes) and y (fine dots) axes. Red dike trajectories are run with original topography, green ones with updated topography. In right panel, topographic profiles along respective cross-sections show original (red) and updated (green) topography. Magenta dots mark arrival points of dikes run with updated topography. e): Two-Reservoirs. f): Elliptic-Caldera: insets in right panel show the Beta distribution z_0^k are drawn from. General conventions as follows. Topography in left panels has a vertical exaggeration factor of 5. Dike starting and arrival points are represented as green circles and blue dots (red in elevation maps), respectively. In right panels of (b), (e) and (f), dike arrival points are magenta dots and blue circles are steps of projected dike trajectories to the free surface. Magma reservoirs: light-red volumes. Large-size versions of each panel may be found in Mantiloni et al. (2023b).

3.3 Results

In the simplest model (Circular-Caldera, Figure 3.5a), dike trajectories are deflected by the gravitational unloading associated to the caldera, and their arrival points punctuate its rim. The tectonic extension is higher along the x-axis, and this leads to the spacing between neighboring arrival points becoming smaller when closer to that axis, even if the starting points are equally spaced.

In Simplified-Coastline, the presence of a coastline between two flat regions at different heights has an evident impact on dike trajectories, which are still deflected away from the caldera, but end up mostly on the mainland (Figure 3.5b). Only the dike starting farthest away from the mainland manages to reach the sea floor. In particular, there is a concentration of arrival points close to the coastline. The effect of deviatoric tectonic stress is most apparent in Tectonic-Shear (Figure 3.5c). Here, the least-compressive principal tectonic stress axis roughly strikes along the bisector of the second and fourth quadrants (NW-SE). Arrival points cluster about such axis, both on the mainland and on the sea floor.

Caldera refilling and the presence of a resurgent dome cause an inward shift of dike trajectories. In Figure 3.5d (Refilling-Caldera), green dikes are still deflected by the caldera unloading, but all reach the surface along or within the caldera rim, some ending up on the resurgent dome. Topographic loads outside the caldera tend to attract dikes from both red and green sets.

Dikes departing from deeper storage regions, as in Two-Reservoirs (Figure 3.5e) show the same pattern as in the previous scenarios, reaching the surface farther away from the caldera.

Dikes in Elliptic-Caldera (Figure 3.5f) feel the competing influence of the elliptic caldera and the loading due to the resurgent dome and the hill west of the caldera. The synthetic vents cluster in two areas, the larger adjacent to the dome and the minor close to the caldera rim and the hill. No vents are present at the top of the dome.

In most scenarios, many dikes stop before reaching the MDT (Table 3.2) when the interplay between the buoyancy force and the external stress gradients is no longer sufficient to drive the dike upward. Dike arrest is often associated to gravitational loading (topographic highs): in Refilling-Caldera and Two-Reservoirs, most dikes ascending below the highest hills stop before reaching the MDT. This is consistent with the outcome of Lateral-Dike (Figure 3.3c,d), where both TIM and SAM dikes stop ascending and propagate laterally beneath a topographic load before stopping.

In summary, topography plays a dominant role in controlling dike pathways in our scenarios. Even relatively small topographic features, such as the ∼5-km-wide resurgent dome in Elliptic-Caldera (Figure 3.5f), influence close trajectories over a distance comparable to their width. In all scenarios, dikes are consistently deflected away from surface unloading and attracted by surface loading. Tectonic stress also influences dike orientation and clustering of arrival points, with a more evident impact in the simplest scenarios (Circular-Caldera, Simplified-Coastline, Tectonic-Shear).

3.4 Discussion and Conclusions

We have shown how our newly-developed 'elementary' dike propagation model (SAM) well reproduces trajectories calculated with a sophisticated numerical model (TIM) by Davis et al. (2020, 2021) (Figures 3.3b,c,d, 3.4), and can effectively model 3D dike pathways in synthetic calderas with tectonic stress and mild surface loading/unloading (Figure 3.5). In particular, SAM and TIM trajectories are similar if TIM dikes start optimally-oriented to the external

principal stress directions (Figure 3.3a), since SAM dikes are always oriented perpendicularly to the local $\vec{v_3}$. Moreover, if stresses change over a distance smaller than c, the calculation of the pressure gradient (Section 3.2.2.1) and, consequently, SAM trajectories, will be more approximated. Large c values, however, are still reliable in our scenarios, since loads/unloads with large horizontal extent (> 5 km) cause smoothly-changing stresses at the scale of most SAM dikes shown here (see Section 3.2.1). Loads/unloads of small extent (< 1 km) would cause rapidly-changing stresses at that same scale, but their effect is significant only at shallow depths and can be neglected here, as we stop dikes at the MDT (Section 3.2.2.1). In this regard, fixing the MDT determines what topographic details are worth considering in our models. Dike propagation in both models is controlled not only by the gradients of external stress, but also by magma buoyancy. SAM is also able to backtrack dike trajectories from a vent to the magma storage region.

Due to our simplifying assumptions, our models have many potential limitations. The assumptions include homogeneous elastic parameters for the host rock. Rigidity and density layering may substantially affect dike propagation. For instance, dike trajectories can be deflected when crossing interfaces between layers with strong rigidity contrasts, as shown in 2D by Maccaferri et al. (2010). Further studies are needed to grasp the effects of layer interfaces in 3D. Nevertheless, as shown by Mantiloni et al. (2021b) through analog experiments, homogeneous models well reproduce the observed pathways provided that 'effective' stress parameters are employed, rather than those actually imposed on the gelatin.

We also assume an elastic medium. Volcanic regions are known to host inelastic processes such as seismicity, damage, thermoplasticity, infiltration of and alteration by hydrothermal and magmatic fluids, that can affect both stresses and dike propagation. In particular, these inelastic processes compete with stress-generating mechanisms by homogenizing stresses (e.g. McGarr and Gay, 1978; Stephansson, 1988; Savage et al., 1992). Repeating magmatic intrusions may also bring the state of stress to isotropic in the long run: since they tend to open perpendicularly to $\vec{v_3}$, the strain they cause tends to bring σ_3 closer to σ_1 (Chadwick and Dieterich, 1995; Bagnardi et al., 2013; Corbi et al., 2015, 2016). Additionally, faulting and earthquakes may dissipate shear stresses over time. In other words, the stress contributions in Equation 3.1 can change or be altered. An accurate calibration of the stress state needs to take into account the relaxation of each stress contribution over time and space, discriminating between stress sources (in particular topography-altering events) that became active at different times. These processes are difficult to constrain and are currently accounted for through rough approximations. For instance, some works set the deviatoric stresses arising from gravitational loading of the edifice to zero (Heimisson et al., 2015; Davis et al., 2021). Corbi et al. (2015) found that superposing the effect of caldera unloading to a volcanic edifice where the state of stress is set to isotropic, rather than fully loaded, better explained the orientation of eruptive fissures at Fernandina, Galápagos. Here we neglected such processes by creating scenarios where dikes propagate below and around a caldera but not within an edifice, as the height of all topographic highs in our scenarios (Section 3.2.3) is lower than or comparable to the MDT (Section 3.2.2.1).

As shown in Figure 3.1c, stress contributions of magma reservoirs are dominant only in the proximity of the stress source. Such effect, nonetheless, can be important in determining nucleation points for dikes (Gudmundsson, 2006; Grosfils et al., 2015), that we do not model precisely here, as well as attracting or repelling incoming dikes if the reservoir pressure is increasing or decreasing, respectively (Pansino and Taisne, 2019).

Stress contributions due to previous large earthquakes may also deviate dikes or arrest their propagation. This has been considered both through theoretical (Maccaferri et al., 2014, 2016) and analog (Le Corvec et al., 2013a) modeling. The fault-generated stresses do not influence dike trajectories significantly unless they come to close proximity (e.g. Maccaferri et al., 2014).

However, Maccaferri et al. (2016) showed how an incoming dike can trigger the slipping of a pre-stressed fault, and be stopped by the resulting compressive stress. Faults and dikes may also interact with each other, for instance alternately accommodating tectonic extension (Gómez-Vasconcelos et al., 2020).

Lastly, the emplacement of dikes affects the local stress field as well, as both analytical (Rubin and Gillard, 1998) and numerical models (Ito and Martel, 2002) have shown. The interaction of dike intrusions can result in the deflection of subsequent dike trajectories (e.g. Takada, 1997; Kühn and Dahm, 2008), and may also dictate the architecture of reservoirs (Kühn and Dahm, 2008; Ferrante et al., 2022). Moreover, the cumulative effect of such interaction can modify the overall stress state (e.g. Cayol and Cornet, 1998).

All these stress sources can be integrated in our models as they stand now. Including stress mechanisms that are not well-constrained, however, ultimately adds more uncertainty to a model rather than improve it.

One major simplification in SAM is that of linear pressure gradients across the plane of SAM cracks (Section 3.2.2.1). SAM, as a simplified model, cannot deal with stresses that are too heterogeneous, although in the example shown in Lateral-Dike (Figure 3.3b,c,d) it well compared to TIM, which can deal with stress heterogeneity at the scale of the individual triangular dislocations composing the dike meshes. An additional issue, not discussed here, is the potential heterogeneity in the dike internal pressure arising from the viscous flow of magma (Lister and Kerr, 1991) or pockets of bubble-rich magma within the dike (Costa et al., 2009). Non-linear gradients in the internal pressure may affect the direction of propagation of SAM dikes. In this regard, the analytical model by Pollard and Townsend (2018) computes the stress intensity factor at the tip of a 2D vertical crack under arbitrary distributions of normal tractions, and may be used in future works to estimate the error in K when using the linear pressure gradient assumption in SAM.

The outcomes of our synthetic scenarios show that dikes are deflected away from topographic lows (calderas), and attracted by topographic highs (hills, resurgent domes), even small-sized ones (e.g. the resurgent dome in Elliptic-Caldera). This is consistent with previous dike prop-agation and stress models considering topographic loading/unloading (Dahm, 2000a; Roman and Jaupart, 2014; Corbi et al., 2016; Rivalta et al., 2019) and with results from gelatin-based analog models (Gaete et al., 2019; Mantiloni et al., 2021b). The few synthetic scenarios we present here, however, are not designed to reproduce the wide variety of vent patterns observed at real calderas. They do, nonetheless, reproduce some common features of vent distribution in calderas. When a coastline is involved in our scenarios (Figure 3.5b,c,d,e), most or all dikes end up on the mainland. This is compatible with vent patterns in similar natural settings, such as Campi Flegrei (Smith et al., 2011) or Aira caldera, Japan (Geshi et al., 2020). In our tests, no dike trajectories end up within the caldera, except in Refilling-Caldera and Elliptic-Caldera. Cases where past eruptive vents lie predominantly at or outside the caldera rim include most Galápagos volcanoes (Chadwick and Howard, 1991) and Aira caldera, Japan, (Geshi et al., 2020). Vents opening within a caldera can be observed in several other settings, like Newberry caldera, Oregon (MacLeod et al., 1982), Santorini caldera, Greece (Sigurdsson et al., 2006), or Campi Flegrei caldera, Italy (Smith et al., 2011). Intracaldera vent openings are predicted when the caldera is very shallow, unloading is reduced by refilling (Refilling-Caldera), or a resurgent dome is present (Elliptic-Caldera). Nonetheless, these factors are not always associ-ated with intracaldera vents in nature (e.g. no eruptions have occurred at Long Valley caldera's resurgent dome after doming inception, Hildreth, 2004). Applying a model to a real caldera entails a deeper understanding of its evolution, stratigraphy and eruptive history, and requires dedicated work. For this reason, we chose not to apply our models to real calderas in this work, as running our model for a real scenario without a proper calibration of the stress state is no

different than setting up a synthetic scenario with arbitrary stress. The fast dike propagation model we presented here is particularly suited for stress calibration procedures, such as the one by Rivalta et al. (2019). This will be the subject of future work.

Our model does not consider the viscous flow of magma within dikes and, as such, does not model dike velocity. The two approaches may be integrated by combining the pathways predicted by our model with existing models of dike velocity (Pinel et al., 2017; Davis et al., 2023) or growth, such as Zia and Lecampion (2020), introducing a numerical model of propagation of planar 3D hydraulic fractures, or Möri and Lecampion (2022); Pansino et al. (2022). We also remark that different magma compositions may involve large differences in magma viscosity and density, and neglecting the viscous flow may undermine the predictive power of our dike models in case of high-viscosity magmas.

In both SAM and TIM, dikes are assumed to break away from the magma reservoir after nucleation, as dike propagation is entirely driven by external stress and magma buoyancy force. In a more general case, the dike may be coupled to a reservoir, as past dike intrusion episodes have suggested (e.g. Maccaferri et al., 2016; Gudmundsson et al., 2016). The direction of dike propagation, however, may still be controlled by the gradient of internal pressure and external stress rather than the pressure imparted by the chamber, even though accounting for the viscous flow may change that. Analytical models of propagating dikes coupled with a magma chamber (Segall et al., 2001; Rivalta, 2010; Townsend and Huber, 2020) are only available for fixed dike orientations and, as such, cannot be applied to 3D dike trajectories. In our context, increasing the volume of a TIM dike as it advances could be a rough approximation of a dike-magma chamber coupling. Our results from comparing TIM and SAM (Section 3.2.4) suggest that the trajectories would not differ much even for large volumes of TIM dikes, as long as they start aligned to the external stress field (see Figures 3.3a and 3.4a,c). Including dike-reservoir coupling in SAM or TIM, however, requires dedicated work.

In conclusion, we have developed a fast and flexible dike propagation model, complementing the numerical model by Davis et al. (2020, 2021) Stress models, however, are still critical and not yet fully understood. In a real-case application, our scenarios would be the end point of a stress calibration, whereby the stress state of a volcanic region is constrained through a statistical procedure aiming at matching dike simulations with observations, such as past vent locations (Rivalta et al., 2019), orientation of exposed dikes (Maerten et al., 2022) or focal mechanisms (Zhan et al., 2022). Our model is well-suited for such purpose. Once the stress is calibrated, it may be used to perform a long-term forecast on future vent locations, while the more sophisticated model may be employed to produce short-term propagation scenarios for incipient dike intrusions.

Acknowledgments

Data availability statement

The open-source software *DistMesh* is found at http://persson.berkeley.edu/distmesh/. The open-source Boundary-Element tool *Cut&Displace* is found at https://doi.org/10.5281/zenodo.3694164.

The open-source Julia code used for TIM is found at https://doi.org/10.5281/zenodo.4726796 and https://doi.org/10.5281/zenodo.4727208. The code for SAM and the data of the synthetic scenarios are available at https://doi.org/10.5880/GFZ.2.1.2023.001 (Mantiloni et al., 2023b).

Chapter 4

A framework for physics-based forecast of eruptive vent locations in calderas

Abstract

Constraining the crustal stress state of volcanoes is critical to understand many mechanical processes associated with volcanic activity. Dike pathways, in particular, are modulated by the orientation of principal stress axes. Accurate models of dike trajectories rely, therefore, on accurate estimates of stresses in the subsurface. Those same models are also a key element in volcanic hazard assessment, as they may be used to forecast the locations of future eruptive vents. This work develops a framework to constrain the stress state of calderas combining physics-based models of crustal stress and stress-driven dike pathways in three dimensions with a Monte Carlo approach, and using past vent locations as observables. Then, it shows how to employ the retrieved stress state to produce probability maps of future vent opening across a caldera. We test our stress inversion and vent forecast approach on synthetic scenarios, and find it successful to varying degrees. We discuss how the performance of the approach is sensitive to the assumptions in the models and prior information on the model parameters, explore its potential and limitations, and discuss how it may be applied to real calderas.

4.1 Introduction

Volcanoes host a wide range of mechanical processes modulated by stress, from seismicity to the emplacement of magmatic intrusions. The stress in the subsurface of volcanic systems results from the interplay of several mechanisms, such as the gravitational loading due to the progressive accumulation of erupted material (McGuire and Pullen, 1989; Walter et al., 2005; Roman and Jaupart, 2014), the inflation or deflation of a magma reservoir (Muller and Pollard, 1977; Pansino and Taisne, 2019) or the viscoelastic relaxation of overheated rocks (Del Negro et al., 2009; Head et al., 2019). The stress changes induced by such mechanisms trigger seismicity and faulting (e.g. Rubin and Gillard, 1998; Roman and Cashman, 2006). Fluid circulation in hydrothermal systems is also influenced by stresses, as they promote or hinder rock failure and, thus, may change rock permeability (Beeler and Hickman, 2004; Taira and Brenguier, 2016). Hydrothermal activity, in turn, is a significant source of deformation and stress change at many volcanoes (Rinaldi et al., 2010; Fournier and Chardot, 2012; Currenti et al., 2017).

Among the numerous stress-driven and stress-modifying processes, magmatic dikes are especially important in the context of volcanic eruptions. Dike-fed eruptive vents are commonly observed at volcanoes worldwide (Acocella and Neri, 2003; Michon et al., 2015; Patrick et al., 2019b), regardless of whether an open conduit is available (Jónsson et al., 1999; Smittarello

et al., 2022). As widely discussed in previous works (see e.g. Anderson, 1937; Dahm, 2000a; Roman and Jaupart, 2014; Rivalta et al., 2015) and suggested by empirical evidence (e.g. Muller and Pollard, 1977; Gudmundsson, 1995), dike pathways in the subsurface, as well as the orientation of dike-fed fissures, are roughly controlled by the local orientation of the elastic principal stress axes in the host rock. Thus, models of dike pathways rely on accurate models of the stress field (Davis et al., 2020), and modeling the stress state of a volcano with a sufficient spatial resolution might hold the key to forecast where a dike will breach the surface. This would mark an important advance in volcanic hazard assessment, since many models of volcanic hazards, such as lava flows (e.g. Connor et al., 2015; Gallant et al., 2018; Musacchio et al., 2021) and pyroclastic density currents (e.g. Neri et al., 2015; Reyes et al., 2018), rely on the estimate of where future eruptions are more likely to occur (Connor et al., 2015).

Quantifying the stress field in volcanic areas with the sufficient spatial resolution to determine the local curvature of dike pathways is not trivial, as *in-situ* measurements (see e.g. Jaeger et al., 2007, chap. 13.6, 13.7) are typically sparse, and so are stress indicators such as earthquake focal mechanisms (e.g. Roman et al., 2004; D'Auria et al., 2015; Aoki, 2022). Recently, new strategies have been proposed. Rivalta et al. (2019) calibrated the crustal stress of the Campi Flegrei caldera, Italy, so that the location of the magma chambers and the trajectories leading dikes from such chambers to the surface were consistent with the locations of past vents. To do so, they combined a Monte Carlo optimization approach with a physics-based model of stress-driven dike pathways in two dimensions (2D). The optimized parameters were the magnitudes of tectonic extension and the gravitational unloading generated by the presence of the caldera depression. Mantiloni et al. (2021b) tested the strategy further with analog models. They recorded the arrival points of air-filled cracks propagating through gelatin blocks, splitting them into a training and a validation set. They used the former to constrain the stress state within the gelatin through an efficient Markov Chain Monte Carlo (MCMC) approach, minimizing the misfit between arrival points of modeled and observed crack trajectories. Starting points for cracks in the models were fixed *a priori* to the actual ones of the experiments. The forecast approach was then tested on the observed arrivals of the validation set. Dike propagation and stress models, however, were still 2D.

More recently, Maerten et al. (2022) presented a stress inversion strategy for exposed dike distributions in inactive volcanic fields. The strategy constrains tectonic stress and magma chamber overpressure by matching dike trajectories predicted by modeled orientations of principal stresses with those observed from exposed dikes or past eruptive fissures. Their strategy, however, is difficult to apply to active volcanoes, where the pathways of past dikes are not known. Moreover, gravitational loading stresses, which are often found to be dominant in volcanic settings (Roman and Jaupart, 2014; Corbi et al., 2015; Heimisson et al., 2015), were neglected. Zhan et al. (2022) considered focal mechanisms of recorded earthquakes to constrain stress. They modeled the evolving stress field (i.e., the observed rotation of fault plane solutions) during an unrest episode at Augustine volcano, Alaska, using a trial-and-error optimization with a range of three-dimensional (3D) stress models. Such models considered tectonic stress, gravitational loading due to the volcanic edifice and a static dike with fixed size, shape and orientation. As such, they rely on assumptions on one stress source, namely the inflating dike, to constrain the others.

All the stress optimization strategies mentioned so far have the potential to improve our understanding of the stress state in volcanoes. Future advances should combine 3D models with realistic topographies (Zhan et al., 2022) and automated stress optimization frameworks (Rivalta et al., 2019; Maerten et al., 2022), rather than relying on trial-and-error approaches. Rivalta et al. (2019) and Mantiloni et al. (2021b) went a step further and used the results of the stress inversion to make quantitative predictions on the locations of future eruptions.

Moreover, they used only a subset of the available observations to constrain the stress field, and set aside the rest for testing the forecast. However, the strategy of Rivalta et al. (2019) comes with several limitations: most importantly, the stress model was 2D plane strain, and dike pathways were modeled as 2D streamlines perpendicular to the least-compressive principal stress axis (Anderson, 1937). Moreover, dikes were assumed to start at the edge of a sill-like magma reservoir, and the stress optimization algorithm required an extremely large number of stress models and simulations of dike trajectories. Such limitations have hindered the potential of the strategy.

While 3D stress models have been available for decades (e.g. McTigue and Mei, 1987; McGuire and Pullen, 1989), fully 3D models of dike trajectories have been developed only recently by Davis et al. (2020, 2021). A stress optimization strategy, however, requires large numbers of simulations and, therefore, a 3D dike model with minimal computational cost. Such a model was recently developed by Mantiloni et al. (2023a). Other issues, such as how to optimize the parameters of a 3D stress field with realistic topographies, are still unresolved. Another critical point, only hinted by Rivalta et al. (2019), is that gravitational loading/unloading is due to both topography and rock density layering, and a 3D stress optimization needs to constrain both.

In this study, we develop a stress inversion method in 3D that accounts for gravitational loading due to realistic topographies, and allows us to forecast the future locations of vents. First, we describe the information on magma storage and dike nucleation zones in the crust with probability density functions. Then, we backtrack dikes from known vents down through the crust, and optimize the stress model so that the backtracked trajectories intersect the regions of highest melt availability or dike nucleation probability. We eventually calculate forward dike trajectories on the basis of the outcomes of the stress inversion, and produce probability maps of future eruptive vents.

We test our strategy on the synthetic scenarios from Mantiloni et al. (2023a), so that we can explore the performance and drawbacks of the strategy on known settings.

4.2 Methods

4.2.1 Forward and Inverse Problem Formulation

Consider the setting of Figure 4.1a, described in a Cartesian reference frame where the z-axis is positive upward. We observe N vents, V_k, $k = 1, ..., N$, across a volcanic area. V_k are the results of a physical process that leads dikes from a dike nucleation zone, D, to the surface. In nature, eruptions are often initiated with a dike breaching the surface and opening one or more fissures (Reches and Fink, 1988; Muirhead et al., 2016), which may progressively evolve into spatter cones (Ida, 1992; Fukushima et al., 2010; Pedersen et al., 2022). Consequently, defining the location of an eruptive vent as a point in space is a drastic simplification and involves some uncertainty. Here, we take a simplifying assumption and define the vent locations, V_k, as points, with each V_k produced by a different dike. We later discuss how to include both the fissure orientation and the spatial uncertainty on V_k in our method.

Identifying D is also challenging, since it requires both knowledge of where magma is stored in the subsurface, and assumptions on where dike nucleation is more likely to occur. We describe D in terms of a probability density function (PDF) $p(x, y, z)$ such that the probability of dike nucleation in a volume Ω in the crust is

$$\int_\Omega p(x, y, z) dV \tag{4.1}$$
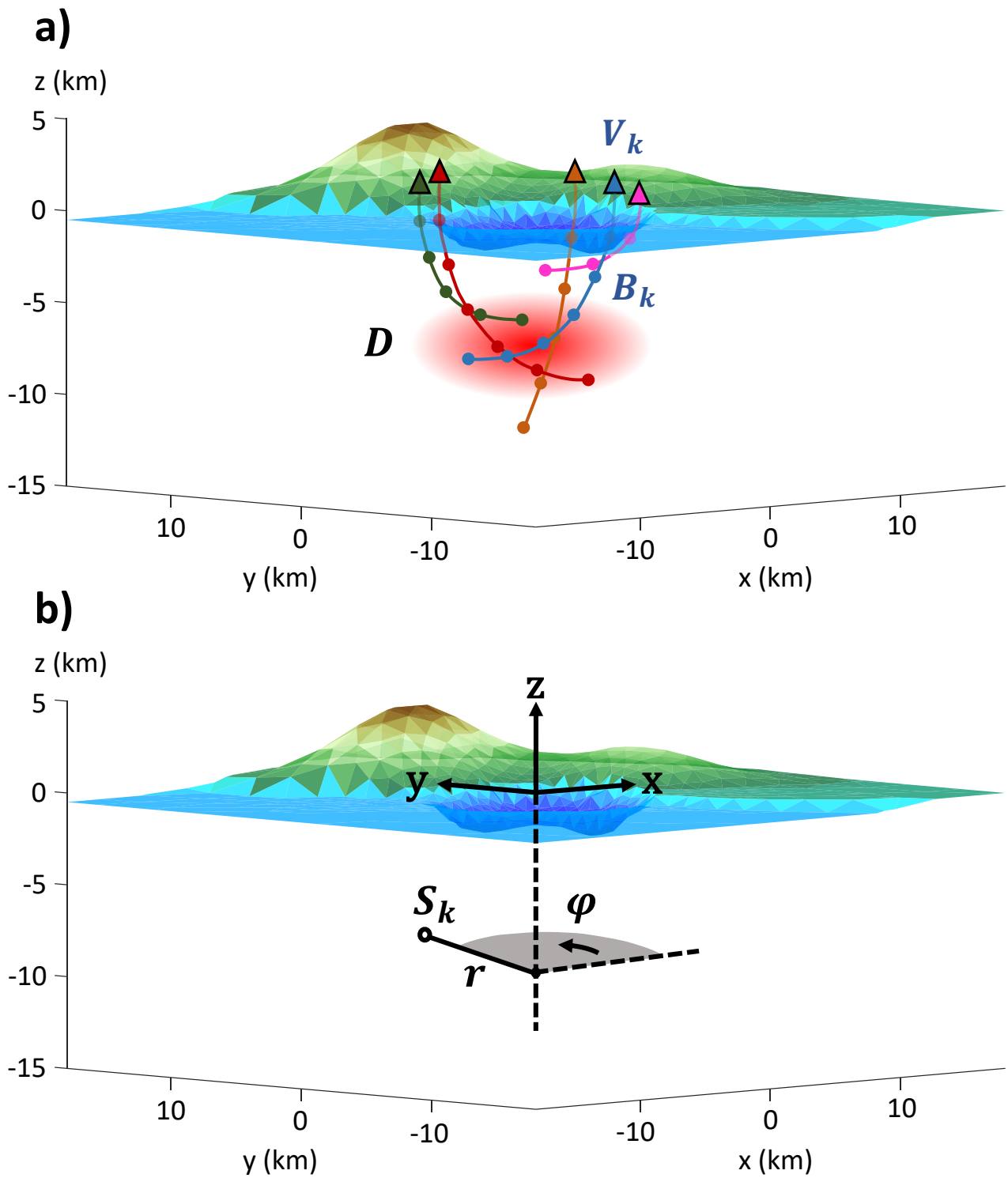
Figure 4.1: Synthetic caldera setting and inverse problem. a): $N=5$ eruptive vents (triangles) with locations V_k, and respective backtracked dike trajectories, B_k (colored curves), crossing the dike nucleation zone, D. D is described by the probability density function p. Red gradients represent the value of p from higher (intense red) to lower (white). b): Cartesian reference frame, with the origin at the center of the caldera, and coordinates r, ϕ of the cylindrical reference frame with the same origin.

where $dV = dxdydz$. We discuss the specific choices of p used in this study in Section 4.2.4.1.

Dike pathways from D to V_k are controlled by the stress field in the host rock. We assume the host rock is homogeneous, isotropic and linearly elastic, with density ρ_r, Young's modulus E and Poisson's ratio ν. We describe the state of stress in the host rock by a stress tensor $\sigma_{ij}(x, y, z)$. Tensional stresses are positive. We refer to the magnitudes of principal stresses, from most compressive to least compressive, as σ_1, σ_2, σ_3, and to the principal stress eigenvectors as $\vec{v_1}$, $\vec{v_2}$, $\vec{v_3}$, respectively.

We consider a model of dike trajectories, controlled by q stress parameters $(\theta_1, ..., \theta_q \equiv \vec{\theta})$ and m dike parameters $(\zeta_1, ..., \zeta_m \equiv \vec{\zeta})$. The model takes a starting point, $S_k \in D$, and calculates a dike trajectory, F_k: a curve that links S_k to the vent location V_k unambiguously:

$$F_k = f(\vec{\theta}, \vec{\zeta}, S_k) : S_k \in D \rightarrow V_k, \quad k = 1, ..., N \tag{4.2}$$

We describe $S_k \equiv (r^k, \phi^k, z^k)$ with a cylindrical reference frame where $r = \sqrt{x^2 + y^2}$ and ϕ is the angle measured on the $x - y$ plane counterclockwise from the positive x-axis, as shown in Figure 4.1b. This describes the direct problem of dike pathways calculation.

The known quantities are generally the vent locations V_k, while the stresses and the starting points S_k are typically unknown. Dike trajectories F_k may be partially known in eroded volcanic systems (e.g. Poland et al., 2008; Roman and Jaupart, 2014) or in few well-monitored dike emplacement episodes (e.g. Sigmundsson et al., 2015; Xu et al., 2016; Davis et al., 2020), but are here treated as unknown. We then formulate the backward problem as:

$$B_k = f_B(\vec{\theta}, \vec{\zeta^B}, V_k) : V_k \rightarrow D, \quad k = 1, ..., N \tag{4.3}$$

that is, we employ a model f_B which backtracks the k-th dike trajectory, B_k, from the vent down through the crust. B_k intersects regions of different dike nucleation probabilities, depending on the model parameters. We aim to optimize the parameters of the model f_B so that B_k intersects the volumes where that probability is highest.

In order to do so, we define $p_k = max[p(B_k)]$, that is, the maximum value of p along B_k. The point of B_k meeting this condition is taken as the 'backtracked' S_k. Then, for N backtracked trajectories from N vents, we calculate the joint probability density $\prod_{k=1}^{N} p_k$. The inverse problem consists in finding the combination of model parameters $\vec{\theta}, \vec{\zeta}$ maximizing the joint probability density. This is equivalent to minimizing a cost function, s, defined as:

$$s = -2 \sum_{k=1}^{N} \log(p_k) \tag{4.4}$$

(see e.g. Laine et al., 2008), where each p_k corresponds to a 'probable' dike starting point, S_k, given a set of stress parameters. Thus, by minimizing s, we constrain both the model parameters $(\vec{\theta}, \vec{\zeta})$ and the coordinates of the dike starting points $(S_k, k = 1, ..., N)$. The solution to the inverse problem we seek, however, is not limited to finding a model that best fits the data. Rather, we adopt a Bayesian approach and aim to sample the parameter space of $\vec{\theta}$ and $\vec{\zeta}$ to recover probabilistic estimates of each model parameter. Such estimates will take the form of PDFs accounting for uncertainties in observations and the model itself.

In the following sections, we describe the stress and dike models, outline the statistical method we use to minimize s, and introduce the synthetic scenarios used to test such a method. We anticipate that, in the implementation presented in this work, we fix the dike parameters $(\vec{\zeta})$ and sample only the distributions of the stress parameters $(\vec{\theta})$. We collect all abbreviations and parameters introduced throughout this work in Table 4.1.

Table 4.1: Abbreviations, symbols and parameters.

Description	Symbol	Units
Abbreviations		
PDF	Probability Density Function	
BE	Boundary Element	
MCMC	Markov Chain Monte Carlo	
General framework		
Coordinates (cartesian)	x, y, z	m
Coordinates (cylindrical)	r, ϕ, z	m,rad,m
Vent locations	$V_k(x, y, z)$	
Number of vents	N	
Dike starting points	$S_k(r, \phi, z)$	
Dike nucleation zone	D	
PDF describing D	$p(x, y, z)$	
Stress parameters vector	$\vec{\theta}$	
Dike parameters vector (forward/backward)	$\vec{\zeta}/\vec{\zeta^B}$	
Dike parameters		
Magma density	ρ_m	kg/m^3
Forward/backtracked dike trajectories	F_k/B_k	
Dike radius	c	m
Backtracked dike radius	c_B	m
Number of observation points along the dike tip-line	n	
Host rock properties and stress field		
Host rock density	ρ_r	kg/m^3
Mode I stress intensity factor	K	Pa$\sqrt{\text{m}}$
Fracture toughness	K_C	Pa$\sqrt{\text{m}}$
Young's modulus	E	Pa
Poisson's ratio	ν	
Stress tensor	$\sigma_{ij}(x, y, z)$	Pa
Principal stress axes	$\vec{v_1}, \vec{v_2}, \vec{v_3}$	
Principal stress intensities	$\sigma_1, \sigma_2, \sigma_3$	Pa
Stress parameters		
Caldera depth	d	m
Resurgent dome height	h	m
Tectonic stress tensor	σ_{ij}^T	Pa
MCMC, p parameters and vent forecast		
Data vector	$\vec{d}$	
Model vector	$\vec{m}$	
Number of MCMC iterations	M	
Proposal distribution	N	
N covariance matrix	Σ_{prop}	
Cost function	s	
p mean vector	$\vec{\mu}$	m
p covariance matrix	Σ	m^2
p shape vector	$\vec{\lambda}$	
Standard deviation	δ	
Number of forecast simulations	M^F	
Vent density	V_D	

4.2.2 Dike Propagation Model

We adopt the 'Simplified Analytical Model', or 'SAM', developed by Mantiloni et al. (2023a), as our forward and backward model of dike trajectories in Equations 4.2 and 4.3. SAM is a simplified but computationally efficient model of dike pathways in 3D, and provides an equivalent to the $\vec{v_3}$-perpendicular streamline approach in 2D (see e.g. Anderson, 1937; Pollard, 1987; Rivalta et al., 2019). SAM is also capable of backtracking dike trajectories from a point, either on or below the surface, down through the crust.

The dike is modeled as a penny-shaped crack with fixed radius c (called 'backtrack radius', c_B, when backtracking trajectories). The crack starts perpendicular to the local $\vec{v_3}$, and remains so along the whole trajectory. The crack advances in the direction of the maximum mode-I stress intensity factor K, computed at n points along its tip-line. K is determined by the gradient of the density contrast between magma and host rock and that of the external stresses, calculated across the plane of the crack (Mantiloni et al., 2023a). Thus, SAM requires a model for the stress field within the host rock, as well as the magma density, ρ_m. The sets c, n, ρ_m and c_B, n, ρ_m constitute the dike parameters $\vec{\zeta}$ and $\vec{\zeta^B}$ in Equations 4.2 and 4.3, respectively. SAM is not equipped to model dike propagation at very shallow depths (≤ 1 km), where inelastic processes (e.g. plastic and poroelastic deformation) might play a significant role. Besides, in the simulations presented here, SAM trajectories are stopped before drawing near the free surface, as clarified later.

We also consider a dike pathway model where the 3D shape of the dike is free to change in response to external conditions and magma pressure. We refer to the model, developed by Davis et al. (2020, 2021), as 'Three-dimensional Intrusion Model', or 'TIM'. TIM dikes have a fixed volume, V, and are represented by a mesh of triangular dislocations (Nikkhoo and Walter, 2015). The meshed crack can start with arbitrary shape and orientation. During propagation, it advances and retreats according to the ratio between K computed at all the dislocations lying on the dike tip-line (Davis et al., 2019) and the fracture toughness of the host rock, K_C. When TIM is used, the set V, K_C, ρ_m constitute the dike parameters ζ_i in Equation 4.2. Although we do not apply TIM in this study, the model was employed in some of the synthetic scenarios by Mantiloni et al. (2023a) which we later use to test our stress inversion.

4.2.3 Stress Model: a Modular Description of Gravitational Loading

The stress model in our inverse problem needs to meet the following requirements: 1) parsimonious, that is, dependent on few parameters that can be effectively constrained with scarce and sparse data; 2) fast and flexible, so that large numbers of stress calculations can be carried out for arbitrary variations of one or multiple parameters; 3) accurate at depth, but not necessarily so near the surface, since we do not model shallow dike propagation.

As a consequence of 1), the stress model needs to capture the dominant stress sources in volcanic systems in the simplest way possible. Tectonic stresses and gravitational loading/unloading are the dominant stress sources in many volcanic regions (see e.g. Roman and Jaupart, 2014; Corbi et al., 2015; Heimisson et al., 2015; Rivalta et al., 2019; Mantiloni et al., 2023a). Following that reasoning, we limit our stress model to these two stress mechanisms. We focus our modeling effort on gravitational loading/unloading, while we assume uniform tectonic stresses throughout the crust.

Gravitational loading/unloading can be broken down to two contributions: one due to the topography, and one originating from layers or inclusions of varying density in the subsurface. In fact, a flat topography having important local shallow density heterogeneities, such as the infill of a caldera, leads to stress heterogeneities in the crust similar to the ones caused by

surface loads. Most models of gravitational loading/unloading can be summarized into two approaches. In the first, positive or negative pressures, standing for the loads or decompression due to a relief or a depression, respectively, are locally imposed on a flat free surface (e.g. Dahm, 2000a; Muller et al., 2001; Pinel and Jaupart, 2004). Surface pressures can be adjusted to account for shallow density heterogeneities (e.g. Maccaferri et al., 2014; Corbi et al., 2015). In the second approach, more sophisticated numerical models consider the real topography and the effect of gravity (e.g. McGuire and Pullen, 1989; Chadwick and Dieterich, 1995; Corbi et al., 2016). Stresses are then calculated both within the topography and in the underlying crust. In both cases, the crust is often assigned a uniform density, although a layered crust can also be considered, at the price of a more complex model.

The two approaches give similar results (e.g. Ferrante et al., 2022). However, the first approach has the limitation that dikes cannot propagate within the topography itself, which is required if we are to backtrack dike trajectories from vents that do not lie on a flat surface. Thus, we adopt the second approach, and modify it in order to account for the often important density heterogeneities in the shallow crust of volcanic areas. This is done by adjusting the height of specific topographic elements in a volcanic area to constrain an 'effective stress model' that includes the effect of local crustal density layering, while assuming a homogeneous density (Figure 4.2a,b). We neglect the effect of large inclusions having different densities, although in volcanic areas they may be present (e.g. Chiarabba et al., 2000; Peacock et al., 2015) and have a significant effect on the stress state.

Consider the example drawn in Figure 4.2a, with a caldera of depth d and density layers within the caldera infill. We can model the combined gravitational loading of the caldera depression and infill through an 'effective topography', by adjusting the current caldera floor according to an 'effective depth' d', while assuming a homogeneous density ρ_r for the whole crust, as shown in Figure 4.2b.

In general, d' is unknown and we aim at recovering it from the stress inversion procedure. The 'effective unloading pressure' of the caldera is then given by $P^U = \rho_r g d'$. The d' we constrain depends on the ρ_r we fix, but different combinations of d' and ρ_r yield the same P^U. At the level of approximation of the stress field that we seek here, we may assume that the shape of the effective caldera topography may be similar to the current caldera floor topography, except that it is scaled so that its maximum depth matches d'.

The same argument can be applied to other topographic features, and we can retrieve for each of them an effective depth or height that accounts for the unknown density layering within them. Such effective depths and heights can then be employed to adjust the elevation of the respective topographic elements and calculate a comprehensive stress model. We note that, in principle, we could fix the topographic elevation and constrain, instead, an 'effective rock density' for each topographic element.

We write our stress model following Rivalta et al. (2019) and Mantiloni et al. (2023a) as:

$$\sigma_{ij}(x,y,z) - \sigma_{ij}^0(z) = \sigma_{ij}^T + \sigma_{ij}^{ST}(x,y,z) + P^U G_{ij}^U(x,y,z) + P^L G_{ij}^L(x,y,z) \qquad (4.5)$$

where σ_{ij}^T represents the horizontal tectonic stresses, and the gravitational loading/unloading contribution is separated into three parts as follows. $\sigma_{ij}^{ST}(x,y,z)$ is the stress associated to the 'set topography' (ST): that is, topography which predates the volcanic activity and has not been significantly altered by it. $\sigma_{ij}^{ST}(x,y,z)$ is treated here as a known stress contribution. The remaining two contributions arise from topography that has been generated by volcanic activity. $P^U G_{ij}^U(x,y,z)$ is the contribution of the unloading due to the formation of topographic depressions, such as calderas, while $P^L G_{ij}^L(x,y,z)$ is the contribution of the loading due to
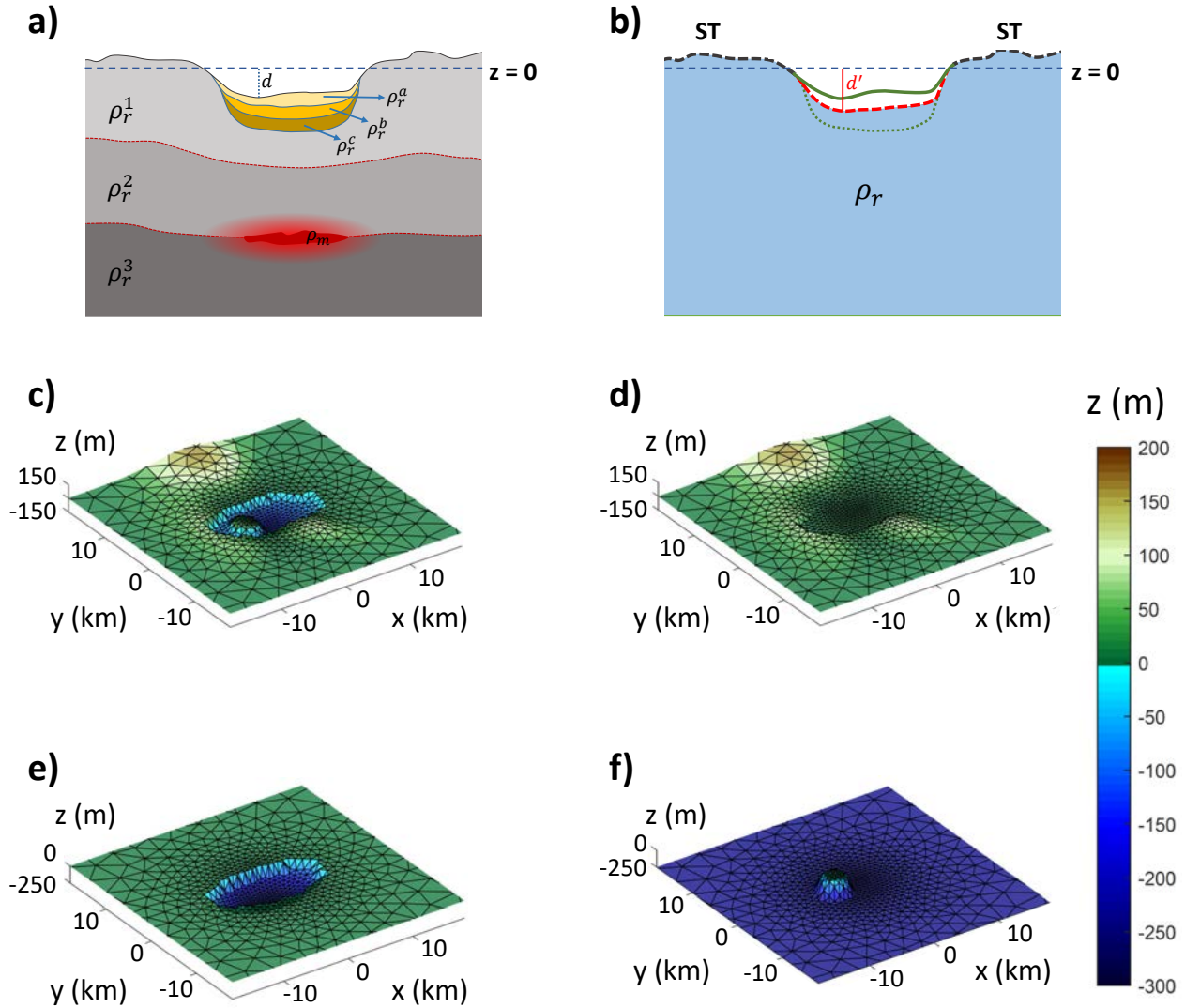
Figure 4.2: Illustration of the single-mesh and compound-stress methods. a): Cross section of a realistic caldera of depth d_1, where the collapse floor is buried at depth d_0. The deep melt accumulation volume and the rock layers of various densities outside and within the caldera collapse floor are represented with different colors. b): Modeling of the setting in (a) according to the compound-stress method. We assume the same density for the whole crust. The topography outside the caldera is taken as ST, whilst we account for the density layering of the caldera refill by adjusting the depth d' of the mesh representing the caldera. c): Original topographic mesh employed in the 'Elliptic-Caldera' scenario by Mantiloni et al. (2023a). The depth and height of the caldera and the resurgent dome are, respectively, d and h. d): Mesh representing the Set Topography (ST). e): Mesh representing the 'reference caldera' with depth d^{ref}; here, $d^{ref} > d$. f): Mesh representing the 'reference dome' with height h^{ref}; here, $h^{ref} > h$. (c), (d), (e) and (f) share the same color scale, shown on the right side of the figure.

topographic highs, such as cones or resurgent domes. $G_{ij}^k(x, y, z)$ are adimensional, space-dependent functions expressing how each stress mechanism acts at any point in space, while $P^{U,L}$ represent the unloading/loading pressures associated with the topographic features. We write them as:

$$P_U = \rho_r g d; \quad P_L = \rho_r g h \tag{4.6}$$

where g is the acceleration due to gravity, and d and h represent, respectively, the maximum effective depth and maximum effective height of a depression and a relief. If multiple topographic features are present, the terms $P^U G_{ij}^U(x, y, z)$ and $P^L G_{ij}^L(x, y, z)$ in Equation 4.5 may be repeated accordingly. Here, we treat ρ_r as a fixed parameter, and d and h as free parameters, together with the components of σ_{ij}^T. The inverse problem, thus, translates in an inversion for d, h and σ_{ij}^T.

A notable result by both Rivalta et al. (2019) and Mantiloni et al. (2021b) was that dike trajectories are controlled not so much by the individual stress parameters as by their ratios. Hence, we write the ratios between the tectonic stress components and the loading/unloading pressures:

$$R_{xx} = \frac{\sigma_{xx}^T}{P^U}; \quad R_{yy} = \frac{\sigma_{yy}^T}{P^U}; \quad R_{xy} = \frac{\sigma_{xy}^T}{P^U}; \quad R_h = \frac{P^L}{P^U} = \frac{h}{d} \tag{4.7}$$

In summary, our stress inversion aims at constraining the stress parameters d, h and the three independent components of σ_{ij}^T, or the ratios R_{ij} and R_h ($i,j = x,y$). We note that constraining σ_{ij}^T is equivalent to constraining the principal tectonic stresses and their orientation.

We calculate gravitational loading/unloading with two methods, which we call 'single-mesh' and 'compound-stress', tailored for single-purpose stress calculations and for stress parameter optimization, respectively. In both methods, we use the Boundary-Element (BE) tool *Cut&Displace* (Davis et al., 2017, 2019). The single-mesh method works by representing the entire topography with a mesh of triangular dislocations (Nikkhoo and Walter, 2015), acting as BEs. First, we fix a datum level $z = 0$ (Mantiloni et al., 2023a) and, later, assign to each BE stress boundary conditions so as to achieve a free surface condition (Martel and Muller, 2000; Slim et al., 2015). As discussed by Mantiloni et al. (2023a), different topographic features may require different datum levels: hence, it is important to separate the P^U and P^L terms in Equation 4.5, even though they arise from the same stress-generating mechanism. We create meshes using the open-source tool *DistMesh* by Persson and Strang (2004).

The single-mesh method, however, is ill-suited for running the large number of stress models needed to sample the effective d and h. Hence, we introduce the compound-stress method, which involves calculating separate meshes for the stress contributions due to different topographic features. For example, consider the synthetic scenario 'Elliptic-Caldera' from Mantiloni et al. (2023a), reported in Figure 4.2c. The scenario includes a caldera hosting a resurgent dome and surrounded by gently-sloping topography. In the single-mesh method, all such topographic features are included in the same mesh and share the same datum level. In the compound-stress method, instead, the stress calculation is broken down into three parts: ST (Figure 4.2d), unloading due to the caldera (Figure 4.2e) and loading due to the resurgent dome (Figure 4.2f). In order to do so, we employ three different meshes for each part. Such meshes are flat and set to the respective datum level everywhere, except for the topographic element they are associated with.

We rewrite Equation 4.5 as

$$\sigma_{ij}(x, y, z) - \sigma_{ij}^0(z) = \sigma_{ij}^T + \sigma_{ij}^{ST}(x, y, z) + P_U I_{ij}^{dref}(x, y, z) + P_L I_{ij}^{href}(x, y, z) \tag{4.8}$$

where $\sigma_{ij}^{ST}(x, y, z)$, $I_{ij}^{dref}(x, y, z)$ and $I_{ij}^{href}(x, y, z)$ are the stress contributions of ST, caldera and resurgent dome, respectively. $\sigma_{ij}^{ST}(x, y, z)$ is the stress field due exclusively to the gravitational

loading of the topography outside the caldera, and is calculated through the ST mesh (Figure 4.2d). Such a mesh reproduces the topography of Figure 4.2c everywhere except within the caldera rim, where it is flat and set to the datum level of the topography outside the rim. The caldera mesh (Figure 4.2e) includes a 'reference caldera' whose depth is set to a 'reference' value, d^{ref}, while having the same shape and lateral extent as the one in Figure 4.2c. Then, $I_{ij}^{d^{ref}}(x,y,z)$ is the stress field induced solely by the reference caldera, normalized by $\rho_r g d^{ref}$. The stress contribution of a deeper or shallower caldera with depth d is calculated by rescaling $I_{ij}^{d^{ref}}$ by $P_U = \rho_r g d$. The resurgent dome mesh (Figure 4.2f) includes a 'reference resurgent dome' with 'reference height' h^{ref}. Away from it, the mesh is flattened to the datum level of the dome, that is, the floor of the reference caldera in Figure 4.2e. Then, $I_{ij}^{h^{ref}}(x,y,z)$ is the stress field induced solely by the reference resurgent dome, and is calculated similarly to $I_{ij}^{d^{ref}}$. Likewise, we obtain the stress contribution of a resurgent dome with $h \neq h^{ref}$ by scaling $I_{ij}^{h^{ref}}$ by $P_U = \rho_r g h$. If multiple topographic lows and highs are present, more terms $P_U I_{ij}^{d^{ref}}$ and $P_L I_{ij}^{h^{ref}}$ can be added, each associated with its own mesh. We note that all the meshes we use stem from the same 'flat' mesh: that is, the horizontal coordinates of the mesh nodes never change, we only adjust their height from one mesh to another, as shown in Figure 4.2c,d,e,f.

In a stress inversion, we set d^{ref} and h^{ref} (Equation 4.8) to the midpoint of the sampling ranges of d and h, respectively. Next, we run three separate single-mesh models for the three topographic contributions (Figure 4.2d,e,f). We interpolate the resulting $I_{ij}^{d^{ref}}(x,y,z)$, $I_{ij}^{h^{ref}}(x,y,z)$ and $\sigma_{ij}^{ST}(x,y,z)$ over a grid of observation points in the subsurface by linear interpolation on a 3D Delaunay triangulation (e.g. Aurenhammer et al., 2013) of the grid. Such calculations need to be performed only once at the start of the stress inversion. Finally, we linearly superpose the interpolated stresses to retrieve the stress for any d and h. For example, if we have currently sampled $d = d^m$ and $h = h^m$, the total stress tensor σ_{ij} is given by:

$$\sigma_{ij}(x,y,z) = \sigma_0(z) + \sigma_{ij}^{T,m} + \sigma_{ij}^{ST}(x,y,z) + P_U^m I_{ij}^{d^{ref}}(x,y,z) + P_L^m I_{ij}^{h^{ref}}(x,y,z) \qquad (4.9)$$

where $P_U^m = \rho_r g d^m$, $P_L^m = \rho_r g h^m$, and $\sigma_{ij}^{T,m}$ is the current tectonic stress tensor. This approach effectively cuts the running time of a stress inversion roughly by a factor of about 100.

In order to illustrate the limitations of the compound-stress method, we test it against the single-mesh method. We consider two end-member cases for the Elliptic-Caldera scenario (Figure 4.2c), fixing d and h so that they are shallow/short ($d=-50$ m, $h=50$ m, Figure 4.3a,b), or deep/tall ($d=-500$ m, $h=500$ m, Figure 4.3c,d). We compare the single-mesh results with the corresponding compound-stress calculations, having intermediate $d^{ref}=-225$ m and $h^{ref}=225$ m.

We calculate $I_{ij}^{d,h^{ref}}$ on a grid of points spaced by 400 m along x and y, and by 300 m along z. We do not include points shallower than 800 m below the mesh, so as to avoid artifacts in the calculations. In Figure 4.3, we compare the orientations of $\vec{v}_3$ and the gradients of σ_3 in the x, y and z direction because they control the orientation and driving pressure of the penny-shaped cracks representing dikes in SAM (Section 4.2.2). Gradients are calculated by computing σ_3 on the same grid, shifted by 1 km in the three directions. Such distance is comparable to the SAM radii (c) employed in this work. We notice how $\vec{v}_3$ orientations and gradients for the single-mesh and compound-stress are similar when the caldera and resurgent dome are shallow/short (Figure 4.3a,b). In contrast, when d and h are large (Figure 4.3c,d), we see some discrepancies, especially in the region below the resurgent dome (dark-red boxes in Figure 4.3a,c, having width and depth equal to the width of the resurgent dome). Discrepancies are largest below the resurgent dome in the case of $\vec{v}_3$ orientations, while we see some discrepancies in the σ_3 gradients also outside of the boxes, limited to a few hundreds Pa/m, which is small compared to the loading pressure of either resurgent domes (e.g., $\rho_r g d = \sim 1.2$ MPa for the short dome,
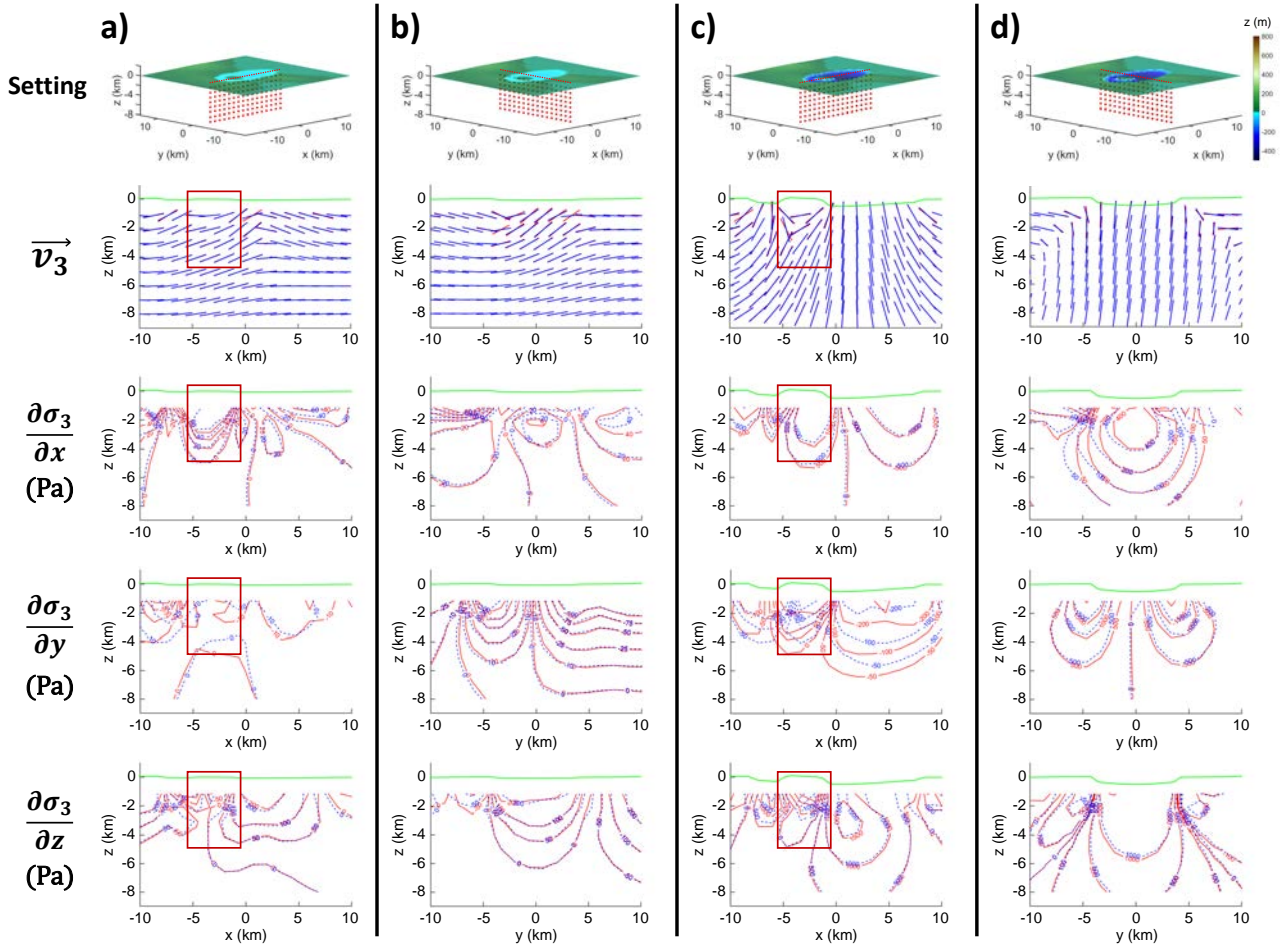
Figure 4.3: $\vec{v}_3$ directions and σ_3 gradients calculated for the Elliptic-Caldera scenario with the single-mesh and compound-stress methods. Results from the single-mesh method are shown in red, those from the compound-stress method in blue. All rows include, from top to bottom: view of the setting and the observation points where stresses are evaluated; comparison between $\vec{v}_3$ directions; comparison between σ_3 gradient along the x, y and z direction. In all tests, the reference depth and height employed in the compound-stress methods are $d^{ref}=-225$ m and $h^{ref}=225$ m, respectively. a): The setting considered here has $d=-50$ m, $h=50$ m; the observation point grid lies along the x-axis. b): Same setting as (a), grid along the y-axis. c): The setting considered here has $d=-500$ m, $h=500$ m; the observation point grid lies along the x-axis. d): Same setting as (c), grid along the y-axis. The green profiles in the stress plots are the topographic profiles shown in the first row as red, dotted lines on the meshes. The dark-red boxes in columns (a) and (c) mark the width of the resurgent dome ($\sim$5 km) and the depth interval where we expect the stress contribution of the resurgent dome to be significant, and the largest differences in $\vec{v}_3$ orientations and gradients to occur.

with ρ_r=2500 kg/m^3). In conclusion, the compound-stress results are, at least in the presented case, an acceptable approximation of single-mesh stresses at depth, but much less so as we approach to the surface, and may differ considerably if complex and prominent topographies are considered. In particular, a tall resurgent dome (Figure 4.3c) seems to affect the results much more than a deep caldera (Figure 4.3d). Given the way the compound-stress calculation is constructed, the free surface condition will not be met exactly across the topography. Therefore, we advise caution with its use, and suggest testing it thoroughly against the single-mesh method for the end-members of any sampling range of stress parameters, and adjusting them if large discrepancies are found.

4.2.4 Stress Inversion Approach

The last element needed to solve the inverse problem defined in Section 4.2.1 is an efficient method to sample the parameter space and retrieve posterior PDFs for the stress parameters. Following Bayes' Theorem (e.g. Gelman et al., 2013) and the inverse problem formulation of Section 4.2.1, we calculate the posterior PDF as:

$$P(\vec{m}|\vec{d}) \propto P(\vec{d}|\vec{m})P(\vec{m}) \qquad (4.10)$$

where $\vec{m}$ and $\vec{d}$ are the model and data vectors, respectively. The likelihood function $P(\vec{d}|\vec{m})$ is the cost function s defined in Equation 4.4, and $P(\vec{m})$ is the prior information on the model parameters.

In general, $\vec{m}$ includes both the stress ($\vec{\theta}$) and dike ($\vec{\zeta}^B$) parameters in Equation 4.3), as well as the dike nucleation PDF, p, introduced in Section 4.2.1. Here, we fix SAM parameters ($\vec{\zeta}^B$) and the host rock properties (Table 4.1), so that the model vector is:

$$\vec{m} = \vec{\theta} = [d, h, \sigma_{xx}^T, \sigma_{yy}^T, \sigma_{xy}^T, p] \qquad (4.11)$$

We note that p is both an input and an output of our stress inversion. Thus, the p we assume before starting the procedure is part of the prior information, $P(\vec{m})$. We do not invert for p directly, but rather recover a posterior p through the distribution of backtracked dike starting points from the stress inversion (see Section 4.2.1).

The data vector, $\vec{d}$, consists of the locations V_k of N vents:

$$\vec{d} = [V_k], \quad k = 1, ..., N \qquad (4.12)$$

Similar formulations of Bayesian inverse procedures including physics-based models have been adopted by Anderson and Segall (2013); Anderson and Poland (2016).

Here, we sample $P(\vec{m}|\vec{d})$ by adopting the Delayed Rejection and Adaptive Metropolis Markov Chain Monte Carlo algorithm (MCMC for brevity) by Haario et al. (2006). We employ the open-source MCMC Toolbox by Laine (2013).

We fix M as the number of iterations of the MCMC. The MCMC chain starts with a set of stress parameters drawn randomly from their respective prior distributions. Then, for each iteration, the MCMC samples a set of stress parameters as:

$$\vec{\theta}^m = \vec{\theta}^{m-1} + \vec{\xi} \qquad (4.13)$$

where m is the current iteration and $\vec{\xi}$ is drawn from the proposal distribution $N(\vec{0}, \Sigma_{prop})$, that is, a multivariate normal distribution with null mean vector and covariance matrix Σ_{prop}.
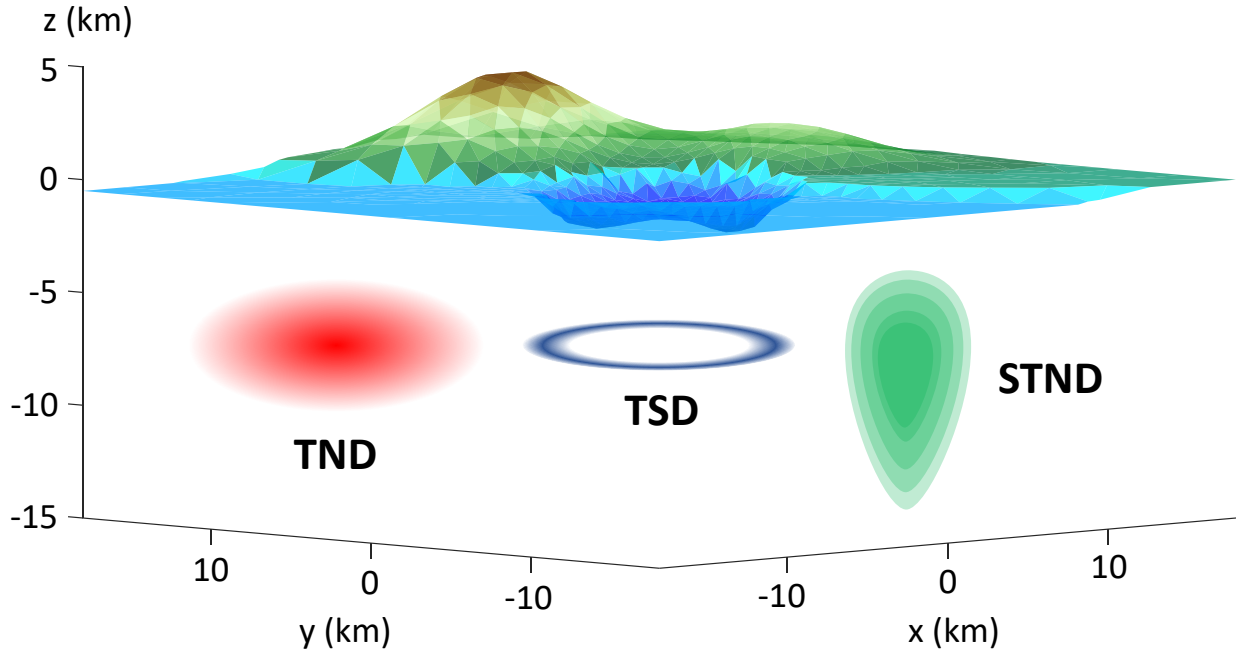
Figure 4.4: Illustration of the three types of PDF for the dike nucleation zone considered in this work. The trivariate normal distribution (TND) is shown in red, the torus-shaped distribution (TSD) in blue, and the skewed, trivariate normal distribution (STND) in green. Color gradients represent the value of p from higher (intense color) to lower (white).

Next, we compute the stress model associated to $\vec{\theta}^m$ and backtrack N dike trajectories from N vents. Backtracked dike trajectories (B_k, $k = 1, .., N$) are stopped once they become horizontal and start ascending or, alternatively, reach a given threshold in r or z (see Figure 4.1). We fix such threshold to $r = 10$ km, $z = -10$ km throughout the work. We then interpolate each B_k by Piecewise Cubic Hermite Interpolation (e.g. Rabbath and Corriveau, 2019), and find the point where $p(x, y, z)$ is highest. Finally, we evaluate the cost function s (Equation 4.4).

4.2.4.1 Dike Nucleation Zone PDFs

The cost function s is informed by the choice of p (Equation 4.4). Such a choice is, in turn, informed by the knowledge we have about the magma storage system and the processes that promote or hinder dike nucleation. For instance, we may have some information on the location, size and shape of a magma reservoir from seismic tomography or inversion of ground deformation data. If the reservoir is sill-like, we may deem dike nucleation to be favored along the edge of the sill, due to the high stress concentration predicted there by elastic deformation source models (e.g. Fialko et al., 2001). D could then be described by a torus-shaped p, peaking along the boundary of the magma reservoir.

We consider three types of p: a trivariate normal distribution (TND), a torus-shaped distribution (TSD) and a skewed, trivariate normal distribution (STND). They are examples of possible choices for p, each applying to different assumptions on the reservoir size and shape, as well as where dikes nucleate from. Examples of the three PDFs are illustrated in Figure 4.4.

The TND PDF (e.g. Prince, 2012) is written as:

$$p^{TND}(x, y, z) = \frac{1}{(2\pi)^{\frac{3}{2}} |\Sigma|^{\frac{1}{2}}} \exp\left[-\frac{1}{2}(\vec{x} - \vec{\mu})^T \Sigma^{-1} (\vec{x} - \vec{\mu})\right] \qquad (4.14)$$

where Σ is the covariance matrix, $|\Sigma|$ its determinant, $\vec{x} = (x, y, z)$ and $\vec{\mu}$ is a vector identifying the mean of the distribution, that is, the center of the reservoir, with components (μ_x, μ_y, μ_z). Σ, which we always assume diagonal, accounts for the uncertainty on the size of the reservoir. When we employ the TND, we assume that dikes may have nucleated from anywhere in the magma storage region, with higher probability closer to its center.

The TSD PDF is obtained from a bivariate normal distribution defined over the r, z cylindrical coordinates, normalized by 2π:

$$p^{TSD}(r, z) = \frac{1}{(2\pi)^2 |\Sigma|^{\frac{1}{2}}} \exp\left[-\frac{1}{2}(\vec{q} - \vec{\mu})^T \Sigma^{-1} (\vec{q} - \vec{\mu})\right] \tag{4.15}$$

where Σ is the correlation matrix, $\vec{q} = (r, z)$ and $\vec{\mu}$ is the mean of the distribution, with components (μ_r, μ_z). We assume a diagonal Σ here as well. When we employ the TSD, we assign the highest probability of dike nucleation on a torus surrounding the boundary of the reservoir.

We use the STND to assign higher probability of dike nucleation to the shallower region of a reservoir. The STND PDF (O'Hagan and Leonard, 1976) is written as:

$$p^{STND}(x, y, z) = 2p^{TND}(x, y, z)\Phi(\vec{\lambda}, \vec{x}) \tag{4.16}$$

where $p^{TND}(x, y, z)$ is the TND described in Equation 4.14, and $\Phi(\vec{\lambda}, \vec{x})$ is the cumulative distribution of a standard normal PDF, where the components of $\vec{x}$ are scaled by the shape parameters $\vec{\lambda} = (\lambda_x, \lambda_y, \lambda_z)$:

$$\Phi(\vec{\lambda}, \vec{x}) = \frac{1}{2}\left[1 + erf\left(\frac{\vec{\lambda} \cdot \vec{x}}{\sqrt{2}}\right)\right] \tag{4.17}$$

We remark that such PDFs are non-truncated, as p is non-zero everywhere. While this formally means that we assign a non-zero probability of dike nucleation above the free surface, it poses no issue, since SAM may backtrack dikes only in the subsurface.

4.2.5 Forecast Approach

The output of the stress inversion described in Section 4.2.4 is a set of posterior PDFs for the stress parameters (d, h, σ_{xx}^T, σ_{yy}^T, σ_{xy}^T), as well as the dike starting points ($S_k \equiv [r^k, \phi^k, z^k]$, $k = 1, ..., N$). The posterior PDFs of the stress parameters ratios (R_{xx}, R_{yy}, R_{xy}, R_h, see Equation 4.7) are retrieved through post-processing.

We now describe how we use the stress inversion results to produce a probability map of eruptive vent opening:

1. We fix the number M^F of simulations of dike trajectories we want to perform. These are calculated by SAM in forward mode (Section 4.2.2).

2. We draw M^F random d, h, σ_{ij}^T from their respective PDFs.

3. We draw M^F random starting points for the current dike trajectory from the PDFs of S_k. If the PDFs of ϕ_k are peaked about specific starting angles of dikes, we may smooth the ϕ_k PDFs before doing so. We explain this point in detail later.

4. We set the forward SAM radius c to the c_B assumed in the respective stress inversion, and treat the magma density (ρ_m) and the host rock parameters (Table 4.1) as known quantities.

5. We calculate the M^F stress models with the compound-stress method, where we fix d^{ref} and h^{ref} to the median values of the d and h PDFs.

6. We run M^F simulations of forward dike trajectories with SAM, each corresponding to a set of stress parameters.

7. We set aside the M^F_{stop} dike trajectories which stopped before reaching the MDT.

8. We stack the arrival points of the remaining $M^F - M^F_{stop}$ dike trajectories and produce a map of vent locations and fissure strikes across the caldera.

9. We calculate the vent density, V_D, that is, the number of vents falling within each triangular dislocation of the topography mesh, normalized by $M^F - M^F_{stop}$ and the area of the dislocations.

10. We compare the vent distributions and V_D maps to the location of validation vents that were not considered in the stress inversion.

As we show later, the PDFs of the dike starting angles, ϕ_k, may be peaked around specific values. Consequently, if we sample starting angles from those PDFs in point (3) of our forecast strategy, the arrival points of forward SAM trajectories may cluster in very localized areas. Furthermore, doing so implies the assumption that dike nucleation is favored only at specific angles, without potential physical justifications. Thus, in such cases, we adopt a more conservative approach and smooth the ϕ_k PDFs through kernel density estimation (see e.g. Silverman, 1986).

We also present a 3D upgrade of the stress-update technique in vent forecasting introduced by Rivalta et al. (2019) and later tested by Mantiloni et al. (2021b). Consider a scenario where the topography of a caldera is changed between two epochs of eruptive activity (e.g. by refill or resurgence). We perform the stress inversion on the vents that opened before such a change occurred, and constrain the effective depth d relative to that epoch. Then, we want to test our forecast on the most recent vents, but in order to do so, we need to account for the topography and, thus, stress change in the system which cannot have been captured by the inversion. Since the minimum depth of the refilled caldera, d_R, is known, we shift the PDF of d, recovered from the inversion, so that its median value matches d_R. We also shift the upper boundary of the distribution to $d = 0$, that is, a completely refilled caldera. Then, in point (2) of the forecast, we use the shifted PDF to draw M^F values of d. Next, in the compound-stress method (point 5), we use the topography of the refilled caldera, which is also known, to build the reference caldera, and set $d^{ref} = d_R$. The forecast can then be tested by comparing its results to the locations of the most recent vents.

4.3 Testing the Stress Inversion and Vent Forecast

4.3.1 Stress Inversion and Forecast Setup

We test our stress inversion on seven out of the nine synthetic scenarios presented by Mantiloni et al. (2023a). The scenarios consider progressively more complex topographies, all featuring a caldera, possibly hosting a resurgent dome and surrounded by different topographic elements, such as hill ranges and a coastline.

Besides the topographic setting, the scenarios comprise a set of dike trajectories departing from a magma storage volume below the caldera. Starting points are either equally-spaced or randomly drawn along the edge of a horizontal sill, two sills at different depths, or within a vertically-elongated reservoir. Dike trajectories are calculated through SAM or, in one case, TIM, producing a set of N arrival points. Both SAM and TIM trajectories stop before exceeding a Minimum Distance Threshold (MDT, fixed to 800 m) from the closest triangular dislocation of the topography mesh, in order to avoid artifacts in the stress field. The SAM option of connecting the arrival point at depth with the surface is sometimes used (Mantiloni et al., 2023a). Thus, the dike arrival points lie below the surface in some scenarios, and on the surface in others. All such arrival points are referred to as 'vents' in the following.

For each scenario, we divide the vents into a training and a validation set, and employ the first to constrain the stress parameters through the inversion algorithm described in Section 4.2.4. In the following, we refer to vents belonging to the training and validation sets as training and validation vents, respectively.

As anticipated, we fix the Young's modulus ($E = 15$ GPa), Poisson's ratio ($\nu = 0.25$) and density (ρ_r) of the host rock, as well as the magma density ($\rho_m = 2300$ kg/m^3), as known parameters. Regarding SAM parameters (Section 4.2.2), we fix $n = 12$. The choice of c_B is critical, since SAM backtracks a dike trajectory accurately only if $c_B = c$, that is, if the original radius of the forward dike is known. We test both $c_B = c$ and $c_B \neq c$ in the inversions (Table 4.2).

We run eight stress inversions, named after the scenarios by Mantiloni et al. (2023a). We fix the number of iterations for the MCMC as $M = 20,000$ in all our tests. We assume a p to describe the dike nucleation zone, choosing among the types described in Section 4.2.4.1. We assign sampling ranges to the stress parameters, and assume the prior PDFs in Equation 4.10 uniform within the respective ranges. Such prior PDFs, together with the assumed p, constitute the prior information $P(\vec{m})$ in Equation 4.10. We initially take Σ_{prop} of the proposal distribution (Equation 4.13) as an identity matrix, and let it be adapted during the MCMC (see Haario et al., 2006). The fixed parameters are listed in Table 4.2.

We run forecasts on the four stress inversion tests that we deem most instructive. We fix $M^F = 20,000$ in all our tests. We set the magma density to $\rho_m=2300$ kg/m^3, unless we specify otherwise.

4.3.2 Synthetic Scenarios, Stress Inversion and Forecast Results

Our synthetic tests show that, if the prior knowledge of the original models by Mantiloni et al. (2023a) is used to set dike parameters and dike nucleation zone PDF, then the stress parameters and/or ratios are constrained with accuracy and small bias. If we add uncertainty in our assumptions, the performance of the stress inversion is poorer, leading to more or less unconstrained or biased posterior PDFs. Individual stress parameters are especially sensitive to the quality of the prior knowledge, while ratios are generally well-constrained. As a consequence, vent forecasts are generally quite successful in constraining areas of high vent density that match the locations of training vents from the original scenarios.

The first stress inversion, 'Circular-Caldera-Inv', is performed on the most simplified scenario, where a circular, axisymmetric caldera lies on a flat surface. Circular-Caldera-Inv represents a 'dummy test' where all assumptions closely reflect the original scenario. The results confirm the conclusions by Rivalta et al. (2019) and Mantiloni et al. (2021b) on 2D settings (Figure 4.5a): while the PDFs of individual stress parameters are either unconstrained or peaked around the wrong value, the ratios between tectonic stresses and unloading pressure (R_{xx}, R_{yy}) are

Table 4.2: Stress inversion: fixed parameters and p distributions. FS: free surface. 'Yes': dike trajectories are backtracked from vents on the free surface; 'No': they are backtracked from points at or near the minimum distance threshold.

Inversion	From FS	c_B (km)	ρ_r (kg/m^3)	p	$\vec{\mu}$ (km)	$\sqrt{\Sigma}$ (km)	$\vec{\lambda}$
Circular-Caldera-Inv	No	1.2	2500	TSD	[2, −6]	[0.6, 0.2]	-
Simplified-Coastline-1-Inv	No	0.9	2500	TSD	[2, −6]	[1, 0.3]	-
Simplified-Coastline-2-Inv	Yes	1.2	2500	TND	[0, 0, −6]	[1.5, 1.5, 0.25]	-
Tectonic-Shear-Inv	No	1.2	2500	TSD	[2, −6]	[1.2, 0.5]	-
Refilling-Caldera-Inv	No	1.2	2800	TSD	[3, −4]	[1.5, 0.3]	-
Two-Reservoirs-Inv	Yes	1.2	2800	TND	[0, 0, −4]	[1.5, 1.5, 0.2]	-
Elliptic-Caldera-Inv	Yes	0.9	2500	STND	[−3, 0, −4.5]	[0.5, 0.5, 1.2]	[0, 0, −5]
Complex-Coastline-Inv	No	0.9	2800	TSD	[3, −6]	[0.6, 0.2]	-

Table 4.3: Stress inversion results.

Original stress parameters and ratios									
Scenario	d (m)	h (m)	σ^T_{xx} (MPa)	σ^T_{yy} (MPa)	σ^T_{xy} (MPa)	R_h	R_{xx} $\cdot 10^{-1}$	R_{yy} $\cdot 10^{-1}$	R_{xy} $\cdot 10^{-1}$
Circular-Caldera	-500		1.0	0.5	0		-0.82	-0.41	
Simplified-Coastline	-450		1.0	1.0	0		-0.91	-0.91	
Tectonic-Shear	-450		0.8	0.8	-1.0		-0.73	-0.73	0.91
Refilling-Caldera	-424		1.0	0.4	0		-0.86	-0.34	
Two-Reservoirs	-424		1.0	0.4	0		-0.86	-0.34	
Elliptic-Caldera	-150	150	1.0	0.6	0	-1.0	-2.72	-1.63	
Complex-Coastline	-424		1.0	0.4	0		-0.86	-0.34	

Median values from stress inversions									
Inversion	d^{med} (m)	h^{med} (m)	$\sigma^{T,med}_{xx}$ (MPa)	$\sigma^{T,med}_{yy}$ (MPa)	$\sigma^{T,med}_{xy}$ (MPa)	R^{med}_h	R^{med}_{xx} $\cdot 10^{-1}$	R^{med}_{yy} $\cdot 10^{-1}$	R^{med}_{xy} $\cdot 10^{-1}$
Circular-Caldera-Inv	-780		1.6	0.8			-0.82	-0.44	
Simplified-Coastline-1-Inv	-1720		2.8	3.0			-0.70	-0.71	
Simplified-Coastline-2-Inv	-490		1.1	0.9			-0.99	-0.74	
Tectonic-Shear-Inv	-590		0.9	0.9	-1.1		-0.57	-0.57	0.68
Refilling-Caldera-Inv	-340		1.0	0.9			-1.03	-0.89	
Two-Reservoirs-Inv	-940		1.0	1.0			-0.41	-0.40	
Elliptic-Caldera-Inv	-250	220	1.5	1.3		-0.9	-2.40	-2.06	
Complex-Coastline-Inv	-500		1.1	1.1			-0.73	-0.72	

Standard deviation									
Inversion	δd (m)	δh (m)	$\delta\sigma^T_{xx}$ (MPa)	$\delta\sigma^T_{yy}$ (MPa)	$\delta\sigma^T_{xy}$ (MPa)	δR_h	δR_{xx} $\cdot 10^{-1}$	δR_{yy} $\cdot 10^{-1}$	δR_{xy} $\cdot 10^{-1}$
Circular-Caldera-Inv	220		0.4	0.3			0.09	0.09	
Simplified-Coastline-1-Inv	320		0.6	0.7			0.14	0.10	
Simplified-Coastline-2-Inv	150		0.4	0.5			0.26	0.37	
Tectonic-Shear-Inv	270		0.4	0.4	1.0		0.38	0.41	0.72
Refilling-Caldera-Inv	110		0.4	0.4			0.42	0.47	
Two-Reservoirs-Inv	360		0.6	0.6			0.50	0.46	
Elliptic-Caldera-Inv	70	100	0.4	0.6		0.18	0.91	1.01	
Complex-Coastline-Inv	320		0.6	0.6			0.82	0.78	

accurately constrained, their PDFs having the smallest δ among our results and their medians falling within one δ from the original values (Table 4.3). The coordinates of the dike starting points are remarkably well-retrieved (Figure 4.7a).

The axisymmetry of the topography is broken in the 'Simplified-Coastline' scenario. Here, a step-like coastline divides the topography into two flat regions of different elevation. We use this scenario with two inversions. In 'Simplified-Coastline-1-Inv' we take $c_B \neq c$, while in 'Simplified-Coastline-2-Inv' we backtrack dikes from the free surface and assume a TND for p, which does not match well the original dike starting points. In these tests, not only the ratios, but also the individual stress parameters are either well-constrained, or show a clear peak in their PDFs (Figure 4.5c and Figure 4.5b, respectively).

In Simplified-Coastline-1-Inv, using $c_B \neq c$ biases the results, as all PDFs are peaked away from the original values (Table 4.3). In contrast, the PDFs of dike starting coordinates are well-constrained, especially z_k (Figure 4.7b). We use the results of Simplified-Coastline-1-Inv to run the first forecast, 'Simplified-Coastline-1-For'. We sample stress parameters from the 'biased' stress state recovered in the inversion, and dike starting points from the respective S_k PDFs (Figure 4.7b). The V_D map in Figure 4.8a shows that, even though the recovered stresses do not match the original stress model, the forecast is still successful in reproducing the locations of the training vents and predicting those of the validation vents. The area of highest V_D is narrow and focused around the rim where the original vents lie. Vents tend to cluster in small areas, as shown by the V_D contrasts between many neighboring BEs. This is a consequence of the fact that we do not smooth the PDF of ϕ_k. On the contrary, the highest-V_D area on the sea side is close to, but does not include, the only offshore vent.

In all our forecasts, a fraction of the M^F simulated dikes stops before reaching the MDT. That fraction generally amounts to roughly $M^F/5$. In Simplified-Coastline-1-For, however, roughly three fourths of dikes stopped in the subsurface if the original magma density of Simplified-Coastline ($\rho_m = 2300 \ kg/m^3$) is employed. This is due to the fact that ρ_m controls the driving pressure in SAM cracks, together with the gradient of σ_3 across the crack surface. If σ_3 is more compressive at the top of the crack rather than at its bottom, the dike stops if ρ_m is not large enough. The stress parameters retrieved in Simplified-Coastline-1-Inv do not match those of the original scenario. Consequently, a dike that reaches the MDT along a specific pathway in the original scenario may stop before the MDT while following a similar pathway in Simplified-Coastline-1-For, because σ_3 is different in the two cases. If we lower ρ_m, the fraction of stopped dikes aligns with that of the other tests. Therefore, in the results in Figure 4.8a, we fix the magma density to the unrealistic value of $\rho_m = 2000 \ kg/m^3$.

Simplified-Coastline-2-Inv is successful in constraining both the stress parameters and the ratios, although the PDF of σ_{yy} and R_{yy} are more spread-out than those of the other parameters (Table 4.3). z_k is also well-constrained (Figure 4.7c), while the PDF of r_k peaks close to the origin. The PDF of ϕ_k also shows peaks corresponding to the original starting angles, but is more spread-out than in the previous inversions.

The 'Tectonic-Shear' scenario maintains the topography of Simplified-Coastline, but considers a non-zero shear component of the tectonic stress tensor (σ_{xy}^T): that is, the principal tectonic stresses are rotated with respect to the coordinate axes. Thus, in 'Tectonic-Shear-Inv', we consider four stress parameters. Also in this case, the prior knowledge reflects the original scenario. We fail to constrain any individual parameter, with the exception of d, but we constrain the ratios R_{xx}, R_{yy}, R_{xy} with sufficient accuracy (Figure 4.6a, Table 4.3). From the PDFs of the σ_{ij}^T components, we also compute the PDFs of the most and least-compressive principal tectonic stresses ($\vec{v}_1^T$ and $\vec{v}_3^T$, respectively), and we find that their magnitudes (σ_1^T and σ_3^T) and, especially, directions are accurately constrained (Figure 4.6a). The ratios R_1^T, R_3^T
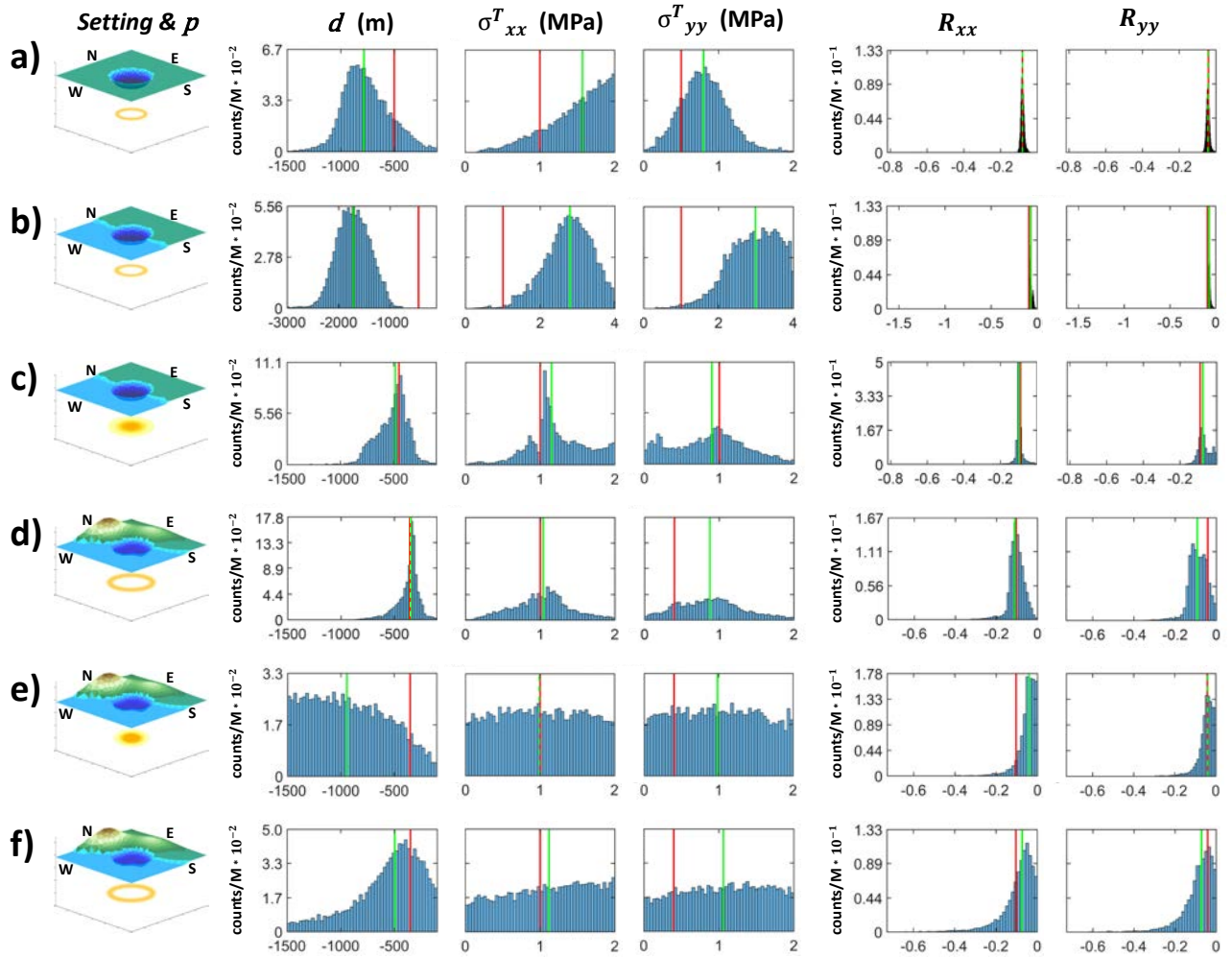
Figure 4.5: Stress inversion results. Each row corresponds to one stress inversion. Results of Tectonic-Shear-Inv and Elliptic-Caldera-Inv are displayed in Figure 4.6. The first column from left includes a view of the topographic setting of the scenario which the inversion is run on, together with a diagram of p. Such diagrams do not represent the actual p used in the inversion, and are meant to identify the type of p, according to Section 4.2.4.1. The remaining columns collect the posterior probability density functions (PDFs) of the stress parameters and their ratios, defined in Equations 4.6 and 4.7, respectively. Red lines mark the value of the parameter or ratio imposed in the original scenarios from Mantiloni et al. (2023a); green lines mark the median of the PDFs. a): Circular-Caldera-Inv. b): Simplified-Coastline-1-Inv. c): Simplified-Coastline-2-Inv. d): Refilling-Caldera-Inv. e): Two-Reservoirs-Inv. f): Complex-Coastline-Inv.
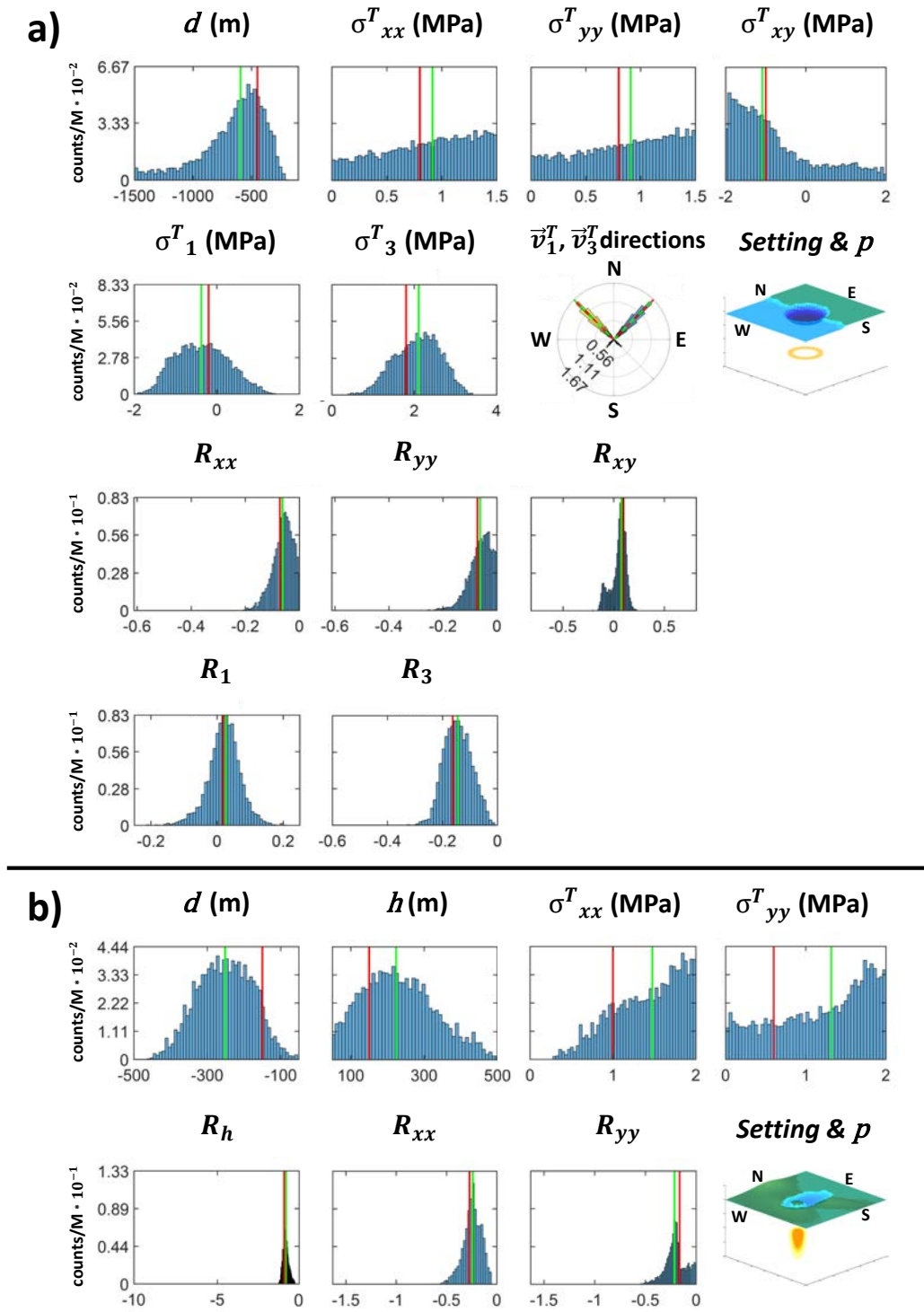
Figure 4.6: Stress inversion results for tests considering four stess parameters. a): Tectonic-Shear-Inv. The first row from the top collects the posterior probability density functions (PDFs) of four stress parameters. The second row includes PDFs of the intensity (σ_1^T, σ_3^T) and direction ($\vec{v}_1^T$, $\vec{v}_3^T$) of tectonic principal stresses, as well as a view of the topographic setting, with a diagram of p. The third row collects the PDFs of the ratios defined in Equation 4.7, while the fourth row includes PDFs of the ratios between σ_1^T, σ_3^T and $\rho_r g d$. b): Elliptic-Caldera-Inv. The first row from the top collects the PDFs of four stress parameters. The second row includes PDFs of the ratios defined in Equation 4.7, as well as a view of the topographic setting, with a diagram of p. Red lines mark the value of the parameter or ratio imposed in the original scenarios from Mantiloni et al. (2023a); green lines mark the median of the PDFs.
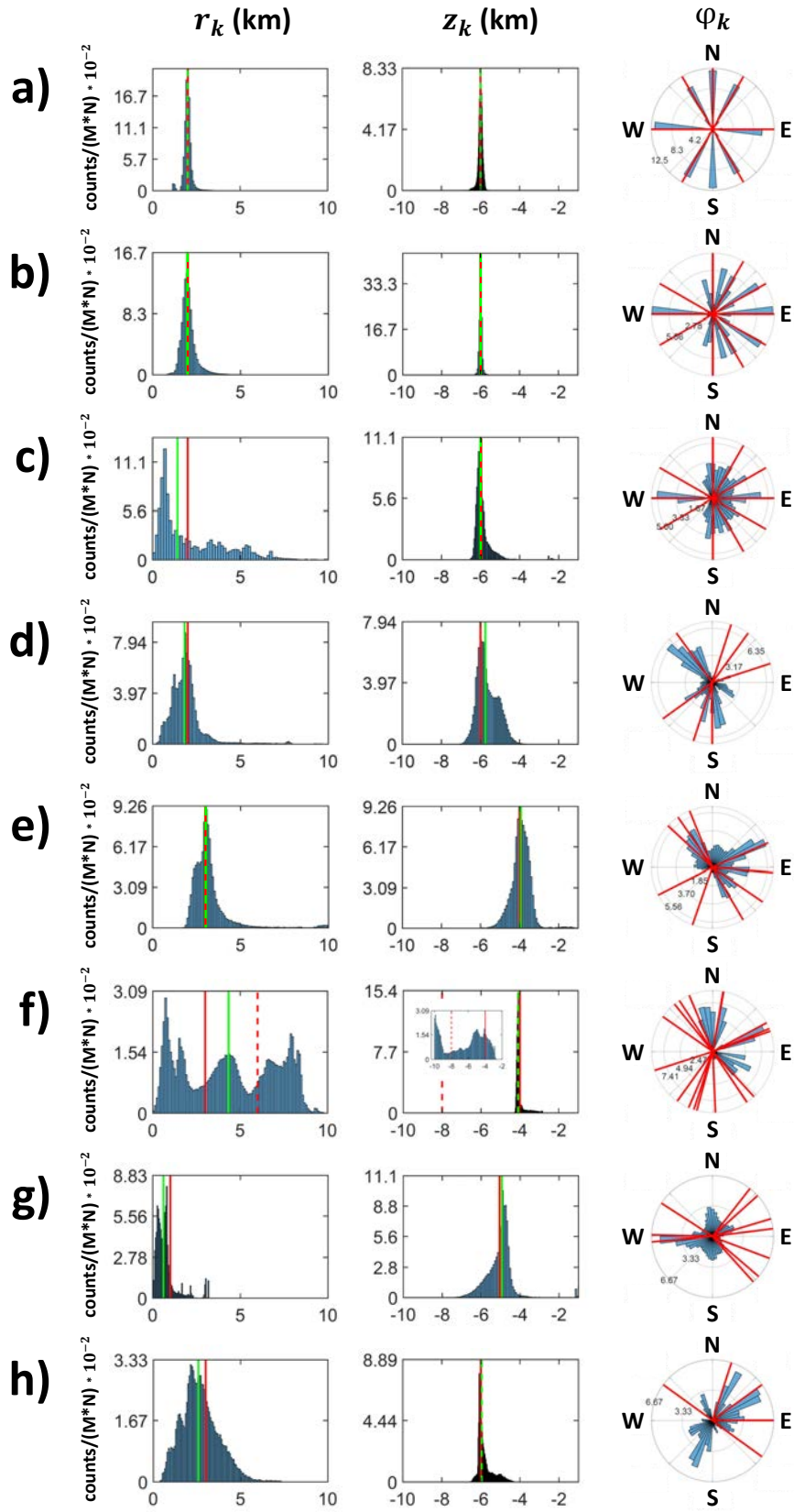
Figure 4.7: Stress inversion results: posterior probability density function (PDFs) of the dike starting points, $S_k=[r_k, z_k, \phi_k]$, described in the cylindrical reference frame of Figure 4.1b. Red lines mark the coordinates of the dike starting points assigned in the original scenarios from Mantiloni et al. (2023a); green lines, if present, mark the median of the PDFs. a): Circular-Caldera-Inv. b): Simplified-Coastline-1-Inv. c): Simplified-Coastline-2-Inv. d): Tectonic-Shear-Inv. e): Refilling-Caldera-Inv. f): Two-Reservoirs-Inv. Dotted red lines mark the radius and depth of the deep reservoir neglected in the inversion. The plot of the z_k PDF includes an inset with the PDF of the vertical coordinate of the points where backward SAM trajectories stop, to be compared with the depth of the neglected reservoir (dotted red line). g): Elliptic-Caldera-Inv. h): Complex-Coastline-Inv.

between σ_1^T, σ_3^T and the caldera unloading pressure ($\rho_r g d$) are also well-constrained. r_k and z_k are well constrained, but their PDFs are considerably spread, while ϕ_k are poorly constrained (Figure 4.7d).

The 'Refilling-Caldera' scenario still considers a caldera lying on a coastline, but with a complex caldera floor and a hill range on the mainland. The validation vents are produced with a modified setting, where the caldera is partially filled and its floor has a higher elevation. In 'Refilling-Caldera-Inv', we run the stress inversion with the vents produced before the caldera refilling, but in the forecast, 'Refilling-Caldera-For', we update the PDF of d according to the method described in Section 4.2.5 and test it on the training vents. The assumptions in the stress inversion reflect the original scenario, but the TSD assumed for the dike nucleation zone is wider, that is, has a larger uncertainty, than the ones considered in the previous inversions (Table 4.2). From Figure 4.5d and Table 4.3 we can see how d is well-constrained, while the PDFs of σ_{xx} and σ_{yy} are spread-out. σ_{yy} and R_{yy} are particularly poorly-constrained. Figure 4.7e shows similar results to Tectonic-Shear-Inv, as the PDFs of r_k and z_k are spread-out, but peaked around the original values. The PDF of ϕ_k fails to constrain most of the starting angles, but captures the fact that most dikes reaching the surface in the original scenario started from the mainland side of a sill-like reservoir.

Simulated vents in the forecast tend to cluster along the north-eastern rim of the caldera and around the caldera center, where a mild topographic relief is present. The high V_D areas generally match the locations of validation vents, but not those of the training vents (blue/green dots in Figure 4.8b, respectively). In particular, they miss the offshore vent completely. These results are obtained by smoothing the ϕ_k PDF from Refilling-Caldera-Inv to a roughly uniform distribution. If the ϕ_k PDF is not smoothed, the V_D map fails to reproduce the distribution of validation vents (not shown in Figure 4.8b).

In 'Two-Reservoirs', the topography is the same as in 'Refilled-Caldera', but dikes start from two sill-like reservoirs at different depths and with different radii. Then, in 'Two-Reservoirs-Inv', we show the consequences of a p that does not match the original dike nucleation zone, as we neglect the presence of the deeper reservoir while including in the training set some of the dikes that originated from it. Consequently, the inversion fails in constraining any parameter (Figure 4.5e, Table 4.3). However, the PDF of r_k displays secondary peaks, one of which is close to the radius of the neglected reservoir (Figure 4.7f). Moreover, while z_k of the shallow reservoir is constrained extremely well, the PDF of the depth where SAM trajectories stop is very spread, with a peak about the 10-km depth threshold, not far from the depth of the neglected reservoir (inset in Figure 4.7f). The implication is that the PDFs of S_k provide posterior information that could be used, in potential applications to real scenarios, to improve our assumption on D, and lead to a more successful stress inversion. In a test not reported here, we run a second inversion using the posterior PDFs of S_k to define p, but did not obtain significantly better results. The method, however, is worth further testing: for instance, running subsequent MCMC chains, where p is updated until the algorithm converges to stable distributions.

Considering an additional topographic feature, such as a resurgent dome, adds a further source of uncertainty to our tests. The 'Elliptic-Caldera' scenario, already mentioned in Section 4.2.3 and shown in Figure 4.1c, includes a resurgent dome within an elliptic caldera surrounded by mild topographic highs. Dike starting points are sampled within a vertically-elongated reservoir, with higher chances at shallower depths Mantiloni et al. (2023a). In 'Elliptic-Caldera-Inv', then, we consider the height h of the resurgent dome as an additional stress parameter, and we assume a p that is skewed towards the surface (TSND, Section 4.2.4.1). The assumptions in the stress inversion are all unfavorable, as we backtrack dikes from the free surface and take $c_B \neq c$ (Table 4.2). Although the PDFs of d and h show a peak, we fail to constrain the stress parameters. In particular, d and h are biased in a similar way to Simplified-

Coastline-1-Inv, while the tectonic stress components are unconstrained. In contrast, the ratios are well constrained, with R_h being recovered remarkably well (Figure 4.6b and Table 4.3). In this case, contrary to Simplified-Coastline-1-Inv, we deem that the bias in d and h is not so much due to $c_B \neq c$, as to the choice of p and the application of the compound-stress method to a complex topography including a resurgent dome. The most significant discrepancies between the single-mesh and compound-stress results are found below the resurgent dome (Figure 4.3). Besides, the vertically-elongated p may be equally well-intercepted by dike trajectories calculated with different stress parameters. We note that there is no bias in the ratios, unlike in Simplified-Coastline-1-Inv. Both r_k and z_k are well constrained, even though the PDF of r_k shows multiple peaks. On the other hand, the inversion generally fails to constrain ϕ_k (Figure 4.7g). We run the third forecast, 'Elliptic-Caldera-For', on the results of this inversion, smoothing the PDF of r^k but not the one of ϕ_k (Figure 4.9c). Simulated vents cluster in the western side of the resurgent dome and, to a much lesser extent, along the western rim of the elliptic caldera, but most of the training and validation vents fall short of the highest V_D area. The main reason for such a discrepancy, besides the compound-stress approximation, is that, in the original scenario by Mantiloni et al. (2023a), all dikes started at a fixed radial distance from the axis of the reservoir, contrarily to the present forecast.

We run the last stress inversion on the 'Complex-Coastline' scenario, where the dike trajectories and vents are produced by TIM (Mantiloni et al., 2023a, Figure 4a). Although TIM and SAM are grounded on the same principles of fracture mechanics (Davis et al., 2020; Mantiloni et al., 2023a), the representation of dikes in the two models (mesh of triangular dislocations advancing by fractions of the dislocation size in TIM, penny-shaped crack advancing by its radius in SAM) are radically different. In 'Complex-Coastline-Inv', we assume a TSD for p and backtrack TIM dike trajectories with SAM, assuming an arbitrary value for c_B (Table 4.2). The inversion is successful in constraining d, but fails to constrain the tectonic stress components, while the ratios PDFs are peaked not far from the original values of R_{xx}, R_{yy} (Figure 4.5f, Table 4.3). Both r_k and z_k are well constrained, but the PDF of r_k is very spread-out. Two of the original dike starting angles are well constrained in the PDF of ϕ_k, but the same is not true for the remaining angles (Figure 4.7h). We use the results of this inversion to run the last forecast, 'Complex-Coastline-For'. The distribution of simulated vents is scattered, with many vents falling within the caldera. The high V_D areas, nonetheless, match the locations of the original vents, especially the ones of the validation set (Figure 4.9d).

We can point out some common trends in the stress inversion results. First, with the exception of Two-Reservoirs-Inv (Figure 4.6), the depth of the caldera, d, is usually well constrained (Table 4.3), and even otherwise (Circular-Caldera-Inv, Simplified-Coastline-Inv-1, Elliptic-Caldera-Inv), its PDF always shows a clear peak (Figures 4.5, 4.6). Secondly, the ratios between stress parameters (Equation 4.7) are always well constrained, or have PDFs showing a single maximum. Hence, the inversions recognize that surface unloading has the largest influence on the behavior of dike trajectories in our scenarios. Constraining the components of the tectonic stress tensor is generally more difficult, with worse results when the vents of the training set are all clustered on one side of the caldera (e.g. Complex-Caldera-Inv, where all vents lie on the mainland, see Figure 4.9d).

The choice of p, that is, the assumption on the dike nucleation zone, has generally the largest control on the outcomes of the inversions, as can be seen in Two-Reservoirs-Inv. The PDFs of the dike starting points (Figure 4.7) are also sensitive to p. When a TSD is considered, the PDF of r_k is centred on the radius of the original reservoir (e.g. Circular-Caldera-Inv, Refilling-Caldera-Inv), while, when a TND is chosen, it peaks closer to the origin (Simplified-Coastline-Inv-2). PDFs of z_k are generally well-constrained in all inversions, though with different standard deviations, and reflect the assumption on the depth and shape of the dike nucleation zone. The
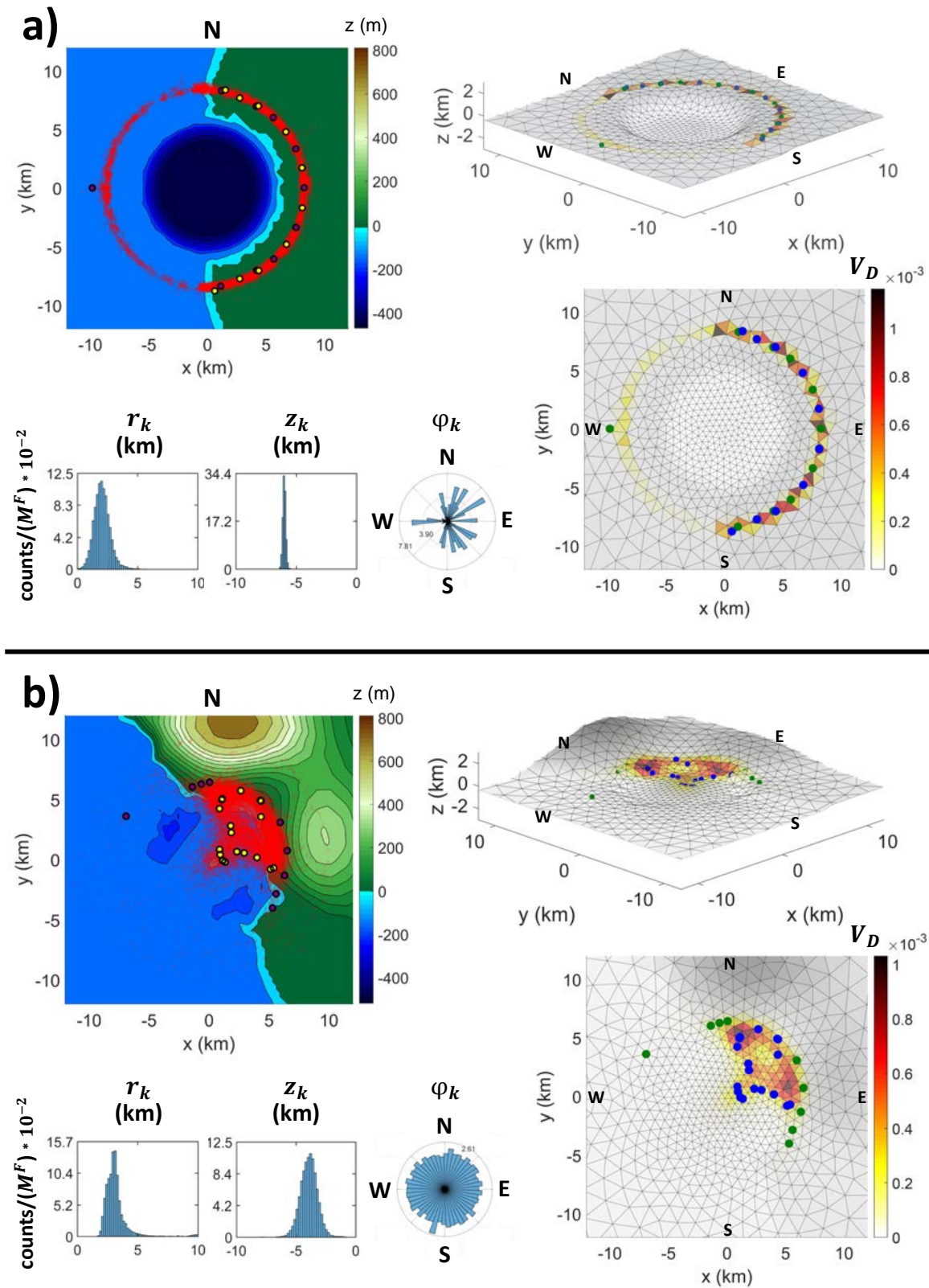
Figure 4.8: Vent forecast results, part 1. Each panel includes, from the top-left corner clockwise: map view of the distribution of simulated vents and their strike (red segments), superimposed to an elevation map of the synthetic caldera; dimetric view of the vent density (V_D) map and topography mesh; map view of V_D with color scale; distributions of the cylindrical coordinates (Figure 4.1b) of the dike starting points employed in the SAM simulations, to be compared to the PDFs retrieved from the stress inversions in Figure 4.7. a): Simplified-Coastline-1-For. b): Refilling-Caldera-For. Training and validation vents are represented in all maps as green/purple and blue/yellow dots, respectively.
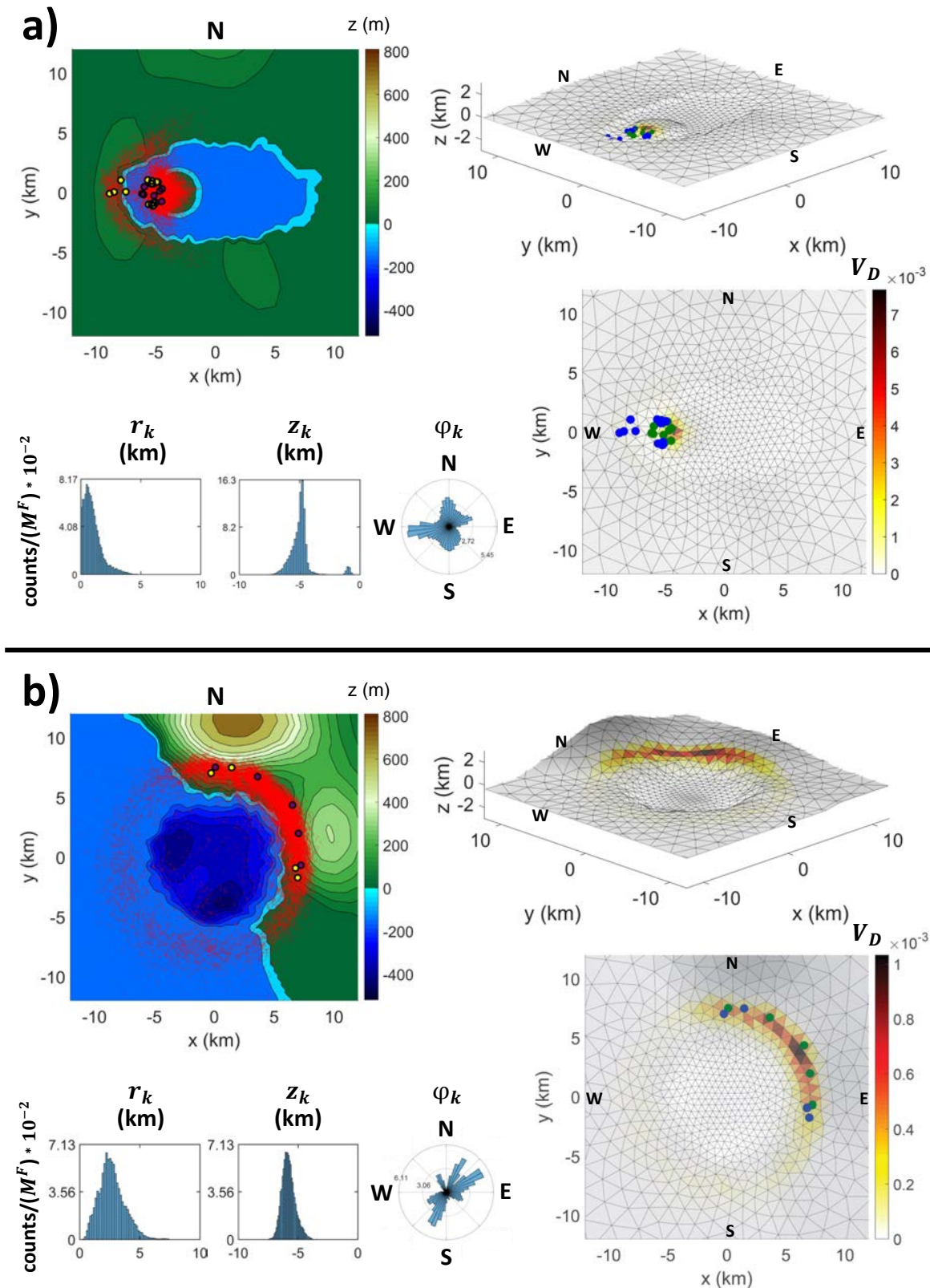
Figure 4.9: Vent forecast results, part 2. Each panel includes, from the top-left corner clockwise: map view of the distribution of simulated vents and their strike (red segments), superimposed to an elevation map of the synthetic caldera; dimetric view of the vent density (V_D) map and topography mesh; map view of V_D with color scale; distributions of the cylindrical coordinates (Figure 4.1b) of the dike starting points employed in the SAM simulations, to be compared to the PDFs retrieved from the stress inversions in Figure 4.7. a): Elliptic-Caldera-For. b): Complex-Coastline-For. Training and validation vents are represented in all maps as green/purple and blue/yellow dots, respectively.

PDFs of ϕ_k are more complex, and mostly fail to accurately constrain the individual starting angles, except in the most simplified settings.

Fixing $c_B \neq c$ biases the results of Simplified-Coastline-Inv-1, when the topography is simplified and the assumption on p reflects the original dike nucleation zone (Figure 4.5, Table 4.3), but is not as significant in more complex scenarios, such as Elliptic-Caldera-Inv, where other sources of uncertainty (multiple topographic elements, backtracking dikes from the free surface) play a larger role.

4.4 Discussion

In this work, we outline a new framework to 1) determine the stress state of volcanoes at high spatial resolution, constrained by the locations of past eruptive vents and magma reservoir, 2) determine the spatial probability of future vent opening. Moreover, we complete a set of 3D tools for computationally efficient dike trajectory simulations and stress calculation to make the framework applicable to real volcanic systems. In particular, we propose the compound-stress method as a computationally efficient approach to stress inversions including gravitational loading/unloading. We test the method with a few end-member scenarios (Figure 4.3), and find that, while the results are unreliable near the surface, the stress field at depth is recovered with sufficient accuracy to result in well-modeled dike trajectories. Additionally, we discuss how the compound-stress method can be used to constrain the gravitational loading/unloading of not only individual topographic features, but also density layering in the crust.

We test our framework on synthetic data produced by Mantiloni et al. (2023a) to determine whether the compound-stress method is able to recover the original stress state with sufficient accuracy. Testing our strategy and tools synthetic scenarios, where the parameters we aim to constrain are known, enables us to explore the uncertainty arising from the approximations we make in the stress inversion and vent forecast. Our tools allow to perform all calculations on personal computers in reasonable computation times (up to roughly two days for the inversions and forecasts performed here). They can be easily implemented/adapted with other modeling approaches.

Our stress inversions generally succeed in constraining the stress parameters or, at least, their ratios (Table 4.3; Figures 4.5, 4.6, 4.7). The forecasts are generally successful in matching areas of high vent density with the locations of validation vents (Figures 4.8 and 4.9), although their performance is worse for more complex scenarios. Here, we first summarize the technical issues of our methods. Then, we explore the opportunities and challenges of applying our strategy to real scenarios.

Stress inversions are affected by various sources of uncertainty. The assumption on the dike nucleation zone has the largest influence. The choice of c_B biases the PDFs of stress parameters and ratios, but this is more evident in simplified settings and when the uncertainty on the vertical size of D is small (compare Simplified-Coastline-1-Inv to Elliptic-Caldera-Inv in Figure 4.5). Backtracking dikes with SAM from the free surface adds more uncertainty, but does not prevent successful inversions. Finally, the compound-stress method contributes to the uncertainty, especially when considering multiple topographic features (e.g. the caldera and resurgent dome in Elliptic-Caldera) of large vertical size (Figure 4.3). This may be the reason why in Elliptic-Caldera-Inv, where a resurgent dome is included, the PDFs of individual stress parameters are spread-out and biased (Figure 4.6b), although the ratios are well-recovered, and Elliptic-Caldera-For is less successful than others in constraining the locations of validation vents (Figure 4.9c).

The stress inversion yields mixed results when applied to a set of vents produced with TIM, as shown in Complex-Coastline-Inv, where the effective caldera depth is constrained, while the tectonic stress is not. Mantiloni et al. (2023a) discussed how the accuracy of SAM in backtracking TIM pathways improves if c_B is calibrated according to the volumes of TIM dikes. Thus, in principle, knowing the volumes of the dikes that fed the V_k vents may inform the choice of c_B and improve the accuracy of the stress inversion. Assigning a different c_B to each V_k is also possible. Estimating the volume of a dike that fed an eruption in the past, however, is difficult, even with a reliable estimate of the erupted volume.

An additional source of uncertainty in the forecast arises from fixing the magma density (ρ_m), as it controls the crack driving pressure in SAM. Different assumptions on ρ_m lead to a different number of dike trajectories stopping before reaching the MDT, as Simplified-Coastline-1-For demonstrates. One solution in future applications may be to assign a PDF to ρ_m according to our knowledge of magma composition in past eruptions, and sample ρ_m from it for each forecast simulation. Alternatively, we may fix ρ_m to the lowest possible value, and run the forecast under the assumption that any future dike will be buoyant enough to reach the free surface. Finally, Refilling-Caldera-For shows the effectiveness of our stress update method (Section 4.2.5). The forecast relies on the results of Refilling-Caldera-Inv, run on a data set produced before the caldera is partially refilled. However, once the stress update is applied to the caldera depth PDF, the vent density map (Figure 4.8b) correctly predicts the locations of vents produced after the caldera refilling. This is 3D upgrade of the stress-update method by Rivalta et al. (2019) and Mantiloni et al. (2021b), and it may be applied to systems where major topographic changes have occurred since the last volcanic activity, such as caldera refilling and resurgence. Here too, further tests on more complex settings are needed.

Applying our strategy to real scenarios will come with many further challenges. First, the stress and dike propagation models which we adopt, described in Mantiloni et al. (2023a), require further testing to prove that they are adequate for representing stresses and dike pathways in real calderas. Here, we remark that a major limitation in their approach is that they do not account for stress modifications over time, due to processes such as viscoelasticity (e.g. Stephansson, 1988; Savage et al., 1992) and repeated dike intrusions (e.g. Bagnardi et al., 2013; Corbi et al., 2015; Dumont et al., 2022). Such processes may be neglected in recently-formed calderas, as the time scales are too short for viscoelastic processes to play a significant role, and dike intrusions and eruptions are generally less frequent than in other active volcanoes. Our framework, however, may be less effective in different settings, especially at large volcanic edifices where the above-mentioned processes have a much larger influence.

If a model serves a statistical purpose, its predictive power increases if its complexity is reduced (see e.g. Forster and Sober, 1994). Hence, our models aim to depend on as few parameters as possible. In fact, inversions with more parameters (Tectonic-Shear-Inv, Elliptic-Caldera-Inv) show greater uncertainty on the results. This principle also applies to our assumptions of a homogeneous host rock, which may be a very rough approximation for natural settings, but results in an 'effective stress model' that may still produce accurate forecasts, as tested and discussed by Mantiloni et al. (2021b). In this work, we have fixed the host rock elastic parameters (E, ν, Table 4.1), even though they are generally poorly known in real settings, and incorrect assumptions may bias the stress inversion results. We could, in principle, include such quantities in the model vector $\vec{m}$ (Equation 4.11) and invert for them as well.

The compound-stress method is helpful when running stress inversions with easily-available computational resources, but, as discussed in Sections 4.2.3 and 4.3.2, adds a further degree of uncertainty, especially when multiple topographic features are considered. Applying the single-mesh method to the inversions would remove such uncertainty: this can still be done with more computational resources. Despite being an approximation, we foresee that the compound-stress

method will be useful in the thorough testing on natural cases required to validate our strategy. The development of more efficient and accurate implementation of the compound-stress method is also an objective for future works.

The results of the inversions show how critical the choice of p is. Choosing p accurately will be challenging in real volcanoes, as it implies accurate knowledge about the magma storage system and the mechanisms of dike nucleation. If multiple reservoirs or melt accumulation volumes are present, it may be difficult to assign individual vents to a specific dike nucleation zone, although petrological studies on the magma composition of the associated eruptions may help. The size of a reservoir can also change between one diking episode and the next. This is a further source of uncertainty that we have not included in our tests. Simplified-Coastline-2-Inv and Elliptic-Caldera-Inv, however, show that stress inversions can be accurate even if p is not peaked about the radius where dikes started in the original scenarios.

Our vent forecast strategy is not as sensitive to missing vent locations as data-driven strategies (Selva et al., 2012; Bevilacqua et al., 2015) are. Well-established approaches to probability maps of future vent opening in calderas and monogenetic volcanic fields rely on the assumption that areas with the largest number of past vents are the ones more likely to host new vents. The implication is that, if some past vents are missing, those areas will be assigned a lower probability in the resulting maps. Conversely, in our approach, different training vents do not generally lead to significantly different PDFs of the stress parameters and, thus, forecast. However, this is not true if the training vents are clustered in a limited area, and vents from a different area are missing entirely. In such cases, stress inversion and forecast results are considerably worse. In tests not included here, Simplified-Coastline-2-Inv and Refilling-Caldera-Inv performed much worse when the offshore vents were not included in the training sets.

We do not include uncertainty in the vent locations. In future applications, we may model it by assigning a PDF to each vent. The orientation of a past eruptive fissure, if known, could also be used to constrain the stress state in the subsurface. SAM does not model shallow processes in dike propagation, and our dike trajectories stop at a minimum distance threshold from the topography mesh (Mantiloni et al., 2023a). Accounting for the influence of factors such as faulting and inelasticity in the last ∼1 km of crust, as well as the process of vent opening itself, is an interesting point for future developments in dike propagation modeling.

The models and approaches we discuss here are ready to be applied to real calderas. However, many applications are needed to further develop the stress inversion and vent forecast strategy, highlight new limitations, and mitigate them by future modeling advances. The few synthetic scenarios we considered here span over a wide range of caldera settings, which in nature may be associated with remarkably different systems. For instance, Refilling-Caldera resembles the topography and regional setting of Campi Flegrei caldera (e.g. Orsi et al., 1996; Di Vito et al., 2016), while the morphology of Elliptic-Caldera is similar to that of Long Valley caldera (e.g. Hildreth, 2004), two volcanoes with very different ages, eruptive histories and magmatic systems. Thus, the synthetic scenarios included here cannot represent the wide variability that we expect in real calderas. Applications to specific calderas will require specific assumptions, and may benefit from dedicated synthetic tests before running any stress inversion. For example, a test may consider the present-day topography in the stress model, then backtrack dikes from known vents and check if and where the backtracked trajectories overlap to refine the assumption on p, which has to be validated with prior information on the magmatic system.

An optimal case study for the applications of our models would be a caldera with a good record of eruptive activity, well-known locations of past vents and a well-constrained magma plumbing system. Knowledge of topographic evolution over time and stratigraphy would also help improving the forecast, especially if the caldera has been refilled or uplifted, or if other

events have modified the topography since the last eruptive activity. One of such examples is Campi Flegrei in Italy, a restless and well-monitored caldera which was the case study of Rivalta et al. (2019). Applying our strategy to other volcanic systems, such as large volcanic edifices, is more challenging, since, as discussed by Mantiloni et al. (2023a), our current stress models are not yet adequate to represent such settings accurately, given the influence of stress-altering processes (e.g. repeated dike emplacement, visco-elasticity, faulting) that we currently neglect.

Nonetheless, the stress optimization framework we have outlined here may be implemented with any stress model and, as such, has a wide range of potential applications that reaches beyond volcanic hazard assessment. In fact, constraining the stress state of the Earth's crust is critical to many fields of applied geophysics (McGarr and Gay, 1978), such as hydraulic fracturing in oil and gas fields (e.g. Busetti and Reches, 2014), geothermal exploration (e.g. Cloetingh et al., 2010) and the design of underground facilities for the disposal of hazardous waste (e.g. Jo et al., 2019).

4.5 Conclusions

In this work, we outline a new framework for stress optimization (Section 4.2.4) and eruptive vent forecast (Section 4.2.5) that can be implemented with different modeling approaches. We also apply a set of modeling tools, namely the model of dike trajectories SAM, developed by Mantiloni et al. (2023a), and the compound-stress method, introduced here, designed to make the problem of stress optimization tractable with minimal computing resources. We present synthetic tests that are useful to explore some of the uncertainties associated with our method, but extensive testing on natural scenarios is required to validate them. Although further advances in stress modeling are needed for some volcanic settings, our models and tools are ready for such a challenge, and lend themselves to a variety of applications in other critical geophysical problems.

Acknowledgments

Data availability statement

The open-source software *DistMesh* is found at
http://persson.berkeley.edu/distmesh/. The open-source Boundary-Element tool *Cut&Displace* is found at https://doi.org/10.5281/zenodo.3694164. The code for SAM and the data of the synthetic scenarios are available at Mantiloni et al. (2023b) and
https://github.com/LorenzoMantiloni/

Chapter 5

Lithospheric sill intrusions and present-day ground deformation at Rhenish Massif, Central Europe

Abstract

The Rhenish Massif in Central Europe, which includes the Eifel Volcanic Fields, has shown ongoing ground deformation and signs of possible magmatic activity. A buoyant plume exerting uplift forces at the bottom of the lithosphere has been proposed to explain such deformation; the hypothesis that melt is accumulating in the crust or lithospheric mantle has not been explored yet. Here, we test deformation models in an elastic half space considering sources of varying aspect ratio, size and depth. We explore the effects of data coverage, noise and uncertainty on the inferred source parameters. We find that melt accumulation within the lithosphere cannot be ruled out if it occurs in sub-horizontal sill-like structures expanding at the rate of ∼0.045 km^3/yr. We discuss our results in the context of plume and underplating models worldwide and elaborate on further observations which may help constrain the structure of the Eifel magmatic system.

Plain Language Summary

Geodetic observations over the last 20 years have recorded small but steady ground deformation over a wide area centered on the Eifel Volcanic Fields, Germany, where volcanism has occurred as recently as 11000 years ago. Together with additional geophysical and geochemical evidence of possible ongoing magmatic activity, the observed deformation has renewed interest over the origin of volcanism in the region. The deformation has previously been tentatively explained as due to a buoyant plume in the asthenosphere. Here, we use available deformation data to test whether, alternatively, deformation may be, at least partially, originating in the lithosphere. We find that deformation data are also consistent with melt intrusions in one or more horizontal lenses located in the lithosphere. We discuss how the inferred form and rate of magma accumulation compare to other volcanic regions, and what additional data may improve our knowledge on how magma is stored under the Eifel.

5.1 Introduction

The Rhenish Massif (RHM) is a large lithospheric block located in Central Europe (green contour in Figure 5.1) embedding several volcanic fields, as Westerwald, Eifel, and Siebengebirge (e.g Prodehl et al., 2006). These are part of the Central European Volcanic Fields (CEVF)

which developed during the Tertiary, and partly in the Quaternary, over a belt region spanning France, central Germany, Czech Republic, and south-west Poland (Schmincke, 2007). Activity at Eifel Volcanic Fields (EVF) started in the Tertiary with the formation of the Hocheifel volcanic field (Fekiacova et al., 2007). In the Quaternary two volcanic fields formed west and east of Hocheifel (West EVF and East EVF; green dots in Figure 5.1). The late Quaternary volcanism continued until ∼11 ka and culminated in the Laacher See Volcano eruption in East EVF at 13 ka (volcanic explosivity index VEI = 6) (Nowell et al., 2006; Schmincke, 2007; Förster et al., 2020; Reinig et al., 2021). The RHM experienced several periods of uplift with variable rates in space and time (Demoulin and Hallot, 2009), up to 0.3 mm/yr starting from the Quaternary (Meyer and Stets, 2007).

The predominant physical mechanism behind CEVF intraplate magmatism, and in particular of RHM, is still debated. Based on geochemical and geophysical evidence (deep-mantle features of volcanic rocks and gases, low seismic velocity anomaly from ∼50 to ∼410 km depth), magmatism is often related to a mantle plume located underneath RHM (e.g Ritter et al., 2001; Ritter, 2007; Walker et al., 2007). This hypothesis is, however, inconsistent with the lack of a clear space-time progression in the RHM volcanism pattern, which would suggest a hotspot track, and the volume of erupted magma is small compared to established intraplate hotspot volcanic regions as Iceland or Hawaii. Several geochemical, petrological, and geodynamic studies support alternative models linking the magmatism at RHM to plate tectonic processes associated with the Alpine collision. In this case, volcanism may be the product of fluid pathways created by induced dilatancy along shear bands in the upper mantle/lower crust and/or decompression-induced partial melting of the asthenospheric mantle due to lithospheric extension (e.g. Wilson and Downes, 1992; Regenauer-Lieb, 1998; Jung et al., 2005; Lustrino and Carminati, 2007).

Debate over the source of volcanism, availability of new/reprocessed data and signs of possible ongoing magmatic activity at EVF have renewed the interest about this area. Recent reappraisal of past seismic datasets (Dahm et al., 2020) and existing petrological and geophysical studies (Bräuer et al., 2013; Hensch et al., 2019) provided evidences of melt in lower crust/upper mantle. In particular, a long-range seismic refraction experiment in 1978-79 (Mechie et al., 1983) showed a decrease in seismic compressional wave velocities (from 8.1 to 6.3 km/s) in the upper mantle, at the crust-mantle boundary (Moho), below the currently uplifting RHM. Dahm et al. (2020) interpreted this as a sub-horizontal, thin (∼ 6 km), wide (∼ 300 km), magma reservoir with a peak melt fraction of ∼10%. Signs of ongoing magmatic activity involve degassing at mofettes and mineral springs (Bräuer et al., 2013; Caracausi et al., 2016), occurrence, since 2013, of deep low-frequency earthquakes in the lower crust and upper mantle beneath Laacher See Volcano (Hensch et al., 2019), and ongoing surface deformation (Henrion et al., 2020; Kreemer et al., 2020). Global Navigation Satellite System (GNSS) data over the last ∼20 years show uplift in RHM area with peak rates >1 mm/yr, and lower horizontal velocities with heterogeneous directions, but revealing areal dilatation approximately coincident with the uplifting area. This deformation was interpreted by Kreemer et al. (2020) as the effect of a buoyant plume impinging the lithosphere, modeled through a distribution of half-space vertical forces exerted on a plane at ∼50 km depth.

Given the geophysical indication of layers with melt concentration and large lateral extent beneath the Moho and the lack of consensus about a deep mantle plume below EVF, it appears important to explore the hypothesis that the observed deformation originates in full or partly within the lithosphere. Understanding whether melt is accumulating in the lithosphere is important to constrain the underlying mechanisms and the episodic nature of volcanism at EVF, with implications for hazard assessment here and at other anorogenic distributed continental volcanic fields. This is nonetheless challenging due to the regional scale of the observed

deformation, its overall small rates and the uncertainty on its actual timescale. Here we used the GNSS long-term linear trends (velocities) estimated by Kreemer et al. (2020) to examine whether the current deformation may be associated with a melt accumulation within the lithosphere. We explored different source solutions, shapes and depths and we analyzed the effect of different data coverage, noise and uncertainty.

5.2 Data

Kreemer et al. (2020) computed velocities both at available GNSS sites and as gridded values (at 0.1° steps, i.e. ∼10 km) obtained after data post-processing. This involves steps of de-speckling velocities computed at GNSS sites (i.e., levelling out velocity values against outliers) and subsequent gridding. The vertical gridded component was further corrected for the effect of glacial isostatic adjustment (GIA), as modelled by Husson et al. (2018). The GNSS horizontal velocities were used to compute strain-rate distribution, from which gridded horizontal velocities have been modeled. We used both dataset (at GNSS sites and as gridded values) since they represent two end-members: from originally observed velocities at GNSS sites to fully post-processed gridded values.

We focused on an area of about 400 km x 400 km (3.5° to 9.5° E, 48.5° to 51.9° N) that embeds the uplift region around the RHM (Figure 5.1) comprising 250 GNSS sites and 2135 grid nodes. We projected the GNSS sites/gridded longitude, latitude coordinates into a local metric Cartesian reference frame (X along west-east, Y along south-north) referred to the center of the study area (6.5°E, 50.2°N).

Unlike the gridded data, the provided vertical velocities at GNSS sites were not corrected for GIA. We therefore derived the GIA correction from the difference between the provided corrected and not-corrected gridded velocities and removed it from the vertical GNSS velocities (Figure S1). The vertical data show a spatially coherent uplift area over the Rhenish Massif region with highest values (∼1–3 mm/yr) at EVF (Figure 5.1b, 5.1d), while subsidence is probably related to noise and/or residual trends at continental scale (Kreemer et al., 2020).

In general, the horizontal velocities are lower than vertical ones (∼0.33 mm/yr of maximum horizontal separation rate across the uplift anomaly) and show a less clear pattern (Figure 5.1a). However, they reveal an extension region slightly offset north-west from the highest uplift area Kreemer et al. (2020) (grey line in Figures 5.1, S2).

GNSS velocity uncertainties as estimated by Kreemer et al. (2020) have median values of ∼0.1 mm/yr and ∼0.3 mm/yr respectively for the horizontal and vertical components (Figure S3a, S3b). For the vertical gridded velocities, Kreemer et al. (2020) provided two different uncertainty estimation based on the comparison between gridded velocity values and, respectively, raw (hereafter "std1", Figure S3d) or despeckled (hereafter "std2", Figure S3f) GNSS vertical velocities. std1 results larger (up to 3 times) than std2.

We therefore consider three different three-dimensional (3D: horizontal and vertical) velocity datasets: (i) raw velocities at GNSS sites and related uncertainties (hereafter "GNSS-sites"; Figures 5.1a, 5.1b, S3a, and S3b); (ii) gridded velocities with std1 vertical uncertainties (hereafter "gridded-std1"; Figures 5.1c, 5.1d, S3d); (iii) gridded velocities with std2 vertical uncertainties (hereafter "gridded-std2"; Figures 5.1c, 5.1d, S3f). In the last two cases we assumed a uniform value of 0.1 mm/yr for the uncertainties associated to the gridded horizontal velocities (Figure S3c, S3e).

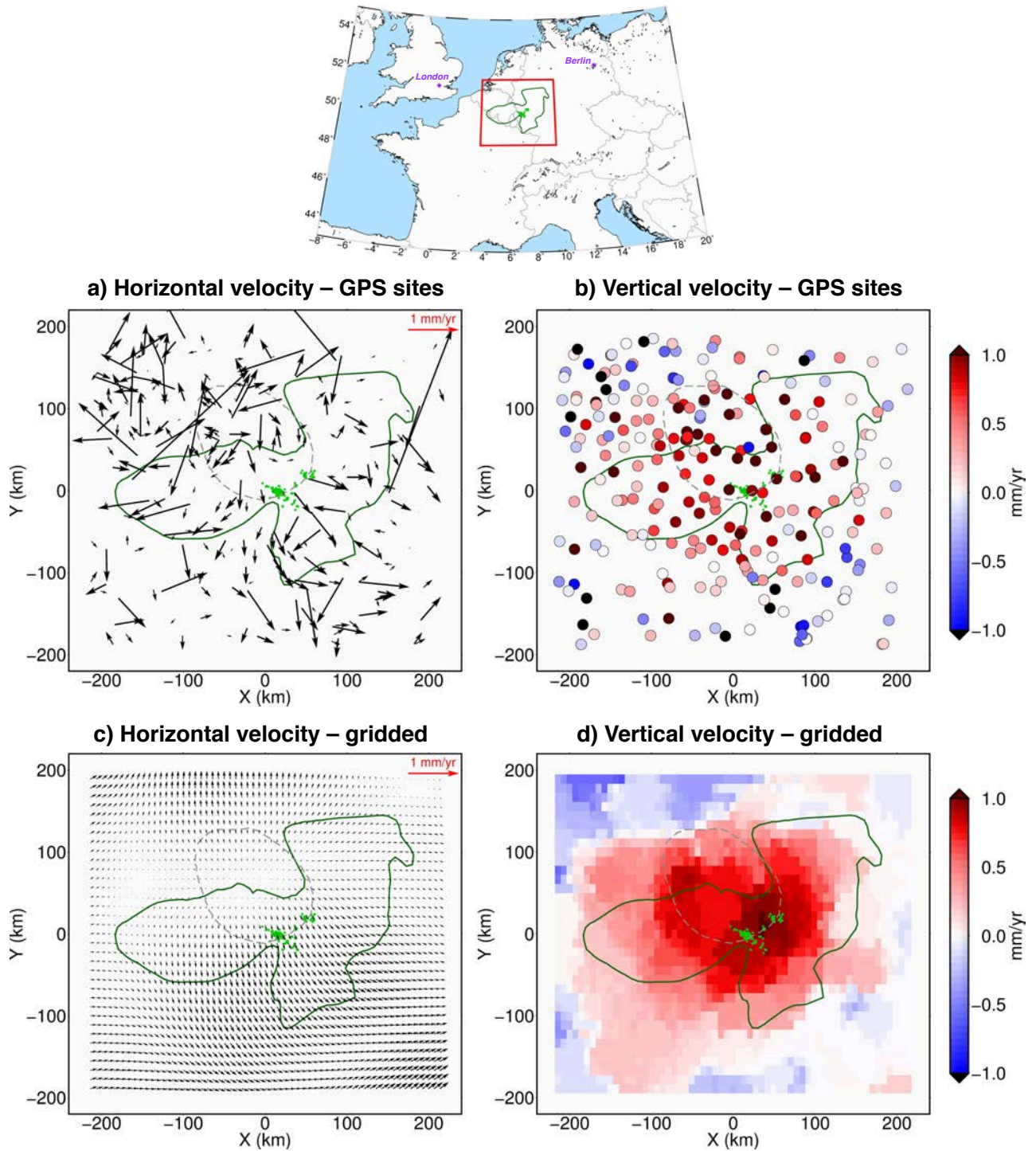**Figure 5.1:** Velocity spatial distribution at GNSS sites (a, b) and gridded values (c, d) from Kreemer et al. (2020). Inset: Geographic location of the study region (red rectangle). Green dots are centres of Quaternary EVF activity, dark green line contours the Rhenish Massif and dashed grey contour outlines area of significant (>2σ) dilatation rate estimated from Kreemer et al. (2020).

5.3 Methods

Nearly-horizontal planar volcanic sources, such as sill-like magma intrusions, typically generate a single region of uplift at the surface and are inefficient at generating horizontal deformation (e.g Troise et al., 2007; Segall, 2010). Thus, a nearly horizontal sill could be a good candidate to explain the observed deformation. Pressurized sills-related deformation can be modeled using Tensile Rectangular Dislocations (TRDs) (Okada, 1985) with prescribed uniform opening embedded in a homogeneous elastic half-space (e.g. Jonsson, 2009; Delgado and Grandin, 2021). Here we employed the TRDs solutions of Nikkhoo et al. (2017). Each TRD is defined by its position, dimensions, orientation and opening. Since we are dealing with velocities, hereafter we refer to opening rates. In order to estimate a variable distribution of opening rates, we defined a grid of TRDs ("patches") with 30 km sides and 0° dip (i.e. horizontal), strike and plunge (i.e. oriented North-South) angles. The patches dimension was chosen as compromise between the horizontal spacing of GNSS and gridded data points to reduce artefacts in the retrieved opening rate distribution (Amoruso et al., 2013). We fixed the overall source extent to the study region size (400 km x 400 km). We first set the source depth at 30 km based on the seismic waves velocity anomaly observed by Mechie et al. (1983) and Dahm et al. (2020) (Section 5.1). We additionally tested source depths between 10 and 80 km.

For a given TRDs geometry, the velocities and opening rates are linearly related as

$$\mathbf{d} = \mathbf{Gm} + \epsilon \tag{5.1}$$

where $\mathbf{d}$ is a $3N$x1 data-vector (N number of GNSS sites/grid nodes) collecting the 3D observed velocity values, $\mathbf{m}$ is a Mx1 model-vector (M number of TRD patches) collecting the distribution of opening rates, and ϵ is a $3N$x1 vector containing observation uncertainties. $\mathbf{G}$ is a $3N$xM matrix expressing the effect of unitary opening rates and estimated assuming a homogeneous half-space with Poisson's ratio of 0.25. To avoid data over-fitting and nonphysical sharp spatial irregularities in the opening rates distribution, we applied a smoothing regularization via finite-difference approximation of the Laplacian operator ($\mathbf{L}$) (Matthews, 1993). The smoothing amount to balance data-fit and opening rates-roughness is controlled through a regularization parameter k. The forward model therefore is

$$\begin{bmatrix} \mathbf{Wd} \\ \mathbf{0} \end{bmatrix} = \begin{bmatrix} \mathbf{WG} \\ k\mathbf{L} \end{bmatrix} \mathbf{m} \tag{5.2}$$

where $\mathbf{W}$ is a diagonal weighting matrix formed by the inverse of data uncertainties ($\mathbf{W}^T\mathbf{W} = \Sigma^{-1}$, with Σ as data variance-covariance matrix). Furthermore, we imposed a positivity constraint on $\mathbf{m}$ to reproduce an inflation process (uplift). We solved the resulting weighted damped least-squares problem with inequality constraints using the non-negative least-squares (NNLS) iterative method by Lawson and Hanson (1995) (*lsqnonneg* Matlab function).

To select the optimal k, we tested both the L-curve (Harris and Segall, 1987; Hansen and O'Leary, 1993) and cross-validation (CV) (Matthews and Segall, 1993; Hreinsdóttir et al., 2003) methods and we finally used CV for the GNSS-data case and L-curve for the gridded-data cases (Table 5.1; further details in Text S1 and Figure S4). Conversely, the positivity constraint precludes the use of the Akaike's Bayesian information criterion-based method (Yabuki and Matsu'ura, 1992; Fukuda and Johnson, 2008).

Iterative NNLS methods do not construct an explicit expression for $\mathbf{m}$, hindering an explicit computation of the model parameters uncertainty (e.g. Menke, 2012). We therefore employed the bootstrap method (1500 runs; Text S1) (Efron and Tibshirani, 1986).

As a further test on source parameters, we employed the horizontal penny-shaped crack model by Fialko et al. (2001) (routines by Battaglia et al., 2013). We inverted for the depth,

Table 5.1: Inversion results for TRDs and penny-shaped crack models.

4	**TRDs**			
GNSS-sites				
Depth[a]	Smoothing factor	Volume growth rate	WRSS	RMSE
(km)	(m*yr)	(m^3/yr)		(mm/yr)
10	8e12	4.899e7 $\pm$ 1.000e7	8705.909	0.5319
20	7e12	5.024e7 $\pm$ 1.165e7	8480.445	0.5316
30	6e12	4.976e7 $\pm$ 1.269e7	8396.177	0.5316
40	5e12	4.938e7 $\pm$ 1.395e7	8367.555	0.5322
50	5e12	4.883e7 $\pm$ 1.407e7	8398.961	0.5334
60	4e12	4.923e7 $\pm$ 1.582e7	8401.579	0.5343
80	3e12	5.053e7 $\pm$ 1.858e7	8452.646	0.5365
Gridded-std1				
Depth[a]	Smoothing factor	Volume growth rate	WRSS	RMSE
(km)	(m*yr)	(m^3/yr)		(mm/yr)
10	1.5e13	4.513e7 $\pm$ 1.643e6	2668.756	0.1044
30	8e12	4.301e7 $\pm$ 1.946e6	2673.179	0.1094
60	4e12	4.079e7 $\pm$ 3.574e6	3200.680	0.1260
80	4e12	4.118e7 $\pm$ 3.934e6	3494.734	0.1351
Gridded-std2				
Depth[a]	Smoothing factor	Volume growth rate	WRSS	RMSE
(km)	(m*yr)	(m^3/yr)		(mm/yr)
10	2e13	4.385e7 $\pm$ 2.010e6	11838.209	0.0959
30	1.5e13	4.388e7 $\pm$ 2.096e6	13396.295	0.0995
60	5e12	4.503e7 $\pm$ 4.961e6	17216.117	0.1125
80	4e12	4.584e7 $\pm$ 6.924e6	20829.661	0.1208

4	**Penny-shaped crack**				
Data	Depth	Radius	Excess pressure-rate[b]	Volume growth rate	RMSE
	(km)	(km)	(1/yr)	(m^3/yr)	(mm/yr)
GNSS-sites	48	173	8e-10	4.457e7	0.5351
Gridded-std1	26	176	4e-11	3.164e7	0.1210
Gridded-std2	23	224	1e-10	4.998e7	0.1233

[a]Fixed a priori.

[b]Excess pressure is defined as pressure/shear modulus

radius and dimensionless excess-pressure (pressure/shear modulus) rate of a source centered at $(X = 0, Y = 0)$ through a non-linear Nelder-Mead optimization (Lagarias et al., 1998) testing different starting values for the inverted parameters.

We finally tested whether more isotropic sources could better explain the data using: (i) the quasi-analytical solutions for surface deformation due to pressurization of a single finite (triaxial) ellipsoidal cavity in a half-space by Nikkhoo and Rivalta (2022b); (ii) point compound dislocation model (point CDM) by Nikkhoo et al. (2017). The latter is composed by three mutually-orthogonal rectangular dislocations representing planar and volumetric sources of various aspect ratios. We considered a horizontal grid of point CDMs located at the center of each TRD and at 30 km depth. We inverted for the source potency in three directions (ΔV_x, ΔV_y, ΔV_z) for each point CDM, using a weighted damped NNLS method analogous to the TRDs. A horizontal TRD-like model would correspond to a point CDM with only $\Delta V_z \neq 0$, whereas non-null values of ΔV_x and/or ΔV_y would indicate more equidimensional-like sources.
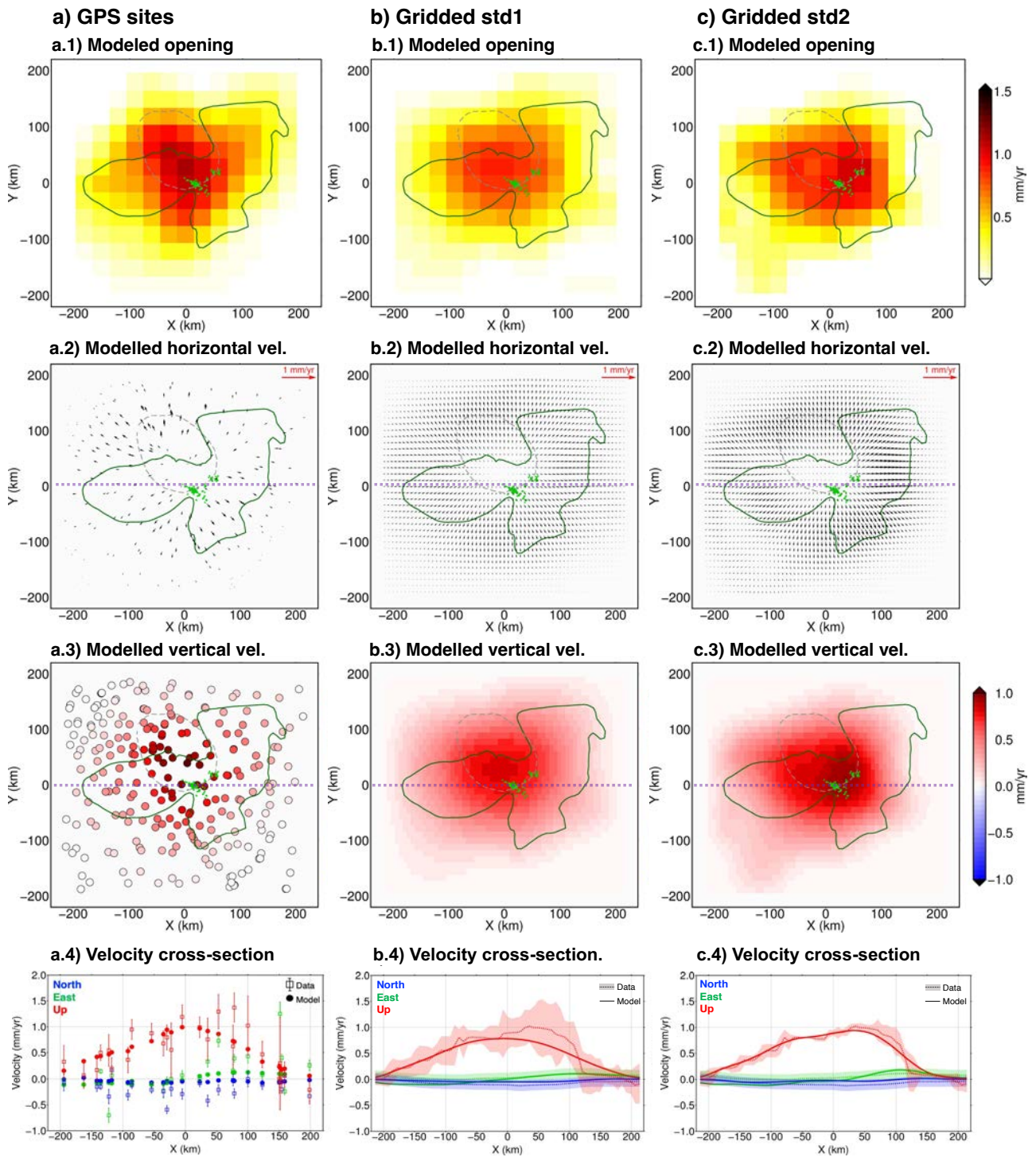
Figure 5.2: Model results for a sill at 30 km depth obtained using the different kinds of surface velocity data. The last row show modeled vs. observed data cross-sections at Y=0 (dotted purple lines in maps). All other elements are the same as Figure 5.1.

5.4 Results

TRDs inversion results suggest that the inflation of a sill of $\sim$300x300 km^2 seated at 30 km depth with volume growth rate of about 0.047 km^3/yr is compatible with the observed surface deformation (Table 5.1, Figure 5.2 and S5). The retrieved opening rate spatial distribution is mostly consistent across the three datasets reaching highest values ($\sim 0.8 \div 1.3$ mm/yr) at the center of RHM. In particular, for GNSS-sites and gridded-std1 cases the highest opening rate is mostly concentrated slightly to the north-west of the Quaternary EVF activity location (Figure 5.2a.1, 5.2b.1) and produces a horizontal velocity pattern mostly compatible with the area of significant dilatation rate (Kreemer et al., 2020) (Figure 5.2a.2, 5.2b.2). In the gridded-std2 case, instead, the highest opening rate coincides with the Quaternary EVF activity location, where the highest uplift is observed (Figure 5.2c.1). This difference is mainly due to the overall higher uncertainty (lower weight) of vertical velocities for the GNSS and gridded-std1 cases (Figures S3, S5). The effect of the low signal-to-noise ratio of vertical data is also clear from solutions obtained imposing equal weights ($\mathbf{W} = \mathbf{I}$); the main features are still consistent with the "weighted" solutions (Figure S6). The estimated volume growth rates are consistent for the three datasets ($\sim 0.043 \div 0.050$ km^3/yr), with a slightly higher ($\sim 13\%$) value in the GNSS-data case. As expected, due to the lower site coverage and higher data noise, opening rates uncertainty is higher for the GNSS-data case (Figure S7), resulting in a higher volume growth rate uncertainty (0.01 km^3/yr, Table 5.1). The modelled deformation matches reasonably well the observed one, with root-mean-square error RMSE $\sim$0.5 mm/yr and 0.1 mm/yr respectively for GNSS and gridded datasets. Further tests we conducted (adding rigid translation rates common to the whole dataset, similar to Kreemer et al. (2020); assuming a slight – up to 10° – dip angle; cleaning the GNSS dataset by spatial filtering, and removing horizontal outliers, and/or vertical negative values) resulted in minor differences and in associated volume growth rates consistent across all models.

The results for TRDs tests with different source depths (Table 5.1) show a tendency to lower smoothing factors with higher depths, since fewer patches with higher opening rates have a similar effect to smoother, spatially spread, opening rates distributions at shallower depths. Deeper sources result in slightly worse data fit, particularly for the gridded datasets (RMSE difference up to 20%). However, the misfit differences are not significant compared to data uncertainties and the results could be affected by some intrinsic level of subjectivity in the smoothing factor selection. Whereas the source depth is hard to constrain, the volume growth rates at different depths remain consistent with each other and the estimated volume growth rate uncertainty associated with the 30 km depth solution.
Results for the horizontal penny-shaped crack are consistent with the TRDs model, with optimal source depth between 25 and 50 km and corresponding volume growth rates between 0.031 and 0.050 km^3/yr (Table 5.1).

The point CDM sources test shows that, besides some inversion instabilities at the grid edges, horizontal-to-vertical potency ratios (Figure S8) have low values (<0.3) below the RHM when gridded data are used. Results for GNSS-sites data, even still indicating higher ΔV_z values below the RHM, show a more complex pattern. The inversion is however quite sensitive to the low signal-to-noise ratio of the data. The total volume growth rate associated with the point CDM model ($0.044 \div 0.052$ km^3/yr) is consistent with other tested models. We conclude that the TRDs model is suitable to explain the observed deformation and the threefold number of parameters involved in point CDMs is not needed.
Finally the tests for different source shapes using the solution from Nikkhoo and Rivalta (2022a), provide satisfying data-fit with sill-like source and consistent volume growth rate values, while excluding prolate spheroidal to explain the observed deformation.

5.5 Discussion and Conclusions

As a further hypothesis to that of a buoyant volume impinging the lithosphere by Kreemer et al. (2020), we show that the current deformation at RHS is also consistent with magma accumulation in subhorizontal structures in the lower crust/upper mantle. In order to match the deformation pattern, the source needs to be shaped as a sub-horizontal sill-like body inflating at the rate of about 0.04 ± 0.01 km^3/yr (Table 5.1). The source depth is poorly constrained due to the low signal-to-noise ratio of the observed deformation, especially for the horizontal component. Our preferred models indicate depths between 20 and 60 km. Additional challenges in our inversions are posed by (i) the source large spatial extent and the relatively shallow inferred depth, which put the source in the very-near field requiring finite-dimension source models at the limit of applicability of half-space analytical solutions (e.g. Fialko et al., 2001); (ii) the slight offset between the areas of maximum uplift and of maximum dilatation, which may be, however, at least partly related to data resolution, post-processing and gridding procedures and remaining effects of other ongoing processes (e.g., antropic activity). Further complexities such as earth curvature, topographic loading, and material heterogeneities might also play a non-negligible role.

The inferred sill dimension and volume expansion rate are large, but not implausible. Volume expansion rates similar to this value ($\sim 10^{-2}$ km^3/yr) have been observed below active volcanoes in the past, e.g. at Sierra Negra, Galapagos, in the years preceding the 2018 eruption (Bell et al., 2021). Several evidences of large sills exist ($10^2 \div 10^3$ km radius; e.g. Thybo and Artemieva, 2013; Cruden et al., 2018; Acocella, 2021). An extensive sill which hosted ~ 500 km^3 of magma, has been recently imaged in the lower crust (~ 20 km) below the North Sea rift (Wrona et al., 2019).

Possible implications for such estimated volume growth rate can be inferred based on the study from Galetto et al. (2022). The authors analysed episodes of magma supply in crustal reservoirs and found that volume increase at rates >0.1 km^3/yr have led in 100% of cases to magma propagation and eruption within 1 year, whereas rates <0.01 km^3/yr have not led to magma propagation in 90% of cases. They explained such rate thresholds in terms of stress relaxation timescale due to rock viscoelasticity controlling whether a critical overpressure is reached or not during magma supply. The magma supply episodes analysed by Galetto et al. (2022) were all located in the middle-to-upper crust, so in the RHM case the eruption likelihood would be lower. Still this deserves attention, as magma may ascend relatively swiftly from large depths (e.g. Mayotte and Cumbre Vieja, La Palma, eruptions; Cesca et al., 2020).

Prior estimates of magma extraction rate for EVF are smaller than our value of volume growth rate, but are mostly based on erupted material at local scales (e.g., lower-crust intrusion rates of $10^{-3} \div 10^{-4}$ km^3/yr beneath the East EVF; Dahm et al., 2020).

Our model would represent a magma stagnation in the lithosphere over a large region beneath RHS, and not concentrated below localized volcanic areas. In line with the alternative models proposed for RHM volcanism, magma in the sill might originate from the rise of a mantle plume underneath, decompression-induced melting from passive rifting, or a combination of the two (Acocella, 2021). Sills in lower crust might indeed form because of a rheological transition between crust and mantle, or stress field conditions in continental rift zones (Maccaferri et al., 2014). Melt ponding in subhorizontal fractures in the elastic lithosphere (underplating) has been documented in other regions to explain long-term uplift rates and surface deformation (Thybo and Artemieva, 2013; Pedraza De Marchi et al., 2021). Active magmatic underplating (Thybo and Artemieva, 2013) has been hypothesized for the region beneath the Eger rift and Cheb basin (Hrubcová et al., 2017), and for the Limagne graben (Michon and Merle, 2001), which are thought to have a common rift formation mechanism to the EVF. Further analysis is required to check whether this is the case for the Rhine Graben tectonic stress environment.

Estimates of carbon dioxide fluxes from the whole Eifel region are in the order of 0.5-1 Mt/yr (Puchelt, 1983). Assuming a magma density of 2600 kg/m^3, our volume growth rate corresponds to a mass accumulation rate of $1.2 \cdot 10^{11}$ kg/yr. This means that the CO_2 fluxes would correspond to about 1% of the magma mass rate. Similar ratios of CO_2 in parental magmas are found in continental rift regions, such as Nyamuragira volcano, Congo (Aiuppa et al., 2021).

Our estimated volume growth rate should be considered as an upper value, since inelastic rheologies such as viscoleastic relaxation and/or thermal expansion of the surrounding rock may account for part of the estimated value (e.g Newman et al., 2006; Lisowski et al., 2021). At the examined depths (few tens of km) and time scales (20 years, possibly up to hundreds of years), temperatures are already elevated, so that additional magma accumulation may have further weakened the host rock making elastic rheology an unrealistic idealization. Modeling a rheologically-complex lithosphere is however challenging due to a lack of constraints on the history of the deformation. Indeed, uplift rates in the RHM have varied considerably in time. The available GNSS time-series span a maximum of ∼20 years, but the present-day uplift rate of ∼1 mm/yr might be traceable back to several decades (e.g Mälzer et al., 1983; Ziegler, 1992).

Our inferred deformation source could correspond to the wide layer of low seismic wave velocity inferred by (Dahm et al., 2020) (Section 5.1). Furthermore, the presence of tabular zones of magma accumulation and differentiation located at several depths, possibly forming a transcrustal magma system, has been suggested by recent seismicity, tomography, and petrological studies, multi-isotope gas analysis and magnetotelluric methods (e.g Jödicke et al., 1983; Schmincke, 2007; Bräuer et al., 2013; Hensch et al., 2019; Dahm et al., 2020; Rizzo et al., 2021). We assumed the presence of a single large sill at different depths, but a series of stacked horizontal intrusions of equal cumulative volume expansion rate and sitting within the same depth range would generate a similar deformation field (e.g Amoruso and Crescentini, 2009).
Our pressurized sill model is not necessarily alternative to the presence of a mantle plume underneath, since a combination of one or more sills and a buoyant body could also reproduce the observed deformation. An additional model combining the two approaches could consider both the sill over-pressurization and any buoyancy due to the density contrast between the magma within the sill and the host rock (Sigmundsson et al., 2020). The buoyant-body model used by Kreemer et al. (2020) has weaknesses, since it implies a buoyancy force distribution over an area of about 150-180 km radius. A classical plume head leading to a mushroom-like seismic velocity anomaly has however not been imaged by seismic data, only showing a ∼60 km diameter plume stem (Ritter et al., 2001; Ritter, 2007), even if, according to some plume models, this might be due to data resolution (Wüllner et al., 2006).

Understanding the process causing the current RHM uplift and the recent unrest at EVF still requires further studies and, importantly, new and complementary observations at multiple spatial and temporal scales (e.g., deformation, seismicity, tomography, geochemistry). The spatial extent of the area under examination and the low deformation magnitude represent a challenge. GNSS data have proven to be fundamental in revealing the ongoing deformation and its spatial features, helping to better understand the deformation source. Better constraint of the deformation source would however require longer, more accurate, and possibly spatially denser measurements, together with further understanding of other ongoing processes at large (e.g. GIA), regional (e.g., faulting and seismicity within the Lower Rhine Graben) and local scales (e.g. human activity). In particular, a better-constrained ratio between horizontal and vertical surface displacements might be helpful to distinguish among different deformation-source scenarios (e.g., high-accuracy measurement of horizontal baselines across the uplifting area).
Even if previous studies showed no significant gravity anomaly unequivocally related to the EVF plume or to the regional uplift (Ritter et al., 2007; Van Camp et al., 2011), accurate

gravity measurements could in principle constrain the total mass and the nature (density) of the potentially intruding material (e.g. Nikkhoo and Rivalta, 2022a). The expected gravity changes at the free surface associated with our TRDs model is $< 0.5 \, \mu$Gal/yr (Text S2), showing that significant gravity changes (above measure uncertainties) would require long observation periods. However, absolute gravimeters campaigns of sub-μGal accuracy may help, if carried out over protracted time periods, to measure the uplift with higher accuracy, provided a careful identification and removal of effects from other deformation sources such as hydrological and anthropic activity (Van Camp et al., 2011; Nikkhoo and Rivalta, 2022a).

Located in an intraplate, stable continental environment, the RHM represents an interesting starting case for research about other volcanic areas with low deformation rates on regional scales (e.g., New Zealand). Currently ongoing measuring campaigns (e.g. dense seismic networks) at EVF will potentially contribute to shed new light on the underlying magmatic system and its implications.

Acknowledgments

Chapter 6

Conclusions

6.1 Summary

In this dissertation, I developed a comprehensive 3D framework for constraining the stress state in volcanic regions, illustrated the advantages of combining physics-based models of magma transport with statistics to improve the forecasting of future vent locations, and showed how such a method is now mature for applications to real settings. This work expands the stress inversion and vent forecast strategy of Rivalta et al. (2019) with 3D models of crustal stress and dike pathways, together with a new statistical approach where sampling of model parameters is more efficient. The inverse problem of stress state in calderas is re-defined in terms of backtracking past vents to the magma storage volume that fed them.

In the following, I summarize the achievements and results of each chapter.

- In Chapter 2, I and the co-authors demonstrate the potential of the strategy by Rivalta et al. (2019) by applying it to air-filled cracks propagating in stressed gelatin blocks. I constrain the stress state of gelatin so that the observed arrival points of cracks at the free surface match the ones of simulated crack trajectories, and forecast the arrival points of additional observed cracks. This work relies on 2D models and plane strain assumption, but improves on Rivalta et al. (2019) in terms of both stress modeling and a more efficient MCMC scheme for the stress inversion. The gelatin stress model relies on two parameters, related to the lateral strain applied to the blocks (analog for tectonic processes) and the unloading pressure of the surface excavations. Stress inversions provide posterior PDFs for the two parameters, as well as their ratio. The main result is that crack trajectories are controlled not so much by the individual parameters as their ratio, and forecast is successful as long as latter is well constrained. A notable result is also the successful forecast performed while neglecting layering in the gelatin.

- In Chapter 3, we describe the new 'Simplified Analytical Model' of dike pathways in 3D (SAM), a 3D equivalent of the 'elementary', $\vec{v}_3$-perpendicular streamline approach widely employed in 2D. SAM can also backtrack dike trajectories from a vent down through the crust. I compare SAM dike pathways to the ones predicted by the numerical model of 3D dike propagation developed independently by Davis et al. (2020, 2021) (here referred to as 'Three-dimensional Intrusion Model', TIM). I also discuss the application in 3D of the BE approach to gravitational loading/unloading by Martel and Muller (2000), and combine it with SAM and TIM to produce a set of synthetic scenarios of magma transport in calderas, where dikes nucleate from magma storage regions of different shapes and size and propagate under increasingly complex topographies. SAM and TIM pathways prove to be consistent, as long as dikes in both models start already aligned to $\vec{v}_3$. The importance of including the effect of the magma buoyancy force is also highlighted, as

SAM dike pathways can be different for the same external stress field, if the magma density changes.

- In Chapter 4, we combine SAM and the crustal stress model described in Chapter 3 with the MCMC algorithm adopted in Chapter 2 to build a strategy of stress inversion and forecast of eruptive vent locations in 3D. The strategy relies on backtracking dike trajectories from vents on the surface to a probable magma storage volume at depth, described in terms of a PDF, and optimizing the stress model so that the trajectories intersect the volumes where such PDF is maximum. I test that strategy on the synthetic scenarios of Chapter 3, with different assumptions on the magma storage PDFs, the starting points of backtracked trajectories, and the known parameters in the stress inversion. The posterior PDFs of stress parameters and their ratios are discussed as in Chapter 2, highlighting advantages and drawbacks of the new approach. In particular, when topographies are strongly non-axisymmetric, individual stress parameters can be constrained as well as their ratios. The stress inversion also returns PDFs for the dike starting points at depth. Probability maps for the locations of future eruptive vents are produced and tested on synthetic vents not employed in the inversion. The drawbacks and critical points are analyzed, but the overall performance indicates that the strategy is ready to be tested on real scenarios.

- In Chapter 5, I help performing inversions of varying deformation source models on ground deformation rates across the Rhenish Massif in Central Europe. I and the authors test the hypothesis that the ongoing ground deformation may be due to magmatic under-plating, in alternative or in conjunction with an impinging, buoyant mantle plume. The Rhenish Massif includes the Eifel Volcanic Fields in Germany, which have witnessed volcanism as recently as $\sim$11 ka BP and are currently experiencing unrest. We find that the observed deformation rates are compatible with melt accumulation in sub-horizontal, sill-like structures within the lithosphere, occurring at the rate of $\sim$0.045 km^3/yr. We also discuss what additional observations are needed to constrain the structure of the Eifel magmatic system.

6.2 Discussion

6.2.1 Why physics-based models matter in vent forecast

The assumption that future eruptions are likely to occur close to where they have in the past, or where the crust is weakened by fractures and hydrothermal activity, is often intertwined with the concept that magma tends to reach the surface through pre-existing pathways.

The rationale that pre-existing faults and fractures channel and control magma propagation through the Earth's crust is an intuitive one. Many volcanoes, indeed, exhibit open conduits where magma is either pooling for long time scales (lava lakes, e.g. Kilauea, Patrick et al., 2019b; Nyiragongo, Burgi et al., 2014) or frequently erupting (e.g. Stromboli, Carapezza et al., 2004). Yet, these volcanoes may also experience flank eruptions unrelated to the main conduit (e.g. Patrick et al., 2019a; Smittarello et al., 2022). Additionally, several volcanic systems display no open or stable magma pathway, but rather ever-changing distribution of vents. This is especially true for calderas and monogenetic volcanic fields. Even in such cases, many previous works have associated volcanism with the presence of faults, implying that they provide a readily-available pathway to ascending magma and ultimately control where it reaches the surface. Such association has been frequently made for vents near the rim of calderas and the relative rim faults (De Vita et al., 1999; Selva et al., 2012), or vents near tectonic faults

(Girard and Stix, 2010). Field observations, however, indicate that eruptive vents often align to, but do not coincide with, regional tectonic structures such as faults (Reches and Fink, 1988), rifts (Mazzarini et al., 2016) and grabens (Gómez-Vasconcelos et al., 2017). Fault-driven magma propagation has a major drawback, implicit in its formulation. The concept that magma propagation is favored where the host rock is already fractured offers no insight on which fracture magma should follow, even if we possessed detailed knowledge of the fracture network within the medium. As crustal rocks are often densely fractured and the fracture networks cannot be mapped accurately, it is then impossible to make any prediction of how magma will ascend. It may be argued that, since fractures are ubiquitous in rocks, there is no way to falsify the hypothesis that pre-existing pathways control magma propagation. On the contrary, physics-based models of magma transport, such as the ones considered here, reduce the problem to a few, tractable components, which can be understood, constrained and used to forecast future magma pathways. If they fail to match observations, they may be then falsified, but our understanding of magma propagation would still advance.

6.2.2 Achievements and features

The main achievement of this thesis is the definition of a 3D framework to constrain the stress state of a volcano and predict the locations of future vents across its area. The concept of such a framework was laid out by Rivalta et al. (2019), but developing the modeling tools and procedures needed for a 3D upgrade entailed several challenges, each requiring a long process of testing and optimization. Such challenges can be distinguished in two categories: 1) 3D models were available, but needed to be adapted for our purposes; 2) no 3D model with the desired characteristics was available. Category 1) refers to the BE numerical model of gravitational loading/unloading used in Chapter 2, and then upgraded to 3D in Chapter 3. The model is an implementation of the approach by Martel and Muller (2000) with the BE toolbox *Cut&Displace* (Davis et al., 2019) and, as such, offers no innovation *per se*. However, what Chapter 3 provides is a better understanding of the model itself, as it establishes the importance of defining a datum level and the ambiguity in doing so. Chapter 4 goes further, explaining how the approach by Martel and Muller (2000) can be used to constrain the gravitational loading/unloading of not only the topography, but also of local density layering in the shallow crust. The idea of adjusting the elevation of individual topographic features, such as the depth of a caldera, to account for the mass deficit or surplus due to unknown layers of varying density in the subsurface was already realized in 2D, but not clearly explained, by Rivalta et al. (2019). The concept of 'effective depth/height' established in Chapter 4 sets the stage for the application of that idea to realistic settings. Chapter 4 also introduces the 'compound-stress' model, which is an approximation of the original Martel and Muller (2000)'s model designed to perform fast stress calculations during stress inversions. The discrepancies between the two models are generally minor at large depths (< 2 km), but the compound-stress method is unreliable close to the topography, and is to be regarded as a first step towards future developments. Notwithstanding its limitations, it allows users to perform stress inversions within reasonable times ($\sim$30 hours for 20k iterations and 10 vents, i.e. 10 dike trajectories per iteration) with easily-available computational resources. This aspect will prove critical in the extensive testing that is needed to validate the stress inversion strategy with real-case scenarios.

Category 2 refers to SAM, developed in Chapter 3. Since the publication of Rivalta et al. (2019)'s approach, new modeling tools of dike propagation in 3D were developed by Davis et al. (2020, 2021). However, the computational cost of TIM simulations, while relatively low (typically a few minutes for a 10-km-long dike pathway), was impractical for statistical applications. What was needed was a simplified, but fast and flexible model that could upgrade the 2D, $\vec{v}_3$-perpendicular streamline approach to 3D. SAM delivers that upgrade, but is more than that,

since it includes the effect of the magma buoyancy force. Thus, it combines the flexibility and computational efficiency of the streamline approach with the possibility of reproducing realistic dike trajectories. As showed in Chapter 3, SAM and TIM simulations are consistent as long as dikes in both models start aligned to $\vec{v_3}$. On top of that, owing to its simplicity, SAM, quite uniquely, is able to backtrack dike trajectories. This leads us back to the main achievement of this thesis. The 3D stress inversion framework introduced in Chapter 4 relies on backtracking dike pathways from the vents on the surface down through the crust, and finding the stress models that bring most trajectories through the assumed dike nucleation zone. Taking vents as the starting points exempts us from assigning dike starting points at depth, which, without accurate knowledge or physical justifications, amounts to simplistic and possibly arbitrary assumptions: for instance, fixing the dike starting points at the edge of a reservoir, as done in some scenarios in Chapter 3. Re-defining the inverse problem of stress inversion in volcanoes as in Chapter 4 drastically reduces the variables and assumptions needed, and paves the way to a general framework of stress inversion and vent forecast that may be implemented with models and tools different than the ones employed in this thesis.

6.2.3 Limitations of stress and dike pathways models

The stress and dike models employed throughout this dissertation are approximations of complex natural processes and, as such, come with several limitations.

The first main assumption, common to both past and current models of dike pathways, is that of a homogeneous, isotropic host rock for dikes. This is a necessary approximation if the number of parameters to be constrained in a stress inversion is to be kept minimal, but the effects of crust heterogeneity, such as the impact of rigidity layering on dike trajectories (Maccaferri et al., 2010; Geshi et al., 2012), are neglected. This issue is tackled in Chapter 2, where rigidity layering was introduced in some gelatin blocks and, then, purposefully discarded in the models. The results show how, although neglecting the layering does have a bias on the outcomes of stress inversion, subsequent crack trajectories are still forecast successfully. The implication is that, as long as an 'effective' stress state is constrained, the missing information on rock heterogeneities may be included in the uncertainty on the stress parameters, without undermining vent forecast. We also note that large-enough dikes in nature will not respond to small-scale heterogeneities during their propagation, due to the large stress induced in the host rock at their tip.

A further limitation, common to both SAM and TIM, is that the complexity of shallow dike propagation ($<\sim$1 km depth) is completely neglected. Contrary to Chapters 3 and 4, SAM trajectories may reach the free surface if an analytical or Finite-Element model of gravitational loading/unloading was employed. Regardless, dike propagation at shallow depths can be affected by numerous processes, including e.g. faulting, inelasticity, the presence of water and loose sediments, and models grounded on Linear Elastic Fracture Mechanics, such as SAM and TIM, are unlikely to be of any avail. Addressing this limitation will involve dedicated modeling of the above-mentioned processes. The resulting models will likely be too complex to be effectively integrated into a statistical framework, but would prove useful in vent opening simulations for individual dikes.

Modeling the stress state in volcanoes is still riddled with challenges. The approach by Martel and Muller (2000), which we adopt in 2D and 3D throughout the dissertation, describes the state of stress of a solid which is emplaced at once and subject to the force of gravity. Such is the case of the homogeneous gelatin blocks presented in Chapter 2. Volcanic edifices, on the contrary, are built through a radically different process, which entails the progressive accumulation of layers of eruptive material one over another, and further processes that change the stress state in

such layers over time, as detailed in Chapter 3 and 4. Neglecting such processes may be a good approximation in calderas, where intrusions and eruptions are generally rare, if compared to stratovolcanoes and shield volcanoes. Moreover, caldera formation is a relatively abrupt event, where a large mass removal occurs over short time scales. The resulting surface unloading can, thus, be effectively modeled as illustrated in Chapter 2 and 3, provided the caldera-forming event is recent enough, so that the impact of viscoelastic processes is negligible. As such, the stress inversion strategy may be applied, as it is, to existing calderas.

The same does not apply to volcanic edifices, where stress changes are far more frequent, and both the analog and the numerical models employed in this work fail to reproduce common vent patterns when applied to such settings. This is the reason why the stress inversion and forecast are tested exclusively on caldera-like settings in this work. As discussed in Chapter 3, a simple solution to account for stress-changing processes in volcanic edifices is to scale the stress components resulting from full gravitational loading by a factor that brings shear stresses close to zero, and the diagonal components of the stress tensor close to one another (Corbi et al., 2015; Davis et al., 2021). Regardless, further advances in the understanding of stress in volcanic edifices are necessary.

The models employed here also neglect the stress contribution of pressurized reservoirs. Chapter 3 explains how such contribution is significant only in the proximity of a reservoir, and thus is not relevant in the modeling of dike pathways at larger scales, although it can play a leading role in controlling dike nucleation.

All the previously-mentioned limitations may be removed or mitigated in future works. It is worth noting, however, that simple models have a distinct advantage over more sophisticated ones: constraining a smaller set of parameters require less data and less assumptions on quantities that are generally poorly-known (e.g. TIM dikes require a volume, SAM dikes do not). Moreover, complex, *ad-hoc* models may reproduce a specific set of data with great accuracy, but may fail if new data are introduced. Confining our modeling effort to the dominant mechanisms modulating a physical process (in our case, dike propagation) ensures that our model may reproduce all sets of data with sufficient accuracy. The implication is that, in statistical applications, the predictive power of a model increases, if it can capture the first-order state of a system with the smallest number of parameters (Forster and Sober, 1994).

The final and main limitation of the models and concepts presented in this thesis is that they have been tested with analog models and synthetic scenarios, but lack applications to nature. As a result, it is still unclear in what circumstances they may be adequate or too simplistic to represent natural processes. Thus, extensive testing on calderas, monogenetic volcanic fields and, in the long run, stratovolcanoes and shield volcanoes is required to assess the validity of the tools developed so far.

6.2.4 Uncertainties from models and observables

The stress inversion described in Chapter 4 provides posterior information on the parameters controlling the stress model. The uncertainty on the information is determined by several factors, some arising from the characteristics of the models, some from observations, and some intrinsic to the problem itself.

Model uncertainties are due to the approximations made when implementing the models of stress and dike trajectories in the stress inversion and vent forecast. As discussed in Chapters 3 and 4, backtracking dike trajectories with SAM is less accurate when starting from surface vents. Assumptions on SAM parameters, such as the dike radius and the magma density, are also a source of uncertainty. The most significant model uncertainty, however, is due to the compound-stress method developed in Chapter 4. Such a method is a rather coarse approximation of the

method by Martel and Muller (2000) which I apply in Chapter 3. The discrepancies between the two approaches become significant at distances from the topography mesh equal to roughly twice the average size of the mesh dislocations, and the method is utterly unreliable at distances of ∼1 km from the free surface, as it involves the superposition of stress models calculated with meshes of different elevation. Thus, stress calculations at shallow depths and within the topography itself are impossible with the compound-stress method. This is not an issue in the tests discussed in this thesis, where the elevation of topographic highs is smaller than the MDT defined in Chapter 3, so that dikes are not propagated within them. Nevertheless, the compound-stress method, as it currently stands, is not applicable to model dike propagation within large volcanic edifices, and needs to be further developed. We remind that the issue can be avoided by applying the original approach by Martel and Muller (2000) (single-mesh method in Chapter 4) to stress inversions, at the cost of much longer running times. If the aim is to reduce the computational cost, then an approximation of the single-mesh method is needed. Any approximation, no matter how much more accurate than the compound-stress method, will inevitably involve some discrepancies.

Uncertainties arise from the observables a well. Uncertainty on vent locations, which may be very large for poorly-known past eruptive events, translates into uncertainty on the starting points of backtracked dike trajectories. Although in Chapter 4 we take the drastic assumption that vents are fixed points, we can model such uncertainty by assigning a PDF to the vent location, possibly also informed by the fissure orientation. In contrast to fully data-driven approaches to vent forecast (e.g. Selva et al., 2012; Bevilacqua et al., 2015), missing a vent in a specific area does not necessarily mean that such an area will be assigned a low probability of vent opening. However, an incomplete record of past vent locations may still bias the stress inversion results, as discussed in Chapter 4, especially when the known vents are all clustered in a localized area. In a real case, no matter how accurate the knowledge on past vent locations is, some vents may have been buried by volcanic products in subsequent eruptions, thus removing potential data. Furthermore, many dikes, both in nature and in the models, stop before reaching the surface (Rubin, 1995; Maccaferri et al., 2016; Smittarello et al., 2022), and are difficult to identify in the crust (through e.g. seismic tomography). There is no obvious solution to such missing data. Dividing the available vents into various training sets and testing the stress inversion with each of them may be useful, as significantly different results may suggest that data are too scarce to accurately constrain the stress state.

On the contrary, uncertainty on the location, size and shape of the dike nucleation zone, as defined in Chapter 4, is directly related to the performance of the stress inversion. Identifying a dike nucleation zone implies, on one hand, reliable knowledge of the magma plumbing system of a given volcano, which can be gained by a variety of geodetic and geophysical techniques (e.g. seismic tomography, petrographic analysis, inversion of ground deformation data). On the other hand, it entails a deeper understanding of the process of dike nucleation and the mechanisms that favor and control it. Chapter 5 demonstrates the challenges inherent to constraining the magmatic system of a volcano, especially when dealing with large regions of distributed volcanism such as the Eifel Volcanic Fields (EVF). The interpretation of the ground deformation rates across the Rhenish Massif given in Chapter 5 envisions magma accumulation in sill-like structures over an extremely large area in the lithosphere, but the presence of magma lenses stacked at varying depths cannot be ruled out, as well as that of a mantle plume impinging on the lithosphere. Results from past seismic tomography (Mechie et al., 1983; Dahm et al., 2020) do highlight a region of decreased seismic compressional wave velocities beneath the Rhenish Massif, but offer so far no unambiguous interpretation. Focusing on the EVF alone, the structure of the local magmatic system may be more complex, with possible shallow reservoirs and melt accumulation at shallower depths in the crust (Hensch et al., 2019). An application of the vent forecast strategy outlined in this thesis to the EVF would rely on all such information

on the magmatic system to define the dike nucleation zone in the most accurate way possible. For instance, the deformation source models constrained in Chapter 5 would be the preliminary step in defining a PDF for the deep dike nucleation zone of the EVF region.

6.2.5 Alternative stress inversion strategies

Alternative strategies to constrain the stress state in volcanoes have been proposed in recent years by Zhan et al. (2022) and Maerten et al. (2022). As discussed in Chapter 4, they consider observables different than past vents, namely, focal mechanisms of recorded earthquakes (Zhan et al., 2022) and exposed dike trajectories or the orientation of eruptive fissures (Maerten et al., 2022). Neither of the two approaches, however, offers a comprehensive solution to realistic stress inversion. Zhan et al. (2022) adopt a trial-and-error approach to stress optimization, while Maerten et al. (2022), despite using a 3D stress model, project the exposed dikes or the strikes of eruptive fissures on a 2D plane, where stress calculations are made. They show, nonetheless, the advantage of considering observables other than the location of past vents in stress inversion. Numerous works in the past have monitored stress changes in volcanoes through observed seismicity (e.g. Dieterich et al., 2000; Aoki, 2022). Stress inversion methods based on focal mechanisms of observed earthquakes have been applied to oil, gas and geothermal reservoirs as well. On the contrary, exposed dike pathways are rarely available, and are usually found in heavily-eroded and no longer active volcanic systems, which hold little interest for volcanic hazard assessment. Maerten et al. (2022), however, use the orientation of eruptive fissures as an indicator of the local stress state in a volcano, since it is related to the orientation of the underlying dike. Modeling shallow dike propagation and vent formation is beyond the scope of this work, as it involves complex processes such as the interaction between a dike and the free surface and non-elastic rheology of shallow rock layers. Nonetheless, the orientation of past eruptive fissures is an additional observable that may be integrated into our strategy, together with observed seismicity.

6.3 Outlook

6.3.1 Application to real cases

The vent forecast strategy presented here is equipped with the 3D stress and dike pathway modeling tools to be tested on existing calderas and distributed volcanic fields. Plenty of potential case studies are available worldwide, where large populations are exposed to major risks of life and economic losses (e.g. Campi Flegrei caldera, Italy, > 4 million people, De Vivo et al. 2019; Auckland Volcanic Field, New Zealand, > 1.3 million people, Lindsay 2010).

The reliability of stress inversion and forecast results will likely be affected by the quantity and quality of observables. More specifically, an optimal case study requires a detailed and long-spanning eruptive history, with a large record of eruptions and well-constrained locations of the respective vents. The size, shape and location of magma storage volumes should also be well-constrained, while petrological and geochemical analysis may associate specific eruptions with different storage depths of a magma reservoir. More generally, it should be possible to divide the eruptive history into distinct epochs of activity, on the basis of changes in the eruption style, magma composition and vent distribution. These epochs of activity, in turn, would mark different 'reference states' of the system over time, which would be constrained by stress inversions relying only on the vents belonging to each epoch. The knowledge of how the topography has changed as a consequence of eruptive events, such as the progressive refilling of the caldera, resurgent domes, craters and scoria cones, would help distinguishing between such reference states, and possibly updating the retrieved stress state for the most recent epoch

to the current conditions of the region, as illustrated in Chapter 4. Finally, a well-constrained stratigraphy of the caldera or volcanic field would inform the assumptions on rock density and elastic parameters in the models. Collecting and managing such diverse information for any given volcanic region involves cooperation between experts in different fields of geology and geophysics. In particular, the contribution of geochemists and structural geologists will be critical. The result may be a more comprehensive overview of the system and its evolution, a deeper insight into the processes that have shaped it, and a better understanding of the hazards it poses.

The model limitations discussed earlier, however, mean that some case studies are more suited than others for an application of the strategy. Calderas that formed in the relatively recent past, such as Campi Flegrei ($\sim 40,000 - 39,000$ years BP for the Campanian Ignimbrite eruption, see e.g. Giaccio et al., 2017), are better candidates than calderas with a longer history, such as Long Valley, California (Hildreth, 2004). The reason is that the stresses induced by the caldera formation are less likely to have been changed or relaxed by inelastic processes if the caldera is younger, and, therefore, our stress model may be more accurate. Campi Flegrei caldera, in particular, is a prime candidate for application, as it is a well-monitored system with a long record of eruptive activity (Orsi, 2022), many well-constrained vent locations (Smith et al., 2011) and a magmatic system which, though not entirely resolved, has been modeled by numerous works (Trasatti et al., 2011, 2015; Di Vito et al., 2016; Montagna et al., 2022). Nonetheless, Campi Flegrei presents several modeling challenges, such as complex stratigraphy and fault networks (Orsi et al., 1996) and a large hydrothermal system that may significantly contribute to ground deformation in periods of unrest (Lima et al., 2009; Calò and Tramelli, 2018; Mantiloni et al., 2020).

Monogenetic volcanic fields are also candidates for application, but present an additional challenge, since they often have no obvious relation to a well-resolved magma storage system, as it is often the case for calderas. This is the case, for instance, of the Auckland Volcanic Field in New Zealand (Hopkins et al., 2021). As shown in Chapter 4, assumptions on the dike nucleation zone have the largest influence on the outcomes of stress inversions, and depend on the prior knowledge on the magmatic system of a volcano. Monogenetic volcanic fields also encompass a wide range of volcanic systems, spanning over varying spatial and temporal scales (e.g. Connor et al., 2000). Individual cases might then be more or less suited for applications.

In this regard, Chapter 5 offers some insight on a potential application of vent forecast to a rather challenging case study: the Eifel monogenetic Volcanic Field (EVF) in Germany. Although the volcanic hazard in the area is not deemed as high as in other volcanic systems, the risk posed by an event comparable to the Laacher See eruption ($\sim 12,900$ years BP) is considerable, in terms of life and economic losses (Leder et al., 2017; Hensch et al., 2019). In contrast to other case studies, such as the Campi Flegrei caldera, the location and age of past vents are generally poorly constrained, and the magmatic system, both locally at shallow depths and regionally across the lithosphere, has not been resolved yet (Dahm et al., 2020). As mentioned earlier, the debate over the source of volcanism in the EVF is still ongoing, as well as that over the cause of the ground deformation across the larger Rhenish Massif region. Chapter 5 explores the hypothesis of melt accumulation over very large tabular structures in the lithosphere, constraining the varying deformation source models with GNSS data by Kreemer et al. (2020). Such results, however, only help resolving the deep, large-scale magmatic system below the Rhenish Massif, which may have fed volcanism in the EVF over time. Local magma storage at shallower depths must also be accounted for: in the EVF, the presence of local crustal reservoirs that may have fed eruptions in the past has been suggested by petrological, geochemical and seismic evidence (Schmincke, 2007; Hensch et al., 2019; Dahm et al., 2020). The distinction between large-scale, deep and local, shallow melt accumulation volumes hints at

two possible applications of the vent forecast strategy. In the first case, a stress inversion may be performed by matching the EVF vents with a large magma reservoir at the crust/mantle boundary, such as the one discussed in Chapter 5. Given the extent of the considered region, vent locations may be assumed point-like. The resulting probability map of future vent opening would provide a general picture of the areas across the Rhenish Massif most likely to host volcanism. The second application, instead, may focus on individual volcanic centers and clusters of vents, and would require the accurate constraint of both vent locations and local magma storage. Uncertainty on vent locations would also have to be included. The end product would be more detailed probability maps focused on specific portions of the EVF, and suited for assessing volcanic hazard locally. The prerequisites for both applications are 1) a better understanding of magma storage at different depths and lateral scales; 2) a more comprehensive and detailed record of past eruptive activity, with well-resolved vent locations and ages. As long as those prerequisites are not met, any application of the vent forecast strategy would be speculative.

Applications to large volcanic edifices, such as stratovolcanoes and shield volcanoes, are not viable with the stress model as it currently stands, for the reasons explained in Chapter 3. Testing on such settings will be possible only after meaningful advances in the modeling of stress-changing processes within volcanic edifices. All the challenges and uncertainties listed so far (e.g. unconstrained vent locations and/or magma storage) will still apply.

In summary, applications to nature require, first, establishing what settings are more suited to the models that are currently available. Next, it is necessary to gather as much prior information as possible on past eruptive activity and past/current magma storage. If such information is not readily-available in literature, new data may be acquired through different geodetic/geophysical techniques. Once this preliminary process is complete, testing of stress inversion and vent forecast may lead to new uncertainties and limitations that need to be explored and, possibly, overcome. It is a challenging endeavor, but the potential improvement in volcanic hazard assessment makes it worthwhile.

6.3.2 Volcanic edifices

As mentioned earlier, modeling the stress state within large volcanic edifices requires additional effort. Taking into account all the known processes that may alter stresses over time, such as viscoelasticity, faulting and magmatic intrusions, with a comprehensive model is challenging, since each of them is currently modeled with different degrees of sophistication, and all models rely on parameters which are often poorly constrained. A more feasible ask in the short term could be integrating the approach to gravitational loading and tectonic stress employed here with the stress changes induced by repeated dike intrusions within the edifice. Recently, Dumont et al. (2022) showed the leading role played by previous dike intrusions in controlling the emplacement of subsequent dikes in Piton de la Fournaise, Réunion Islands. Current dike propagation models, including SAM and especially TIM, are able to reproduce the strain induced by such intrusions on the surrounding rock. Applying such models to large and well-constrained data sets, as the one by Dumont et al. (2022), would improve our understanding of stress evolution within volcanic edifices. With a more accurate stress model, the present stress inversion strategy may be applied to such settings as well, possibly integrating past vent locations and orientations with other stress indicators, like seismicity (Zhan et al., 2022).

6.3.3 Dike velocity

The dike propagation models discussed in this dissertation are not able to predict the velocity of dike propagation, as discussed in Chapter 3. Knowledge of dike velocity, however, is critical

in the context of short-term forecast, as it provides an estimate of the timing between the onset of magma propagation deep in the volcanic system and the eventual eruption. Such physics-based, short-term scenarios for individual volcanic crisis would be fundamental in minimizing life and property losses, yet are currently unavailable, and cannot be addressed by the forecast strategy presented here. The solution, however, might not be too far. Modeling of dike velocity, in both 2D and 3D, has advanced remarkably in the last decade. Pinel et al. (2017) developed a 2D model which, first, resolves for the dike trajectory (Maccaferri et al., 2011) and, next, runs a one-dimensional dynamical model of dike propagation along the trajectory, thus resolving for the dike velocity as well. More recently, Zia and Lecampion (2020) developed *PyFrac*, a numerical simulator of 3D planar hydraulic fracture growth, based on the algorithm by Peirce and Detournay (2008). The tool includes, among other features, the lubrication flow of fluid within the fracture and the possibility to account for elastic anisotropy in the host rock. *PyFrac* was later applied by Möri and Lecampion (2022) to study the transition of a vertical hydraulic fracture, subject to a constant rate of volume injection, from an initially radial fracture to an elongated, buoyant growth. Davis et al. (2023) developed an analytical solution for the size and ascent speed of 3D fractures with a fixed volume of fluid, and used *PyFrac* to benchmark their analytical results. The growth of hydraulic fractures has also been studied by Pansino et al. (2022), who applied a numerical model of a fixed-shape dike growing vertically and laterally, under both constant and variable influx of fluid, to analog experiments and the growth of dikes observed in Piton de la Fournaise (Peltier et al., 2005). Finally, Furst et al. (2023) developed a BE numerical model which calculates the growth and dynamic shape of a fluid-filled crack as a function of fluid viscosity and crack velocity in a heterogeneous external stress field, under plane strain assumption.

The models of dike propagation presented in this thesis can provide some of these approaches with pre-calculated 3D pathways, where dike velocity may be computed. Furthermore, external stress, which the stress inversion strategy of Chapter 4 aims to constrain, is a critical input in the previously-mentioned models. Future developments in this field may soon deliver a model capable of resolving for the 3D pathway, shape and velocity of dikes under varying conditions and assumptions (e.g. constant or variable volume or host rock heterogeneities).

6.3.4 Integration with different approaches

The vent forecast strategy developed here may be an important component of larger, more comprehensive frameworks of volcanic activity forecasting. As suggested by Bartolini et al. (2013) and Marti and Felpeto (2010), physics-based and data-driven approaches to future vent forecast are not necessarily competing, and may rather complement each other. More generally, both approaches may be included into event trees (Marzocchi et al., 2008; Connor et al., 2015), where the possible evolution of an eruption is represented by nodes and branches describing the particular outcome of specific events and hazards, each with an assigned probability, and long- and short-term forecast are combined into a unified framework (Poland and Anderson, 2020). Physics-based vent forecast provides a spatial probability of eruption occurrence, and would help informing the event tree. Yet, physics-based models are rarely used in this context, as acknowledged by Poland and Anderson (2020), meaning that a wide range of potential applications lies ahead.

6.3.5 Beyond volcanic hazard: Why stress matters

As discussed in Chapter 4, the potential of accurate models of crustal stress reaches beyond the domain of volcanic hazard assessment, and has significant implications for several fields of applied geophysics (McGarr and Gay, 1978).

Determining the intensities of local principal stresses and the orientation of their axes is critical in predicting hydraulic fracturing in oil and gas fields (e.g. Busetti and Reches, 2014), together with reliable models of fluid-filled crack propagation such as the ones discussed in this thesis (see e.g. Davis et al., 2020). Furthermore, the local stress state dictates wellbore failure and sand production in oil drilling (Wiprut and Zoback, 2000), as well as reservoir stability under fluid injection or extraction (Martínez-Garzón et al., 2013). Geothermal exploration and production is particularly dependent on accurate assessment of subsurface stresses (Cloetingh et al., 2010), and many of the areas that host such activities coincide with active volcanic systems: for example, the Krafla geothermal field, Iceland (Nielsen et al., 2000), the Mammoth Geothermal Complex in California (Bertani, 2016), and the geothermal fields in the Taupo Volcanic Zone, New Zealand (White and Chambefort, 2016). The development of reliable methods of stress inversion applied to such regions can lead to a more efficient exploitation of natural resources, waste reduction and reduced environmental impact of human activity. Finally, the design and construction of underground storage facilities for oil, gas (e.g. Jeanne et al., 2020) or hazardous waste (e.g. Jo et al., 2019) also relies on assessing the stress state of the rock mass that will host them.

Hence, the models and strategies developed in this dissertation can benefit multiple fields of research, and improve the understanding of different geophysical processes.

Supporting Information for Chapter 2

The present Supplement includes information on scaling factors and measured parameters of the experiments we considered in the main text (Tables S2.1 and S2.2) and the data sets we employed for inversions and forecasts (Tables S2.3 and S2.4), as well as further results from the inversions (Table S2.5).

We also show larger versions of the pictures of the experiments displayed in the main text (Figures S2.1 and S2.2), together with pictures of three discarded compressional experiments (Figure S2.3). Additional results of two tests we performed are shown in Figure S2.4.

The data displayed in Tables S2.1, S2.2, S2.3, S2.4 and S2.5 were either collected or evaluated between September 17, 2019 and May 25, 2020. Surface arrival points in Table S2.3 were measured with a ruler directly on the surface of the gelatin blocks as soon as the experiments were over. w in Table S2.2 was measured likewise. Imposed values of parameters d and h were measured with a digital caliper (in the case of h the measure was repeated 3 times on different points of the excavation floor), and T_{surf} was measured with a digital thermometer.

Information on possible discarded crack trajectories in the experiments are reported in the captions of Figures S2.1 and S2.2.

Table S2.1: Scaling factors between reference cases in nature (rift-like or caldera-like settings) and our experimental setup. The parameters L^* and σ^* are defined in the main text (Section 2.2.1).

	Parameter (units) or equation	Nature (k=r)	Experiments (k=gel)	Scaling ratio
Medium and fluid properties				
Host medium density	$\rho_k\ (\frac{kg}{m^3})$	2500	1020	
Fluid density	$\rho_f\ (\frac{kg}{m^3})$	2400	1	
Density contrast	$\Delta\rho_k = \rho_k - \rho_f\ (\frac{kg}{m^3})$	100	1019	
Poisson's ratio	ν	0.25	0.49	
Fracture toughness	$K_c^k\ (Pa \cdot m^{\frac{1}{2}})$	$0.2\text{-}1 \cdot 10^9$	60-80	
Gravitational acceleration	$g\ (\frac{m}{s^2})$	9.81	9.81	
Geometry				
Rift/Caldera diameter	w (m)	$5\text{-}25 \cdot 10^3$	$60\text{-}70 \cdot 10^{-3}$	$2.4 \cdot 10^{-6}\text{-}1.4 \cdot 10^{-5}$
Rift/Caldera depth	h (m)	$0.1\text{-}1 \cdot 10^3$	$21\text{-}72 \cdot 10^{-3}$	$2.1 \cdot 10^{-5}\text{-}7.2 \cdot 10^{-4}$
Depth of intrusion	z^{start} (m)	$1\text{-}5 \cdot 10^4$	$1\text{-}1.5 \cdot 10^{-1}$	$2 \cdot 10^{-6}\text{-}7.5 \cdot 10^{-6}$
Scaling expressions				
Lengths				
Buoyancy length	$L = \left(\frac{K_c}{\pi^{\frac{1}{2}}\Delta\rho g}\right)^{\frac{2}{3}}$	$2.37\text{-}6.92 \cdot 10^3$	$2.3\text{-}2.8 \cdot 10^{-2}$	$L^* = 3.3 \cdot 10^{-5}\text{-}1.2 \cdot 10^{-6}$
Stress				
Young's modulus	E (Pa)	$10 \cdot 10^9\text{-}10 \cdot 10^{10}$	$2.3\text{-}3.15 \cdot 10^3$	$2.3 \cdot 10^{-8}\text{-}3.15 \cdot 10^{-7}$
Tectonic stress	$\sigma_x = \frac{4}{3}Ee$ (Pa)	$1 \cdot 10^6\text{-}1 \cdot 10^7$	$3.83 \cdot 10^1\text{-}5.25 \cdot 10^1$	$3.83 \cdot 10^{-6}\text{-}5.25 \cdot 10^{-5}$
Unloading	$\sigma_U = \rho_k g h$ (Pa)	$2.45 \cdot 10^6\text{-}2.45 \cdot 10^7$	$2.1 \cdot 10^2\text{-}7.2 \cdot 10^2$	$\sigma^* = 8.6 \cdot 10^{-6}\text{-}2.9 \cdot 10^{-4}$

Table S2.2: Additional measured parameters for the experiments. The last row refers to the mean values assumed in the pooling of data from experiments 2DLA-6 and 2DLA-7. Column 2,3 & 5: "t" = top; "b" = bottom layers. Column 5: values of Young's modulus E in parentheses are estimates for the top layers assuming average values from the measured E of the homogeneous experiments at 2.0 $wt\%$ (2DLA-3) and on an independent set of gelatin samples at 2.5 $wt\%$ (2DLA-4). Column 6: temperature measured at the surface of the gelatin blocks immediately after their removal from the fridge. The fridge temperature is $T = 8°$ C.

# Exp.	$wt\ \%$	H	w	E	T_{surf}
		± 1	± 1		± 0.1
		mm	mm	Pa	°C
2DLA-1	2.0	190	70	2930 ± 120	10.5
2DLA-2	2.0	210	60	2740 ± 130	9.6
2DLA-3	t: 2.0	t: 120	70	t: 3150 ± 110 (2730 ± 240)	9.6
	b: 2.5	b: 110		b: 5250 ± 460	
2DLA-4	t: 2.5	t: 88	70	t: 2300 ± 70 (3800 ± 560)	9.8
	b: 2.0	b: 107		b: 1390 ± 50	
2DLA-5	2.0	196	70	2800 ± 70	8
2DLA-6	2.0	219	60	2480 ± 50	11
2DLA-7	2.0	219	60	2800 ± 60	9.8
2DLA-6&7	2.0	219	60	2640 ± 50	10.4

Table S2.3: Measured x-coordinate of arrival points of observed cracks for the experiments considered in the main text (see Section 2.2.1 and Table 2.1): x_i^{obs} and $x_i^{obs,F}$ were used for inversions and forecasts, respectively (see Sections 2.2.4 and 2.2.5). All quantities are measured according to the reference system shown in Figure 2.1a.

| # Exp. | N^I (Inversion) | | | | N^F (Forecast) | | | |
| | ± 1 mm | | | | | | | |
	x_1^{obs}	x_2^{obs}	x_3^{obs}	x_4^{obs}	$x_1^{obs,F}$	$x_2^{obs,F}$	$x_3^{obs,F}$	$x_4^{obs,F}$
2DLA-1	-86	-67	72	81	69			
2DLA-2	-118	139			126			
2DLA-3	-90	63	88		76			
2DLA-4	-70	-63	51	57	-84			
2DLA-5	-114	-95	105		-55	72	87	
2DLA-6	-90	-79			60	75	82	103
2DLA-7	82	94	102		-80	-73		

Table S2.4: Assumed depth (z^{start}) and measured x-coordinate (x_i^{start}) of the tips of observed cracks at $z = z^{start}$ for the experiments considered in the main text (see Section 2.2.3 and Table 2.1): x_i^{start} and $x_i^{start,F}$ were used for inversions and forecasts, respectively (see Sections 2.2.4 and 2.2.5). All quantities are measured according to the reference system shown in Figure 2.1a.

| # Exp. | N^I (Inversion) | | | | | N^F (Forecast) | | | |
| | ± 1 mm | | | | | | | | |
	z^{start}	x_1^{start}	x_2^{start}	x_3^{start}	x_4^{start}	$x_1^{start,F}$	$x_2^{start,F}$	$x_3^{start,F}$	$x_4^{start,F}$
2DLA-1	-100	-75	-40	51	74	5			
2DLA-2	-100	-40	85			40			
2DLA-3	-150	-70	20	70		40			
2DLA-4	-150	-40	-35	10	25	-70			
2DLA-5	-150	-90	-30	80		-1	30	50	
2DLA-6	-150	-60	-30			20	45	60	85
2DLA-7	-150	20	60	80		-40	-60		

Table S2.5: Comparison between imposed and retrieved parameters. Column 2, 5 and 8: imposed parameters. Column 3, 6 and 9: medians of the respective retrieved posterior distributions. Column 4, 7 and 10: standard deviation of the respective posterior distributions.

| # Exp. | d | d^{med} | δx_d | h | h^{med} | δx_h | R | R^{med} | δx_R |
| | ± 0.1 | | | ± 1 | | | $(\times 10^{-3})$ | $(\times 10^{-3})$ | |
	mm	mm	mm	mm	mm	mm			
2DLA-1	2.5	4.9	2.7	50	51	24	63 ± 4	100	124
2DLA-2	-2.5	-3.5	2.7	44	73	20	-57 ± 4	-55	33
2DLA-3	2.5	3.9	2.4	21	63	25	120 ± 10	69	90
2DLA-4	2.5	5.8	2.4	24	59	26	104 ± 8	102	72
2DLA-5	0	0.4	3.6	24	64	23	0 ± 10^{-2}	81×10^{-3}	78
2DLA-6&7	2.5	2.5	2.0	65	64	22	43 ± 2	39	37
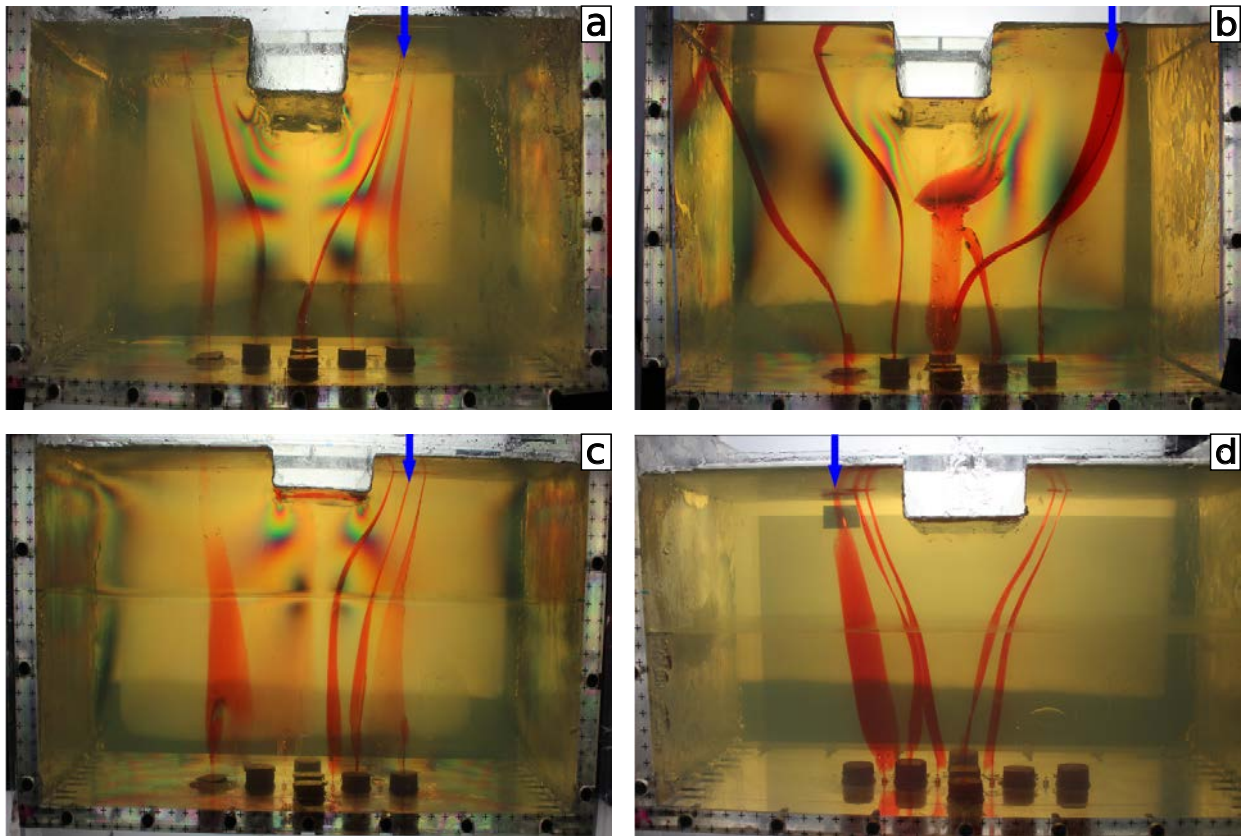
Figure S2.1: Detailed pictures of experiments with fixed imposed parameters d, h. The blue arrows point to the surface arrivals we considered for the forecasts ($x_i^{obs,F}$). a): 2DLA-1 (extension). b): 2DLA-2 (compression). The crack in the middle of the box became stuck beneath the unload as a sill-like intrusion; it eventually hit the back wall and reached the surface by further air injection. The leftmost crack was likely affected by a stress concentration due to a slight misplacement of the left side plate. Both were discarded (Table S3). c): 2DLA-3 and d): 2DLA-4 (extension + layering).

Figure S2.2: Detailed pictures of experiments with imposed parameters updated midway through their execution (either d or h). a): 2DLA-5 (extension induced in the second half of the experiment). b) 2DLA-6 and c) 2DLA-7: the surface excavations were refilled with water up to ∼55 % of their original depth after the injection of the crack sets on the left and on the right,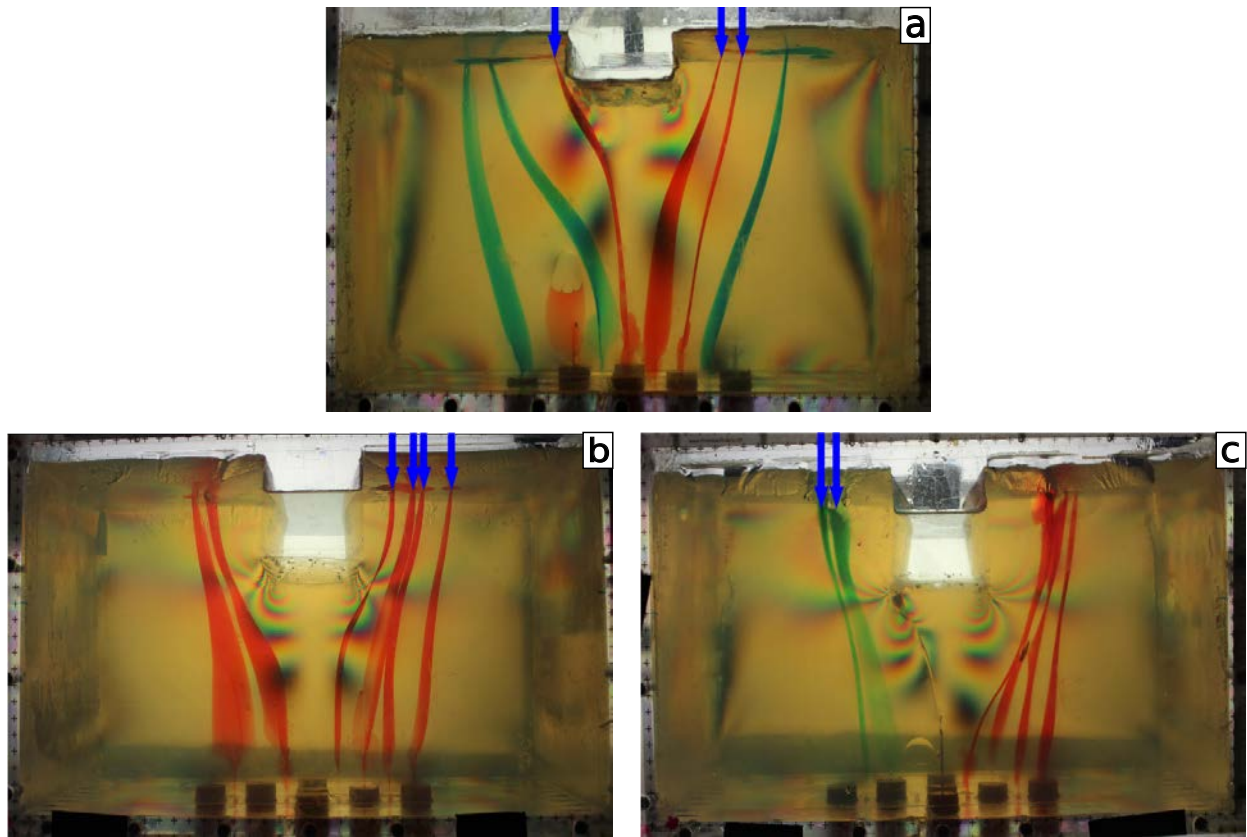 respectively, while extension was imposed in both cases. The blue arrows point to the surface arrivals we considered for the forecasts ($x_i^{obs,F}$). The difference in the color of the post-injection ink in (a) and (c) corresponds to the sets injected before and after the stress update (from green to red in (a) and reverse in (c)). The first red crack from left to right in (c) merged with the next one before reaching the surface.
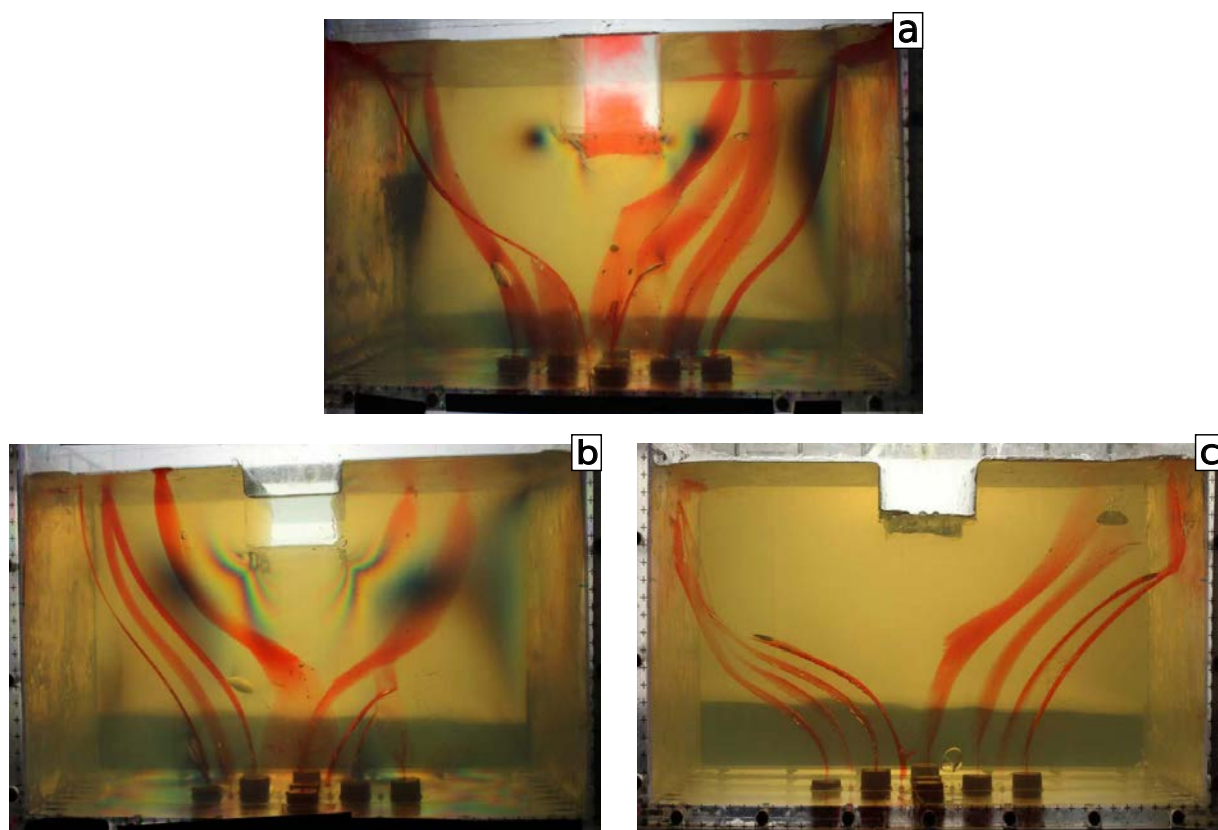
Figure S2.3: Detailed pictures of discarded experiments with imposed compression. a): 2DLA-8. b): 2DLA-9. c): 2DLA-10.
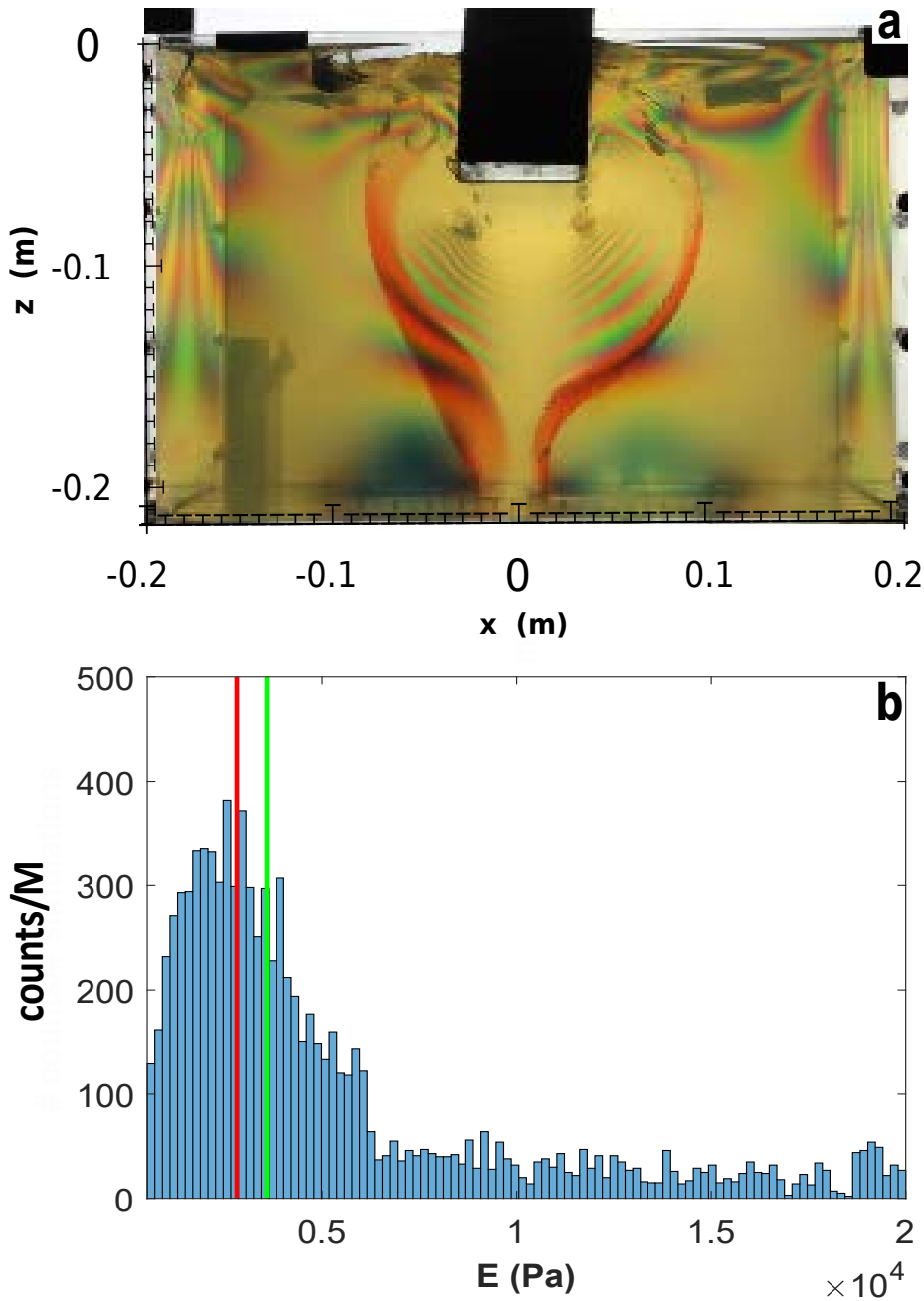
Figure S2.4: Additional tests for our strategy mentioned in Sections 2.4.1 and 2.4.2. a): Experiment 2DLA-11 (not reported in Tables 2.1 and S2.2) with $h = 10$ cm and $w = 7$ cm. The purpose of the experiment was to verify the re-focusing of crack trajectories towards the center of the surface unload once, after having been deflected by the unloading, they approach the surface. This effect was observed in numerical simulations for surface excavations with $\frac{h}{w} \gg 1$ (see Section 2.4.2). b): Posterior probability density of the Young's modulus E performed on the N^F data set of experiment 2DLA-5 (Tables 2.1 and S2.2). Here we fixed d and h as known parameters. The measured value of E is represented by a red line; the median E^{med} by a green line. E falls at the 37th percentile of the sampled PPD (see Section 2.4).

Supporting Information for Chapter 5

Contents of this file

1. Text S1 to S2

2. Figures S1 to S8

Introduction

This supporting information includes further details about the inversion methods and gravity change estimation introduced in the main text, and complementary figures for the data and results description.

Text S1. Methods of regularization parameter selection and model parameters uncertainty estimation

Once the forward problem is defined as in equation (2) of the main text, different methods exist to select the optimal value for the regularization parameter k. The L-curve method consists in picking k from the knee of a trade-off curve between model-roughness ($\sqrt{(\mathbf{Lm})^T \mathbf{Lm}}/M$) and data-misfit (in terms of – unitless – weighted residual sum of squares WRSS $= (\mathbf{d\text{-}Gm})^T \mathbf{W}^T \mathbf{W} (\mathbf{d\text{-}Gm})$) produced by solving the slip inversion with different values of k. This method is intuitive and fast to implement, but the selection retains a level of subjectivity if the knee curve point is not well defined. The cross-validation (CV) method is based on the idea that the model parameters recovered by the inversion of a subsample of the dataset (the training set) should be able to predict the data that were not used in the inversion (the validation set). The original data set is randomly partitioned into n subsamples, a single subsample is considered as the validation set, and the remaining $n-1$ subsamples are used as the training set. This test is performed for different values of the smoothing parameter, that are then compared in terms of the CVSS (cross-validation sum of squares of the predicted residuals), representing a measure of the model ability to predict observation. The most appropriate smoothing parameter is the one resulting in the lowest CVSS.

Testing both methods, we found that L-curve and CV give compatible results for the GNSS-sites case, with CV providing a clearer minimum (Figure S5.4a). For the gridded-data cases, instead, the L-curve produces a better-defined knee, whereas the CV solutions tend to be slightly under-smoothed, particularly for the gridded-std2 case (Figure S5.4b, S5.4c). We therefore selected smoothing factors through CV for the GNSS-data case and through L-curve for the gridded-data cases.

We have applied the bootstrap statistical method (Efron and Tibshirani, 1986) in order to estimate opening rates uncertainties. This technique consists in creating synthetic datasets by randomly selecting, with replacement, N points from the original dataset, where N is the number of GPS sites/grid points. For the new sample of N points (some of which are redundant selections from the original sample, while some points in the original sample are missing), the opening-rate distribution is recomputed using the same inversion method explained in Section 3 of the main text. By implementing this process many times, a distribution of opening rates values is constructed for each patch and, from this, a meaningful statistical uncertainty value can be estimated.

Text S2. Gravity change estimation

We estimated the total expected gravity changes at the free surface of an elastic half-space associated to our TRDs model (assuming 30 km depth) using the solutions from Okubo (1992) as implemented by Beauducel (2022). The expected gravity signal is dominated by the free-air effect so that its spatial pattern is similar to the modeled uplift. Assuming a half-space density of 2600 kg/m^3 and a lower density for the intruding material, we obtain a total gravity change up to about -0.3 μGal/yr. This corresponds to 0.1 μGal/yr after removal of the free-air contribution estimated using the predicted uplift and the theoretical free-air gradient -308.6 μGal/m.

a) Vertical vel. before GIA correction – gridded   **d) Vertical vel. before GIA correction – GPS sites**

b) Vertical vel. GIA contribution – gridded   **e) Vertical vel. GIA contribution – GPS sites**

c) Vertical vel. corrected for GIA – gridded   **f) Vertical vel. corrected for GIA – GPS sites**
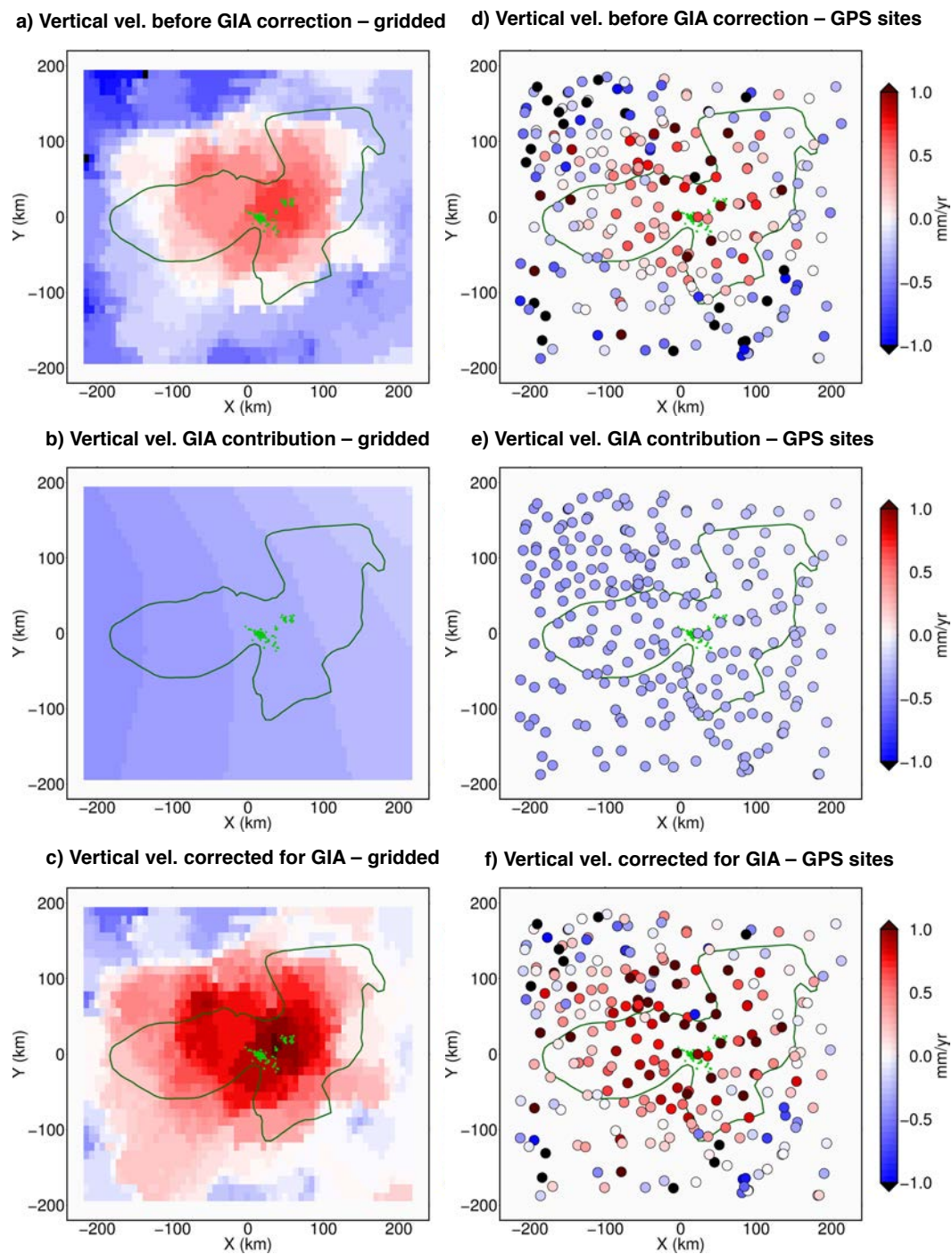
Figure S5.1: Vertical velocities correction for the GIA contribution. Data in (a), (c) and (d) are provided by Kreemer et al. (2020); (b) represents the GIA contribution as estimated from the difference between (a) and (c). This contribution has been then interpolated at the GPS sites locations (e) and used to correct the vertical velocities at GNSS sites in (d). The final result is showed in (f). All other elements are the same as Figure 5.1 in the main text.

a) Horizontal velocity – GPS sites   **b) Vertical velocity – GPS sites**
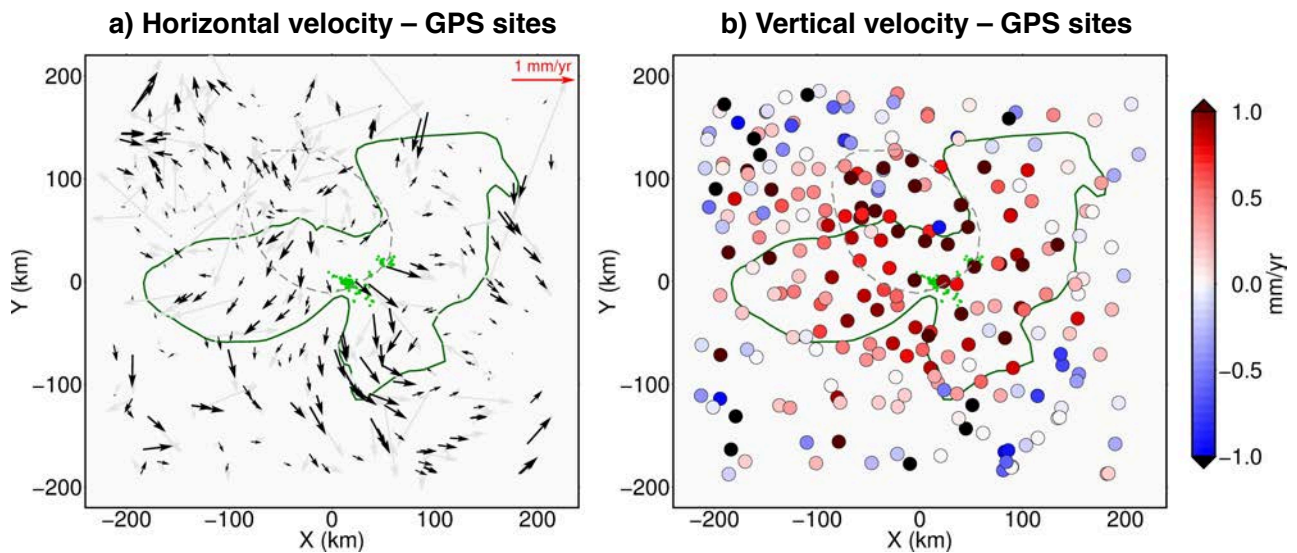
Figure S5.2: Same as Figure 5.1a, 5.1b in the main text, but filtered horizontal velocities (black arrows) are shown together with the original ones (grey arrows) in order to highlight and show more clearly the underlying horizontal deformation. The filtering consists in first applying a block average by L1 norm and then continuous curvature splines over 30 km spacing grid (using respectively *blockmedian* and *surface* algorithms by Generic Mapping Tool; Wessel et al., 2013).

a) Horizontal vel. uncertainties – GPS sites

b) Vertical vel. uncertainties – GPS sites

c) Horizontal vel. uncertainties – gridded

d) Vertical velocity unc. – gridded (std1)

e) Horizontal vel. uncertainties – gridded

f) Vertical vel. uncertainties – gridded (std2)
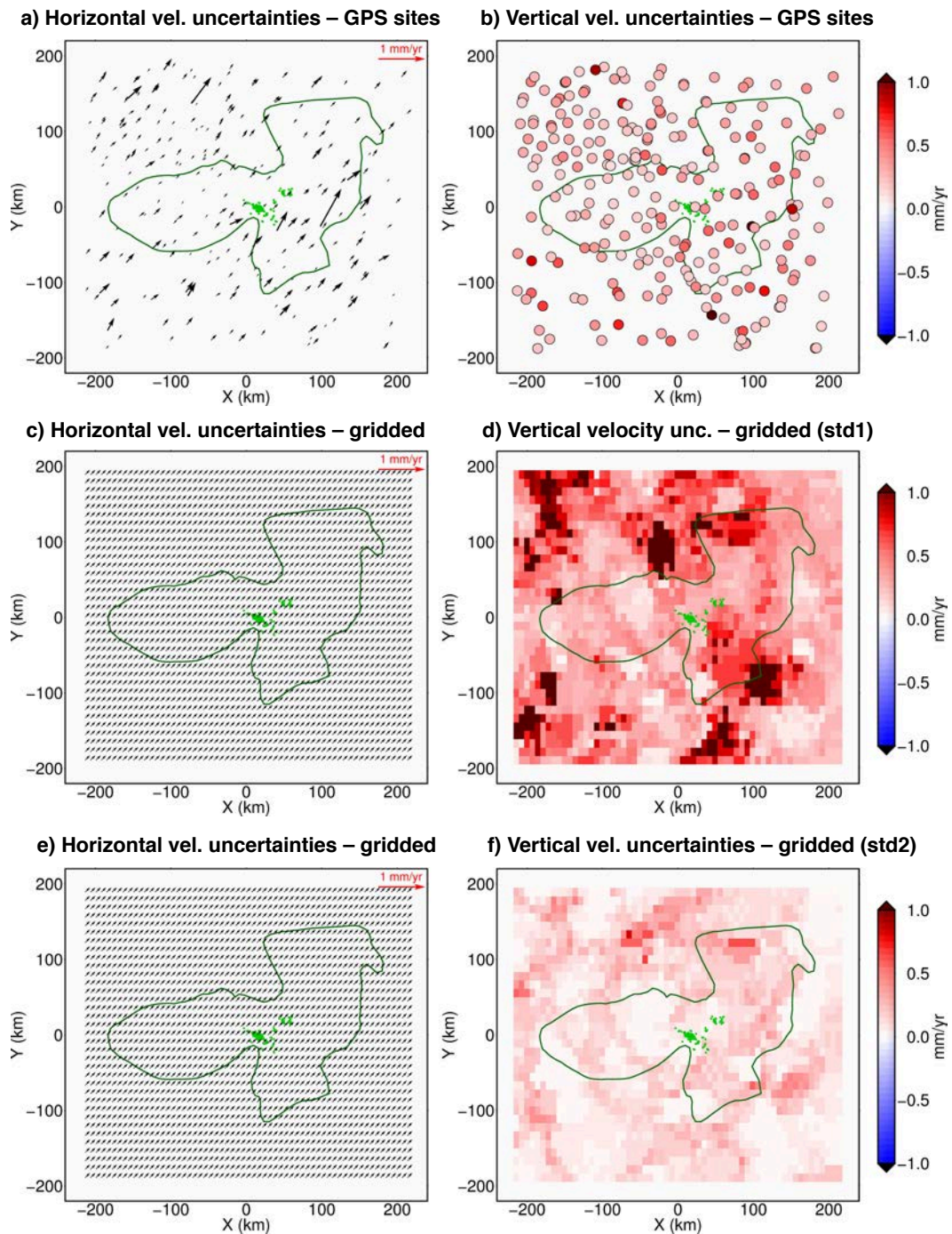
Figure S5.3: Spatial distribution of velocity uncertainties at GNSS sites (a, b) and gridded values. The latter are shown in two different modes for vertical uncertainty: respectively difference from raw GNSS values (c, d) and from despeckled GNSS values (e, f) (See Kreemer et al. (2020) for further details about uncertainty computation). Green dots are centers of Quaternary EVF activity, and dark green outline is Rhenish Massif. All other elements are the same as Figure 5.1 in the main text.
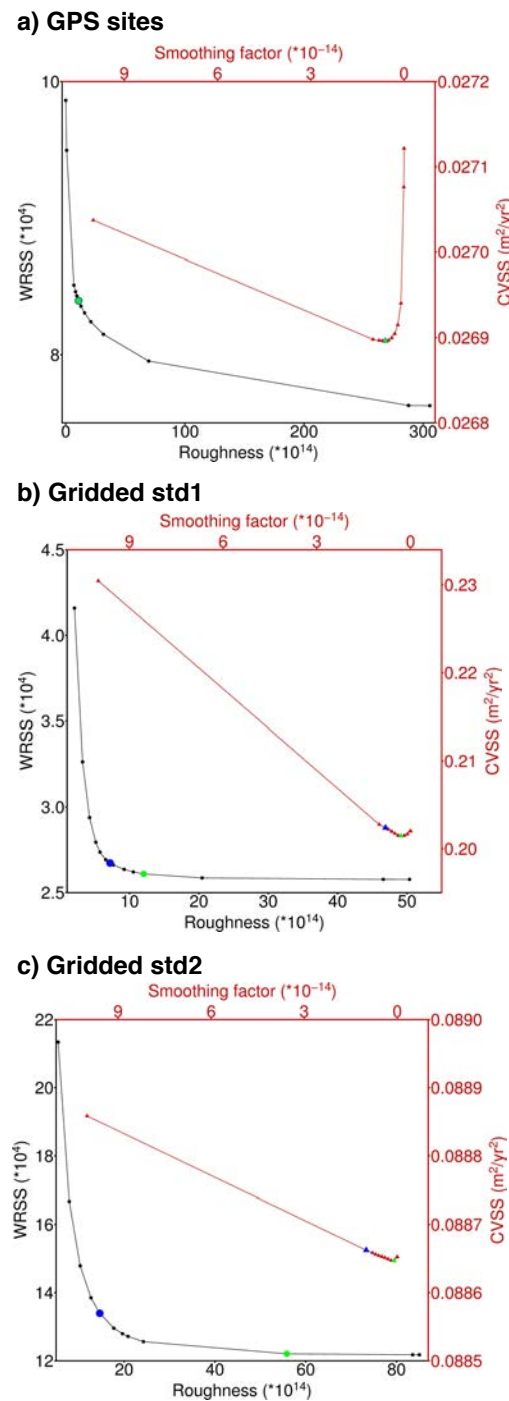
Figure S5.4: Plots of L-curves (black line) and CV curves (red lines) associated with the solutions for a sill at 30 km depth. The blue symbols indicate the selected smoothing factor values from L-curve (corresponding to the solutions in Figure 5.2 of the main text). The green symbols indicate the smoothing factor as selected from CV. Note that the blue and green symbols coincide for the GNSS data case.
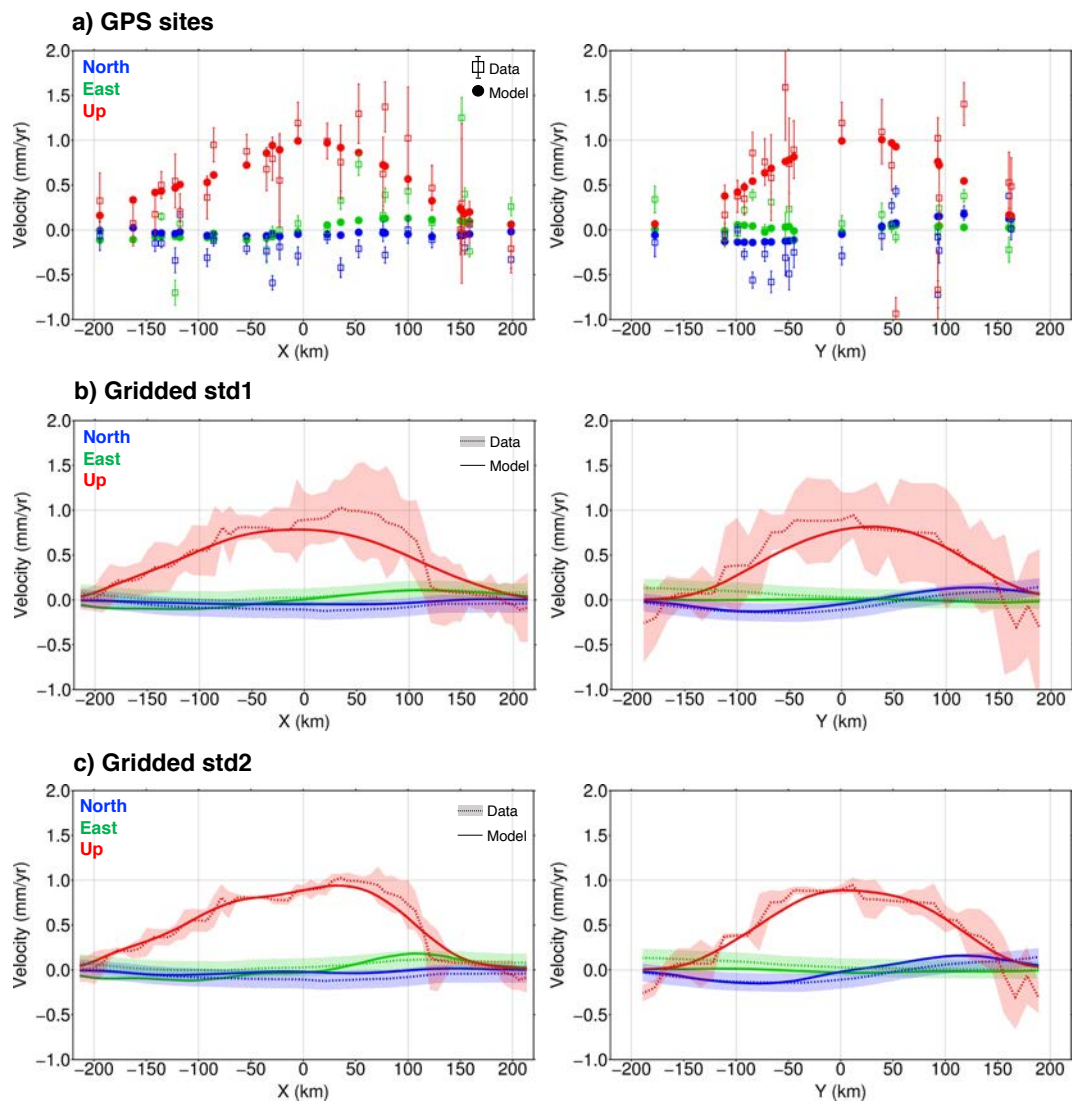
Figure S5.5: Comparison between data (and related uncertainty) and model results along two profiles respectively along east-west (coordinate Y=0; left) and north-south (coordinate X=0; right).

a) GPS sites

a.1) Modeled opening

b) Gridded

b.1) Modeled opening

a.2) Modelled horizontal vel.

b.2) Modelled horizontal vel.

a.3) Modelled vertical vel.

b.3) Modelled vertical vel.
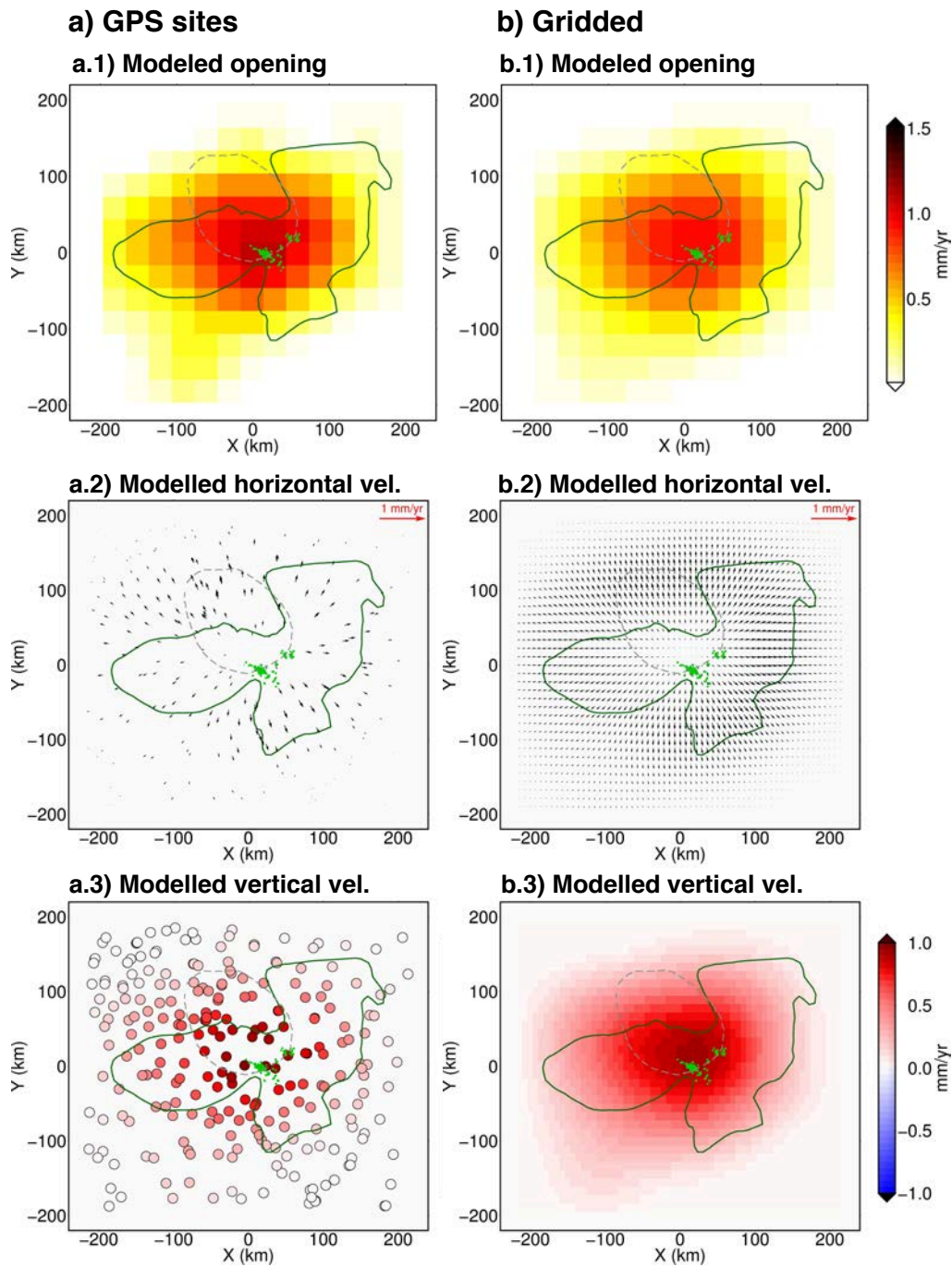
Figure S5.6: Model results for a sill at 30 km depth obtained using the different kinds of surface velocity data and equal weights ($\mathbf{W} = \mathbf{I}$). a) Results for GNSS data (k=1e9 m*yr, RMSE = 0.53 mm/yr, volume rate = 4.65e7 m/yr). b) Results for gridded data (k=2e9 m*yr, RMSE = 0.1 mm/yr, volume rate = 4.38e7 m/yr). All other elements are the same as in Figure 5.1 in the main text.

a) Opening-rate uncertainty - GPS sites
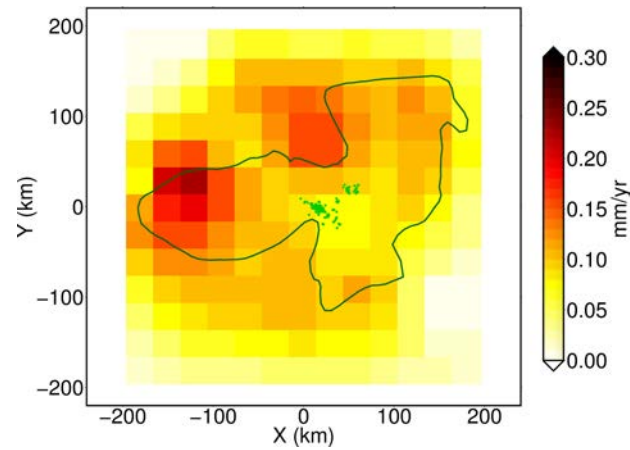
b) Opening-rate uncertainty - gridded std1
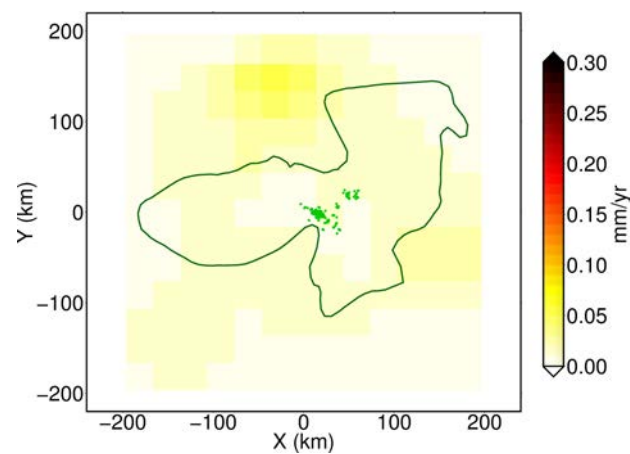
c) Opening-rate uncertainty - gridded std2
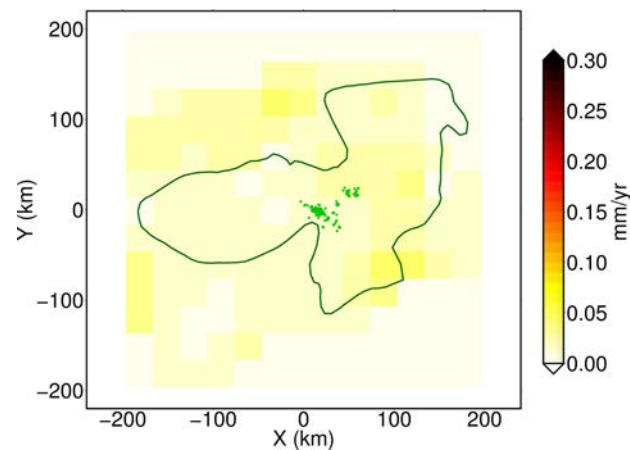
Figure S5.7: Opening-rate uncertainty distribution (1-σ standard deviation for each patch) for a source at 30 km depth, obtained through bootstrap analysis and associated to the solution shown in Figure 5.2 of the main text. All other elements are the same as in Figure 5.1 in the main text.

Figure S5.8: Spatial distribution of ratio between the horizontal (ΔV_x and ΔV_y) and vertical (ΔV_z) potency components of a grid of pCDMs at 30 km depth. Each raw correspond to results obtained using different kinds of data. All other elements are the same as in Figure 5.1 in the main text.

Bibliography

Acocella, V. (2007). Understanding caldera structure and development: An overview of analogue models compared to natural calderas. *Earth-Science Reviews*, 85(3-4):125–160.

Acocella, V. (2021). *Volcano-Tectonic Processes*. Advances in Volcanology. Springer International Publishing.

Acocella, V. and Neri, M. (2003). What makes flank eruptions? the 2001 etna eruption and its possible triggering mechanisms. *Bulletin of Volcanology*, 65:517–529.

Acocella, V., Neri, M., and Sulpizio, R. (2009). Dike propagation within active central volcanic edifices: constraints from somma-vesuvius, etna and analogue models. *Bulletin of volcanology*, 71(2):219–223.

Acocella, V. and Tibaldi, A. (2005). Dike propagation driven by volcano collapse: a general model tested at stromboli, italy. *Geophysical Research Letters*, 32(8).

Aiuppa, A., Casetta, F., Coltorti, M., Stagno, V., and Tamburello, G. (2021). Carbon concentration increases with depth of melting in Earth's upper mantle. *Nature Geoscience*, 14(9):697–703.

Alberico, I., Lirer, L., Petrosino, P., and Scandone, R. (2002). A methodology for the evaluation of long-term volcanic risk from pyroclastic flows in campi flegrei (italy). *Journal of Volcanology and Geothermal Research*, 116(1-2):63–78.

Amadei, B. and Stephansson, O. (1997). *Rock stress and its measurement*. Springer Science & Business Media.

Amadei, B., Stephansson, O., Amadei, B., and Stephansson, O. (1997). Jacking methods. *Rock Stress and Its Measurement*, pages 277–288.

Amoruso, A., Barba, S., Crescentini, L., and Megna, A. (2013). Inversion of synthetic geodetic data for dip-slip faults: clues to the effects of lateral heterogeneities and data distribution in geological environments typical of the Apennines (Italy). *Geophysical Journal International*, 192(2):745–758.

Amoruso, A. and Crescentini, L. (2009). Shape and volume change of pressurized ellipsoidal cavities from deformation and seismic data. *Journal of Geophysical Research: Solid Earth*, 114(B2).

Anderson, E. M. (1937). Ix.—the dynamics of the formation of cone-sheets, ring-dykes, and caldron-subsidences. *Proceedings of the Royal Society of Edinburgh*, 56:128–157.

Anderson, E. M. (1951). *The dynamics of faulting and dyke formation with applications to Britain*. Hafner Pub. Co.

Anderson, K. and Segall, P. (2013). Bayesian inversion of data from effusive volcanic eruptions using physics-based models: Application to mount st. helens 2004–2008. *Journal of Geophysical Research: Solid Earth*, 118(5):2017–2037.

Anderson, K. R. and Poland, M. P. (2016). Bayesian estimation of magma supply, storage, and eruption rates using a multiphysical volcano model: Kīlauea volcano, 2000–2012. *Earth and Planetary Science Letters*, 447:161–171.

Aoki, Y. (2022). Earthquake focal mechanisms as a stress meter of active volcanoes. *Geophysical Research Letters*, 49(19):e2022GL100482.

Auker, M. R., Sparks, R. S. J., Siebert, L., Crosweller, H. S., and Ewert, J. (2013). A statistical analysis of the global historical volcanic fatalities record. *Journal of Applied Volcanology*, 2:1–24.

Aurenhammer, F., Klein, R., and Lee, D.-T. (2013). *Voronoi diagrams and Delaunay triangulations.* World Scientific Publishing Company.

Bagnardi, M., Amelung, F., and Poland, M. P. (2013). A new model for the growth of basaltic shields based on deformation of fernandina volcano, galápagos islands. *Earth and Planetary Science Letters*, 377:358–366.

Bartolini, S., Cappello, A., Martí, J., and Del Negro, C. (2013). Qvast: a new quantum gis plugin for estimating volcanic susceptibility. *Natural Hazards and Earth System Sciences*, 13(11):3031–3042.

Bathke, H., Nikkhoo, M., Holohan, E., and Walter, T. (2015). Insights into the 3d architecture of an active caldera ring-fault at tendürek volcano through modeling of geodetic data. *Earth and Planetary Science Letters*, 422:157–168.

Battaglia, M., Cervelli, P. F., and Murray, J. R. (2013). dMODELS: A MATLAB software package for modeling crustal deformation near active faults and volcanic centers. *Journal of Volcanology and Geothermal Research*, 254:1–4.

Beauducel, F. (2022). OKUBO: Gravity change due to shear and tensile faults. *MATLAB Central File Exchange.*

Beeler, N. and Hickman, S. (2004). Stress-induced, time-dependent fracture closure at hydrothermal conditions. *Journal of Geophysical Research: Solid Earth*, 109(B2).

Bell, A. F., La Femina, P. C., Ruiz, M., Amelung, F., Bagnardi, M., Bean, C. J., Bernard, B., Ebinger, C., Gleeson, M., Grannell, J., et al. (2021). Caldera resurgence during the 2018 eruption of Sierra Negra volcano, Galápagos Islands. *Nature communications*, 12(1):1–9.

Bertani, R. (2016). Geothermal power generation in the world 2010–2014 update report. *Geothermics*, 60:31–43.

Bevilacqua, A., Isaia, R., Neri, A., Vitale, S., Aspinall, W. P., Bisson, M., Flandoli, F., Baxter, P. J., Bertagnini, A., Esposti Ongaro, T., et al. (2015). Quantifying volcanic hazard at campi flegrei caldera (italy) with uncertainty assessment: 1. vent opening maps. *Journal of Geophysical Research: Solid Earth*, 120(4):2309–2329.

Bonafede, M. and Neri, A. (2000). Effects induced by an earthquake on its fault plane: a boundary element study. *Geophysical Journal International*, 141(1):43–56.

Branca, S., Carbone, D., and Greco, F. (2003). Intrusive mechanism of the 2002 ne-rift eruption at mt. etna (italy) inferred through continuous microgravity data and volcanological evidences. *Geophysical Research Letters*, 30(20).

Brown, S. K., Loughlin, S. C., Sparks, R., Vye-Brown, C., Barclay, J., Calder, E., Cottrell, E., Jolly, G., Komorowski, J., Mandeville, C. W., et al. (2015). Global volcanic hazards and risk.

Bräuer, K., Kämpf, H., Niedermann, S., and Strauch, G. (2013). Indications for the existence of different magmatic reservoirs beneath the Eifel area (Germany): A multi-isotope (C, N, He, Ne, Ar) approach. *Chemical Geology*, 356:193–208.

Burgi, P.-Y., Darrah, T., Tedesco, D., and Eymold, W. (2014). Dynamics of the mount nyiragongo lava lake. *Journal of Geophysical Research: Solid Earth*, 119(5):4106–4122.

Busetti, S. and Reches, Z. (2014). Geomechanics of hydraulic fracturing microseismicity: Part 2. stress state determination. *AAPG Bulletin*, 98(11):2459–2476.

Calò, M. and Tramelli, A. (2018). Anatomy of the campi flegrei caldera using enhanced seismic tomography models. *Scientific reports*, 8(1):1–12.

Cappello, A., Geshi, N., Neri, M., and Del Negro, C. (2015). Lava flow hazards—an impending threat at miyakejima volcano, japan. *Journal of Volcanology and Geothermal Research*, 308:1–9.

Cappello, A., Neri, M., Acocella, V., Gallo, G., Vicari, A., and Del Negro, C. (2012). Spatial vent opening probability map of etna volcano (sicily, italy). *Bulletin of Volcanology*, 74:2083–2094.

Caracausi, A., Avice, G., Burnard, P. G., Füri, E., and Marty, B. (2016). Chondritic xenon in the Earth's mantle. *Nature*, 533.

Carapezza, M. L., Inguaggiato, S., Brusca, L., and Longo, M. (2004). Geochemical precursors of the activity of an open-conduit volcano: The stromboli 2002–2003 eruptive events. *Geophysical Research Letters*, 31(7).

Cayol, V. and Cornet, F. H. (1997). 3D mixed boundary elements for elastostatic deformation field analysis. *International Journal of Rock Mechanics and Mining Sciences*, 34(2):275–287.

Cayol, V. and Cornet, F. H. (1998). Three-dimensional modeling of the 1983–1984 eruption at piton de la fournaise volcano, réunion island. *Journal of Geophysical Research: Solid Earth*, 103(B8):18025–18037.

Cesca, S., Letort, J., Razafindrakoto, H. N., Heimann, S., Rivalta, E., Isken, M. P., Nikkhoo, M., Passarelli, L., Petersen, G. M., Cotton, F., et al. (2020). Drainage of a deep magma reservoir near mayotte inferred from seismicity and deformation. *Nature Geoscience*, 13(1):87–93.

Chadwick, W. W. and Dieterich, J. H. (1995). Mechanical modeling of circumferential and radial dike intrusion on galapagos volcanoes. *Journal of Volcanology and Geothermal Research*, 66(1-4):37–52.

Chadwick, W. W. and Howard, K. A. (1991). The pattern of circumferential and radial eruptive fissures on the volcanoes of fernandina and isabela islands, galapagos. *Bulletin of Volcanology*, 53:259–275.

Chestler, S. R. and Grosfils, E. B. (2013). Using numerical modeling to explore the origin of intrusion patterns on fernandina volcano, galapagos islands, ecuador. *Geophysical research letters*, 40(17):4565–4569.

Chiarabba, C., Amato, A., Boschi, E., and Barberi, F. (2000). Recent seismicity and tomographic modeling of the mount etna plumbing system. *Journal of Geophysical Research: Solid Earth*, 105(B5):10923–10938.

Clifton, A. E. and Kattenhorn, S. A. (2006). Structural architecture of a highly oblique divergent plate boundary segment. *Tectonophysics*, 419(1-4):27–40.

Cloetingh, S., van Wees, J. D., Ziegler, P., Lenkey, L., Beekman, F., Tesauro, M., Förster, A., Norden, B., Kaban, M., Hardebol, N., et al. (2010). Lithosphere tectonics and thermomechanical properties: an integrated modelling approach for enhanced geothermal systems exploration in europe. *Earth-Science Reviews*, 102(3-4):159–206.

Clough, R. W. (1980). The finite element method after twenty-five years: a personal view. *Computers & Structures*, 12(4):361–370.

Cole, J., Milner, D., and Spinks, K. (2005). Calderas and caldera structures: a review. *Earth-Science Reviews*, 69(1-2):1–26.

Comninou, M. and Dundurs, J. (1975). The angular dislocation in a half space. *Journal of Elasticity*, 5:203–216.

Connor, C., Bebbington, M., and Marzocchi, W. (2015). Probabilistic volcanic hazard assessment. In *The Encyclopedia of Volcanoes*, pages 897–910. Elsevier.

Connor, C. B., Conway, F. M., and Sigurdsson, H. (2000). Basaltic volcanic fields. *Encyclopedia of volcanoes*, 1:331–343.

Connor, C. B. and Hill, B. E. (1995). Three nonhomogeneous poisson models for the probability of basaltic volcanism: application to the yucca mountain region, nevada. *Journal of Geophysical Research: Solid Earth*, 100(B6):10107–10125.

Connor, L. J., Connor, C. B., Meliksetian, K., and Savov, I. (2012). Probabilistic approach to modeling lava flow inundation: a lava flow hazard assessment for a nuclear facility in armenia. *Journal of Applied Volcanology*, 1:1–19.

Corbi, F., Rivalta, E., Pinel, V., Maccaferri, F., and Acocella, V. (2016). Understanding the link between circumferential dikes and eruptive fissures around calderas based on numerical and analog models. *Geophysical Research Letters*, 43(12):6212–6219.

Corbi, F., Rivalta, E., Pinel, V., Maccaferri, F., Bagnardi, M., and Acocella, V. (2015). How caldera collapse shapes the shallow emplacement and transfer of magma in active volcanoes. *Earth and Planetary Science Letters*, 431:287–293.

Costa, A., Sparks, R., Macedonio, G., and Melnik, O. (2009). Effects of wall-rock elasticity on magma flow in dykes during explosive eruptions. *Earth and Planetary Science Letters*, 288(3-4):455–462.

Crouch, S. (1976). Solution of plane elasticity problems by the displacement discontinuity method. i. infinite body solution. *International journal for numerical methods in engineering*, 10(2):301–343.

Crouch, S. L., Starfield, A. M., and Rizzo, F. (1983). Boundary element methods in solid mechanics.

Cruden, A. R., McCaffrey, K. J. W., and Bunger, A. P. (2018). *Geometric Scaling of Tabular Igneous Intrusions: Implications for Emplacement and Growth*, pages 11–38. Springer International Publishing, Cham.

Currenti, G., Napoli, R., Coco, A., and Privitera, E. (2017). Effects of hydrothermal unrest on stress and deformation: insights from numerical modeling and application to vulcano island (italy). *Bulletin of Volcanology*, 79(4):28.

Currenti, G. and Williams, C. A. (2014). Numerical modeling of deformation and stress fields around a magma chamber: Constraints on failure conditions and rheology. *Physics of the Earth and Planetary Interiors*, 226:14–27.

Dahm, T. (2000a). Numerical simulations of the propagation path and the arrest of fluid-filled fractures in the earth. *Geophysical Journal International*, 141(3):623–638.

Dahm, T. (2000b). On the shape and velocity of fluid-filled fractures in the earth. *Geophysical Journal International*, 142(1):181–192.

Dahm, T., Stiller, M., Mechie, J., Heimann, S., Hensch, M., Woith, H., Schmidt, B., Gabriel, G., and Weber, M. (2020). Seismological and Geophysical Signatures of the Deep Crustal Magma Systems of the Cenozoic Volcanic Fields Beneath the Eifel, Germany. *Geochemistry, Geophysics, Geosystems*, 21(9):e2020GC009062.

Davis, T., Bagnardi, M., Lundgren, P., and Rivalta, E. (2021). Extreme curvature of shallow magma pathways controlled by competing stresses: insights from the 2018 sierra negra eruption. *Geophysical Research Letters*, 48(13):e2021GL093038.

Davis, T., Healy, D., Bubeck, A., and Walker, R. (2017). Stress concentrations around voids in three dimensions: The roots of failure. *Journal of Structural Geology*, 102:193–207.

Davis, T., Healy, D., and Rivalta, E. (2019). Slip on wavy frictional faults: Is the 3rd dimension a sticking point? *Journal of Structural Geology*, 119:33–49.

Davis, T., Rivalta, E., and Dahm, T. (2020). Critical fluid injection volumes for uncontrolled fracture ascent. *Geophysical Research Letters*, page e2020GL087774.

Davis, T., Rivalta, E., Smittarello, D., and Katz, R. F. (2023). Ascent rates of 3-d fractures driven by a finite batch of buoyant fluid. *Journal of Fluid Mechanics*, 954:A12.

De Luca, C., Valerio, E., Giudicepietro, F., Macedonio, G., Casu, F., and Lanari, R. (2022). Pre-and co-eruptive analysis of the september 2021 eruption at cumbre vieja volcano (la palma, canary islands) through dinsar measurements and analytical modeling. *Geophysical Research Letters*, 49(7):e2021GL097293.

De Vita, S., Orsi, G., Civetta, L., Carandente, A., D'Antonio, M., Deino, A., Di Cesare, T., Di Vito, M., Fisher, R., Isaia, R., et al. (1999). The agnano–monte spina eruption (4100 years bp) in the restless campi flegrei caldera (italy). *Journal of Volcanology and Geothermal Research*, 91(2-4):269–301.

De Vivo, B., Belkin, H. E., and Rolandi, G. (2019). *Vesuvius, Campi Flegrei, and Campanian Volcanism*. Elsevier.

Del Negro, C., Currenti, G., and Scandura, D. (2009). Temperature-dependent viscoelastic modeling of ground deformation: Application to etna volcano during the 1993–1997 inflation period. *Physics of the Earth and Planetary Interiors*, 172(3-4):299–309.

Delaney, P. T., Pollard, D. D., Ziony, J. I., and McKee, E. H. (1986). Field relations between dikes and joints: Emplacement processes and paleostress analysis. *Journal of Geophysical Research: Solid Earth*, 91(B5):4920–4938.

Delgado, F. and Grandin, R. (2021). Dynamics of Episodic Magma Injection and Migration at Yellowstone Caldera: Revisiting the 2004–2009 Episode of Caldera Uplift With InSAR and GPS Data. *Journal of Geophysical Research: Solid Earth*, 126(8):e2021JB022341.

Demoulin, A. and Hallot, E. (2009). Shape and amount of the Quaternary uplift of the western Rhenish shield and the Ardennes (western Europe). *Tectonophysics*, 474(3):696–708.

Di Giuseppe, E., Funiciello, F., Corbi, F., Ranalli, G., and Mojoli, G. (2009). Gelatins as rock analogs: A systematic study of their rheological and physical properties. *Tectonophysics*, 473(3-4):391–403.

Di Vito, M., Lirer, L., Mastrolorenzo, G., and Rolandi, G. (1987). The 1538 monte nuovo eruption (campi flegrei, italy). *Bulletin of Volcanology*, 49:608–615.

Di Vito, M. A., Acocella, V., Aiello, G., Barra, D., Battaglia, M., Carandente, A., Del Gaudio, C., De Vita, S., Ricciardi, G. P., Ricco, C., et al. (2016). Magma transfer at campi flegrei caldera (italy) before the 1538 ad eruption. *Scientific reports*, 6(1):32245.

Dieterich, J., Cayol, V., and Okubo, P. (2000). The use of earthquake rate changes as a stress meter at kilauea volcano. *Nature*, 408(6811):457–460.

Dieterich, J. H. (1988). Growth and persistence of hawaiian volcanic rift zones. *Journal of Geophysical Research: Solid Earth*, 93(B5):4258–4270.

Dieterich, J. H. and Decker, R. W. (1975). Finite element modeling of surface deformation associated with volcanism. *Journal of Geophysical Research*, 80(29):4094–4102.

Dragoni, M. and Magnanensi, C. (1989). Displacement and stress produced by a pressurized, spherical magma chamber, surrounded by a viscoelastic shell. *Physics of the Earth and Planetary Interiors*, 56(3-4):316–328.

Dumont, Q., Cayol, V., Froger, J.-L., and Peltier, A. (2022). 22 years of satellite imagery reveal a major destabilization structure at piton de la fournaise. *Nature Communications*, 13(1):2649.

D'Auria, L., Massa, B., Cristiano, E., Del Gaudio, C., Giudicepietro, F., Ricciardi, G., and Ricco, C. (2015). Retrieving the stress field within the campi flegrei caldera (southern italy) through an integrated geodetical and seismological approach. *Pure and Applied Geophysics*, 172(11):3247–3263.

Ebinger, C., Ayele, A., Keir, D., Rowland, J., Yirgu, G., Wright, T., Belachew, M., and Hamling, I. (2010). Length and timescales of rift faulting and magma intrusion: The afar rifting cycle from 2005 to present. *Annual Review of Earth and Planetary Sciences*, 38(1):439–466.

Efron, B. and Tibshirani, R. (1986). Bootstrap Methods for Standard Errors, Confidence Intervals, and Other Measures of Statistical Accuracy. *Statistical Science*, 1(1):54 – 75.

Einarsson, P., Brandsdottir, B., et al. (1980). Seismological evidence for lateral magma intrusion during the july 1978 deflation of the krafla volcano in ne-iceland. *Journal of Geophysics*, 47(1):160–165.

Erdogan, F. and Sih, G. (1963). On the crack extension in plates under plane loading and transverse shear.

Esposti Ongaro, T., Komorowski, J.-C., Legendre, Y., and Neri, A. (2020). Modelling pyroclastic density currents from a subplinian eruption at la soufrière de guadeloupe (west indies, france). *Bulletin of Volcanology*, 82:1–26.

Fekiacova, Z., Mertz, D. F., and Renne, P. R. (2007). Geodynamic Setting of the Tertiary Hocheifel Volcanism (Germany), Part I: 40Ar/39Ar geochronology. In Ritter, J. R. R. and Christensen, U. R., editors, *Mantle Plumes: A Multidisciplinary Approach*, pages 207–240, Berlin, Heidelberg. Springer Berlin Heidelberg.

Ferrante, G., Rivalta, E., and Maccaferri, F. (2022). Numerical simulation of magma pathways and vent distribution in rifts from the early stages to maturity. *Authorea Preprints*.

Fialko, Y., Khazan, Y., and Simons, M. (2001). Deformation due to a pressurized horizontal circular crack in an elastic half-space, with applications to volcano geodesy. *Geophysical Journal International*, 146(1):181–190.

Forster, M. and Sober, E. (1994). How to tell when simpler, more unified, or less ad hoc theories will provide more accurate predictions. *The British Journal for the Philosophy of Science*, 45(1):1–35.

Fournier, N. and Chardot, L. (2012). Understanding volcano hydrothermal unrest from geodetic observations: Insights from numerical modeling and application to white island volcano, new zealand. *Journal of Geophysical Research: Solid Earth*, 117(B11).

Fukuda, J. and Johnson, K. M. (2008). A Fully Bayesian Inversion for Spatial Distribution of Fault Slip with Objective Smoothing. *Bulletin of the Seismological Society of America*, 98(3):1128–1146.

Fukushima, Y., Cayol, V., Durand, P., and Massonnet, D. (2010). Evolution of magma conduits during the 1998–2000 eruptions of piton de la fournaise volcano, réunion island. *Journal of Geophysical Research: Solid Earth*, 115(B10).

Furst, S., Maccaferri, F., and Pinel, V. (2023). Modeling the shape and velocity of magmatic intrusions, a new numerical approach. *Journal of Geophysical Research: Solid Earth*, page e2022JB025697.

Förster, M. W., Zemlitskaya, A., Otter, L. M., Buhre, S., and Sirocko, F. (2020). Late Pleistocene Eifel eruptions: insights from clinopyroxene and glass geochemistry of tephra layers from Eifel Laminated Sediment Archive sediment cores. *Journal of Quaternary Science*, 35(1-2):186–198.

Gaete, A., Kavanagh, J. L., Rivalta, E., Hazim, S. H., Walter, T. R., and Dennis, D. J. (2019). The impact of unloading stresses on post-caldera magma intrusions. *Earth and Planetary Science Letters*, 508:109–121.

Galetto, F., Acocella, V., Hooper, A., and Bagnardi, M. (2022). Eruption at basaltic calderas forecast by magma flow rate. *Nature Geoscience*, 15:580–584.

Gallant, E., Richardson, J., Connor, C., Wetmore, P., and Connor, L. (2018). A new approach to probabilistic lava flow hazard assessments, applied to the idaho national laboratory, eastern snake river plain, idaho, usa. *Geology*, 46(10):895–898.

Gelman, A., Carlin, J. B., Stern, H. S., Dunson, D. B., Vehtari, A., and Rubin, D. B. (2013). *Bayesian data analysis*. CRC press.

Geshi, N., Kusumoto, S., and Gudmundsson, A. (2012). Effects of mechanical layering of host rocks on dike growth and arrest. *Journal of Volcanology and Geothermal Research*, 223:74–82.

Geshi, N., Yamada, I., Matsumoto, K., Nishihara, A., and Miyagi, I. (2020). Accumulation of rhyolite magma and triggers for a caldera-forming eruption of the aira caldera, japan. *Bulletin of Volcanology*, 82(6):1–18.

Giaccio, B., Hajdas, I., Isaia, R., Deino, A., and Nomade, S. (2017). High-precision 14c and 40ar/39ar dating of the campanian ignimbrite (y-5) reconciles the time-scales of climatic-cultural processes at 40 ka. *Scientific reports*, 7(1):1–10.

Girard, G. and Stix, J. (2010). Rapid extraction of discrete magma batches from a large differentiating magma chamber: the central plateau member rhyolites, yellowstone caldera, wyoming. *Contributions to Mineralogy and Petrology*, 160:441–465.

Gómez-Vasconcelos, M. G., Villamor, P., Cronin, S., Procter, J., Palmer, A., Townsend, D., and Leonard, G. (2017). Crustal extension in the tongariro graben, new zealand: Insights into volcano-tectonic interactions and active deformation in a young continental rift. *GSA Bulletin*, 129(9-10):1085–1099.

Gómez-Vasconcelos, M. G., Villamor, P., Cronin, S. J., Palmer, A., Procter, J., and Stewart, R. B. (2020). Spatio-temporal associations between dike intrusions and fault ruptures in the tongariro volcanic center, new zealand. *Journal of Volcanology and Geothermal Research*, 404:107037.

Goto, Y. and Tomiya, A. (2019). Internal structures and growth style of a quaternary subaerial rhyodacite cryptodome at ogariyama, usu volcano, hokkaido, japan. *Frontiers in Earth Science*, 7:66.

Griffith, A. (1924). The theory of rupture. In *First Int. Cong. Appl. Mech*, pages 55–63.

Griffith, A. A. (1921). Vi. the phenomena of rupture and flow in solids. *Philosophical transactions of the royal society of london. Series A, containing papers of a mathematical or physical character*, 221(582-593):163–198.

Grosfils, E. B. and Head, J. W. (1994). Emplacement of a radiating dike swarm in western vinmara planitia, venus: Interpretation of the regional stress field orientation and subsurface magmatic configuration. *Earth, Moon, and Planets*, 66(2):153–171.

Grosfils, E. B., McGovern, P. J., Gregg, P. M., Galgana, G. A., Hurwitz, D. M., Long, S. M., and Chestler, S. R. (2015). Elastic models of magma reservoir mechanics: a key tool for investigating planetary volcanism. *Geological Society, London, Special Publications*, 401(1):239–267.

Gudmundsson, A. (1983). Form and dimensions of dykes in eastern iceland. *Tectonophysics*, 95(3-4):295–307.

Gudmundsson, A. (1995). Infrastructure and mechanics of volcanic systems in iceland. *Journal of Volcanology and Geothermal Research*, 64(1-2):1–22.

Gudmundsson, A. (1998). Magma chambers modeled as cavities explain the formation of rift zone central volcanoes and their eruption and intrusion statistics. *Journal of Geophysical Research: Solid Earth*, 103(B4):7401–7412.

Gudmundsson, A. (2002). Emplacement and arrest of sheets and dykes in central volcanoes. *Journal of Volcanology and Geothermal Research*, 116(3-4):279–298.

Gudmundsson, A. (2006). How local stresses control magma-chamber ruptures, dyke injections, and eruptions in composite volcanoes. *Earth-science reviews*, 79(1-2):1–31.

Gudmundsson, A. and Brenner, S. L. (2004). How mechanical layering affects local stresses, unrests, and eruptions of volcanoes. *Geophysical Research Letters*, 31(16).

Gudmundsson, M. T., Jónsdóttir, K., Hooper, A., Holohan, E. P., Halldórsson, S. A., Ófeigsson, B. G., Cesca, S., Vogfjörd, K. S., Sigmundsson, F., Högnadóttir, T., et al. (2016). Gradual caldera collapse at bárdarbunga volcano, iceland, regulated by lateral magma outflow. *Science*, 353(6296):aaf8988.

Haario, H., Laine, M., Mira, A., and Saksman, E. (2006). Dram: efficient adaptive mcmc. *Statistics and computing*, 16(4):339–354.

Hansen, P. C. and O'Leary, D. P. (1993). The Use of the L-Curve in the Regularization of Discrete Ill-Posed Problems. *SIAM Journal on Scientific Computing*, 14(6):1487–1503.

Harris, R. A. and Segall, P. (1987). Detection of a locked zone at depth on the Parkfield, California, segment of the San Andreas Fault. *Journal of Geophysical Research: Solid Earth*, 92(B8):7945–7962.

Head, M., Hickey, J., Gottsmann, J., and Fournier, N. (2019). The influence of viscoelastic crustal rheologies on volcanic ground deformation: Insights from models of pressure and volume change. *Journal of Geophysical Research: Solid Earth*, 124(8):8127–8146.

Heidbach, O., Rajabi, M., Reiter, K., Ziegler, M., Team, W., et al. (2016). World stress map database release 2016. *GFZ Data Services*, 10.

Heidbach, O., Reinecker, J., Tingay, M., Müller, B., Sperner, B., Fuchs, K., and Wenzel, F. (2007). Plate boundary forces are not enough: Second-and third-order stress patterns highlighted in the world stress map database. *Tectonics*, 26(6).

Heimisson, E. R., Hooper, A., and Sigmundsson, F. (2015). Forecasting the path of a laterally propagating dike. *Journal of Geophysical Research: Solid Earth*, 120(12):8774–8792.

Henrion, E., Masson, F., Doubre, C., Ulrich, P., and Meghraoui, M. (2020). Present-day deformation in the Upper Rhine Graben from GNSS data. *Geophysical Journal International*, 223(1):599–611.

Hensch, M., Dahm, T., Ritter, J., Heimann, S., Schmidt, B., Stange, S., and Lehmann, K. (2019). Deep low-frequency earthquakes reveal ongoing magmatic recharge beneath Laacher See Volcano (Eifel, Germany). *Geophysical Journal International*, 216(3):2025–2036.

Hildreth, W. (2004). Volcanological perspectives on long valley, mammoth mountain, and mono craters: several contiguous but discrete systems. *Journal of Volcanology and Geothermal Research*, 136(3-4):169–198.

Hildreth, W., Fierstein, J., and Calvert, A. (2017). Early postcaldera rhyolite and structural resurgence at long valley caldera, california. *Journal of Volcanology and Geothermal Research*, 335:1–34.

Hopkins, J. L., Smid, E. R., Eccles, J. D., Hayes, J. L., Hayward, B. W., McGee, L. E., van Wijk, K., Wilson, T. M., Cronin, S. J., Leonard, G. S., et al. (2021). Auckland volcanic field magmatism, volcanism, and hazard: a review. *New Zealand Journal of Geology and Geophysics*, 64(2-3):213–234.

Hreinsdóttir, S., Freymueller, J. T., Fletcher, H. J., Larsen, C. F., and Bürgmann, R. (2003). Coseismic slip distribution of the 2002 MW7.9 Denali fault earthquake, Alaska, determined from GPS measurements. *Geophysical Research Letters*, 30(13).

Hrubcová, P., Geissler, W. H., Bräuer, K., Vavryčuk, V., Tomek, v., and Kämpf, H. (2017). Active magmatic underplating in western eger rift, central europe. *Tectonics*, 36(12):2846–2862.

Hubbert, M. K. and Willis, D. G. (1957). Mechanics of hydraulic fracturing. *Transactions of the AIME*, 210(01):153–168.

Husson, L., Bodin, T., Spada, G., Choblet, G., and Kreemer, C. (2018). Bayesian surface reconstruction of geodetic uplift rates: Mapping the global fingerprint of glacial isostatic adjustment. *Journal of Geodynamics*, 122:25–40.

Ida, Y. (1992). Width change of a planar magma path: implication for the evolution and style of volcanic eruptions. *Physics of the earth and planetary interiors*, 74(3-4):127–138.

Inglis, C. E. (1913). Stresses in a plate due to the presence of cracks and sharp corners. *Trans Inst Naval Archit*, 55:219–241.

Irwin, G. (1958). Fracture handbuch der physik vi. *Flugge Ed. Springer*, 106.

Irwin, G. R. (1957). Analysis of stresses and strains near the end of a crack traversing a plate.

Ito, G. and Martel, S. J. (2002). Focusing of magma in the upper mantle through dike interaction. *Journal of Geophysical Research: Solid Earth*, 107(B10):ECV–6.

Jaeger, J., Cook, N., and Zimmermann, R. (2007). Fundamentals of rock mechanics. blackwell, oxford.

Jeanne, P., Zhang, Y., and Rutqvist, J. (2020). Influence of hysteretic stress path behavior on seal integrity during gas storage operation in a depleted reservoir. *Journal of Rock Mechanics and Geotechnical Engineering*, 12(4):886–899.

Jensen, R. A. and Donnelly-Nolan, J. M. (2017). Field-trip guide to the geologic highlights of newberry volcano, oregon. Technical report, US Geological Survey.

Jeyakumaran, M., Rudnicki, J., and Keer, L. (1992). Modeling slip zones with triangular dislocation elements. *Bulletin of the Seismological Society of America*, 82(5):2153–2169.

Jo, Y., Chang, C., Ji, S.-H., and Park, K.-W. (2019). In situ stress states at kurt, an underground research laboratory in south korea for the study of high-level radioactive waste disposal. *Engineering Geology*, 259:105198.

Jödicke, H., Untiedt, J., Olgemann, W., Schulte, L., and Wagenitz, V. (1983). Electrical conductivity structure of the crust and upper mantle beneath the rhenish massif. In Fuchs, K., von Gehlen, K., Mälzer, H., Murawski, H., and Semmel, A., editors, *Plateau Uplift*, pages 288–302, Berlin, Heidelberg. Springer Berlin Heidelberg.

Johnson, N. L., Kotz, S., and Balakrishnan, N. (1994). Beta distributions. *Continuous uni-variate distributions. 2nd ed. New York, NY: John Wiley and Sons*, pages 221–235.

Jonsson, S. (2009). Stress interaction between magma accumulation and trapdoor faulting on sierra negra volcano, galapagos. *Tectonophysics*, 471(1):36–44.

Jónsson, S., Zebker, H., Cervelli, P., Segall, P., Garbeil, H., Mouginis-Mark, P., and Rowland, S. (1999). A shallow-dipping dike fed the 1995 flank eruption at fernandina volcano, galápagos, observed by satellite radar interferometry. *Geophysical Research Letters*, 26(8):1077–1080.

Jung, S., Pfänder, J. A., Brügmann, G., and Stracke, A. (2005). Sources of primitive alkaline volcanic rocks from the Central European Volcanic Province (Rhön, Germany) inferred from Hf, Os and Pb isotopes. *Contributions to Mineralogy and Petrology*, 150(5):546–559.

Kavanagh, J., Menand, T., and Daniels, K. A. (2013). Gelatine as a crustal analogue: Determining elastic properties for modelling magmatic intrusions. *Tectonophysics*, 582:101–111.

Kavanagh, J., Rogers, B., Boutelier, D., and Cruden, A. (2017). Controls on sill and dyke-sill hybrid geometry and propagation in the crust: The role of fracture toughness. *Tectonophysics*, 698:109–120.

Kiyoo, M. (1958). Relations between the eruptions of various volcanoes and the deformations of the ground surfaces around them. *Earthq Res Inst*, 36:99–134.

Kreemer, C., Blewitt, G., and Davis, P. M. (2020). Geodetic evidence for a buoyant mantle plume beneath the Eifel volcanic area, NW Europe. *Geophysical Journal International*, 222(2):1316–1332.

Kühn, D. and Dahm, T. (2008). Numerical modelling of dyke interaction and its influence on oceanic crust formation. *Tectonophysics*, 447(1-4):53–65.

Lagarias, J. C., Reeds, J. A., Wright, M. H., and Wright, P. E. (1998). Convergence Properties of the Nelder–Mead Simplex Method in Low Dimensions. *SIAM Journal on Optimization*, 9(1):112–147.

Laine, M. (2013). Mcmc toolbox for matlab, 2013. *URL: http://helios. fmi. fi/˜ lainema/mcmc.*

Laine, M. et al. (2008). *Adaptive MCMC methods with applications in environmental and geophysical models.* Finnish Meteorological Institute.

Lawson, C. L. and Hanson, R. J. (1995). *Solving least squares problems*, volume 15 of *Classics in Applied Mathematics*. Society for Industrial and Applied Mathematics (SIAM), Philadelphia, PA. Revised reprint of the 1974 original.

Le Corvec, N., Menand, T., and Lindsay, J. (2013a). Interaction of ascending magma with pre-existing crustal fractures in monogenetic basaltic volcanism: an experimental approach. *Journal of Geophysical Research: Solid Earth*, 118(3):968–984.

Le Corvec, N., Spörli, K. B., Rowland, J., and Lindsay, J. (2013b). Spatial distribution and alignments of volcanic centers: clues to the formation of monogenetic volcanic fields. *Earth-Science Reviews*, 124:96–114.

Leder, J., Wenzel, F., Daniell, J. E., and Gottschämmer, E. (2017). Loss of residential buildings in the event of a re-awakening of the laacher see volcano (germany). *Journal of Volcanology and Geothermal Research*, 337:111–123.

Lima, A., De Vivo, B., Spera, F. J., Bodnar, R. J., Milia, A., Nunziata, C., Belkin, H. E., and Cannatelli, C. (2009). Thermodynamic model for uplift and deflation episodes (bradyseism) associated with magmatic–hydrothermal activity at the campi flegrei (italy). *Earth-Science Reviews*, 97(1-4):44–58.

Lindsay, J. (2010). Volcanoes in the big smoke: a review of hazard and risk in the auckland volcanic field. In *Geologically Active. Delegate Papers of the 11th Congress of the International Association for Engineering Geology and the Environment (IAEG)*.

Lisowski, M., McCaffrey, R., Wicks, C. W., and Dzurisin, D. (2021). Geodetic Constraints on a 25-year Magmatic Inflation Episode Near Three Sisters, Central Oregon. *Journal of Geophysical Research: Solid Earth*, 126(12):e2021JB022360.

Lister, J. R. (1990). Buoyancy-driven fluid fracture: similarity solutions for the horizontal and vertical propagation of fluid-filled cracks. *Journal of Fluid Mechanics*, 217:213–239.

Lister, J. R. and Kerr, R. C. (1991). Fluid-mechanical models of crack propagation and their application to magma transport in dykes. *Journal of Geophysical Research: Solid Earth*, 96(B6):10049–10077.

Lustrino, M. and Carminati, E. (2007). Phantom plumes in Europe and the circum-Mediterranean region. In *Plates, Plumes and Planetary Processes*. Geological Society of America.

Lutz, T. M. and Gutmann, J. T. (1995). An improved method for determining and characterizing alignments of pointlike features and its implications for the pinacate volcanic field, sonora, mexico. *Journal of Geophysical Research: Solid Earth*, 100(B9):17659–17670.

Maccaferri, F., Bonafede, M., and Rivalta, E. (2010). A numerical model of dyke propagation in layered elastic media. *Geophysical Journal International*, 180(3):1107–1123.

Maccaferri, F., Bonafede, M., and Rivalta, E. (2011). A quantitative study of the mechanisms governing dike propagation, dike arrest and sill formation. *Journal of Volcanology and Geothermal Research*, 208(1-2):39–50.

Maccaferri, F., Richter, N., and Walter, T. R. (2017). The effect of giant lateral collapses on magma pathways and the location of volcanism. *Nature communications*, 8(1):1–11.

Maccaferri, F., Rivalta, E., Keir, D., and Acocella, V. (2014). Off-rift volcanism in rift zones determined by crustal unloading. *Nature Geoscience*, 7(4):297–300.

Maccaferri, F., Rivalta, E., Passarelli, L., and Aoki, Y. (2016). On the mechanisms governing dike arrest: Insight from the 2000 miyakejima dike injection. *Earth and Planetary Science Letters*, 434:64–74.

Maccaferri, F., Smittarello, D., Pinel, V., and Cayol, V. (2019). On the propagation path of magma-filled dikes and hydrofractures: The competition between external stress, internal pressure, and crack length. *Geochemistry, Geophysics, Geosystems*, 20(4):2064–2081.

MacLeod, N. S., Sherrod, D. R., Chitwood, L. A., and Jensen, R. A. (1982). *Geologic map of Newberry Volcano, Deschutes, Klamath, and Lake Counties, Oregon*. Geological Survey.

Maerten, F. (2010). Adaptive cross-approximation applied to the solution of system of equations and post-processing for 3d elastostatic problems using the boundary element method. *Engineering Analysis with Boundary Elements*, 34(5):483–491.

Maerten, F., Maerten, L., Plateaux, R., and Cornard, P. (2022). Joint inversion of tectonic stress and magma pressures using dyke trajectories. Technical report, Copernicus Meetings.

Mälzer, H., Hein, G., and Zippelt, K. (1983). Height changes in the rhenish massif: Determination and analysis. In Fuchs, K., von Gehlen, K., Mälzer, H., Murawski, H., and Semmel, A., editors, *Plateau Uplift*, pages 164–176, Berlin, Heidelberg. Springer Berlin Heidelberg.

Mantiloni, L., Davis, T., Gaete, A., and Rivalta, E. (2021a). Gelatin-based analog models simulating dike propagation in the upper crust. https://doi.org/10.5880/GFZ.2.1.2021.001.

Mantiloni, L., Davis, T., Gaete Rojas, A. B., and Rivalta, E. (2021b). Stress inversion in a gelatin box: testing eruptive vent location forecasts with analog models. *Geophysical Research Letters*, 48(6).

Mantiloni, L., Nespoli, M., Belardinelli, M. E., and Bonafede, M. (2020). Deformation and stress in hydrothermal regions: The case of a disk-shaped inclusion in a half-space. *Journal of Volcanology and Geothermal Research*, 403:107011.

Mantiloni, L., Rivalta, E., and Davis, T. (2023a). Mechanical modeling of pre-eruptive magma propagation scenarios at calderas. *Journal of Geophysical Research: Solid Earth*, 128(3):e2022JB025956.

Mantiloni, L., Rivalta, E., and Davis, T. (2023b). Sam: Simplified analytical model of dyke pathways in three dimensions. https://doi.org/10.5880/GFZ.2.1.2023.001.

Martel, S. J. and Muller, J. R. (2000). A two-dimensional boundary element method for calculating elastic gravitational stresses in slopes. *Pure and Applied Geophysics*, 157(6-8):989–1007.

Martí, J., Becerril, L., and Rodríguez, A. (2022). How long-term hazard assessment may help to anticipate volcanic eruptions: The case of la palma eruption 2021 (canary islands). *Journal of Volcanology and Geothermal Research*, page 107669.

Marti, J. and Felpeto, A. (2010). Methodology for the computation of volcanic susceptibility: an example for mafic and felsic eruptions on tenerife (canary islands). *Journal of Volcanology and Geothermal Research*, 195(1):69–77.

Martin, A. J., Umeda, K., Connor, C. B., Weller, J. N., Zhao, D., and Takahashi, M. (2004). Modeling long-term volcanic hazards through bayesian inference: An example from the tohoku volcanic arc, japan. *Journal of Geophysical Research: Solid Earth*, 109(B10).

Martínez-Garzón, P., Bohnhoff, M., Kwiatek, G., and Dresen, G. (2013). Stress tensor changes related to fluid injection at the geysers geothermal field, california. *Geophysical Research Letters*, 40(11):2596–2601.

Marzocchi, W., Sandri, L., and Selva, J. (2008). Bet_ef: a probabilistic tool for long-and short-term eruption forecasting. *Bulletin of Volcanology*, 70:623–632.

Matthews, M. (1993). Statistical inversion of crustal deformation data and estimation of the depth distribution of slip in the 1906 earthquake. *J. geophys. Res.*, 98:12153–12163.

Matthews, M. and Segall, P. (1993). Estimation of depth-dependent fault slip from measured surface deformation with application to the 1906 San Francisco Earthquake. *Journal of Geophysical Research: Solid Earth*, 98(B7):12153–12163.

Mazzarini, F., Le Corvec, N., Isola, I., and Favalli, M. (2016). Volcanic field elongation, vent distribution, and tectonic evolution of a continental rift: The main ethiopian rift example. *Geosphere*, 12(3):706–720.

McGarr, A. and Gay, N. (1978). State of stress in the earth's crust. *Annual Review of Earth and Planetary Sciences*, 6(1):405–436.

McGuire, W. and Pullen, A. (1989). Location and orientation of eruptive fissures and feeder dykes at mount etna; influence of gravitational and regional tectonic stress regimes. *Journal of Volcanology and Geothermal Research*, 38(3-4):325–344.

McKenzie, D. (1978). Some remarks on the development of sedimentary basins. *Earth and Planetary science letters*, 40(1):25–32.

McTigue, D. F. and Mei, C. C. (1981). Gravity-induced stresses near topography of small slope. *Journal of Geophysical Research: Solid Earth*, 86(B10):9268–9278.

McTigue, D. F. and Mei, C. C. (1987). Gravity-induced stresses near axisymmetric topography of small slope. *International Journal for Numerical and Analytical Methods in Geomechanics*, 11(3):257–268.

Mechie, J., Prodehl, C., and Fuchs, K. (1983). The Long-Range Seismic Refraction Experiment in the Rhenish Massif. *In: Fuchs K., von Gehlen K., Mälzer H., Murawski H., Semmel A. (eds) Plateau Uplift. Springer, Berlin, Heidelberg.*

Menand, T., Daniels, K., and Benghiat, P. (2010). Dyke propagation and sill formation in a compressive tectonic environment. *Journal of Geophysical Research: Solid Earth*, 115(B8).

Menke, W. (2012). *Geophysical Data Analysis: Discrete Inverse Theory.* Academic Press, Boston, third edition.

Meyer, W. and Stets, J. (2007). *Quaternary Uplift in the Eifel Area*, pages 369–378. Springer Berlin Heidelberg, Berlin, Heidelberg.

Michon, L., Ferrazzini, V., Di Muro, A., Villeneuve, N., and Famin, V. (2015). Rift zones and magma plumbing system of piton de la fournaise volcano: How do they differ from hawaii and etna? *Journal of Volcanology and Geothermal Research*, 303:112–129.

Michon, L. and Merle, O. (2001). The evolution of the Massif Central Rift; spatio-temporal distribution of the volcanism. *Bulletin de la Société géologique de France*, 172(2):201–211.

Montagna, C. P., Papale, P., and Longo, A. (2022). Magma chamber dynamics at the campi flegrei caldera, italy. In *Campi Flegrei: A Restless Caldera in a Densely Populated Area*, pages 201–217. Springer.

Möri, A. and Lecampion, B. (2022). Three-dimensional buoyant hydraulic fractures: constant release from a point source. *Journal of Fluid Mechanics*, 950:A12.

Muirhead, J. D., Van Eaton, A. R., Re, G., White, J. D., and Ort, M. H. (2016). Monogenetic volcanoes fed by interconnected dikes and sills in the hopi buttes volcanic field, navajo nation, usa. *Bulletin of Volcanology*, 78:1–16.

Müller, B., Zoback, M. L., Fuchs, K., Mastin, L., Gregersen, S., Pavoni, N., Stephansson, O., and Ljunggren, C. (1992). Regional patterns of tectonic stress in europe. *Journal of Geophysical Research: Solid Earth*, 97(B8):11783–11803.

Muller, J. R., Ito, G., and Martel, S. J. (2001). Effects of volcano loading on dike propagation in an elastic half-space. *Journal of Geophysical Research: Solid Earth*, 106(B6):11101–11113.

Muller, O. H. and Pollard, D. D. (1977). The stress state near spanish peaks, colorado determined from a dike pattern. *Pure and Applied Geophysics*, 115(1-2):69–86.

Murakami, Y. et al. (1987). Handbook of stress intensity factors. In *Pergamon Press, Oxford (UK).*, page 1011.

Musacchio, M., Silvestri, M., Rabuffi, F., Buongiorno, M. F., and Falcone, S. (2021). Kīlauea–leilani 2018 lava flow delineation using sentinel2 and landsat8 images. *Geological Society, London, Special Publications*, 519.

Nakada, S., Nagai, M., Kaneko, T., Nozawa, A., and Suzuki-Kamata, K. (2005). Chronology and products of the 2000 eruption of miyakejima volcano, japan. *Bulletin of Volcanology*, 67(3):205–218.

Nakamura, K. (1977). Volcanoes as possible indicators of tectonic stress orientation—principle and proposal. *Journal of Volcanology and Geothermal Research*, 2(1):1–16.

Nakashima, Y. (1993). Static stability and propagation of a fluid-filled edge crack in rock: Implication for fluid transport in magmatism and metamorphism. *Journal of Physics of the Earth*, 41(3):189–202.

Neri, A., Bevilacqua, A., Esposti Ongaro, T., Isaia, R., Aspinall, W. P., Bisson, M., Flandoli, F., Baxter, P. J., Bertagnini, A., Iannuzzi, E., et al. (2015). Quantifying volcanic hazard at campi flegrei caldera (italy) with uncertainty assessment: 2. pyroclastic density current invasion maps. *Journal of Geophysical Research: Solid Earth*, 120(4):2330–2349.

Neri, M., Rivalta, E., Maccaferri, F., Acocella, V., and Cirrincione, R. (2018). Etnean and hyblean volcanism shifted away from the malta escarpment by crustal stresses. *Earth and Planetary Science Letters*, 486:15–22.

Newman, A. V., Dixon, T. H., and Gourmelen, N. (2006). A four-dimensional viscoelastic deformation model for long valley caldera, california, between 1995 and 2000. *Journal of volcanology and geothermal research*, 150(1-3):244–269.

Nielsen, G., Maack, R., Gudmundsson, A., and Gunnarsson, G. I. (2000). Completion of krafla geothermal power plant. In *Proc. World Geothermal Congress*, pages 3259–3264.

Nieto-Torres, A. and Del Pozzo, A. L. M. (2019). Spatio-temporal hazard assessment of a monogenetic volcanic field, near méxico city. *Journal of Volcanology and Geothermal Research*, 371:46–58.

Nikkhoo, M. and Rivalta, E. (2022a). Analytical solutions for gravity changes caused by triaxial volumetric sources. *Geophysical Research Letters*, 49(8):e2021GL095442.

Nikkhoo, M. and Rivalta, E. (2022b). Surface deformations and gravity changes caused by pressurized finite ellipsoidal cavities. *Geophysical Journal International*, 232(1):643–655.

Nikkhoo, M. and Walter, T. R. (2015). Triangular dislocation: an analytical, artefact-free solution. *Geophysical Journal International*, 201(2):1119–1141.

Nikkhoo, M., Walter, T. R., Lundgren, P. R., and Prats-Iraola, P. (2017). Compound dislocation models (CDMs) for volcano deformation analyses. *Geophysical Journal International*, 208(2):877–894.

Nowell, D. A. G., Jones, M. C., and Pyle, D. M. (2006). Episodic Quaternary volcanism in France and Germany. *Journal of Quaternary Science*, 21(6):645–675.

Nunn, J. A. (1996). Buoyancy-driven propagation of isolated fluid-filled fractures: Implications for fluid transport in gulf of mexico geopressured sediments. *Journal of Geophysical Research: Solid Earth*, 101(B2):2963–2970.

O'Hagan, A. and Leonard, T. (1976). Bayes estimation subject to uncertainty about parameter constraints. *Biometrika*, 63(1):201–203.

Okada, Y. (1985). Surface deformation due to shear and tensile faults in a half-space. *Bulletin of the Seismological Society of America*, 75(4):1135–1154.

Okada, Y. (1992). Internal deformation due to shear and tensile faults in a half-space. *Bulletin of the seismological society of America*, 82(2):1018–1040.

Okubo, S. (1992). Gravity and potential changes due to shear and tensile faults in a half-space. *Journal of Geophysical Research: Solid Earth*, 97(B5):7137–7144.

Olson, J. E. (1991). *Fracture mechanics analysis of joints and veins*. Stanford University.

Orsi, G. (2022). Volcanic and deformation history of the campi flegrei volcanic field, italy. *Campi Flegrei: A Restless Caldera in a Densely Populated Area*, pages 1–53.

Orsi, G., De Vita, S., and Di Vito, M. (1996). The restless, resurgent campi flegrei nested caldera (italy): constraints on its evolution and configuration. *Journal of Volcanology and Geothermal Research*, 74(3-4):179–214.

Pansino, S., Emadzadeh, A., and Taisne, B. (2022). Modeling dike propagation in both vertical length and horizontal breadth. *Journal of Geophysical Research: Solid Earth*, page e2022JB024593.

Pansino, S. and Taisne, B. (2019). How magmatic storage regions attract and repel propagating dikes. *Journal of Geophysical Research: Solid Earth*, 124(1):274–290.

Paris, P. C. (2014). A brief history of the crack tip stress intensity factor and its application. *Meccanica*, 49:759–764.

Patrick, M., Orr, T., Anderson, K., and Swanson, D. (2019a). Eruptions in sync: Improved constraints on kīlauea volcano's hydraulic connection. *Earth and Planetary Science Letters*, 507:50–61.

Patrick, M., Swanson, D., and Orr, T. (2019b). A review of controls on lava lake level: insights from halema 'uma 'u crater, kīlauea volcano. *Bulletin of Volcanology*, 81:1–26.

Patrick, M. R., Houghton, B. F., Anderson, K. R., Poland, M. P., Montgomery-Brown, E., Johanson, I., Thelen, W., and Elias, T. (2020). The cascading origin of the 2018 kīlauea eruption and implications for future forecasting. *Nature Communications*, 11(1):1–13.

Peacock, J. R., Mangan, M. T., McPhee, D., and Ponce, D. A. (2015). Imaging the magmatic system of mono basin, california, with magnetotellurics in three dimensions. *Journal of Geophysical Research: Solid Earth*, 120(11):7273–7289.

Pedersen, G. B., Belart, J. M., Óskarsson, B. V., Gudmundsson, M. T., Gies, N., Högnadóttir, T., Hjartardóttir, Á. R., Pinel, V., Berthier, E., Dürig, T., et al. (2022). Volume, effusion rate, and lava transport during the 2021 fagradalsfjall eruption: Results from near real-time photogrammetric monitoring. *Geophysical Research Letters*, 49(13):e2021GL097125.

Pedraza De Marchi, A. C., Ghidella, M. E., Tocho, C. N., and Franzese, J. R. (2021). Flexural uplift and magmatic underplating anomaly on the argentine continental margin: profile at 43.5°s. *Marine Geophysical Research*, 42(2):16.

Peirce, A. and Detournay, E. (2008). An implicit level set method for modeling hydraulically driven fractures. *Computer Methods in Applied Mechanics and Engineering*, 197(33-40):2858–2885.

Peltier, A., Ferrazzini, V., Staudacher, T., and Bachèlery, P. (2005). Imaging the dynamics of dyke propagation prior to the 2000–2003 flank eruptions at piton de la fournaise, reunion island. *Geophysical Research Letters*, 32(22).

Persson, P.-O. and Strang, G. (2004). A simple mesh generator in matlab. *SIAM review*, 46(2):329–345.

Pierdominici, S. and Heidbach, O. (2012). Stress field of italy—mean stress orientation at different depths and wave-length of the stress pattern. *Tectonophysics*, 532:301–311.

Pinel, V., Carrara, A., Maccaferri, F., Rivalta, E., and Corbi, F. (2017). A two-step model for dynamical dike propagation in two dimensions: Application to the july 2001 etna eruption. *Journal of Geophysical Research: Solid Earth*, 122(2):1107–1125.

Pinel, V., Furst, S., Maccaferri, F., and Smittarello, D. (2022). Buoyancy versus local stress field control on the velocity of magma propagation: Insight from analog and numerical modelling. front. *Earth Sci*, 10:838318.

Pinel, V. and Jaupart, C. (2004). Magma storage and horizontal dyke injection beneath a volcanic edifice. *Earth and Planetary Science Letters*, 221(1-4):245–262.

Pinel, V., Smittarello, D., Maccaferri, F., Rivalta, E., and Cayol, V. (2019). Stress field control on magma path and velocity. *AGUFM*, 2019:V12A–01.

Poland, M. P. and Anderson, K. R. (2020). Partly cloudy with a chance of lava flows: Forecasting volcanic eruptions in the twenty-first century. *Journal of Geophysical Research: Solid Earth*, 125(1):e2018JB016974.

Poland, M. P., Moats, W. P., and Fink, J. H. (2008). A model for radial dike emplacement in composite cones based on observations from summer coon volcano, colorado, usa. *Bulletin of Volcanology*, 70:861–875.

Pollard, D. D. (1987). Elementary fracture mechanics applied to the structural interpretation of dykes. In *Mafic dyke swarms*, volume 34, pages 5–24.

Pollard, D. D., Fletcher, R. C., et al. (2005). *Fundamentals of structural geology*. Cambridge University Press.

Pollard, D. D. and Holzhausen, G. (1979). On the mechanical interaction between a fluid-filled fracture and the earth's surface. *Tectonophysics*, 53(1-2):27–57.

Pollard, D. D. and Townsend, M. R. (2018). Fluid-filled fractures in earth's lithosphere: gravitational loading, interpenetration, and stable height of dikes and veins. *Journal of Structural Geology*, 109:38–54.

Poppe, S., Galland, O., de Winter, N., Goderis, S., Claeys, P., Debaille, V., Boulvais, P., and Kervyn, M. (2020). Structural and geochemical interactions between magma and sedimentary host rock: the hovedøya case, oslo rift, norway. *Geochemistry, Geophysics, Geosystems*, 21(3):e2019GC008685.

Poppe, S., Holohan, E. P., Galland, O., Buls, N., Van Gompel, G., Keelson, B., Tournigand, P.-Y., Brancart, J., Hollis, D., Nila, A., et al. (2019). An inside perspective on magma intrusion: Quantifying 3d displacement and strain in laboratory experiments by dynamic x-ray computed tomography. *Frontiers in Earth Science*, 7:62.

Prince, S. J. (2012). *Computer vision: models, learning, and inference.* Cambridge University Press.

Prodehl, C., Mueller, S., and Haak, V. (2006). Chapter 4 The european cenozoic rift system. In Olsen, K., editor, *Continental rifts:evolution, structure, tectonics*, volume 25 of *Developments in Geotectonics*, pages 133–212. Elsevier.

Puchelt, H. (1983). Carbon dioxide in the rhenish massif. In Fuchs, K., von Gehlen, K., Mälzer, H., Murawski, H., and Semmel, A., editors, *Plateau Uplift*, pages 152–152, Berlin, Heidelberg. Springer Berlin Heidelberg.

Rabbath, C. and Corriveau, D. (2019). A comparison of piecewise cubic hermite interpolating polynomials, cubic splines and piecewise linear functions for the approximation of projectile aerodynamics. *Defence Technology*, 15(5):741–757.

Reches, Z. and Fink, J. (1988). The mechanism of intrusion of the inyo dike, long valley caldera, california. *Journal of Geophysical Research: Solid Earth*, 93(B5):4321–4334.

Reddy, J. N. (2019). *Introduction to the finite element method.* McGraw-Hill Education.

Regenauer-Lieb, K. (1998). Dilatant plasticity applied to Alpine collision: ductile void growth in the intraplate area beneath the Eifel volcanic field. *Journal of Geodynamics*, 27(1):1–21.

Reinig, F., Wacker, L., Jöris, O., Oppenheimer, C., Guidobaldi, G., Nievergelt, D., Adolphi, F., Cherubini, P., Engels, S., Esper, J., Land, A., Lane, C., Pfanz, H., Remmele, S., Sigl, M., Sookdeo, A., and Büntgen, U. (2021). Precise date for the Laacher See eruption synchronizes the Younger Dryas. *Nature*, 595(7865):66–69.

Reyes, P. J. D., Bornas, M. A. V., Dominey-Howes, D., Pidlaoan, A. C., Magill, C. R., and Solidum Jr, R. U. (2018). A synthesis and review of historical eruptions at taal volcano, southern luzon, philippines. *Earth-science reviews*, 177:565–588.

Richter, N., Favalli, M., de Zeeuw-van Dalfsen, E., Fornaciai, A., da Silva Fernandes, R. M., Pérez, N. M., Levy, J., Victória, S. S., and Walter, T. R. (2016). Lava flow hazard at fogo volcano, cabo verde, before and after the 2014–2015 eruption. *Natural Hazards and Earth System Sciences*, 16(8):1925–1951.

Rinaldi, A., Todesco, M., and Bonafede, M. (2010). Hydrothermal instability and ground displacement at the campi flegrei caldera. *Physics of the Earth and Planetary Interiors*, 178(3-4):155–161.

Ritter, J. R. R. (2007). *The Seismic Signature of the Eifel Plume*, pages 379–404. Springer Berlin Heidelberg, Berlin, Heidelberg.

Ritter, J. R. R., Jordan, M., Christensen, U. R., and Achaue, U. (2001). A mantle plume below the Eifel volcanic fields, Germany. *Earth and Planetary Science Letters*, 186(1):7–14.

Ritter, J. R. R., Mathar, J. P., Jordan, M., and Gabriel, G. (2007). *Gravity Observations in the Western Rhenish Massif and Forward Modelling of the Eifel Plume Bouguer Anomaly*, pages 465–476. Springer Berlin Heidelberg, Berlin, Heidelberg.

Rivalta, E. (2010). Evidence that coupling to magma chambers controls the volume history and velocity of laterally propagating intrusions. *Journal of Geophysical Research: Solid Earth*, 115(B7).

Rivalta, E., Corbi, F., Passarelli, L., Acocella, V., Davis, T., and Di Vito, M. A. (2019). Stress inversions to forecast magma pathways and eruptive vent location. *Science advances*, 5(7):eaau9784.

Rivalta, E., Taisne, B., Bunger, A., and Katz, R. (2015). A review of mechanical models of dike propagation: Schools of thought, results and future directions. *Tectonophysics*, 638:1–42.

Rizzo, A. L., Faccini, B., Casetta, F., Faccincani, L., Ntaflos, T., Italiano, F., and Coltorti, M. (2021). Melting and metasomatism in West Eifel and Siebengebirge Sub-Continental Lithospheric Mantle: Evidence from concentrations of volatiles in fluid inclusions and petrology of ultramafic xenoliths. *Chemical Geology*, 581:120400.

Roman, A. and Jaupart, C. (2014). The impact of a volcanic edifice on intrusive and eruptive activity. *Earth and Planetary Science Letters*, 408:1–8.

Roman, D. C. and Cashman, K. V. (2006). The origin of volcano-tectonic earthquake swarms. *Geology*, 34(6):457–460.

Roman, D. C., Moran, S. C., Power, J. A., and Cashman, K. V. (2004). Temporal and spatial variation of local stress fields before and after the 1992 eruptions of crater peak vent, mount spurr volcano, alaska. *Bulletin of the Seismological Society of America*, 94(6):2366–2379.

Rubin, A. M. (1995). Propagation of magma-filled cracks. *Annual Review of Earth and Planetary Sciences*, 23(1):287–336.

Rubin, A. M. and Gillard, D. (1998). Dike-induced earthquakes: Theoretical considerations. *Journal of Geophysical Research: Solid Earth*, 103(B5):10017–10030.

Salzer, J. T., Nikkhoo, M., Walter, T. R., Sudhaus, H., Reyes-Dávila, G., Bretón, M., and Arámbula, R. (2014). Satellite radar data reveal short-term pre-explosive displacements and a complex conduit system at volcán de colima, mexico. *Frontiers in Earth Science*, 2:12.

Savage, W., Swolfs, H., and Amadei, B. (1992). On the state of stress in the near-surface of the earth's crust. *Pure and Applied Geophysics*, 138(2):207–228.

Savage, W., Swolfs, H., and Powers, P. (1985). Gravitational stresses in long symmetric ridges and valleys. In *International Journal of Rock Mechanics and Mining Sciences & Geomechanics Abstracts*, volume 22, pages 291–302. Elsevier.

Schmincke, H.-U. (2007). *The Quaternary Volcanic Fields of the East and West Eifel (Germany)*, pages 241–322. Springer Berlin Heidelberg, Berlin, Heidelberg.

Scudero, S., De Guidi, G., and Gudmundsson, A. (2019). Size distributions of fractures, dykes, and eruptions on etna, italy: Implications for magma-chamber volume and eruption potential. *Scientific reports*, 9(1):4139.

Secor Jr, D. T. and Pollard, D. D. (1975). On the stability of open hydraulic fractures in the earth's crust. *Geophysical Research Letters*, 2(11):510–513.

Segall, P. (2010). *Earthquake and Volcano Deformation*, volume 15. Princeton University Press, Princeton, NJ.

Segall, P., Cervelli, P., Owen, S., Lisowski, M., and Miklius, A. (2001). Constraints on dike propagation from continuous gps measurements. *Journal of Geophysical Research: Solid Earth*, 106(B9):19301–19317.

Selva, J., Orsi, G., Di Vito, M. A., Marzocchi, W., and Sandri, L. (2012). Probability hazard map for future vent opening at the campi flegrei caldera, italy. *Bulletin of volcanology*, 74(2):497–510.

Seymour, N., Singleton, J., Mavor, S., Gomila, R., Stockli, D., Heuser, G., and Arancibia, G. (2020). The relationship between magmatism and deformation along the intra-arc strike-slip atacama fault system, northern chile. *Tectonics*, 39(3):e2019TC005702.

Sigmundsson, F., Hooper, A., Hreinsdóttir, S., Vogfjörd, K. S., Ófeigsson, B. G., Heimisson, E. R., Dumont, S., Parks, M., Spaans, K., Gudmundsson, G. B., et al. (2015). Segmented lateral dyke growth in a rifting event at bárdarbunga volcanic system, iceland. *Nature*, 517(7533):191–195.

Sigmundsson, F., Pinel, V., Grapenthin, R., Hooper, A., Halldórsson, S. A., Einarsson, P., Ófeigsson, B. G., Heimisson, E. R., Jónsdóttir, K., Gudmundsson, M. T., Vogfjörd, K., Parks, M., Li, S., Drouin, V., Geirsson, H., Dumont, S., Fridriksdottir, H. M., Gudmundsson, G. B., Wright, T. J., and Yamasaki, T. (2020). Unexpected large eruptions from buoyant magma bodies within viscoelastic crust. *Nature Communications*, 11(1):2403.

Sigurdsson, H., Carey, S., Alexandri, M., Vougioukalakis, G., Croff, K., Roman, C., Sakellariou, D., Anagnostou, C., Rousakis, G., Ioakim, C., et al. (2006). Marine investigations of greece's santorini volcanic field. *Eos, Transactions American Geophysical Union*, 87(34):337–342.

Silverman, B. W. (1986). *Density estimation for statistics and data analysis*, volume 26. CRC press.

Sizikov, V. S. et al. (2011). Well-posed, ill-posed, and intermediate problems with applications. In *Well-posed, Ill-posed, and Intermediate Problems with Applications*. De Gruyter.

Slim, M., Perron, J. T., Martel, S. J., and Singha, K. (2015). Topographic stress and rock fracture: A two-dimensional numerical model for arbitrary topography and preliminary comparison with borehole observations. *Earth Surface Processes and Landforms*, 40(4):512–529.

Smith, V., Isaia, R., and Pearce, N. (2011). Tephrostratigraphy and glass compositions of post-15 kyr campi flegrei eruptions: implications for eruption history and chronostratigraphic markers. *Quaternary Science Reviews*, 30(25-26):3638–3660.

Smittarello, D. (2019). *Propagation des intrusions basaltiques. Modélisation analogique et suivi temporel par inversion des données de déplacements*. PhD thesis, Université Grenoble Alpes.

Smittarello, D., Smets, B., Barrière, J., Michellier, C., Oth, A., Shreve, T., Grandin, R., Theys, N., Brenot, H., Cayol, V., et al. (2022). Precursor-free eruption triggered by edifice rupture at nyiragongo volcano. *Nature*, 609(7925):83–88.

Spacapan, J. B., Galland, O., Leanza, H. A., and Planke, S. (2017). Igneous sill and finger emplacement mechanism in shale-dominated formations: a field study at cuesta del chihuido, neuquén basin, argentina. *Journal of the Geological Society*, 174(3):422–433.

Sparks, R. S. J. (2003). Forecasting volcanic eruptions. *Earth and Planetary Science Letters*, 210(1-2):1–15.

Steketee, J. (1958). On volterra's dislocations in a semi-infinite elastic medium. *Canadian Journal of Physics*, 36(2):192–205.

Stephansson, O. (1988). Ridge push and glacial rebound as rock stress generators in fennoscandia. *Bulletin of the Geological Institutions of the University of Uppsala*, 14:39–48.

Tada, H., Paris, P., and Irwin, G. (2000). American society of mechanical engineers., asm international., the stress analysis of cracks handbook.

Taira, T. and Brenguier, F. (2016). Response of hydrothermal system to stress transients at lassen volcanic center, california, inferred from seismic interferometry with ambient noise. *Earth, Planets and Space*, 68(1):1–13.

Taisne, B., Tait, S., and Jaupart, C. (2011). Conditions for the arrest of a vertical propagating dyke. *Bulletin of Volcanology*, 73(2):191–204.

Takada, A. (1997). Cyclic flank-vent and central-vent eruption patterns. *Bulletin of volcanology*, 58(7):539–556.

Thybo, H. and Artemieva, I. (2013). Moho and magmatic underplating in continental lithosphere. *Tectonophysics*, 609:605–619.

Tibaldi, A. (2004). Major changes in volcano behaviour after a sector collapse: insights from stromboli, italy. *Terra Nova*, 16(1):2–8.

Todesco, M., Neri, A., Esposti Ongaro, T., Papale, P., and Rosi, M. (2006). Pyroclastic flow dynamics and hazard in a caldera setting: Application to phlegrean fields (italy). *Geochemistry, Geophysics, Geosystems*, 7(11).

Townsend, M. and Huber, C. (2020). A critical magma chamber size for volcanic eruptions. *Geology*, 48(5):431–435.

Townsend, M. R., Pollard, D. D., and Smith, R. P. (2017). Mechanical models for dikes: A third school of thought. *Tectonophysics*, 703:98–118.

Trasatti, E., Bonafede, M., Ferrari, C., Giunchi, C., and Berrino, G. (2011). On deformation sources in volcanic areas: modeling the campi flegrei (italy) 1982–84 unrest. *Earth and Planetary Science Letters*, 306(3-4):175–185.

Trasatti, E., Polcari, M., Bonafede, M., and Stramondo, S. (2015). Geodetic constraints to the source mechanism of the 2011–2013 unrest at campi flegrei (italy) caldera. *Geophysical Research Letters*, 42(10):3847–3854.

Troise, C., De Natale, G., Pingue, F., Obrizzo, F., De Martino, P., Tammaro, U., and Boschi, E. (2007). Renewed ground uplift at Campi Flegrei caldera (Italy): New insight on magmatic processes and forecast. *Geophysical Research Letters*, 34(3).

Uhira, K., Baba, T., Mori, H., Katayama, H., and Hamada, N. (2005). Earthquake swarms preceding the 2000 eruption of miyakejima volcano, japan. *Bulletin of Volcanology*, 67(3):219–230.

Urbani, S., Acocella, V., Rivalta, E., and Corbi, F. (2017). Propagation and arrest of dikes under topography: Models applied to the 2014 bardarbunga (iceland) rifting event. *Geophysical Research Letters*, 44(13):6692–6701.

Valentine, G. A. and Krogh, K. E. (2006). Emplacement of shallow dikes and sills beneath a small basaltic volcanic center–the role of pre-existing structure (paiute ridge, southern nevada, usa). *Earth and Planetary Science Letters*, 246(3-4):217–230.

Van Camp, M., de Viron, O., Scherneck, H.-G., Hinzen, K.-G., Williams, S. D. P., Lecocq, T., Quinif, Y., and Camelbeeck, T. (2011). Repeated absolute gravity measurements for monitoring slow intraplate vertical deformation in western Europe. *Journal of Geophysical Research: Solid Earth*, 116(B8).

van Otterloo, J. and Cruden, A. R. (2016). Rheology of pig skin gelatine: Defining the elastic domain and its thermal and mechanical properties for geological analogue experiment applications. *Tectonophysics*, 683:86–97.

Ventura, G., Vilardo, G., and Bruno, P. P. (1999). The role of flank failure in modifying the shallow plumbing system of volcanoes: an example from somma-vesuvius, italy. *Geophysical Research Letters*, 26(24):3681–3684.

Volterra, V. (1907). Sur l'équilibre des corps élastiques multiplement connexes. In *Annales scientifiques de l'École normale supérieure*, volume 24, pages 401–517.

Wadge, G., Young, P., and McKendrick, I. (1994). Mapping lava flow hazards using computer simulation. *Journal of Geophysical Research: Solid Earth*, 99(B1):489–504.

Walker, K., Bokelmann, G., Klemperer, S., and Bock, G. (2007). The Eifel Plume Team (2007) Seismic Anisotropy in the Asthenosphere Beneath the Eifel Region, Western Germany. *In: Ritter J.R.R., Christensen U.R. (eds) Mantle Plumes. Springer, Berlin, Heidelberg.*

Walter, T. R., Troll, V. R., Cailleau, B., Belousov, A., Schmincke, H.-U., Amelung, F., et al. (2005). Rift zone reorganization through flank instability in ocean island volcanoes: an example from tenerife, canary islands. *Bulletin of Volcanology*, 67(4):281–291.

Watanabe, T., Masuyama, T., Nagaoka, K., and Tahara, T. (2002). Analog experiments on magma-filled cracks. *Earth, planets and space*, 54(12):1247–1261.

Weertman, J. (1971). Theory of water-filled crevasses in glaciers applied to vertical magma transport beneath oceanic ridges. *Journal of Geophysical Research*, 76(5):1171–1183.

Wessel, P., Smith, W. H., Scharroo, R., Luis, J., and Wobbe, F. (2013). Generic mapping tools: improved version released. *Eos, Transactions American Geophysical Union*, 94(45):409–410.

White, B. R. and Chambefort, I. (2016). Geothermal development history of the taupo volcanic zone. *Geothermics*, 59:148–167.

Wilson, M. and Downes, H. (1992). Mafic alkaline magmatism associated with the European Cenozoic rift system. *Tectonophysics*, 208(1):173–182.

Wiprut, D. and Zoback, M. (2000). Constraining the stress tensor in the visund field, norwegian north sea: Application to wellbore stability and sand production. *International Journal of Rock Mechanics and Mining Sciences*, 37(1-2):317–336.

Wright, T. J., Sigmundsson, F., Pagli, C., Belachew, M., Hamling, I. J., Brandsdóttir, B., Keir, D., Pedersen, R., Ayele, A., Ebinger, C., et al. (2012). Geophysical constraints on the dynamics of spreading centres from rifting episodes on land. *Nature Geoscience*, 5(4):242–250.

Wrona, T., Magee, C., Fossen, H., Gawthorpe, R., Bell, R., Jackson, C.-L., and Faleide, J. (2019). 3-D seismic images of an extensive igneous sill in the lower crust. *Geology*, 47(8):729–733.

Wüllner, U., Christensen, U. R., and Jordan, M. (2006). Joint geodynamical and seismic modelling of the Eifel plume. *Geophysical Journal International*, 165(1):357–372.

Xu, W. and Jónsson, S. (2014). The 2007–8 volcanic eruption on jebel at tair island (red sea) observed by satellite radar and optical images. *Bulletin of Volcanology*, 76(2):1–14.

Xu, W., Jónsson, S., Corbi, F., and Rivalta, E. (2016). Graben formation and dike arrest during the 2009 harrat lunayyir dike intrusion in saudi arabia: Insights from insar, stress calculations and analog experiments. *Journal of Geophysical Research: Solid Earth*, 121(4):2837–2851.

Yabuki, T. and Matsu'ura, M. (1992). Geodetic data inversion using a Bayesian information criterion for spatial distribution of fault slip. *Geophysical Journal International*, 109(2):363–375.

Yang, S., Huang, L., Xie, F., Cui, X., and Yao, R. (2014). Quantitative analysis of the shallow crustal tectonic stress field in china mainland based on in situ stress data. *Journal of Asian Earth Sciences*, 85:154–162.

Yang, X.-M., Davis, P. M., and Dieterich, J. H. (1988). Deformation from inflation of a dipping finite prolate spheroid in an elastic half-space as a model for volcanic stressing. *Journal of Geophysical Research: Solid Earth*, 93(B5):4249–4257.

Zhan, Y., Roman, D. C., Le Mével, H., and Power, J. A. (2022). Earthquakes indicated stress field change during the 2006 unrest of augustine volcano, alaska. *Geophysical Research Letters*, page e2022GL097958.

Zia, H. and Lecampion, B. (2020). Pyfrac: A planar 3d hydraulic fracture simulator. *Computer Physics Communications*, 255:107368.

Ziegler, P. A. (1992). European Cenozoic rift system. *Tectonophysics*, 208(1):91–111.

Ziv, A., Rubin, A. M., and Agnon, A. (2000). Stability of dike intrusion along preexisting fractures. *Journal of Geophysical Research: Solid Earth*, 105(B3):5947–5961.

Zoback, M. D. and Healy, J. H. (1992). In situ stress measurements to 3.5 km depth in the cajon pass scientific research borehole: implications for the mechanics of crustal faulting. *Journal of Geophysical Research: Solid Earth*, 97(B4):5039–5057.

Zoback, M. L. (1992). First-and second-order patterns of stress in the lithosphere: The world stress map project. *Journal of Geophysical Research: Solid Earth*, 97(B8):11703–11728.

Zoback, M. L., Zoback, M. D., Pakiser, L., and Mooney, W. (1989). Tectonic stress field of the continental united states. *Geophysical framework of the continental United States*, 172:523–539.